GENETIC ALGORITHM OPTIMIZATION OF A FILM COOLING ARRAY ON A MODERN TURBINE INLET VANE

DISSERTATION

Jamie J. Johnson, Major, USAF

AFIT/DS/ENY/12-02

DEPARTMENT OF THE AIR FORCE
AIR UNIVERSITY

AIR FORCE INSTITUTE OF TECHNOLOGY

Wright-Patterson Air Force Base, Ohio

AFIT/DS/ENY/12-02

GENETIC ALGORITHM OPTIMIZATION OF A FILM COOLING ARRAY ON A MODERN TURBINE INLET VANE

DISSERTATION

Presented to the Faculty

Department of Aeronautical and Astronautical Engineering

Graduate School of Engineering and Management

Air Force Institute of Technology

Air University

Air Education and Training Command

In Partial Fulfillment of the Requirements for the

Degree of Doctor of Philosophy in Aeronautical Engineering

Jamie J. Johnson, B.S.A.E, M.S.A.E

Major, USAF

September 2012

AFIT/DS/ENY/12-02

GENETIC ALGORITHM OPTIMIZATION OF A FILM COOLING ARRAY ON A MODERN TURBINE INLET VANE

DISSERTATION

Jamie J. Johnson, B.S.A.E., M.S.A.E.

Major, USAF

Approved:

//SIGNED//	30 Aug 2012
Paul I. King	Date
//SIGNED//	30 Aug 2012
John P. Clark	Date
//SIGNED//	30 Aug 2012
Marc D. Polanka	Date
//SIGNED//	30 Aug 2012
Patrick Chapin	Date

Accepted:

//SIGNED//	30 Aug 2012
M. U. Thomas Dean, Graduate School of Engineering Management	Date

Abstract

In response to the need for more advanced gas turbine cooling design methods that factor in the 3-D flowfield and heat transfer characteristics, this study involves the computational optimization of a pressure side film cooling array on a modern turbine inlet vane. Latin hypersquare sampling, genetic algorithm reproduction, and Reynolds-Averaged Navier Stokes (RANS) computational fluid dynamics (CFD) as an evaluation step are used to assess a total of 1,800 film cooling designs over 13 generations. The process was efficient due to the *Leo* CFD code's ability to estimate cooling mass flux at surface grid cells using a transpiration boundary condition, eliminating the need for remeshing between designs. The optimization resulted in a unique cooling design relative to the baseline with new injection angles, compound angles, cooling row patterns, hole sizes, a redistribution of cooling holes away from the over-cooled midspan to hot areas near the shroud, and a lower maximum surface temperature. To experimentally confirm relative design trends between the optimized and baseline designs, flat plate infrared thermography assessments were carried out at design flow conditions. Use of flat plate experiments to model vane pressure side cooling was justified through a conjugate heat transfer CFD comparison of the 3-D vane and flat plate which showed similar cooling performance trends at multiple span locations. The optimized flat plate model exhibited lower minimum surface temperatures at multiple span locations compared to the baseline. Overall, this work shows promise of optimizing film cooling to reduce design cycle time and save cooling mass flow in a gas turbine.

Acknowledgments

This thesis effort would not have been possible without a certain special group of people. First, I am indebted to my faculty advisor, Dr. Paul I. King, for approving this thesis idea and for his guidance and support throughout the research process. The insight and experience pertaining to my study area was very helpful. Next, I would like to give many thanks to my thesis sponsor and friend, Dr. John P. Clark, from the Air Force Research Laboratory's Propulsion Directorate (AFRL/RZ), for his vast amount of persistent technical advice, design knowledge, and assistance during the execution of this comprehensive thesis work. Additionally, I would like to thank the remaining members of my research committee, Dr. Marc Polanka and Dr. Patrick Chapin for spending a great deal of time and energy reviewing my work and making it more complete. Thank you all for sustaining the critical thinking in my head with respect to all aspects of this work.

I would also like to thank the following people: Mr. Charles Stevens, AFRL/RZTT branch chief, for allowing me to do my dissertation work with the branch and take up office space in his branch for a second time, Dr. Richard Anthony for his rigorous evaluation and distribution of blowdown facility data, Mrs. Emilee Brown for help with document presentation, Dr. Andrew Lethander for his assistance in operating the experimental cooling rig, Mr. Bob Wirrig and Mr. Aaron Brown, Test Cell 21 technicians, for making all instrumentation and flowpath preparations for infrared experiments, Mr. Michael Ooten for his programming assistance and computational contributions in the optimization phase of this work, Mr. Pete Koch for help with CAD work and assessment of conjugate results, Dean Johnson, Jim Hendershot, and Jim Downs at Florida Turbine Technologies for their support in fabrication of flat plate articles, and Dr. Bob Ni and Will Humber at Aerodynamic Solutions for their constant support regarding running and validating the different fluid dynamics codes. Finally, I thank the student body and AFIT faculty and staff for their friendliness and support during my second tour at AFIT.

Jamie J. Johnson

Table of Contents

List of Figures

List of Tables

List of Symbols

Alphabetical

A	= cooling hole area
a	= dielectric (kapton) thickness
b	= airfoil axial chord
c_p	= specific heat capacity
C	= correlation constant
D	= cooling hole diameter
DR	= density ratio
E	= energy
F	= viscous fluxes
f	= fraction of wall cells requiring injection
h	= heat transfer coefficient
I	= momentum flux ratio
i	= axial grid plane
j	= tangential grid plane
j	= number of cells from wall
k	= radial grid plane
k	= thermal conductivity; turbulent kinetic energy
L	= cooling hole length
M	= blowing ratio; Mach number
n	= grid cell height
Nu	= Nusselt number
P	= pressure; cooling hole pitch
Pr	= Prandtl number
$P_{t,c}/P_{t,\infty}$	= coolant-to-mainstream total pressure ratio
Q	= source term; heat removed
q''	= heat flux
Δq_r	= net heat flux reduction
Re	= Reynolds number
S	= cooling hole row spacing; hole size
s	= equivalent slot height
T	= temperature
$T_{t,c}/T_{t,\infty}$	= coolant-to-mainstream total temperature ratio
Tu	= turbulence intensity
u_τ	= friction velocity
U	= freestream flow velocity
x	= streamwise or axial distance
y	= cell height at wall; lateral distance
y^+	= near-wall grid thickness Reynolds number
z	= spanwise distance; radial distance

Acronym

AFRL	= Air Force Research Laboratory
BEM	= boundary element method
CAD	= computer-aided drafting
CEEF	= cooling estimated external flow
CFD	= computational fluid dynamics
CHT	= conjugate heat transfer
CRVP	= counter-rotating vortex pair
DJFC	= double-jet film cooling
DOE	= design of experiments
EDM	= electro-discharge machining
GA	= genetic algorithm
HIT	= High Impact Technologies
HPT	= high pressure turbine
ID	= inner diameter (hub)
IRT	= infrared thermography
LE	= leading edge
LES	= large-eddy simulation
LHS	= Latin hypersquare sampling
MTS	= mini-trench shaped hole
NHFR	= net heat flux reduction
NTR	= net temperature reduction
OD	= outer diameter (shroud)
PS	= pressure side [of vane]
RANS	= Reynolds-Averaged Navier-Stokes
RTV	= Research Turbine Vane
SQP	= sequential quadratic programming
SS	= suction side [of vane]
SST	= shear stress transport
TBC	= thermal barrier coating
TE	= trailing edge
TRF	= Turbine Research Facility
VKI	= Von Karman Institute

Greek

α	= injection angle
β	= compound angle
Δ	= change in value
δ	= boundary layer thickness
ε	= turbulent eddy dissipation rate
η	= adiabatic effectiveness
$\bar{\eta}$	= laterally-averaged adiabatic effectiveness
μ	= dynamic viscosity
ρ	= density
τ	= fluid shear at wall

ϕ = overall effectiveness
ω = specific turbulence dissipation

Subscript

0 = total; pertaining to original state
1 = first cooling hole row
2 = second cooling hole row
aavg = area-averaged
aw = adiabatic wall
c = cooling air
f = film-cooled; fluid
g = gas
e = cooling hole exit
ex = mainstream exit condition
i = cooling hole inlet
in = mainstream inlet condition
is = isentropic
m = metal
max = maximum
min = minimum
nw = near-wall
p = constant pressure
r = recovery
s = surface; solid
t = total
tot = total
u = uncooled
w = wall
x = axial
∞ = freestream or mainstream gas

To Sheana, Owen, Elliot,

and Family

GENETIC ALGORITHM OPTIMIZATION OF A FILM COOLING ARRAY ON A MODERN TURBINE INLET VANE

I. Introduction

Motivation

For aircraft gas turbine engines, durability, thermal efficiency, and power output are all a direct function of inlet temperature in the turbine. Therefore, the physical condition of this location in the engine is crucial to satisfactory performance and engine life. Future gas turbines require ever-increasing high-pressure turbine (HPT) inlet temperatures and higher power engine cycles. Therefore, durability design measures for these components must continue to meet this challenge through the modernization of fundamental cooling design methods, employment of today's computational power in providing estimates of performance, and by using thorough heat transfer experimental techniques, all while maintaining or decreasing design cycle time. Turbine cooling technologies have been developing for well over fifty years. Convective internal turbine cooling, external film-cooling, high-temperature materials and surface thermal barrier coatings have allowed significant advancements in the tolerable maximum temperatures for engine operation. Of all of these, external film cooling has provided the greatest leaps in HPT inlet temperatures. However, while internal impingement and transpiration cooling technologies are further advancing the trend, external film cooling on turbine vanes and blades is still a highly-studied field in academia and industry despite modern turbine vanes having only showerhead leading edge arrays and shaped cooling holes as a result of the many years of study [1]. More work is required to capture primary lessons learned from external film cooling studies over the years, determine better methods for

film cooling design on realistic engine component geometries, and make the best use of available fluid dynamic and heat transfer simulation tools. Figure 1 [1] is the evolution of thermal management trends for air-breathing turbomachinery in the inlet of the HPT.

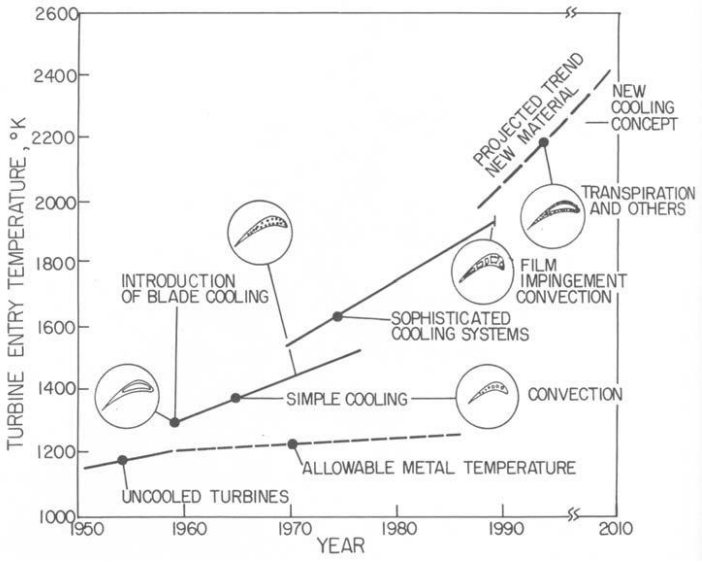

Figure 1 - Past and future trends in turbine inlet temperature requirements and cooling [1].

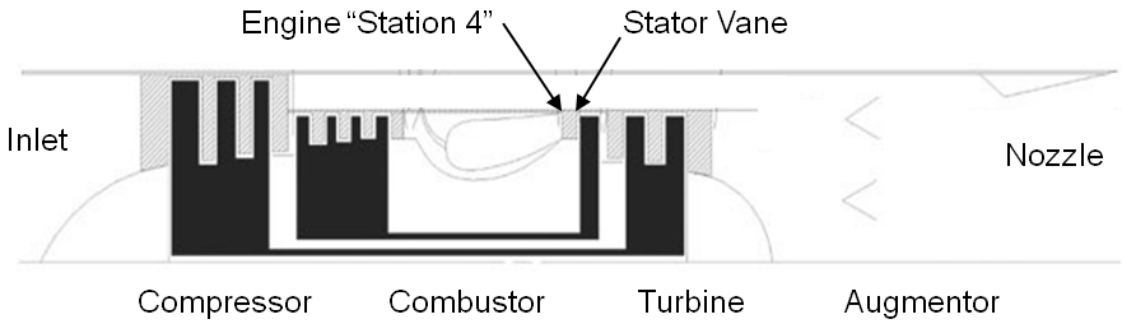

Figure 2 - Traditional low-bypass turbofan engine and inlet vane (stator) location [2].

The turbine inlet vane leading edge is pointed out in Figure 2. It is often called "station 4" within the engine [2]. The cross-section of a typical two-spool turbofan engine can be seen which has an inlet, compressor, combustor, turbine, augmentor, and exit nozzle. Rotating components are black and stationary components are gray. The

inlet vane just downstream of Station 4 is the focus of this work, as it is typically the hottest and most-cooled component in the engine.

Due to incoming products from the upstream combustor, turbine inlet temperatures can be over 1800 K in modern high-demand aircraft engines [1]. These temperatures are commonly well above material limits in the turbine. In addition, HPT components are the most highly stressed components of the engine.

Durability design is challenging because it requires that HPT cooling designs be more effective and that these use cooling air more sparingly to maintain engine efficiency requirements while providing enough cooling to increase component life. Due to loss of mass flow in the compressor, only a limited fraction of overall flow through the engine can be used as coolant before adversely affecting engine performance [3]. Increased compressor bleed air for cooling purposes leads to a performance penalty that is undesirable to the compressor designer as well as the operator. Therefore it is important that turbine designers to cease attempts at increasing cooling flow and instead improve predictions of film-cooled heat loads so they can be mitigated in order to meet future performance goals.

Extreme operating conditions can cause costly maintenance and reductions in system availability not conducive with high-tempo wartime operations. Turbine components subject to high thermal stresses and temperatures are constantly susceptible to failure mechanisms such as cracking, hot corrosion, high-temperature oxidation, and thermal fatigue. Therefore, much of the motivation for research up to now concerns limiting adverse effects in turbines due to hot gases. With ever-increasing trends of thrust-to-weight requirements in new military, commercial and civil aircraft applications

and knowing gas turbine engines will be used in the vast majority of systems over the next century and beyond, research regarding the thermal performance limits of gas turbines is more important than ever before.

Concerning design of gas turbines, historically, effort in perfecting the aerodynamics has overshadowed work done to better understand the heat transfer on turbine airfoils. While many experimental assessments and computational simulations have been done to evaluate a given airfoil shape and cooling configuration, limited optimization work has been accomplished specifically with the goal of reducing the surface temperature and increasing cooling effectiveness. The lack of design work for external film cooling is likely due to the complexities in the three-dimensional, transonic, turbulent mainstream and secondary flows encountered in modern turbine passages with coolant introduction through numerous holes. As increased performance characteristics relate to higher temperatures, and as designers pave the way to future durability technologies, the primary concern should pertain to designing components that perform well under high heat loads relative to previous engine designs. Unlike validation against experiments for pressure phenomena, few computational fluid dynamics (CFD) works in open literature are validated for heat transfer and this is still an emerging area of study. As such, turbine-related heat transfer issues and its prediction accuracy are becoming more critical.

This particular body of work involves the redesign and optimization of a gas turbine engine inlet vane pressure side (PS) film cooling configuration. This work aims to compare a modern film cooling array design to a computationally optimized design and determine the feasibility of such a process in practical design methodologies. The

optimized film cooling design is based purely on placement and orientation of cooling features. As will be shown later in this dissertation, film cooling performance is highly dependent on these variables.

Film cooling is named as such because the cooling flow originating from the internal plenums of turbine vanes and blades passes through passages drilled through surfaces exposed to the hot gas and is smeared out into a film by the fast-moving main flow. Film cooling ultimately creates areas on the surface of lower temperature relative to the freestream. The magnitude of surface temperature of turbomachinery airfoils is due to combined effects of the internal cooling, external cooling film and main flow hot gases. Thermal characteristics over the surface of a vane may vary greatly due to the discrete nature of cooling holes and predicting these characteristics accurately using computational tools can be difficult.

With increased computational capabilities in terms of memory and processing speeds combined with the necessity for future air-breathing engine systems to rely on film-cooling for durability, CFD representations of operationally-realistic configurations in engine-representative flow conditions is necessary. As most of the previous computational studies of film cooling, which often examine one cooling hole or rows of holes, have advantages in understanding the flow physics, current computational capabilities allow simulation of 3-D true-geometry fully-cooled high pressure turbine (HPT) component designs. Such simulations can be used as an accurate evaluation tool for various cooling designs. This research involves the combined use of CFD, genetic algorithm optimization, and experimental measurements to ideally change how future durability engineers efficiently generate reliable film cooling designs.

This work is part of ongoing research at the Air Force Research Laboratory Aerospace Systems Directorate Turbine Division, Turbine Branch (AFRL/RQTT). The reported results of this work will provide critical data to the High Impact Technologies (HIT) Program and pertains to Potential Capability Area #19 of 30 within the Air Force Chief Scientist's Technology Horizons 2010-2030 [5] concerning next-generation high-efficiency turbine engines. Among the 30 PCAs laid out, #19 focuses specifically on component thermal management and is also identified as 1 of 12 PCAs that are categorized to be of highest priority.

Problem Statement

This dissertation addresses the need to update film cooling design methods by creating a new film cooling array using computational optimization and further proving the concept using experiments on flat plate models. In the past, durability designers used rules of thumb and rough correlations based on thirty-year old experiments on basic geometries to obtain streamwise heat transfer properties in order to place cooling holes on stationary and rotating 3-D turbine components. Naturally, much like pressure field phenomena, the heat transfer distribution over the surface of a turbine inlet vane is due to three-dimensional effects. Film cooling performance at one span location cannot be assumed for all span locations. By considering the aerodynamic effects on heat transfer, and with the right tools and updated processes, more efficient placement and design of cooling holes can be achieved. The redesign and optimization of an inlet vane pressure side film cooling array should ideally be:

- **Accurate**: Design methods must use models and CFD that compare well against experimental data through validation tests.
- **Efficient**: Design cycle times must be conserved or decreased if a new film cooling design method is to be widely accepted. The current work takes advantage of increased computational capabilities in evaluating thousands of candidate designs that estimate cooling mass flow using a transpiration boundary condition. This external-flow only type of CFD reduces mesh size, eliminates the need for meshing internal passages of cooling holes, and eliminates the need for remeshing between designs for optimization on parts with constant three-dimensional shape.
- **Practical**: The result of a film cooling optimization or other type of redesign must be translatable to a real engine or at least a ground test rig. Unlike many new film cooling hole designs being studied currently, the new cooling design must have traits and features that are manufacturable, survivable in the harsh engine environment, and not exorbitantly expensive to make.

This work attempts to achieve all three aspects above by varying only the locations, sizes, patterns, and orientation angles of the cooling holes on the pressure side of a modern turbine vane while keeping flow conditions and 3-D airfoil shape constant.

Research Objectives

The primary objective of this project is to demonstrate the feasibility of computationally optimizing a film cooling array in short order using CFD evaluations that yield good accuracy. The primary hypothesis of this problem is that through modern

optimization methods and rigorous yet efficient computational and experimental evaluations, a 3-D HPT vane PS film cooling configuration can be generated that exhibits reduced peak temperatures, reduced area-averaged temperatures, and decreases the magnitude of hot spots within an acceptable amount of processing time. Both the starting point, or baseline vane cooling array, and the optimized PS cooling design are assessed in both CFD and experiments to provide validation of the optimization method. Consequently, specific objectives of this work are:

1. To use current optimization techniques, a novel Turbomachinery Design and Analysis System (TDAAS) [6] used by the Air Force Research Laboratory, and a valid external flow Reynolds-Averaged Navier Stokes (RANS) CFD code called *Leo* to evaluate hundreds of intermediate designs and redesign a baseline vane film cooling array by exploring different film cooling variables and ranges in the problem space.

2. To justify the use of flat plate models in infrared experiments to represent 3-D vane pressure side cooling characteristics, full grid conjugate heat transfer (CHT) CFD predictions of heat transfer characteristics are performed to compare the 3-D vane geometry to the flat plate PS model geometry. CHT CFD, the second type of CFD used in this work, provides more realistic simulations because it includes the combined effects of solid conduction and fluid convection in the predictions.

3. To perform repeatable, non-intrusive, steady-state experimental assessments of cooling performance of the baseline and optimized cooling arrays using full map infrared thermography on flat plate film cooled models that matches the scale, materials, pressure ratios, temperature ratios, and cooling geometry on both the baseline and optimized vane cooling arrays.

4. To help design the second build of AFRL/RQTT's High Impact Technologies Research Turbine Vane (RTV) based on the computationally optimized cooling array and experimental results from infrared thermography experiments to determine the best cooling hole shapes to be chosen. Custom electro-discharge machining (EDM) on available vanes will be done followed by heat flux instrumentation and full testing in the Turbine Research Facility (TRF) blowdown rig. This can then be compared to TRF testing on the vanes with the baseline pressure side film cooling array in future work.

In addition, there are secondary objectives within the overall project that add value to the current research plan and add confidence to the results:

- To validate a 3-D RANS, cooling-estimated external flow (CEEF), turbomachinery CFD code called *Leo* using a modern fully film cooled vane geometry at design engine-representative conditions against experimental temperature and heat flux data obtained by the AFRL TRF blowdown ground test rig. Cooling estimation refers to the transpiration boundary condition used to model film cooling which is addressed in the methodology. External flow means that only the fluid flowing around the outside of the part is being simulated. This validation provides added confidence in the accuracy of the film cooling array design and optimization process.
- To validate a 3-D RANS, CHT, turbomachinery CFD code also called *Leo* using a modern fully film cooled vane geometry at design engine-representative conditions against experimental temperature and heat flux data obtained by the AFRL TRF blowdown ground test rig. CHT CFD results provide insights that

CEEF CFD cannot. A summary of the two types of CFD used is given in the methodology section of this dissertation.

The details and methodology of each goal in this study will be elaborated on in later sections of this paper. Figure 3 is a summary of the work presented in this dissertation based on the objectives described above. Data available from TRF blowdown rig tests on the modern RTV with film cooling was the impetus for this project. The end product from this work, as stated in objective 4, is an optimized array that can eventually be tested in the TRF. The figure also points out in which chapter each topic's results are discussed. The following work takes steps towards a modern solution to a long-studied area in turbomachinery design and contributes to more efficient ways to cool gas turbine components.

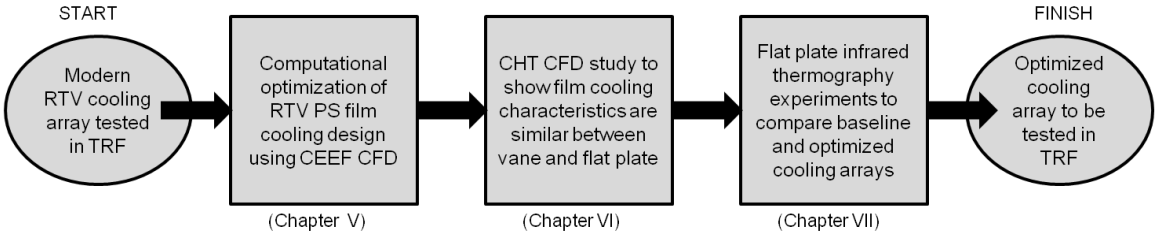

Figure 3 – Dissertation research flow chart.

Preview

The remainder of this dissertation is divided into the following chapters:

II. Background regarding all pertinent theory regarding film cooling, key parameters, origins, and respective equations considered for the problem at hand. The case is made for why a turbine inlet vane pressure side is chosen for this study. The fundamentals of conjugate heat transfer are also outlined here.

III. A review of applicable literature pertaining to: 3-D CFD modeling of high pressure turbine airfoils with and without cooling, conjugate heat transfer CFD on turbine components, design and optimization efforts for turbomachinery and film cooling, a summary of film cooling experiments that use infrared thermography and those that are more like the TRF full scale blowdown rig, and finally a synopsis of novel film cooling hole shapes that are emerging in industry and academia.

IV. Discussion describing the primary article of study, the Research Turbine Vane (RTV), and the methodologies of both the computational and experimental assessments performed on the baseline film cooling design as well as the optimized design will be laid out. Details will be given for both types of CFD used here as well as both types of experiments involved in this work. The fine points of the optimization process are covered here as well.

V. The results of the optimization in general are given as well as CEEF CFD comparisons of the baseline and optimized RTV PS cooling designs.

VI. The results of the 3-D CHT CFD comparisons of the baseline film cooling design on the RTV PS and the flat plate geometries are outlined here.

VII. The results of the flat plate IRT experiments on the uncooled, baseline cooled, and four optimized cooled plates with different cooling hole shapes is covered here.

VIII. All conclusions from all parts of this dissertation work are summarized along with suggested future work.

Through this structure it is seen that this effort has three primary areas of emphasis: design optimization, CFD assessment, and experimental assessment. This

allows for robust examination of both the baseline cooling design and the optimized design.

II. Background and Theory

Heat Transfer in Gas Turbines

The work pioneered by Dunn and Stoddard [7] resulted in some of the first significant experimental transient spatially resolved heat transfer data recorded in turbine-representative flows. Working with a state-of-the-art stator vane half-annulus sector, demonstrating a reputable short flow duration shock tunnel facility, and using pyrex-platinum heat flux gauge technology, which was difficult at the time to fabricate and install, they were able to discover trends in the heat transfer in a turbine environment not seen before and identify heat transfer problem areas. These areas are near the trailing edge of the vane suction side (SS), on the hub wall and end wall near the SS, and near the leading edge on the vane pressure side (PS). Works like these contributed to greater confidence in the placement of film cooling holes on turbomachinery components.

Forcing cooler air into the hot main stream flow provides a significant benefit in gas turbine engines, allowing them to run with high operating temperatures. Using cooler air routed from the compressor core flow, components can be film-cooled in which cooling air enters back into the mainstream higher temperature flow through discrete holes created by laser drilling or EDM techniques. EDM allows more flexibility for hole shapes and locations but is more costly than laser drilling. Holes are usually drilled at some angle with respect to the surface. For this reason, engineers must be conscious of whether a given hole and its orientation can physically be drilled or not. For example, drilling at angles almost parallel to the surface may be very difficult to do. Moreover, film cooling hole shapes have to be amenable to the application of common protective

coatings which provide insulation and oxidation resistance. While the current study focuses primarily on external film-cooling performance, overall airfoil surface temperatures and tolerances are a result of both internal and external cooling effects. The importance of considering these combined effects in calculating external thermal properties comes to light especially when using modern conjugate heat transfer CFD methods.

Within turbine engines, film cooling has been the most beneficial technology used to increase the durability of hot turbine components by decreasing the surface temperature and shielding parts from the harsh effects of recently-combusted hot flow. The purpose of film cooling in turbomachinery is to protect the material surface at the location of cooling injection as well as downstream [8]. The introduction of a secondary fluid into the boundary layer at a temperature lower than the mainstream results in mixing which reduces the material surface temperature in the region downstream of injection. This film dictates the heat transfer driving force between the coolant and the wall, where the further downstream from the hole exit the jet remains attached to the wall, the longer this conduction can take place. The additional cooling mass flow also provides a thicker boundary layer and greater insulation from potentially damaging hot flow. This is commonly known as the jet-in-crossflow problem, where a wake downstream of the jet generates higher levels of turbulence and mixing, giving higher heat transfer coefficients. Therefore, with cooling, heat transfer coefficients are generally higher than without. An array or row of discrete cooling holes allows the coalescence of film cooling coverage over turbomachinery components such as the inlet vane in this work. In the plane of the row of holes, surface temperature varies greatly due to the high thermal conductivity of

the metal, while adiabatic surface temperatures vary much less. This makes averaging of cooling effectiveness very important for evaluation of cooling performance although gradients may be worse near endwalls, making a straight average unreliable. While cooling slots have shown to have greater cooling effectiveness downstream from the injection location and serve as an ideal case, rows of discrete cooling holes provide the necessary structural integrity for the increased thermal stress environment of a high pressure turbine in addition to the beneficial additive nature of cooling effectiveness relative to single or sparsely spaced holes. The goals of gas turbine thermal management are: keeping components isothermal to eliminate internal thermal stresses, keeping components near the hot gas temperature to minimize heat loads and increase efficiency, and minimization of thermal gradients between components and their containment structures [9].

Modern Film Cooling Methods

Cooling holes can generally be split into two categories that are most often used in turbomachinery today, cylindrical and shaped holes. These two types of holes exist on the baseline vane PS cooling array being redesigned in this work. Cylindrical holes, also called round holes, are named as such for their cylindrical passage shape with circular cross-section if you were to look directly down the hole. They have a constant diameter, D, through the length of the hole, L, as well as an oval-shaped exit due to the angle of coolant injection with respect to the surface. Cylindrical holes tend to generate a counter-rotating vortex pair (CRVP) [8] that starts at the hole centerline, moves up, out and away from the centerline, and down and back toward the center (see Figure 4), especially

downstream of the vane leading edge. This vortex pair entrains hot gas underneath the coolant jet. They have a tendency for separation from the surface downstream of the hole exit followed by reattachment farther downstream [3]. This is often called “lift-off”. This results in less effective cooling for high coolant-to-mainstream flow velocities. Depending on the flow conditions of the coolant in terms of density and velocity relative to the hotter combustion product gases, the coolant can stay fully separated and do little good, it can separate at first then reattach, or it can stay attached to the surface from the hole exit until it disperses with the main flow. The last case is the best case, as a layer of film protects the surface for the greatest distance from the hole. As the film develops in length and time, it entrains hot flow in the boundary layer causing greater dilution of the coolant and a gradual decrease in its ability to function as a heat sink [8].

The second common hole type are shaped holes, which have a constant diameter to a point, then there is either a forward expansion, symmetrical lateral expansion, or a combination of both. Since external film cooling in turbomachinery was introduced, shaped holes are the only major advancement in this technology that has been put into widespread use in engines [9]. Expansion in either direction is usually limited to 10 to 15 degrees. The shaping is usually confined to the outer 20-50% of the wall thickness in order to maintain acceptable hole and hole-to-hole stress concentrations. These kinds of holes are also known as laidback fan-shaped holes. However, any hole with a varying area cross-section along the passage can be categorized as a shaped hole. The forward expansion creates a velocity profile across the hole exit in which the higher velocity flow is near the upstream part of the hole, while the flow near the downstream edge exits at a lower velocity and momentum [10]. The lateral expansion allows the flow coolant flow

to expand laterally and coalesce much faster than coolant from cylindrical holes, providing better spanwise-averaged cooling effectiveness [11]. Injection in this case is attributed to the transport of increased turbulent kinetic energy produced inside the shaped holes [12]. The added diffusion of coolant lowers the coolant-to-mainstream velocity ratio, but tends to increase aerodynamic mixing losses, which can be reduced as shaped holes are placed closer to the leading edge, where the injection and mainstream momentum levels are closer in magnitude. Their only major drawback is their cost of manufacturing relative to cylindrical holes which can simply be done with a proper micro drill bit. Shaped holes can refer to other novel shapes as well, such as crescents or conical configurations for example, but in this paper, shaped holes will primarily refer to fan-shaped expanded exit holes as seen in Figure 5 [13]. The shaped hole on the right in the figure also has lateral expansion (diffusion) as well. In Figure 5, T_s is the surface temperature, T_∞ is the freestream gas temperature, and T_c is the coolant temperature before entering the hole.

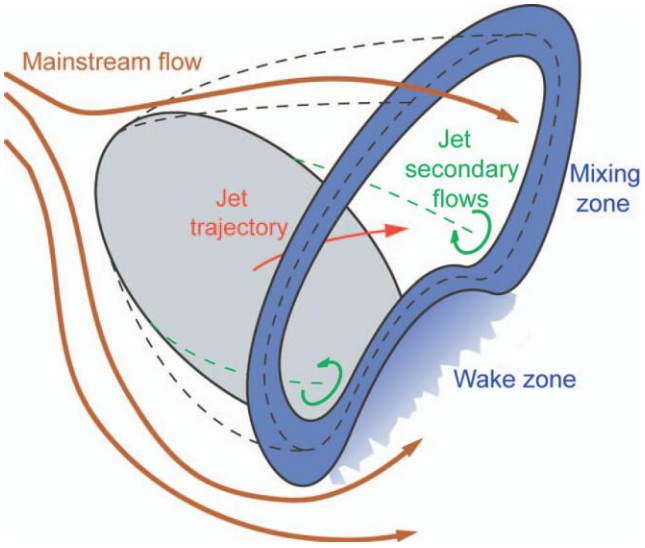

Figure 4 - Counter-rotating vortex pair resulting from cylindrical hole film cooling.

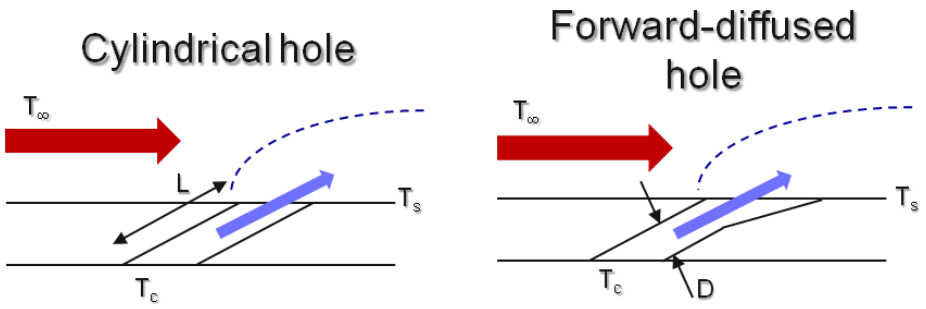

Figure 5 - Cross sections of the two most typical film cooling hole shapes—cylindrical (left) and shaped (right).

Round holes have been around for much longer than shaped holes, however, most HPT airfoils vane use a combination of the two. Round holes tend to be used at the leading edge stagnation-region of an airfoil in what is referred to as the showerhead. Round or shaped holes at some compound angle with the flow are typically used in high-curvature regions, while axially-oriented shaped holes are used over the remainder of the airfoil and closer to the trailing edge. Trailing edges tend to use short slots due to the decreased material thickness available for hole drilling, and as this is the only part of the airfoil that can handle the stress created by this kind of hole shape.

Injection angle, α, is the angle at which the centerline of a given hole is oriented with respect to the surface. Most injection angles for cylindrical and shaped holes in the literature tend to be between 30 and 35 degrees above the surface. With too high an injection angle, there is significant lift-off and a decrease in effectiveness. With a much lower angle, manufacturing limits are reached and undesirable sharp ablative edges can remain at the leading edge of the hole exit.

Compound angle, β, is the angle at which the hole centerline is oriented with respect to the freestream flow direction. For example, a row of holes can be injecting

coolant at some angle in the surface plane toward one endwall, which can increase the mixing losses due to the turning of the jet and increased interaction, but can also provide increase lateral film cooling effectiveness. Typical compound angles for holes not near the leading edge of an airfoil can range from 30 to 60 degrees. Near the leading edge, compound angles can be as much as 90 degrees, or radially oriented, in which coolant is injected at an angle perpendicular to the flow direction. Many holes can have a combination of compound and injection angles. This is why the leading edge cooling holes are often called the showerhead, for their high compound angles and radial injection angles ($\alpha = 90^{o}$). These holes are often called radial because coolant is injected in the radial direction along an airfoil that is one of many in a wheel.

Film cooling of the leading edge is normally done using several closely spaced rows of holes and for a HPT vane there are usually 6 to 8 rows. This type of orientation in the leading edge region is crucial to create a buffer of coolant to protect the metal where the flow direction runs nearly head-on with the coolant injection velocity at the airfoil stagnation point. As the mainstream flow picks up velocity, simple axially-aligned injection is sufficient to create a film for cooling over the surface of the part.

Concerning internal cooling, while today's internal vane and blade cooling passages are quite complex with serpentine passages and impingement layers near the surface, the current study only considers a vane with two simple cooling plenums with single thickness walls. The details of the internal plenums and how they are supplied are addressed for this work in the methodology when considering CFD cooling air conditions, but the focus of this particular work is external film cooling only.

Key Parameters

Decreasing the temperature of the airfoil surface relative to the mainstream flow provides a driving potential for heat transfer to occur, wherein a reduction of just 50 K, part life can increase by a factor of two [1]. Newton's law of cooling takes on the following common representation for surface heat flux in the presence of film cooling:

$$q_f" = h_f(T_{aw} - T_s) \quad (1)$$

The subscript f signifies film cooling, h is the heat transfer coefficient, and T_s is the surface temperature. The heat flux is very sensitive to the temperature difference in Equation 1 which is its driving potential. A reference temperature is required to recognize the difference between the hot main flow and the wall temperature. In flows without cooling this reference would be the main flow total temperature, T_∞. In flows with film cooling, as coolant mixes with hot main flow, the reference temperature is lower. Traditionally, in order to obtain a heat transfer coefficient that is independent of the coolant temperature, a value of temperature of the fluid just above the surface is used. For an adiabatic wall, the temperature T_{aw} is most used as is provides a good reference temperature for the heat flux driving potential, however, as conjugate heat transfer simulations become more common, the accuracy of this estimation is being challenged [14]. This can be especially true in the case of separated jets from cylindrical film cooling holes [15].

Momentum and heat transport downstream of holes is also very hard to predict, and local fluid temperature changes greatly. Thus, h and T_{aw} vary significantly over an airfoil surface due to discrete nature of cooling holes. However, past studies have shown little difference between h_f and h_0, the value without cooling flow, but again, T_{aw} varies

greatly. T_{aw} is significant because it is the limiting value of wall temperature that can be obtained without internal wall cooling. In cases of large temperature differences, significant errors in assumed boundary conditions are introduced making accurate measurements difficult, especially in getting T_{aw} distributions [8]. To find *h*, which is mostly an empirical value, Nusselt number (*Nu*), the ratio of convective conductance in a fluid to thermal conductivity, *k*, of the fluid along an adjacent wall, can be used for flat plate turbulent flows [16] defined by:

$$Nu = \frac{hx}{k} = 0.0296 {Re_x}^{4/5} Pr^{1/3} \tag{2}$$

Pr is Prandtl number, the ratio of kinematic to thermal diffusiveness in a fluid and *Re* is Reynolds number. T_{aw} is also used in the expression for adiabatic effectiveness, η, which is most commonly used in literature to characterize film cooling performance:

$$\eta = \frac{(T_\infty - T_{aw})}{(T_\infty - T_{c,e})} \tag{3}$$

The parameter is a simple ratio of the reference driving potential to the maximum potential achievable due to coolant temperatures at the precise location of the cooling hole exit ($T_{c,e}$). $T_{c,e}$, unlike the temperature of coolant at the hole passage inlet, $T_{c,i}$, can be difficult to measure experimentally. Adiabatic effectiveness is a maximum closest to a cooling hole and decreases downstream of the cooling hole as the coolant mixes with the hot main flow. It is a function of both lateral position and downstream distance. $\bar{\eta}$ denotes a laterally-averaged value of effectiveness and is often reported in open literature. Through extensive experimentation and study, researchers have documented that this parameter is affected by a number of variables: obviously T_∞ and $T_{c,e}$, coolant-to-mainstream density ratio (*DR*), velocity of the coolant flow out of the holes relative to

the main stream flow (also known as blowing ratio, M), mass flux, momentum flux (I), pressure gradients, surface curvature, turbulence intensity (Tu), cooling hole shape, cooling hole flow angles, and their placement over the airfoil surface [4]. These parameters' relative strengths and interactions determine the rate of decay of effectiveness downstream. The flat plate and blowdown rig tests reported in this work are both subsonic and it is known that freestream Mach number has little or no effect on η.

T_∞ may be replaced in Equation 3 with recovery temperature, T_r, which is a local value that depends on Prandtl number and velocity:

$$T_r = T_\infty + (Pr_\infty^{\frac{1}{3}} - 1)\frac{{U_\infty}^2}{2c_{p,\infty}} \tag{4}$$

Recovery temperature is defined as the temperature a moving fluid reaches when brought to rest in an adiabatic process. In the equation, freestream velocity is U_∞ and c_p is specific heat. With the low-Mach number, incompressible nature of turbine inlet flows, T_∞ can be assumed to be equal to T_r, as the second part of the right hand side of Equation 4 becomes zero. In the case of no cooling, $T_{aw} = T_\infty$ and in high-speed flows, $T_{aw} = T_r$ [8].

To understand the relative benefit of film cooling, the heat transfer with and without cooling must is compared using net heat flux reduction (NHFR). It is defined by:

$$NHFR = \Delta q_r = 1 - \frac{q_f^{"}}{q_u^{"}} = 1 - \frac{h_f(T_{aw} - T_s)}{h_u(T_\infty - T_s)} \tag{5}$$

The subscript u means uncooled. This parameter in the realm of predictions requires cooled and uncooled cases for the geometry of interest. In TRF experiments, as discussed in Appendix A, four thin film sensors at the same precise location are required to get one point of NHFR data. Top and bottom gauges (on either side of the insulating

kapton layer) for both cooled and uncooled vanes within the same annulus for the same run are necessary, making it rather expensive to obtain experimental NHFR. This is much simpler in CFD simulations where data is plentiful. Net temperature reduction (NTR) is also a result of interest and it is calculated in a similar manner to NHFR:

$$NTR = 1 - \frac{T_{s,f}}{T_{s,u}} \tag{6}$$

where T_s is surface temperature and f denoted the presence of film cooling and u denotes the absence of cooling.

Another non-dimensional parameter often used in literature, which does not require knowledge of T_{aw} is the overall effectiveness:

$$\phi = \frac{(T_\infty - T_s)}{(T_\infty - T_{c,i})} \tag{7}$$

Unlike η, this term depends on the metal surface temperature and the coolant temperature before it enters the coolant hole, $T_{c,i}$. This difference is important since by conduction, the coolant picks up heat as it passes through the cooling hole passage and exits at a different temperature, $T_{c,e}$. Since direct measuring of the cooling air at the hole exit can be difficult or impractical in experiments, ϕ can be used as estimate of cooling performance as opposed to acquiring η, which often requires multiple tests and specialized configurations to get T_{aw}. Transient experimental methods usually assume 1-D conduction to semi-infinite solid to get h and η from rate of change of surface temperature while, as in the infrared thermography experiment in this work, steady-state methods obtain surface temperature directly. NHFR can also be rewritten as:

$$\Delta q_r = 1 - \frac{h_f}{h_0}\left(\frac{1-\eta}{\phi}\right) \tag{8}$$

Bogard and Thole [3] recognized that there a number of factors that affect the prediction of cooling performance and ultimately the distribution of η with respect to distance downstream for a given cooling configuration. These factors are not necessarily independent of each other and different combinations of the variables can theoretically cause different performance results—hence, the difficulty in predicting η. This idea is the impetus for the cooling array design problem at hand and will be explored more in the optimization methodology, including chosen variables in the problems space and their respective ranges based on historical findings.

When low *DR* studies are conducted as many of the laboratory works in open literature, to match engine-like high *DR* (usually ≈ 2.0 in an operational engine), blowing ratio (*M*) or momentum flux ratio can be used. *M* is a ratio of coolant-to-mainstream mass flux:

$$M = \frac{\rho_c U_c}{\rho_\infty U_\infty} \tag{9}$$

Density is denoted by ρ and velocity by *U*, where the subscript "c" is for the coolant gas. This parameter is most often used to detect streamwise decay of coolant effects on an airfoil surface. Momentum flux ratio is defined by:

$$I = \frac{\rho_c {U_c}^2}{\rho_\infty {U_\infty}^2} \tag{10}$$

It is well-known that coolant jet-separation characteristics scale with *I*, where jets stay attached up to $I = 0.4$ and begin to detach consistently around $I = 0.8$ [17]. Notice that *M* and *I* are related by *DR*, such that for $DR = 1$, momentum flux ratio is simply the square of blowing ratio:

$$I * DR = M^2 \tag{11}$$

Near-hole cooling effectiveness is not greatly affected by a change in *DR* until it reaches a minimum level where there begins to be a slight increase. Higher *DR* tends to give higher effectiveness for higher *I*. Trends between parameters are discussed in more detail in the literature survey.

Measurements in this work are primarily concerned with surface temperature (T_s) and heat flux (q). Heat flux from CFD predictions in this work is found by the following equation for a fluid grid cell at or near the surface:

$$\dot{q}" = -k_\infty \frac{dT}{dy} \tag{12}$$

where k is thermal conductivity of the hot gas and the fractional temperature gradient term accounts for the change in temperature between the grid nodes and y represents the height of the first cell on the vane surface. It will be seen that for CFD validation, experimental heat flux in the vane annulus blowdown rig experiments is measured by high-frequency double-sided thin film gauges in which each reading requires both a "top" and "bottom" gauge to calculate, where the top gauge is capable of measuring surface temperature. In that case, the thickness of the insulating layer separating the gauges is y and k is the thermal conductivity of the insulator. Now that all film cooling parameters are known, the trends researched in the literature survey can be explained in detail.

Origins and Manifestations of Film Cooling Effectiveness

Now that the most important film cooling parameters have been introduced, it is beneficial to look back and see where our most popular definitions of film cooling have come from, test the assumptions going into them, and determine the best parameters to study in the current work. Film cooling was first used to control the thermal

environments of rocket engine nozzles [18]. It was also used in the German V-2 nozzle. In this type of application, a liquid or a gas would be directly injected at the nozzle inner surface at multiple axial locations by means of tangential or nearly tangential coolant holes, slots, or louvers. In this configuration, the liquid would vaporize as it moved along the wall, and the gas would actually protect a larger distance than the original liquid. This forms a film which alters the temperature profile through the boundary layer and decreases the rate of heat transfer to the thermally-loaded walls. The cooling holes were placed at equally spaced increments to maintain a theoretical limit of heat flux. In efforts to reduce the heat flux through the surface at the nozzle throat, some of the first plots of net heat flux reduction with respect to axial distance were generated to understand the benefit of injecting different liquids at different locations and orientations. Before η was well-known by turbine durability engineers as adiabatic effectiveness, it was originally referred to simply as film cooling effectiveness. There was no definition yet of *adiabatic* or *overall* effectiveness. One of the first expressions of film cooling effectiveness was developed in efforts to come up with an efficient de-icing method for aircraft wings [19].

Much like the case of air-breathing engines, film-cooling technology became necessary in rocket engines as advances in rocket motor development have intensified the problem of effectively cooling the nozzle operating under the conditions of high, local heat flux [20]. It was found that regenerative cooling, in which fuel is routed around the nozzle to pull heat away before being burned in the thrust chamber where its higher temperature provides more energy, was not enough to protect the inner walls of the rocket nozzle. Likewise for gas turbine engines, after the advent of internal vane and blade convective cooling, it was found that heat transfer levels were too high and external

film methods were required. Film cooling holes were spaced evenly to ensure a maximum temperature is not exceeded, just as durability designers still do today even on modern turbine vanes, which shows that emphasis can still be devoted to engineering the efficient placement of coolant injection depending on three-dimensional flow conditions. Also, as advances in gas turbine combustor technology progress toward higher temperature turbine inlet environments, component external film cooling will need to advance with it. In both the cases of the rocket engine and gas turbine engine, durability requirements have mostly been driven by the high temperature products of combustion.

Traditionally, to find adiabatic effectiveness (η), knowledge of the value of T_{aw} is necessary, which can in turn be found from heat flux (q'') and the heat transfer coefficient (h). Film cooling experiments in open literature measure η because the results are highly robust and incorporate the conditions of the cooling flow, adiabatic film, and the main flow gas temperature. Since these factors are highly dependent on each other, finding η has advantages in representing isolated external performance of a cooling design independent of temperature settings. Authors still report on η in order to make comparisons to other works and in many cases it requires significant effort to arrive at η or h. Reporting non-dimensional values like η may also be necessary in the assessment of proprietary hardware or in the case where running steady state experiments is not feasible. Additionally, low k materials can be cheaper than using highly-conducting materials in the lab, especially considering cooling hole drilling costs. On the other hand, film cooling experiments with high k materials and cooling channels require added complexity to account for internal convective cooling beneath the material surface being tested. Adiabatic effectiveness is also easily compared to CFD. Since most CFD

performed to date involve only the assessment of the external fluid around a body (non-conjugate methods), requiring the choice of an isothermal or adiabatic solid boundary condition, choosing the adiabatic condition allows for direct comparison to experiments that have measured η.

Data on hand for which CFD conditions here are based show that turbine engines do not run adiabatically. Data in Appendix A from the AFRL Turbine Research Facility (TRF) shows that turbine engines at steady state run more isothermally rather than adiabatically. In fact, there are few instances in turbomachinery where there is zero heat flux. Concerning the two types of CFD used in this work, cooling estimation external flow and conjugate heat transfer, adiabatic wall conditions do not apply in either case. In the two experimental methods in this work, advanced thermal measurement techniques such as double–sided thin film heat flux gauges and full map infrared thermography are used in which they are not designed to obtain adiabatic effectiveness. With additional effort, terms like η and h can be backed out, however, for the sake of expediting the assessment and design process, heat transfer properties that can be directly compared to experimental data are chosen to work with for this project.

Film cooling effectiveness is derived from experiments with rocket nozzles in the 1940s and is best defined in terms of the surface heat fluxes [18]:

$$\eta = \frac{\dot{q_u}" - \dot{q_f}"}{\dot{q_u}" - h_{g,f}(T_c - T_{s,f})} \tag{13}$$

The subscripts *u* and *f* refer to uncooled and film-cooled conditions, respectively. As the AFRL TRF has the ability to find both cooled and uncooled surface heat flux [21], Equation 13 will be used to find film cooling effectiveness on the vane and blade at

different span locations in future work. The second quantity in the denominator which resembles Newton's law of cooling represents the minimum achievable heat flux in the presence of film cooling. Due to the reasoning above and resources available, it is practical that overall effectiveness, ϕ, which relies on easily measurable plenum cooling temperatures and surface temperatures, be reported for the infrared thermography experiments in this work instead of the current definition of adiabatic effectiveness, η.

Even Equation 13, which has eliminated the need for T_{aw}, does not escape some level of empiricism. Heat transfer coefficient is found from turbulent boundary layer *Nu* relations, originally from flat-plate studies. It is often taken for granted that values of *h* are taken from constrained experiments with forced thermal boundary conditions [8]. In a turbine engine, *h* varies locally, especially with film cooling. With the advent of better CFD tools more realistic experimental methods due to advanced instrumentation, a return to a more basic definition of cooling effectiveness is suggested. Harrison and Bogard [14] make a similar argument to this effect. Therefore, in the current work, temperatures and heat flux are directly reported in CFD and experiments. In addition, temperature is pertinent because component life is driven by temperatures that component are exposed to rather than other properties.

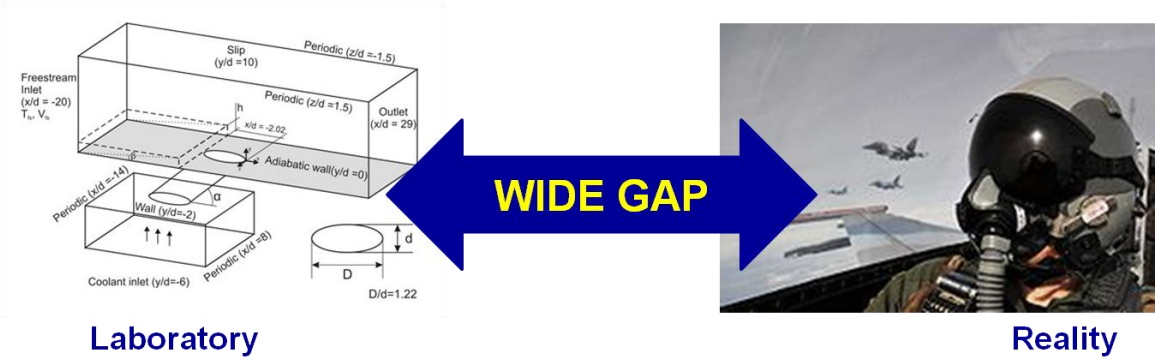

Figure 6 – Turbomachinery durability relevance gap.

Often there may be a wide gap between a given film cooling experiment or CFD simulation and its applicability to operational engines. Not only because many current assessments are on a single hole or single row of holes, but rarely are lessons learned from a given work applied to working engines [9]. Figure 6 is a depiction of the durability relevance gap that spans between the laboratory and reality. In laboratory work, for example, blowing ratio is controlled at some constant value, when in a real component, blowing ratio varies by cooling hole, depending on how cooling is supplied. In another example, span-wise averaged adiabatic effectiveness is often reported in laboratory work, however near endwalls and in more 3-D geometries, η can fluctuate wildly, which may make straight averaging across the span unreliable. Laboratory work in open literature also contributes new cooling hole shapes every year, despite the fact that many of the shapes are either too expensive to EDM drill, impossible to manufacture, or not robust enough to stand up to many cycles in a real engine.

For external film cooling, the laidback fan-shaped hole was the last major improvement implemented in engines [9]. That was many years ago. Yet many current film cooling works still tend to focus on adiabatic assessments, simple geometries, and the flow physics around a single cooling hole or set of holes. Laboratory studies are beneficial for academic purposes and perhaps for those with limited resources but more can be done to fill the gap between lab studies and enhancements the gas turbine engine operator can appreciate. Overarching lessons from previous film cooling studies and new cooling designs from modern studies will allow new technologies to become useful.

To fill the gap in Figure 6, more work pertaining to the following is suggested:

- Lowering cooling mass flow requirements which can increase engine thermal efficiency.
- Conjugate heat transfer simulations that consider solid conduction and use realistic high *k* materials.
- Optimization that explores broad variable spaces and takes advantage of modern computing power.
- Realistic cooling hole length-to-diameter (L/D) ratios.
- Engine-representative full-map PS and SS cooling arrays.
- 3-D flow effects on film cooling.
- Engine-like flow conditions.

The current work involves all of the above and takes a step towards contributing to more realistic studies of film cooling.

Common Correlations and Models

Several different correlations are proposed in the literature for various ranges of mass injection. Correlations are important to turbomachinery durability because it forms much of the basis for how cooling features are placed on HPT vanes and blades. For nominal conditions of a flat surface, low mainstream turbulence, and round holes, cooling performance is well-predicted with empirical correlations. Adding complexities such as surface curvature, shaped holes, and higher turbulence makes it much harder to predict effectiveness. Many of the experiments in film cooling involve flat plates, and some of the earliest works measure the effectiveness of slot film cooling. This is an ideal cooling case because of the high lateral coverage in the spanwise direction and the lack of

rotation in the flow as it exits the slot. This is also known as two-dimensional cooling since there is no dependence on the spanwise direction. Therefore, many hole shapes and configurations are related to this ideal case. Full length slots cannot be used in turbomachinery because of the lack of structural integrity such a cooling design would pose. Thus, rows of discrete holes will never cool as effectively as slots.

Early work at NASA by Papell [22] allowed the updating of tangential slot injection correlations to angled slots and discrete holes with normal injection angles. This is also one of the first works to show increased cooling effectiveness at lower injection angles for a given coolant mass flow. The decay of η with distance has been noted to be inversely proportional to M in multiple works such as that by Teekaram et al. [23]. Their measurements of laterally-averaged η for slots fared well against slot correlations for distances far from injection, for example for α = 45º, by Hartnett et al. [24]:

$$\eta = 16.9\left(\frac{x}{Ms}\right)^{-0.8} \tag{14}$$

The quantity $x/(Ms)$ is called the dimensionless distance from the slot leading edge, which also applies to round-hole centerline characteristics. The distance from the hole exit is x and the equivalent slot height is s which is equal to the area of the hole divided by the hole pitch, P: $s = A/P$. Pitch and streamwise distance are usually normalized by hole diameter D to give P/D and x/D, respectively. The wall-normal and spanwise distance can also be normalized by hole size: y/D and z/D, respectively.

Concerning the hole spacing in a given row, as P decreases, there is greater lateral coverage of coolant. However, it is important to recognize whether the spacing is far enough to allow the jets to act independently, and not too close as to jeopardize the

structural integrity of a part. Literature has shown that best P/D level is between 2 and 3, in which levels of $\bar{\eta}$ increased over a wide range of M. At greater hole spacing, $\bar{\eta}$ was found to decrease for all conditions. At lower cooling hole pitch, $P/D < 1.5$, the cooling behaves more like transpiration cooling than discrete-hole cooling [25]. The correlation of Equation 14 fared well against many data sets, however, most of the agreement was seen for $x/D > 80$, which for the vane in question for the current study, would likely be off the vane surface, even for the first shaped hole row on the PS. Thus, correlations for near-hole characteristics are necessary.

Another film effectiveness correlation as a function of downstream distance that has come to be quite reliable is that by Brown et al. [26]:

$$\eta = \frac{1}{\frac{1}{C_1} + C_2\left(\frac{x}{Ms}\right)^{C_3}} \tag{15}$$

Typically, C_1 equals a coverage value that divided the total span by the maximum width of holes in a row and $C_3 = 0.8$. The constant C_2 can vary depending on the part of the airfoil being considered. For the leading edge [27], it is 0.1963 and for the pressure side [28], it is equal to 0.113.

Correlations are reasonable for one row, but rarely in operational turbomachinery is there only one row of cooling holes. It is necessary to regenerate the cooling film to ensure proper thermal protection and film coverage over most of the surface of the airfoil. Therefore, basic methods were developed to analytically model sets of cooling holes rows. Designers can use a superposition law to predict film cooling effectiveness downstream of multiple injection locations. This was originally introduced by Sellers [29] for multiple slot film cooling. With this method, T_{aw} downstream of an additional

row of holes is predicted by simply substituting the T_{aw} from the upstream injection in for the hot gas temperature in Equation 3 for the adiabatic effectiveness. Assuming equal coolant exit temperatures at both injection points gives a non-linear superposition equation for the total adiabatic effectiveness when all injection is taken into account:

$$\eta_{tot} = \eta_1 + \eta_2(1 - \eta_1) \tag{16}$$

Muska et al. [30] showed that this equation compares well with experimental results for both flat plates and airfoils with round holes, adequate spacing between rows, and lower blowing ratios. The correlation in Equation 15 can used by durability designers to place successive cooling hole rows, in which a minimum acceptable level of η is maintained. However, this only accounts for cooling performance at one span location on a vane or blade. Spanwise-averaged values can be used, but near endwalls on highly 3-D geometries, it may be unreliable. Thus, these correlation cooling design methods require updating to more flow-physics based methods.

Nozzle Guide Vane Pressure Side Problem

Historically, PS characteristics have been easily simulated, perhaps because in favorable pressure gradients, the near-wall acceleration acts to stabilize the boundary layer and counteract effect of free-stream turbulence as seen in the work by Blair [31]. The pressure side generally has a much weaker pressure gradient than the suction side as well as near-negligible curvature effects. That is especially true for the 3-D vane geometry being investigated in this work.

The pressure side is known for having a thicker boundary layer in the case of film cooling, a higher tendency for endwall vortices, and a mostly laminar boundary layer due

to the favorable gradients. A nozzle guide vane was chosen for the current work because it lies in typically the hottest part of the engine. The PS was chosen for a cooling optimization study due to the higher number of cooling hole rows on the baseline vane design and the relatively low-curvature that should permit comparable thermal results between flat plate infrared thermography and results from the 3-D vane geometry. In addition, the area just downstream of the leading edge on the PS of the baseline vane is known to be a distinct area of high heat transfer, which may be significantly reduced with a more effective cooling design.

The pressure side is also known for being much more well-behaved in the face of uncertainties and changes due to manufacturing tolerances. Montomoli et al. [32], inspired by the work of Bunker [33], has recently shown that uncertainties in freestream Turbulence intensity, thermal barrier coating thickness, and pitchwise hot core location values all cause much smaller changes in metal temperature on the PS relative to the SS on a 3-D modern inlet vane with film cooling.

Conjugate Heat Transfer Problem

The vast majority of CFD work to date involves external fluid simulations around a solid body. In turbomachinery, it is important to consider the complex three-dimensional thermal environment. Therefore, the current work offers simulations of the baseline cooling design that include the combined effects of hot external fluid, the convective internal cooling air beneath the metal surface, the fluid flow in each cooling passage, and solid conduction from the vane material.

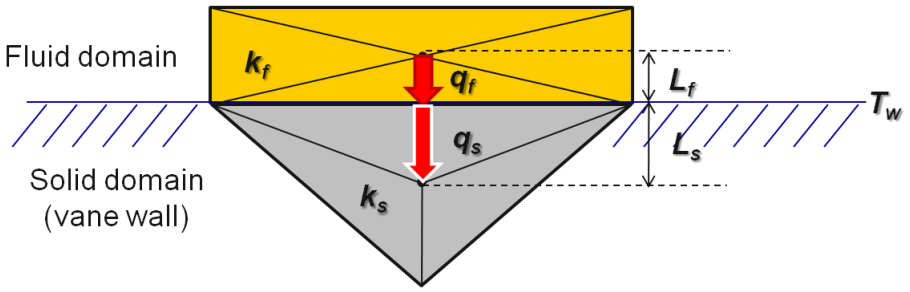

Figure 7 – Conjugate heat transfer CFD heat flux balance at the solid-fluid interface.

CHT studies do not require that adiabatic or isothermal boundary conditions be set at a wall or surface like traditional CFD. The wall temperature is an unknown based on the set fluid and solid conditions. The simulations maintain a heat flux balance at the solid-fluid interface (see Figure 7):

$$\left(-\frac{k_f}{L_f}\right) * \left(T_f - T_w\right) = \left(-\frac{k_s}{L_s}\right) * \left(T_s - T_w\right) \tag{17}$$

In the equation above, T is temperature, k is thermal conductivity, and L is an arbitrary length from a CFD grid cell center to the solid-fluid interface. The subscripts f, w, and s stand for the fluid, wall, and solid, respectively. By rearranging this expression, the wall temperature can be obtained:

$$T_w = \frac{\left(k_s/k_f\right)\left(L_f/L_s\right)T_s + T_f}{1 + \left(k_s/k_f\right)\left(L_f/L_s\right)} \tag{18}$$

It is seen in Figure 7 how an anisotropic prism fluid cell closest to the wall in the boundary layer meets a tetrahedral solid unstructured cell at the solid-fluid interface. Heat transfer is solved in the solid mesh using Fourier's law of conduction (Equation 12). Now that a solid theoretical background is established, the details of past computational and experimental work in film cooling can be laid out.

III. Literature Survey

In this section, a large amount of previous work from industry and academia on gas turbine component film cooling is reviewed. First, different types of turbine heat transfer CFD prediction methods are reviewed along with their relative accuracy and any applicability to past experimental works. Included in the CFD review is works involving conjugate heat transfer that were accomplished over the past decade. Next, a basic history of turbomachinery optimization and redesign methods for aerodynamic and thermal purposes is given along with other uses for genetic algorithms. Then, efforts that examine experimental gas-turbine component heat transfer with film-cooling in representative flow environments and their respective flow facilities, measurement devices, and trends observed is discussed. These experiments span from simple flat plate setups to cascades to full-scale full-wheel blowdown facilities. Despite the body of work regarding film-cooling being over 50 years old, with over 2,700 references in existence pertaining to both experimental and computational work [10], high-integrity numerical evaluation and prediction of turbomachinery and evolving film-cooling designs is a point of emphasis now more than ever.

CFD Simulations of High Pressure Turbine Cooling

Bogard and Thole [3], in their summary of gas turbine film cooling, point out that many simulations have been run for different configurations and conditions, but CFD is still weak in predicting the exact flow physics of jet separation from the wall for coolant injection. This is especially true for the three-dimensional case, regardless of the

turbulence model used. Some work emphasizes the need to reduce the amount of empiricism in heat transfer design practice and to develop truly predictive capabilities for film cooling [34]. The goals of this work are not to make up ground with respect to accurately modeling micro scale flow structures near the wall just downstream of a cooling hole, but to find a reasonable 3-D CFD method for aggregate evaluation of film cooling array designs in computational domains with boundary conditions that model the actual engine environment of the HPT vane. Nonetheless, there is much to be learned from other works in terms of which parameters can be modeled accurately, how to properly mesh the simulated domain, and where enhanced computational capability can take a CFD design effort.

CFD in film cooling can be categorized into different regimes, including surface simulations, usually to predict non-dimensional heat transfer distributions, and field simulations that provide temperature and velocity contours and vector plots at different slices in the 3-D domain of interest. The CFD can also be split between 2-D boundary layer models, 3-D Reynolds-Averaged Navier Stokes (RANS) models, and most recently, conjugate heat transfer (CHT) RANS CFD. Most of the work cited here involves the latter two cases.

It should also be noted that CFD presents challenges involving choosing key elements of a given simulation. The following summarizes the choices available to CFD users in viscous film-cooling applications:

- Flow solver complexity: (In order of increasing simulation detail) RANS which is the most common, Large Eddy Simulation (LES), or Direct Numerical Simulation

(DNS). DNS is typically only used for small-domain simulations to resolve very specific fluid attributes.

- Turbulence models: Zero-equation models like Baldwin-Lomax; one-equation models like Spalart Allmaras; or two-equation models like k-ε, Wilcox k-ω, and k-ω shear stress transport (SST). Two-equation models tend to be used the most.

- Grid: Structured hexahedral meshes or unstructured tetrahedral meshes with narrow prismatic cells in the boundary layer; some works include local refinement and adaptation to increase grid cell count near detailed features. Refinement means that grid density is increased. Adaptation means that the flow physics after a nominal amount of iterations governs the addition of grid cells where flow gradients are the greatest. Overlapping or overset grids and octree-type Cartesian meshes have also been used, but to a much lesser extent.

- Domain: External fluid only (no cooling); cooling estimated external flow (CEEF) that uses a transpiration boundary; full-grid which means internal cooling plenums, all hole passages and external flow is simulated; and CHT CFD which is usually full grid and includes the effects of solid material conduction on the fluid convection. The current work involves CEEF CFD and full grid CHT CFD.

- Spatial Discretization: Finite volume or finite difference; usually second order to manage simulation run time but provide the necessary accuracy.

- Boundary conditions: Typically can choose from symmetry, periodic, pressure inlet or outlet, and viscous “no-slip” walls for the object in the fluid flow (with isothermal, adiabatic, or constant heat flux settings). In the case of conjugate CFD, a heat

flux balance in the solid/fluid interface is maintained, negating the need for an isothermal or adiabatic setting.

Most of the studies reviewed used finite volume RANS solvers with two-equation turbulence models and viscous flow. Ultimately, CFD is important for the current work because the veracity of predictions of surface temperature distributions and resulting thermal stress affect the reliability and life of a gas turbine component.

3-D Modeling

First, concerning the most widely used two-equation turbulence models, the k-ω model tends to be best for wall-bounded flows and curved grids, but in the wake region of jet in crossflow problems, realizable k-ε model has shown to be the best. Meanwhile the standard k-ε suffers from an inability to model the complex turbulent flow field inside a shaped hole while the k-ω model over-predicts effectiveness when compared to experiment due to inaccuracies in modeling jet spreading rate. Each model has their weaknesses. In a RANS film-cooling comparison of models by Hoda et al. [35], the k-ω model was found to under-predict kinetic energy in a wake region but accurately predict the presence of strong vortices and shear stress levels. The k-ε model was not able to predict some vortices, did not resolve the near-wall region very well, and over-predicts the amount of jet spanwise spreading. Overall, the Wilcox k-ω model typically out-performs the k-ε in predicting film cooling details, especially in more realistic curved-wall environments. This most recently been confirmed by Harrison and Bogard [36]. Many of the works in this area have also shown that regardless of cooling hole shape

being interrogated, the modeling of turbulence is of great importance [37], especially when three dimensions are considered.

Due to the fact that 3-D CFD is not constrained like experiments, this allows freedom of assessment of many different parameters and comparisons with different simulated geometries and conditions. One of the most comprehensive simulations of a realistically small *L*/*D* round hole including meshing of the plenum, hole and external flow was accomplished by Leylek and Zerkle [34]. In RANS simulations of a flat plate experiment with round holes using the standard *k*-ε model, they found the flowfield inside a hole to be highly elliptic and strongly coupled in which the strength of the coupling increased with injection angle and as blowing ratio (*M*) decreases. Computations of streamwise η showed over-prediction for all *M*, especially near the hole at higher *M*. Crossflow results for planes normal to the streamwise direction showed a lack of diffusion in the predictions for varying *M*.

Flow in multiple holes on a 2-D extruded section of the VKI rotor was simulated using a finite volume RANS solver with the Baldwin Lomax turbulence model [38]. In varying *M*, as the value increased, coolant traces lifted off the pressure side earlier than the suction side, leading to higher T_{aw} and lower η. This was attributed to increased jet lift-off. Naturally, in a real engine, blowing ratio will not exceed a certain percentage of core flow.

Addressing the need for CFD simulations on realistic geometries, Buck et al. [39] used a near-wall resolved unstructured and adaptive multi-block grid as well as the renormalization group *k*-ε turbulence model to compare to experiments on single-rows of three types of hole configurations. Better agreement with measurements was seen for the

SS over the PS which was attributed to the low relative blowing ratio on the SS. It was also noted that the turbulence model had a shortcoming in that it did not accurately model anisotropic mixing well and that laterally-averaged η was over-predicted near the hole.

Hiedmann et al. [40] modeled the internal plenum, hole passages, and external flows (full-grid) around an extruded 2-D vane span-section to include a realistic array of showerhead, pressure side, and suction side holes for a total of 12 holes. Using a RANS code called LeRC-HT, the Wilcox k-ω turbulence model, and multigrid method, it was found that improved performance of shaped holes on the pressure side is necessary to counteract the typically enhanced coolant diffusion and quickly decaying film effectiveness. With respect to having no cooling, cooling reduces heat flux while increasing heat transfer coefficient (h) over the entire vane. It was also found that the PS thermal mixing region is greater than the SS, causing greater coolant diffusion and decreased relative performance of shaped holes. Finally, the simulations showed that the velocity profile of a shaped hole exit, unlike a more uniform round hole, shows a very low momentum in the center and a sharp maximum at the upstream edge.

Other notable works that provide comprehensive comparisons of film-cooling thermal characteristics in CFD and experiments are that by Walters and Leylek [41] and Kohli and Thole [42]. Both works expanded on previous rigorous CFD and experimental studies and showed some of the best agreement of adiabatic effectiveness downstream of a single cooling hole for varying cooling conditions and hole shapes in open literature. These fundamental studies serve as a solid foundation for future comparisons of full-map cooling array adiabatic effectiveness in operational environments. However, the current

work does not focus closely on the physics of a single cooling hole. Instead, it gives overall properties and trends of the vane for its primary design flow condition.

Concerning pertinent CFD simulations on three-dimensional HPT components with cooling and efforts to match data in notable experiments, Choi et al. [43] performed 3-D Navier-Stokes simulations of a film-cooled turbine blade with an early turbulence model called the Coakley q-ω model and compared them to midspan blade geometry Nu data obtained in the Oxford Isentropic Light Piston Tunnel (ILPT) and showed good agreement. While the work was ahead of its time in terms of CFD capabilities, as they finely gridded the injection pipe for the cooling hole and used grid adaptation and Chimera overlapping at the injection plane of the hole. The blade had one row of cooling holes on the suction side, and this was the same surface location of the only deviations between experiment and predictions. They also used longer than realistic L/D cooling passages in the simulation. Sargison et al. [44] used the Oxford Cold Heat Transfer Tunnel (CHTT) to study used thermochromic liquid crystal measurements and "direct" heat flux gauges to compare cooling effectiveness and heat transfer against a boundary layer CFD code and a 3-D code. There was significant PS under-prediction of η just after the cooling hole rows, however this was one of the first true-geometry vane CFD predictions of surface heat transfer distributions with film cooling.

Laskowski et al. [45] generated predictions of the 3-D film-cooled flow around the highly-reported NASA C3X vane and VKI rotor including the hot gas path, the internal passages and the flowpaths in each individual cooling hole using the CFX v10.0 RANS solver and the shear stress transport (SST) turbulence model. The vane airfoil modeled included multiple rows of leading edge, suction side, and pressure side holes.

Unlike the CEEF CFD in this work, an unstructured grid was used everywhere, the endwalls did not have cooling holes, more than just one flow condition was assessed, and cooling hole rows did not lie past ¼ of the surface distance on either side of the blade. However, like in the current work, experimentally derived wall temperature boundary conditions were applied and the study served as a first step toward a later CHT assessment on the same vane geometry. In comparing their simulations of midspan thermal properties to vane cascade experiments, heat transfer coefficient was slightly under-predicted on both surfaces and leading edge cooling was not predicted closely.

One of the more pertinent experimental works to date is that of the Ohio State University (OSU) group and Haldemann et al. [46] who compared their fully film-cooled short-duration single-stage blowdown facility pressure data to simulations using the RANS viscous code FINE/TURBO with the k-ε turbulence model. Heat flux data of interest was primarily focused on the blade. Double-sided, fast-reacting thin-film heat flux gauges, much like that outlined in Appendix A for the current work, were used at multiple span locations. These require both the bottom and top gauges separated by a kapton layer to work in order to calculate heat flux. Concerning the vane experimental data, five locations of heat flux were given, however the rotor heat flux and temperature data was much more resolved, providing insightful new streamwise and spanwise trends of thermal characteristics in film-cooled, rotating turbomachinery components. More recent work by the OSU group resulted in a plethora of data regarding heat flux in the same stage-and-a-half full-scale rotating rig in which they: captured the effects of upstream vane and purge cooling variation on uncooled blade Stanton number distributions and inlet temperature profiles [47], used CFD to predict the migration of

temperature profiles through a turbine stage [48], studied the effects of cooling mass flow changes on blade surface time-averaged heat flux [49]. From these works they emphasized the challenges of properly modeling film-cooling and comparing cooled heat flux predictions to data in future works, the importance of modeling vane and blade surfaces in CFD as isothermal boundary conditions, and that changes in cooling and inlet temperature profiles had little effects on the blade suction side and almost no effect on the blade pressure side, which may have to do with the near unity DR used. High pressure turbines usually operate with DR > 1.5. Despite the extensive experimental results, these particular works never accomplished comparisons of CFD predictions and experimental vane or blade heat flux with film-cooling.

Tartanville and Hirsch [50] used the same unique CFD methods as the current work to model a single cylindrical cooling hole, blade endwall cooling, and two rows of leading edge holes on a turbine blade. They cited the simplicity and appropriateness of gridding the domain by representing cooling holes through the addition of a local source term at the hole exit.. The method used is computationally inexpensive and requires no grid adaptation in the presence of cooling holes. However, unlike in this work, they used local surface grid refinement within the hole exit plane and downstream of the cooling hole in the streamwise and spanwise directions, which likely aided in providing detailed analyses of the classical kidney-shaped counter-rotating vortex pair produced by flow from the single cylindrical hole geometry. It was ultimately found that increasingly-refined local source term CFD methods converged toward the full meshing approach which gridded the cooling hole passage instead of treating the hole like a transpiration boundary. Experimental results [51] for adiabatic effectiveness on the single hole case

were under-predicted due to the k-ε turbulence model not accurately capturing the lateral turbulent mixing just downstream of the cooling hole. Inaccuracies of this turbulence model and difficulties in resolving the separated region downstream of cooling injection is a well-documented problem in film-cooling literature.

As mentioned by Garg and Gaugler [38], many of the CFD works deal with one film cooling hole, one row, or a couple rows. The challenge today lies in extending accurate detailed studies to a real vane or blade that has hundreds of holes. With modern computers this can be done, but decisions are required regarding what parts of the integrity the analyst is willing to trade-off to keep simulations manageable.

3-D Conjugate Heat Transfer Simulations

The second type of CFD used for this study is a full grid RANS CHT solver that simulates the thermal properties of all solid objects in the domain and the effects on the surrounding flow. Over the past decade, there have been numerous predictive studies accomplished to simulate the conjugate heat transfer in high pressure turbomachinery. CHT studies can be conducted with methods that solve the fluid and solid domains separately or concurrently. If done separately, the fluid domain is solved and then the boundaries of the fluid are used as boundary conditions for the solid domain. For the coupled technique, as in the current work, the solid can be treated as a different block in the overall grid space as the solid and fluid domains interact through interfaces. The first of the two methods requires careful attention to define heat flux across the fluid-solid interface.

The solid domain can be solved two ways. Either the Navier Stokes energy equations can be solved while assuming the velocity is zero and using a proper constant density or the Fourier conduction equation can be used. In this work, however, the Fourier solid conduction equation method is used which facilitates the coupled solid-fluid approach. Most of the work accomplished with CHT simulations has either been with a flat plate model with a single hole or row of holes, or modeling a curved vane, also with a few holes or single row of holes.

Flat Plate Geometries

Of the flat plate variety, Bohn et al. [52] performed conjugate studies of three traditional types of cooling holes, each in a row of four also while comparing the differences between true conjugate and adiabatic surface conditions. A coupled Fourier solid conduction solution method was used as in the current work with the CHTflow code. The shaped holes out-performed the cylindrical holes, as expected, however the shaped hole secondary flow velocities were higher for the adiabatic condition. The conjugate cooling flows are shown to involve higher heat flux, have higher temperatures in the jet, have larger variation in heat transfer coefficient, and exaggeration of the improved performance of laidback fan-shaped holes. Montomoli et al. [53] performed CHT simulations on a cooled flat plate with seven short rows of staggered cylindrical holes using the coupled HybFlow CHT code and compared these to laterally-averaged adiabatic effectiveness and wall-normal temperature distribution data, showing reasonable agreement but admitting that improvement of computation times are necessary due to the solid-fluid interface mechanism in the code. Na et al. [54] studied cylindrical

cooling holes with and without a layer added to account for thermal barrier coatings, including modifying the hole passage to simulate partial blockage of the exit due to the coating. Using a coupled method and the Fluent-UNS code, it was found that with CHT, the surface temperature can be lower than for adiabatic conditions due to forced convection in the cooling hole and internal cooling on the cool side of the flat plate. They indicated that conjugate conditions should be considered when assigning hole spacing between holes in a given row. As will be seen in results of the current work, with CHT, the cooling jet is hotter at the hole exit and the boundary layer approaching the hole is cooler near the wall. Temperatures with TBC were found to be lower than without.

Dhiman and Yavuzkurt [55] used an iterative CHT technique on a flat plate to predict heat transfer coefficients near film cooling holes and reduce computational cost. This loosely coupled technique, unlike the current work, uses the solution from one domain as a boundary condition for the other and the process is iterated to convergence. Using corrections from experimental data to update *h* in the prediction, with cooling and large temperature differences, a 60% difference in heat transfer coefficient and 10% in wall temperature was found relative to the absence of the *h* correction.

Harrison and Bogard [14] used CHT CFD on a classic flat plate computational domain with a single cylindrical cooling hole in one of the first studies to assess the appropriateness of using adiabatic wall temperature to predict heat transfer properties with film cooling. By comparing the heat flux and wall temperature of a film cooled wall using computed values of adiabatic wall temperature and heat transfer coefficient ratio with the results from a conjugate model, they found that when the thermal boundary layer is thinner than the velocity boundary layer, use of adiabatic wall temperature is

acceptable. They also found that when the thermal and velocity boundary layer thicknesses are similar, the freestream gas temperature is better represents the driving temperature. In other words, depending on the flow physics and location relative to a cooling hole, the adiabatic wall temperature, a major part of the adiabatic effectiveness calculation, may not always be the best choice.

Recently, in a similar rigorous CFD study that included conducting walls on a flat plate with a single hole, Zhao and Wang [56] found that the adiabatic wall temperature is the heat flux driving temperature in the case of a theoretically zero wall thickness material, but in the more realistic conjugate case of reversed heat flow from downstream to upstream, where surface temperature can be greater than the adiabatic wall temperature, it is not the driving temperature. Results from this work further emphasize the rather intuitive idea that in laboratory studies with very low thermal conductivity materials, the adiabatic wall temperature should be used, while studies with realistic levels of thermal conductivity should be simulated with conjugate heat transfer models. With film cooling, it should be noted that $T_\infty > T_{aw} > T_s > T_{c,e}$ is rarely true. Depending on the location on the surface of a cooling array, while gas temperature is always hottest, the magnitude of the other three temperatures can change rank readily.

Also testing the validity of adiabatic boundary conditions, one of the latest flat plate CHT studies included a simple single cooling hole domain and four hole types simulated for conjugate versus adiabatic conditions. This study accomplished by Chandran et al. [57] showed for the trenched shaped hole, η was over-predicted by three times the value for conjugate simulations, up to eight hole diameters downstream. Cooling effectiveness distributions near cooling holes were more uniform than for

adiabatic conditions in the streamwise and lateral directions. In addition, shaped holes performed the best in conjugate conditions, followed by trenched cylindrical holes.

One of the most realistic flat plate CHT CFD studies to date compared film cooling for three rows of staggered holes with and without internal impingement [58]. Cooling effectiveness was higher for the length of the plate with the impingement plate included beneath the plate with film cooling holes. Also, comparing the simulations of two materials, steel and low-*k* Perspex, which is essentially another way to compare conjugate and adiabatic studies, cooling effectiveness was lower for the higher *k* steel up to the second row of holes. Clearly, there is much left be discovered in conjugate studies, especially since few works on flat plates have been conducted on realistic film cooling array geometries such as the work mentioned here and that in the current work.

Vane Geometries

Typically the 3-D vanes assessed are simply 2-D cross-sections extruded in the third dimension, like what one would see within a linear cascade experiment. In other words, there has been very little work in open literature on realistic 3-D HPT component geometries that display aspects like twist, varying airfoil cross-sectional area over the span, and varying overall passage area from inlet to exit. For vane geometries, Heidmann et al. [40] modeled the internal and external flows around an extruded vane span section to include a realistic array of showerhead, pressure side, and suction side holes. Using the LeRC-HT code, while this work was not conjugate, it was found that improved performance of shaped holes on the pressure side is necessary to counteract the typically enhanced coolant diffusion and quickly decaying film effectiveness due to existing

pressure gradients and thinning of the boundary layer. They also found that with respect to having no cooling, cooling reduces *q"* while increasing *h* over the entire vane.

Heidmann et al. [59] later used the Glenn-HT multiblock code, a boundary element method (BEM) to model solid conduction, and a decoupled technique with solved for conduction every 100 iterations to find that the adiabatic cases had higher surface temperature relative to conjugate cases and showed the significance heat transfer spreading along the vane wall (in the surface plane) which contributed to high heat flux on the upstream edge of the round showerhead holes.

Concerning coupled and decoupled fluid-solid techniques, Facchini et al. [60] found wall temperature distributions on a vane with three different turbulence models and a coupled CHT method. Distributions of *h* without taking into account transition effects were severely over-predicted. Yamane et al. [61] used a decoupled technique with a heat conduction sub-step to solve for two-dimensional temperature distributions on a vane with three internal cooling passages and no external cooling holes. Kusterer et al. [62] implemented a complex internal flow domain and a coupled approach on a 3-D vane with cooling holes and reported the high sensitivity of leading edge (LE) cooling performance to changes in operating conditions. Montomoli et al. [53] performed CHT simulations on a two-dimensional vane section without external film cooling holes using the coupled HybFlow CHT code and compared this to experimental data, showing reasonable agreement but admitting excessive computation times. Luo and Razinsky [63] validated the STAR-CD code for the NASA C3X transonic vane with the V2F turbulence model in which ten circular internal cooling passages were modeled for conjugate heat transfer and temperature distributions. The turbulence model fared well relative to the *k*-ε model and

compared to experimental temperature data, but room for improvement was noticed in predicting transition and the resulting surface *q"*. This internal cooling case is a proper stepping-stone for external film-cooling CHT simulations. Bamba et al. [64] later used the same internally cooled 2-D vane and RANS solver called UPACS of Yamane et al. [61] to compare turbulence models and found that the shear stress transport (SST) model better predicts transition on both surfaces of the vane using a time-scale bound which is incorporated into the calculation of the eddy viscosity. Zhenfeng et al. [65] used the BEM-HIT-NS code on the Mark II vane geometry with ten internal cooling channels to surface temperature distributions, showing the advantages of BEM simulations as the vane solid does not require interior meshing. Like in many of the works reviewed, difficulties were noticed in predicting the surface properties due to the turbulence model used. Also, these works traded off between accuracy and computational time.

In works challenging the use of adiabatic wall treatments, Ledezma et al. [66] performed CHT CFD simulations of the NASA C3X inlet vane and a LE model, both with a single row of suction side film cooling holes. The hot gas path, cooling passages, and three internal cooling plenums were simulated in the study using the code CFX v11.0 and the k-ω turbulence model. Cooling effectiveness contour trends from CFD compared favorably with infrared two-passage linear cascade measurements in general, except laterally-averaged adiabatic and overall effectiveness was under-predicted up to 15 hole diameters downstream, followed by a region of slight over-prediction for all momentum ratios studied. Inaccuracies of the CFD were attributed to RANS over-prediction of the coolant jet separation, isotropic turbulence, and inherent unsteady effects. Using the same film-cooled vane setup, Dees et al. [67] studied the experimentally-measured

comparisons of conjugate versus adiabatic walls on heat transfer since the traditional assumption of using adiabatic wall temperature as a heat flux driver implies that gas temperature above the wall in unaffected by the growing thermal boundary layer. This study proved to be difficult due to uncertainties in thermal profile measurements; however it was found that near the lateral edges of a cooling jet, conduction caused lower temperatures relative to an adiabatic assumption which agreed with the findings of Heidmann et al. [59]. It was also found that detached cooling jets showed the greatest discernible differences between adiabatic and conducting walls, while attached jets showed smaller variation.

The same group at the University of Texas (UT) at Austin previously challenged the use of adiabatic wall temperature as a heat flux driver through a series of CFD simulations [14] for a single film cooling hole on a flat plate and found that this assumption generally was not inaccurate except in some regions along a cooling jet centerline where heat flux was hard to predict. Dyson et al. [68], also in the UT group, simulated flow over a vane with two internal plenums and impingement for two adjacent cylindrical holes and found that in some cases with a detached jet, the calculation of q'' using T_{aw} would locally over-predict heat flux by double the real value. This causes η to be over-predicted in areas beneath a cooling jet. Even for attached jets, the near wall near wall temperature with CHT was found to be much warmer than T_{aw}.

Regarding engine-like configurations, Ho et al. [69] used ANSYS CFX 12.1 to model uncooled stator CHT effects with external gas flow, internal cooling from one internal plenum, and conduction from realistic inner hub and outer wall attachments. Detailed internal and external h predictions were obtained for comparison to sparse

thermocouple measurements and found good agreement. Mangani et al. [70] simulated the CFX vane profile with LE, near-LE PS, SS, and circular internal cooling using a unique body-fitted structured grid to compare predictions using different turbulence models. It was found that conjugate predictions allowed for much better resolution of the often-matched experimental surface *h* results of Hylton [71] relative to non-conjugate simulations. Montomoli et al. [32] interrogated one of the most realistic 3-D vane geometries to date with internal impingement in two of three internal plenums and external film cooling to study the effects of changes in TBC thickness, hot core location in the mainstream, and turbulence intensity on film cooling performance. Even when considering these uncertainties, predictions of experimental non-dimensional temperature measured by thermocouples beneath a TBC layer were not well matched at the leading edge and on the pressure side near the trailing edge. Lastly, work accomplished in support of AFRL CHT CFD code validation efforts by *Leo* code author Bob Ni [72] on the same 3-D RTV geometry reported in the current work provided significant value regarding the ability to use CHT CFD in properly simulating external film cooling with a sample set of design conditions.

With the advent of conjugate simulations, the thought of reassessing the formulation of proper cooling effectiveness is gaining momentum and will be a major topic of study in coming years. Most of the current issues with CHT CFD lie with the choice of boundary conditions for solid-fluid interfaces, the accuracy of the turbulence model used for the fluid domains especially in regions of separation, and the computational efficiency of simulations with the choice of coupled or uncoupled solid-fluid solution methods.

A vast majority of CHT CFD studies have been for single holes, a couple rows of holes, simple internal passages, or simulated on a two-dimensional vane airfoil geometry extruded in the third dimension, and it can be seen that more work is necessary especially with respect to assessing more realistic film cooling arrays that represent an engine-ready part. Imminent advances in computing power will facilitate increased use of CHT CFD in the turbomachinery heat transfer community. In truly realistic turbomachinery applications, while many CFD codes, conjugate or non-conjugate, have been validated in predicting pressure field phenomena, none have shown to be reliable in predicting characteristics for heat transfer.

The current work takes existing efforts a few steps further by: 1) predicting heat transfer aspects in the internal and external fluid fields with conducting solid effects on a modern fully-cooled (including SS and endwalls) full-scale turbine inlet vane with 648 holes in their true configuration, 2) comparing the CHT CFD simulations with and without film cooling to measurements on the vane in its experimental environment (AFRL TRF blowdown rig) to help validate the code in Appendices B and C, and 3) comparing CHT CFD results between the vane and flat plate PS model for similar flow conditions.

Design and Optimization Efforts

Optimization problems combined with objective functions and thorough evaluation applications have been used extensively since the early 1990s to solve design problems with multiple variables, reasonable constraints, and a large design space. Many different optimization techniques and evaluation methods have been used. Popular

optimization techniques include the use of evolutionary algorithms such as genetic algorithms (GAs) and multi-objective genetic algorithms (MOGAs), gradient-based methods, adjoint methods, sequential quadratic programming (SQP), artificial neural networks (ANN), simulated annealing (SA), or some combination of these. Each type of optimization has its advantages and disadvantages. Different types of optimization provide varying levels of convergence, reliability, and robustness. The work of Dulikravich et al. [73] provides a good summary in this respect. Ideally, an optimization should require the least number of time-consuming objective function evaluations. The number of function evaluations is equal to the number of intermediate designs in the process, which is the number of generations multiplied by the number of designs populating each generation. Overall, non-gradient-based optimizers, such as a GA, tend to have the ability to escape local maximum and minimums to search a large portion of the objective function space and find a global optimum. On the other hand, GAs can take more computational time, have difficulties handling constraint functions, and tends to arrive at a family of very similar solution designs that may lack a level of desired diversity.

Genetic Algorithms

Multiple scholarly optimization works have been completed on wings and airfoils [74, 75, 76, 77], endwalls [80], and turbomachinery stators and rotors. Obayashi and Tsukhara [76] used three different types of optimization algorithms for aerodynamic shape design, in which the purpose was to determine upper and lower surface contours for a wing airfoil in order to maximize lift coefficient. Gradient-based, simulated

annealing (SA) and genetic algorithms (GAs) were compared. While the GA used the most computational time, the GA far out-performed the other algorithms creating a coefficient of lift 25% higher than the next best result. DeFalco [77] used evolutionary algorithms in the direct and inverse design contexts to derive an airfoil cross-section design for wings. It was shown how GAs provide significantly improved designs over conventional methods, how to greatly reduce the time to search for optimal designs, and how evolutionary algorithms can be easily parallelized. CFD, the most common optimization evaluation step used in open literature, was used by Durbin et al. [78] to define optimally-contoured endwalls for a one-blade, two-passage infinite cascade for turbulence modeling studies.

Turbomachinery Optimization

Optimization on turbomachinery can be split into works that use evolutionary algorithms [79, 80, 81, 82, 83, 84, 85, 86, 87, 88, 89, 90, 91, 92, 93] and other gradient-based and adjoint methods [94, 95, 96, 97]. Of the gradient-based optimization methods, Kammerer et al. [94] took advantage of the technique's efficiency relative to GAs combined with SQP and 3-D CFD to validate the design of a turbine stage. Adjoint methods have gained popularity within the last few years due to its ability to perform fast and accurate sensitivity analyses of parameters in the design space. This method uses the control theory of the system of equations being solved in which all gradient information can be found by solving the equations only once, independent of the number of variables being changed [95, 96]. This greatly reduces the number of objective function evaluations and CPU time relative to GAs. However, for the current work, since CPU

capabilities are not a concern and a global optimum in a very large search space is desired, the GA optimization method was chosen.

In the last decade, there has been a dramatic increase in the use of genetic algorithms within optimization methods applied to aerospace applications, especially in the realm of turbomachinery design. Among the many works that used evolutionary algorithms, perhaps the most applicable work has been done by the Pennsylvania State University (PSU) group. Dennis et al. [79, 80] used GAs to minimize pressure loss on a 2-D airfoil cascade row while keeping axial chord, total torque, flow angles, blade cross-section area the same and keeping thickness distribution above a minimum value. Using a RANS CFD solver and k-ε turbulence model to evaluate 45 generations of designs, a much more efficient aerodynamic shape was generated.

Anguita et al. [81] used GAs as part of a Support Vector Machine artificial intelligence concept to design a turbine blade with low loss and high loading. Demeulenaere et al. [82] effectively used multipoint optimization techniques with GAs, custom fitness functions, an artificial neural network to improve the efficiency of a rotor blade by almost 1% and the pressure ratio by over 2%. Arnone et al. [83] used 3-D CFD analyses and GAs with geometric parameterization and complex fitness functions to reduce profile loss on a high-lift blade while keeping other design specifications constant, resulting in a higher performance airfoil. Oyama et al. [84] and Larocca [88] used GAs with 3-D CFD to redesign compressor rotors. In one of few works to optimize for low heat transfer, Johnson et al. [85] used GA optimization and a validated 2-D RANS solver to reduce the overall heat load, leading edge heat flux, and the pressure losses on the midspan geometry of the highly-experimented VKI vane. Oksuz and Akmandor [86, 87]

used these same methods to create both efficiency- and torque-optimized turbine rotor blades. More recent works [88, 89] entail finding the optimum lean, sweep and bow shapes for a stator and rotor within a stage to produce the best structural properties. Even rocket engine turbopump components are being optimized for high efficiency and minimum size using these methods [93]. These works clearly support the use of GAs in a wide variety of design problems, which is used in optimizing the vane PS cooling array in the current work.

Film Cooling Optimization

Concerning optimization for desirable heat transfer characteristics and cooling of axial turbine components, internal and external, there are only a handful of works in this realm [98, 99, 100, 101, 102, 103, 104, 105]. The PSU group has been especially active in this area. In order to make temperature distribution in a blade cross-section as uniform as possible, Dulikravich et al. [98] changed variables like size, shape, and locations of internal cooling passages, internal wall thickness, average wall roughness, and coolant conditions while evaluating using simple conduction relations. Using a GA, surface temperature on the best design was significantly more uniform that the initial design. In another work, the sizing and placement of internal, round vane cooling passages was optimized on a 2-D airfoil constrained to a certain size range and distance from the surface, with a maximum number of passages [103]. The objective was to minimize the amount of heat transferred to the vane while maintaining a maximum temperature lower than an allowable level in which an analytical finite element method was used in evaluations. It was mentioned that taking this kind of optimization to the next level, with

3-D CFD full grid or conjugate heat transfer involved orders of magnitude more complexity and computing time. Mousavi et al. [105] also performed an optimization of this kind.

The work of Dulikravich et al. [98], Talya et al. [101] and Rajadas et al. [100] used non-evolutionary algorithm optimization to find an optimal internal cooling passage sizing along with optimal placement of six straight cooling hole passages at turbine blade root and tip span locations. Large reductions in average and maximum temperatures were achieved. Favaretto et al. [102] used a single-objective GA and the RANS CFX solver with a k-ω SST turbulence model to vary impingement and discharging hole diameters, pin diameter, and pin height to maximize impingement cooling efficiency. In 2-D optimization of blade cooling in order to minimize the necessary cooling flow and keeping heat transfer to a minimum, Muller et al. [99] mention that evolutionary strategies are robust, highly parallelizable, and suitable for multimodal functions without requiring gradient information. Using the steady heat equation as an evaluator and two types of algorithms, the optimized cooling hole row placement revealed a cluster of leading edge rows, even spacing on the suction side, and a few pairs of cooling rows on the pressure side.

Recently, it was shown that a validated immersed mesh technique could be used to simulate cooling holes at different locations on a vane profile which could be handy in an optimization [106]. Using ANSYS CFX as a fluid-only evaluation tool, Latin hypersquare sampling (LHS) initialization, and the combination of GAs and an ANN, a single suction side shaped cooling hole's performance was optimized by El-Ayoubi et al. [107] by varying coolant-to-mainstream total pressure and temperature ratios within

reasonable ranges. These ratios were optimized in order to increase η downstream of the hole and minimize loss. However, this single hole cooling condition optimization has limited application to an engine-representative cooling configuration because other holes on the SS would change optimal conditions dramatically and conditions did not factor in percentage of mass flow relative to core flow. Up to this point, these works have only optimized film cooling for a 2-D profile—not for an entire PS or SS cooling array.

One of the more comprehensive works to date is that by Lee and Kim [104], in which a single 3-D hole shape was optimized using a RANS solver with k-ω SST turbulence model and a highly refined grid as an evaluation tool. With the objective to maximize spatially averaged film cooling effectiveness, four variables were optimized on: injection angle, lateral spreading angle, forward expansion angle, and length-to-diameter ratio for the hole. LHS followed by a weighted average model with basic surrogate models and sequential quadratic programming was used to obtain sensitivity information about individual parameters and come to a maximum-fitness design that had a wider lateral expansion, longer length-to-diameter ratio, slightly greater injection angle, and less forward expansion than the reference hole design. Later, the same authors used similar methods to optimize a hole shape and compare it with two fan-shaped holes and a dumbbell shaped hole [108]. Injection angle, compound angle, and *L/D* were among the variables changed in the study. The new hole performed well at high blowing ratio, but its shape lent it to being very costly to manufacture. These are two of few optimizations on a single 3-D hole shape, however as in the current work, to perform this type of optimization on all the holes on the pressure side of a vane would be very highly computationally expensive, because in this case, changes in the actual 3-D shape of the

hole would have to be incorporated in the optimization loop, which in turn requires CFD grid generation with every new individual genome. A hypothetical optimization such as this is many years down the road in terms of computational capabilities.

Film cooling correlations for film effectiveness typically used today in industry durability designs are mostly derived from works such as that of Hartnett et al. [24], Goldstein et al. [109], Mayle and Camarata [110], and Brown and Saluja [26]. These works were applied to consecutive rows of cooling holes due to superposition derivations by authors like Sellers [29] and Muska et al. [30]. These works are as much as fifty years old. For a given axial location on a cooled airfoil, the superposition model simply uses the film temperatures from all upstream holes as the freestream adiabatic wall temperatures in the local expression for effectiveness. These correlations can be used to maintain a wall temperature below a maximum limit with axial distance or maximize cooling effectiveness over the surface. But this only accounts for flow behavior at one span location, and empirically at that. 3-D CFD methods that identify hot streaks and eliminate them through optimization of an improved cooling array is a much more appropriate method for film cooling design. In addition, computational capabilities today do not at all prohibit that type of routine design assessment, making the methods outlined in this paper more attractive.

In general, few studies have applied mathematical optimization methods to gas turbine film cooling. To the author's knowledge, no cooling hole optimization studies in open literature have been attempted for an entire surface array of film cooling holes. Neither has there yet been work in specifically varying in order to optimize hole size, injection angle (α), compound angle (β), and two-dimensional location in a given row.

Most studies in open literature are still restricted to a single hole, pair of holes, row of a few holes, or a couple successive rows with few of these occurring on curved vane and blade surfaces. Finally, no studies are known to pinpoint industry-standard HPT vane cooling design methodologies and attempt to improve on them. Ideally, the current work represents a step-change in optimizing film cooling for the entire surface of a modern turbomachinery airfoil.

HPT Film Cooling Experiments

Infrared Thermography Assessments

Infrared thermography (IRT) has been used many times in past assessments of turbine component heat transfer and cooling performance, just as in this work, in obtaining flat plate surface temperatures to calculate overall effectiveness. Most experiments involve an IR camera which uses a steady or transient technique that maps the temperature distribution on a two-dimensional surface and digitizes to a processed image depending on the available resolution. The IRT technique is advantageous because it is non-intrusive, it provides full map combined heat transfer data, and can be used to gather many images over short periods of time. Steady flat plate test rigs have been around for a long time, dating back to such works by Muska et al. [30], who used radiometry to measure surface temperature and black high emissivity plates with cylindrical cooling hole row pairs to test theories on classical superposition models for streamwise prediction of cooling effectiveness. Sasaki et al. [111] was the first to look at laterally-averaged η data for multiple staggered rows of holes on a flat plate to compare superposition correlations. Wittig et al. [112] conducted single-hole flat plate tests to

compare a cylindrical, fan-shaped, and laidback fan-shaped hole using an IR camera to measure surface temperature. They used different plate designs to separately obtain T_{aw}, q'', and discharge coefficient for each hole type.

Quasi-transpiration cooling concepts [113], varying film cooling hole shapes [114], investigations to find adiabatic effectiveness for varying flow conditions, cooling hole spacing, and injection angles [115, 116], transient measurement shaped hole studies [117], shaped holes studies in multi-row staggered arrangements [118], as well as assessments of cratered cylindrical holes [119] and anti-vortex holes [120] have been tested on flat plate models using IRT.

IRT has also been used to asses various film cooling properties on other geometries, such as a turbine blade leading edge model [121], the suction side of inlet vane [122, 123], the trailing edge cutback features on the pressure side of a turbine vane [124], and vane geometries with varying types of trenched cooling holes [125]. Trenches are meant to have similar cooling effectiveness results to continuous slots, but provide easily-fabricated diffusion features and structural integrity for cooling array designs. Trenches have also been known to out-perform shaped holes at lower blowing ratios. Transient techniques to find both heat transfer coefficient and adiabatic effectiveness in the same test for a single hole have been used for both steady [126] and pulsed film cooling [127] on leading edge models. A high-speed scanning IRT technique has also been used on the pressure side of rotating turbine blades to obtain surface temperature maps to compare with predictions [128].

Recent works using IRT have assessed the cooling performance of the C3X vane in a cascade with internal cooling passages and one PS hole, three LE holes, and two SS

holes which could be interchanged to study different holes shapes including cylindrical holes, craters, a modified trench, and a standard trench. This work by Davidson et al. [129, 130] is unique in that the hole shapes were generated by using a custom-shaped thermal barrier coating (TBC) layer as the edges of each hole type. This method of carving the hole shape out of the TBC rather than the metal has potential in saving manufacturing costs. It was also more realistic than most works due to the use of a TBC layer (cork) in the assessment. The latter work [130] assessed the same hole shapes against simulated ash deposition (wax) and found that trenched holes were better at reducing contaminant thickness relative to round holes. IRT was also used by Kinell et al. [131] to assess a vane in a single passage cascade with three SS rows of holes and six PS rows, one of the more realistic configurations to date, in which it was found that the presence of showerhead holes greatly enhanced downstream cooling on both the PS and SS. In this study of 21 different cooling row positions, PS *h* increased with more cooling hole rows relative to the SS, especially near the trailing edge.

Together, these works have shown the advantages of rapid-prototyping of easily tested full scale flat plates, they have reaped the benefits of non-intrusive IRT techniques relative to conventional sensors such as liquid crystals and thermocouples in obtaining high-resolution two-dimensional broad-range temperature data, they agreed with well-documented trends in the design of cooling features such as the improved performance of trenched and shaped holes, and they showed that a portion of the work on curved models closely matched the cooling effectiveness on the flat plate experiments. These techniques not only allow for the screening of the latest component designs but also provide

validation data for computational heat transfer and design analysis tools such as the latest conjugate heat transfer (CHT) CFD codes [132].

Most of the above studies are transient IRT techniques. The current work is a steady state assessment requiring more time to reach a constant temperature. Overall, using IRT is well-established and accepted in the turbomachinery research community and it is the preferred method for heat transfer assessment. The current work offers a full-map assessment of a baseline and optimized operationally-ready modern turbine vane pressure side design in which the combined effect of different holes can be seen, rather than just an assessment of a single hole, single hole type, or row of holes. This work is also unique in that the experimental conditions including total pressure and temperature ratios match that of relevant RTV testing using full-scale rotating turbine blowdown rig. The method is a simple and reliable steady-flow assessment that is also highly repeatable with flat plate models that are readily exchangeable. These experiments are thereby less costly than highly instrumented rotating rig assessments that obtain heat flux and surface temperature at only certain span locations of the vane surface [27]. Ultimately, the imaging capability of the IR technique gives quantitative information regarding the relative effects of internal convection, internal conduction, and film cooling on the surface temperature distribution of the flat plates studied here.

Full-Scale 3-D Blowdown Facility Experiments

There are few works in open literature regarding full-scale blowdown rig experimental heat transfer data on vanes and blades except older works by Dunn et al. [7] in the 70s and 80s, and more recent works by Anthony et al. [21] with the AFRL TRF,

and Mathison et al. [46, 47, 48] with the facility at Ohio State. This type of rig is important to the current work because it is the basis for the vane PS film cooling optimization. The optimized cooling design from this work will ultimately be tested in the AFRL TRF with heat flux gauge instrumentation. The plates experimentally tested using IRT in the current work are based on the RTV PS cooling array. Also, both forms of CFD used here are conducted with flow conditions derived from TRF measurements. Other, similar blowdown rigs exist, such as the isentropic light piston tunnels at Oxford [133] and Massachusetts Institute of Technology [134]. The AFRL TRF is superior to these other rigs since the usable run times from which to obtain thermal data are more than five times longer than the next best rig. Details on the TRF are given in Appendix A. This is important knowing that recent findings by AFRL have shown that film cooling flow takes at least a half second to establish itself in this type of rig, lending to the fact that film cooling data taken with run times any less may not capture cooling performance as observed in a more steady engine environment.

Fundamental Trends and Laboratory Studies

This section summarizes much of the film cooling trends observed in open literature and ultimately aids in the decision-making process for the optimization phase of this work, ensuring proper variables and respective ranges are considered. Most of the trends realized here are the results of laboratory-type experimental setups geared towards studying the effects of film cooling key parameter on another. Fundamental film effectiveness data can be highly useful for turbine design purposes when it is performed under compatible engine-like conditions for those parameters most affecting film-cooling

performance. Under noncompatible conditions, the data are not of design use, but rather point to relative results that might distinguish between hole geometries [10]. Many of the studies in literature provide fundamental trends but not exact data for comparison to realistic engine conditions. This point is reemphasized later in this dissertation where CFD is used to model full-scale engine test conditions. Flat plate studies here are assessed for relative performance between baseline and optimized cooling array designs at proper total coolant-to-mainstream temperature and pressure ratios. The flat plate CHT CFD work described in the results serves to gauge the appropriateness of flat plate studies in obtaining thermal (not aerodynamic) performance measurements relative to more engine-like configurations.

Goldstein [135] was one of the first to study shaped holes extensively and found that shaped holes cause two effects: a reduction in momentum flux ratio I at the hole exit leading to less penetration into the mainstream flow, and what is called the Coanda effect in which the coolant jet hugs the surface. Shaped holes tend to have less varying film effectiveness with changing blowing ratio M relative to cylindrical holes and do not tend to have a maximum value of effectiveness downstream of the hole often seen due to jet separation. Typical fan-shaped holes also create an exit flow structure with vortices with less wall-normal disturbance than those created by cylindrical holes. Also, shaped holes with both forward and lateral expansion tend to have better film effectiveness than those with only lateral expansion due to the extra diffusion of the jet and they have more robust effectiveness for higher ranges of M [11]. Unlike shaped holes, cylindrical holes tend to create a horseshoe rollup vortex at the point of jet interaction with the mainstream flow, which wraps around the jet. In the case of round holes at high enough M, the horseshoe

wraps around and underneath the counter rotating vortex pair jet. Baldauf et al. [115] found that as blowing ratio increases from M = 0.2 to 0.6, the peak level of spanwise-averaged η increases, and above M = 0.6, the peak $\bar{\eta}$ begins to decrease again, suggesting that there is an ideal level of blowing. They also found that the location of maximum $\bar{\eta}$ moves downstream as M (and consequently, I) increases. Overall, shaped holes give higher η for M > 0.5, have greater NHFR for I > 1.0, do a better job turning the coolant toward the wall, and have a much lower tendency to separate compared to round holes.

When cooling holes are oriented at some compound angle β, a greater coverage area is generated downstream of the hole and a broader jet profile is presented to the mainstream flow passing over the jet. This gives better η, but also causes an increase in h [3]. In flat plate studies, shaped holes with a 60º compound angle have been shown to have 20-40% higher effectiveness near the hole compared to axially-oriented even with increased lateral hole spacing up to P/D = 6, but much higher h for high levels of I [136]. By downstream distance x/D = 15, however, the increased performance of forward-expanded holes reduced to η levels of the round holes both with and without a compound angle. Recent cascade vane SS studies by Zhang et al. [137] with varying levels of mass flow ratio (based on fraction of engine core flow) have shown positive and negative β to provide better film effectiveness than axially oriented holes, especially at higher M.

Pressure side film cooling performance is a strong function of blowing ratio. At high M, on a concave surface such as a vane PS, a 45º compound angle provided 30% improvement in near-hole film effectiveness over axial shaped holes [138]. Generally, if the coolant jet momentum is less than the mainstream, the curvature of the jet is less than the wall radius of curvature, and the coolant will be pressed to the surface, but if the jet

momentum is greater than the mainstream, the opposite is true about curvature and the jet will move away from the wall [3]. On the concave PS, Taylor-Gortler vortices resulting from flow instabilities tend to develop which can adversely affect film cooling performance. Results have shown that for varying *DR*, effectiveness is higher for convex flows than concave flows [139]. It has been postulated that for concave surfaces there is a cradling effect that causes jet elongation, preventing the lateral spreading as compared to a flat plate case [25]. This provides a longer jet attachment region downstream of the hole. When assessing $\bar{\eta}$, this value was higher with a positive (favorable) pressure gradient than a zero pressure gradient. In addition, it was found that for round holes at α = 45º, as wall radial curvature increases, so does $\bar{\eta}$ for a given *M* up to *x*/*D* = 10. NHFR was found to increase with increased radial curvature for all *M*, to the point that area-averaged η was observed to be independent of *M* and primarily due to curvature. Without curvature, NHFR decreased linearly with *M*. In a favorable pressure gradient, higher *M* conditions experience a greater cooling performance benefit over lower *M*. Also, at high *DR*, the curvature affected area-averaged η to a lesser degree. Teekaram et al. [140] were able to show that in the presence of a strong favorable pressure gradient the film cooling performs far better near coolant injection for high *M*, but streamwise η did not vary greatly for changing pressure gradient.

Concerning shaped hole studies and heat transfer coefficient, a developed boundary layer with cooling will most often be turbulent in nature. A turbulent boundary layer will not be as disturbed by the injection of coolant as will a thin or developing boundary layer. Heat transfer coefficient shows the influence of coolant injection on the heat transfer process due to the fluid dynamic situation in the boundary layer [12]. It is

not dependent on the cooling air temperature, but the fluid dynamic boundary conditions. At low *M*, coolant injection serves to thicken the boundary layer so that *h* is lower than with no cooling [10]. Thinner boundary layers are found near the leading edge of a vane and thicker reaching a maximum near mid-chord, depending on conditions. Chen et al. [138] performed studies with thin boundary layers with $\delta/D < 0.12$ and low DR near 1.0 (where δ is the boundary layer thickness), on a concave surface and found *h* enhancements of about 1.5 for low *M*, which was the same as for a round hole. When *M* was increased to 2.0, *h* rose even more with levels persisting downstream, especially for holes with compound angles. There is a larger effect on η when *I* is such that the penetration distance of the coolant jet is on the order of δ. For shaped holes near the leading edge, a similar trend is seen, where *h* increases with *M* and then decays to a certain level at the same distance downstream, regardless of conditions.

The effect of mainstream turbulence on film effectiveness has been shown to be less for shaped holes than for round holes, but provides for a higher level of *h*. At low *M*, the effect of mainstream turbulence level (*Tu*) on effectiveness is less for shaped holes, while at high *M*, the effect of *Tu* is the same for either hole shape. It has been shown that at high *M*, when much of the jet has lifted off in the low *Tu* case, high *Tu* turns the increased mixing into an asset, entraining coolant that penetrates into the mainstream flow and mixing it with air near the surface [141]. In general, *h* will increase slightly at the point of coolant injection and quickly decrease to the level expected without cooling and a higher freestream *Tu* causes a more rapid decay in η than a low *Tu*. Only for $Tu > 8\%$, will significant decreases in η be seen, and especially for $Tu > 17\%$ where η can be reduced to zero by 20 hole diameters downstream ($x/D = 20$) [142].

Realistic engine levels of *Tu* are between 10 and 15%. Both the flat plate and blowdown rig experiment flowpaths involved in the current work have low *Tu* (< 2%). In high *Tu* environments with leading edge blowing, greater lateral dispersion and fluctuation of coolant is seen on the PS, rather than a break-up of the jets, giving a broader η distribution [143].

Regarding measurements of NHFR, when injection disrupts the boundary layer severely, for example when there is a high *M* for a given hole in a location and δ is low, NHFR can be greater than unity near the hole [144]. In other words, in this case, film cooling actually increases heat flux. This work was one of the first to point out the importance of evaluating film cooling performance in terms of NHFR rather than just η.

For leading edge cooling, coolant in the showerhead region is often injected as much as 5*D* into the mainstream flow even at relatively low *M*, due to the low U_∞ stagnation region traits [145]. At the leading edge, there is less crossflow that would turn the coolant jet toward the wall. Unlike film cooling of flat surfaces, here in a high-curvature region, η generally tends to increase with *M*. Leading edge cooling is also known for large increases in *h*, however since there is a high level of η as well, there is a large reduction in net heat flux. A decrease in performance was found in terms of $\bar{\eta}$ with increasing *M* with showerhead blowing was much less than without, which means blowing from the leading edge helps to mitigate effects of coolant jet separation downstream. Increased turbulence from the showerhead greatly increases dispersion of coolant on the PS. Consistent with previous works, the levels of η with showerhead cooling was less than that expected using a superposition model as in Equation 16, perhaps due to the curvature effects. The effect of leading edge blowing with a

showerhead row at β = 45º on three downstream PS fan-shaped cooling hole rows was measured by Schneider et al. [28] using thermochromic liquid crystals (TLCs) in a single passage vane cascade. There was degradation in $\bar{\eta}$ for the first PS row where there is high curvature and sensitivity to aerodynamic effects like boundary layer transition, but only for very high M that would be unrealistic in an engine. This row also had a high injection angle of α = 55º. Although, the third PS row showed a slight increase in $\bar{\eta}$ up to M = 2.0 and leveled off for higher M.

It has been found within the last fifteen years that the geometry and manner in which coolant flow is fed into a hot mainstream flow has a significant effect on the surface heat transfer and film cooling effectiveness. Channel-fed film, internal channel flow velocity and direction, turbulence generated inside holes, having holes placed near internal plenum rib turbulators, and even internal surface features of holes all have an effect on the resulting cooling [10], and can be summed up through examination of one parameter: discharge coefficient. In addition, to properly match real airfoil cooling in an engine, the length-to-diameter ratio (L/D) must closely match. A realistic value of L/D is usually between 2 and 5, while many studies in open literature have cooling holes with an $L/D > 5$. The flat plate studies conducted in this work use the same value of L/D and coolant-feed configuration as the vanes used in full-scale experiments and ultimately in the engine. Therefore, discharge coefficient is not major concern for the current work. However, this is an important parameter that should always be considered.

Pairing up two rows of holes, known as a double row, has been shown to increase coolant coverage while keeping proper structural strength and at high M two closely spaced hole rows provide greater $\bar{\eta}$ than would be expected from a simple superposition

calculation of the performance of a single row of holes [146]. The first row of holes will significantly increase the boundary layer presented to the second row. Typically, double rows are staggered so that the second row is centered between the holes of the first row and have coolant injection aligned axially with the flow. It is well-known that this is better than lining up the two rows of holes with each other. Saumweber and Schulz [118] studied five configurations of large scale double rows with constant P/D and α and varying spacing between rows. They had a number of important findings: upstream injection increased η 50% for both cylindrical and shaped holes due to the pre-cooled boundary layer, downstream cooling performance was dominated by second row hole shape and M, having a higher M for the second row relative to the first provides optimal cooling overall, and in a staggered configuration, the vortices from the upstream row created a secondary flow oriented toward the wall, pushing the second row coolant jets toward the wall and reducing detachment tendencies. Lastly, it was found that decreasing the axial space between rows increases both η and h simultaneously, giving no major advantage. Sinha et al. [147] found that the thicker boundary layer created by one row of holes causes greater jet penetration into the mainstream flow and lower Tu for the second row. Also, a higher DR tends to lead to larger boundary layers.

Novel Cooling Hole Shapes

Aside from cylindrical or fan-shaped film cooling holes, within the last decade, many new types of holes have been studied. A study of the many different shapes and their respective traits is important for the choice of candidates for experimentation in the flat plate test phase of the current cooling array optimization. Goldstein [8] predicted that

a hole geometry which turns the secondary fluid (and thus the jet momentum) toward the wall as it enters the mainstream would be desirable in terms of optimizing the film cooling performance. The cooling hole shapes created by some of the researchers to follow have shown that this is not always true.

Lu et al. [119] conducted a study of three types of cratered holes at a specified depth and compared them to a trenched hole, a cylindrical hole, and a fan-shaped hole. The intention of cratered holes is to mimic the reduced exit momentum seen in forward and laterally-diffused fan-shaped holes. Overall, the laidback fan-shaped holes out-performed all other holes at all M. Meanwhile, better η was measured for the cratered holes compared to the cylindrical baseline case by about 50%. The cratered holes suffered from strong counter-rotating vortices and increased h relative to the cylindrical hole. The trenched hole provided better lateral spreading, which was also seen as a weakness of the cratered holes. Although, better future results may be found with cratered holes if more than one crater depth was studied. Fric and Campbell [148] studied a cratered hole on a flat plate in which the hole sits in a shallow round depression that is filled prior to coolant issuing into the mainstream. A 50% improvement in effectiveness was found compared to round holes at $M = 1$ and even greater improvement was seen at very high M, as would be seen on a combustor liner.

Rhee et al. [149] assessed the cooling effectiveness of rectangular-exit holes, one with lateral expansion, one without, and compared to round hole performance. One feature of rectangular holes is that the centers of the counter-rotating vortex pair were closer to the wall than the cylindrical holes due to the Coanda effect. The rectangular holes, which are like discrete slots, showed higher $\bar{\eta}$, higher NHFR, and lower h for all M

over a distance up to x/D = 25. The rectangular hole without expansion showed much higher h and much lower η compared to its laterally expanded counterpart, mostly because the latter is essentially a laidback fan-shaped hole, just without forward expansion (and further momentum diffusion). Taking the previous study a step further by arranging the same hole shapes in three staggered rows rather than one row with constant 4D spacing, Rhee at al. [150] used the same thermochromic liquid crystal technique for 2-D η maps and three-axis traversing thermocouple rakes for non-dimensional temperature contours at a given downstream location. The rectangular hole with expanded exit showed less influence of temperature gradient in the wall-normal direction than other hole shapes after the second row, they found that the upstream vortices pushed the downstream-hole vortices toward the wall as found by Suamweber and Schulz [118], and the effects of hole shape and M is reduced from the second row to the third row, relative to the changes seen from the first to second row.

In order to address the aerodynamic inefficiencies of fan shaped holes, Sargison et al. investigated converging slot-hole, or "console", geometry in a flat plate [151] and vane cascade setup [152]. With this kind of hole, area decreases towards exit causing flow to accelerate but not necessarily to choke, giving more stability and lower jet turbulence. Peak lateral η was similar for the fan shaped hole, slot, and console, which were all better than the round hole. The authors argues that the slot and console had the same level of h than a flat plate without film cooling, but the cylindrical and fan shaped hole exhibited lower laterally-averaged heat transfer coefficient, $\bar{h}$. In the cascade, on the vane PS, the fan shaped hole again showed higher η and lower h, but the authors attributed this to the number of consoles they decided to place on the surface.

Dhungel et al. [120] studied round holes with accompanying pairs of smaller, symmetrical, cylindrical anti-vortex holes placed at different locations which are intended to reduce the strength of the kidney-shaped vortices from the main hole, allowing better jet attachment downstream. This arrangement is also easy to manufacture. The second major intention of anti-vortex holes is to reduce the momentum issuing from the main hole and provide better coverage between holes in a row. Anti-vortex holes placed at a moderate distance laterally from the hole aligned with the downstream edge of the hole performed better than all other cases, but none fared as well as a traditional shaped hole.

Trenched holes have gained popularity over the last decade as well. These holes are intended to cause coolant to spread in the lateral direction and fill the trench prior to entering the mainstream flow. It has the advantage of being formed using the protective coatings without machining a trench into the substrate. Trenches usually have cylindrical holes with a trenched exit and upstream and downstream rectangular lips in various positions. Trenched holes perform significantly better than regular cylindrical holes, to the point where half the holes in the lateral direction can be used to provide the same downstream cooling effectiveness [153]. In a proper study of the effects of trench depth, Dorrington et al. [154] found a critical depth of $0.75D$ provided the best film effectiveness, deeper trenches were less sensitive to increasing trench width, and increasing the downstream lip offset beyond $0.5D$ caused significant degradation in performance. This type of hole is equivalent to shaped hole performance in that effectiveness on flat plate tests is increased 50-70% compared to round holes. At low M, narrow trenches have higher near-hole η than cylindrical holes, and those with a rectangular lip just after the hole had the best cooling effectiveness, which was on par

with fan shaped holes [136]. Recent work using IRT on an adiabatic wall flat plate included a trench with upstream shallow tetrahedrons that are intended to shield the incoming film from hot flow and increase lateral η [155]. However, this highly detailed design, like many of the novel shapes discussed here, would be expensive to manufacture.

Double-jet film cooling (DJFC) has been explored by Kusterer et al. [156] in an effort to provide alternatives to expensive shaped-hole manufacturing. DJFC prevents the cooling jet from lifting off the surface increasing lateral spreading through use of an anti-kidney vortex that is generated due to the combined β of the two holes. Knowing holes with compound injection tend to have a dominating vortex on the side of the jet farthest from axial direction, this idea was used to pair-up tow holes, the second hole having an oppositely-directed compound angle as the first, resulting in better lateral diffusion. Comparing IR experiments to conjugate heat transfer CHTflow 3-D RANS code simulations that used an adiabatic boundary condition, it was shown that DJFC holes fared well experimentally against trenches and craters downstream at $x/D > 5$ and DJFC holes outperformed shaped holes at high M above 1.5. Building on this idea, Kusterer et al. [157] also recently tested Nekomimi (Japanese for cat ears) holes, which create a pair of anti-counter rotating vortices. The resulting exit shape of the hole is like a bent kidney bean. This hole shape performed better than shaped and trenched holes at $M = 1.0$ up to $x/D = 10$ in IRT experiments.

Two novel hole shapes that will be tested experimentally using IRT in this work are Vehr holes [158] and miniature trench shaped (MTS) holes [159]. Vehr holes are like laidback fan-shaped holes except they have a square (not circular) cross sections through

the thickness of the material, and instead of expanding laterally in two directions symmetrically, the Vehr hole expands by increasing the length of two adjacent of four sides in the square cross-section. This is analogous to grabbing a corner of the square cross-sectional area and dragging it to increase its size. The MTS hole, created by the author, will be discussed later in more detail, but it has a small trench inside a shaped hole which makes the trench configuration much easier to manufacture. All trenched holes to date use trench configurations with the hole exit lying along the floor of the trench. This can be hard to manufacture since the front lip of the trench can block the drilling tool from making the forward-diffused features of the shaped hole inside. This adds significant cost. The MTS hole uses a smaller trench that is carved after, instead of before, the shaped hole, making for an easy two-step process. Manufacturing thus involves EDM drilling a shaped hole as usual, followed by carving out a trench over the length of any row of shaped holes. It is believed that the smaller trench disturbs the flow over an airfoil less than larger typical trenched hole configurations from past works along with providing the inherent laterally-diffusive cooling benefits provided by a trench. This agrees with work by Bunker [160] that showed narrower trenches out-performing their wider counterparts in flat plate experiments.

Other studies involve the use of double-fan shaped holes to improve the discharge coefficient and losses associated with a fan shaped hole by having a fan-shaped entry from the cooling plenum [161], the use of vortex strength-reducing triangular tabs near the exit of cylindrical holes to increase effectiveness relative to round holes without tabs [162], and computational studies of bean- and dumbbell-shaped holes [163]. Studies have even been done to assess downstream bumps, domes, and short cylinders protruding

into the flow on the performance of shaped holes [164]. Naturally, these would not be practical in the hot environment of a real engine. Lately, novel internal wall impingement schemes are being introduced such as dendritic schemes by Luque et al. [165] at Oxford. This scheme, like many of the novel holes, would be very expensive to fabricate. Unfortunately, some holes discussed to this point cannot be manufactured at all. Overall, fan-shaped holes still perform very well compared to novel designs, while the most promising new hole shapes appear to be trenches and double-jet holes.

IV. Computational and Experimental Methodologies

Research Turbine Vane (RTV)

The object of experimental and computational study for this research is the High-Impact Technologies (HIT) Research Turbine Vane. It is a modern airfoil originally designed for optimum aerodynamic performance and it is also the subject of comprehensive experimental testing in the AFRL TRF. The RTV PS film cooling array is optimized for improved cooling performance in the current work. It has an axial chord length of 4.52 cm and a turning angle of 76.88 degrees. The cooled vane has six showerhead rows of smaller cylindrical cooling holes on the leading edge, four rows of laidback fan-shaped holes on the SS, and six rows of fan shaped holes on the PS. There are only two different cooling hole shape-size combinations on the entire baseline vane cooling scheme, one for the showerhead, the rest for the remaining PS and SS. The showerhead holes have a compound angle of 90° towards midspan with an injection angle of 30°. This means leading edge cooling is injected at an angle perpendicular (radial) to the mainstream flow, causing a pileup of cooling at midspan. All PS and SS holes have axial orientation with a local injection angle of 30°. The vane has a design blowing ratio at the showerhead of approximately 1.5 and a uniform wall thickness of 0.002 m.

RTV parameters are given in Table 1 while 2-D and 3-D geometric details are given in Figure 8 and Figure 9. The RTV design was initially defined by seven cross section shapes each at different spanwise locations. Solidworks^{TM} was used to create a spline between this stack-up of airfoil geometries to create the 3-D shape of the vane.

How the individual cross-sections stack up relative to each other to create the vane shape is seen in Figure 9. The extrapolated root and tip two-dimensional geometries were added to ensure the 3-D vane extended past the ID and OD walls for cropping in Solidworks™ and to eventually ensure a water-tight geometry for grid generation in CFD simulations. It can be seen in Figure 8 that the RTV has a flat PS, which makes it a proper candidate for flat plate tests of film cooling and heat transfer characteristics. The RTV geometry is unique because it is wholly owned by the government whose data will be shared with domestic partners in academia and industry.

Table 1 - RTV Design Parameters.

RTV Meanline Design Parameters:	
Pressure ratio	3.75 total-total
Reaction	49.50%
Flow Coefficient	0.71
Work Coefficient	2.11
AN^2 (in^2 rpm^2)	573 x10^8 (Engine)
Turning	77°
Exit Mach No.	0.88
1V Airfoil Count	23

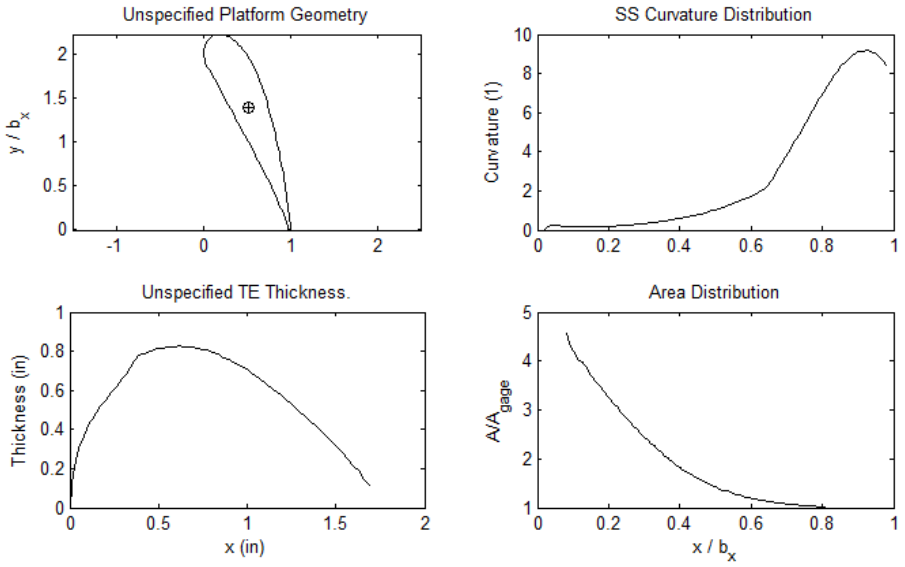

Figure 8 - RTV geometry characteristics.

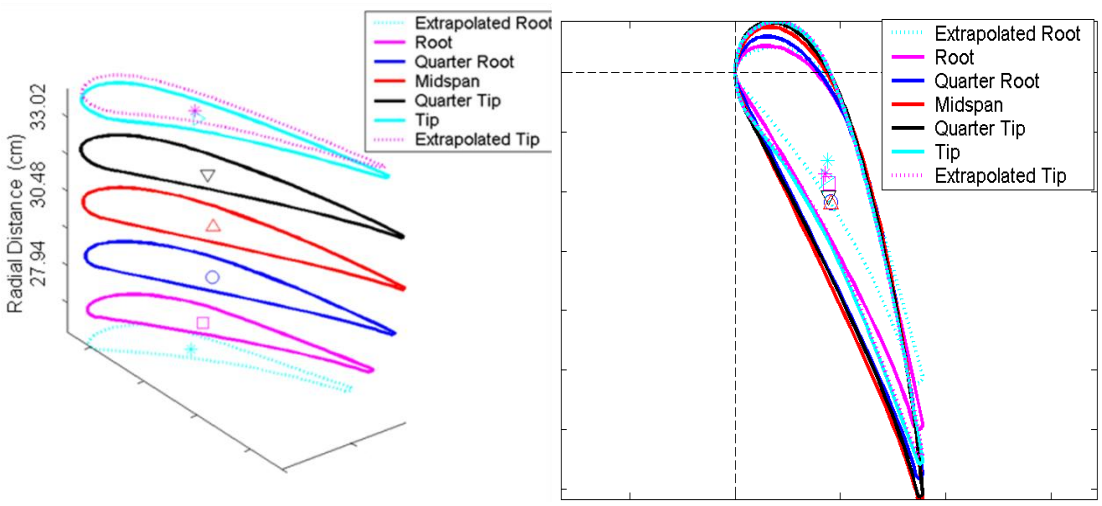

Figure 9 - 3-D stack-up of the HIT RTV (left) and top-down view (right).

The 3-D fully cooled RTV is given in Figure 10 showing a view of the pressure side. CAD renderings like this one were used for meshing purposes in the CHT CFD simulations of the vane. It can be seen that the RTV has a very 3-D shape, with a leading edge (LE) that changes thickness from hub to shroud, larger area at the LE relative to the

trailing edge (TE), increased surface length at midspan causing a bowing in the cooling hole rows especially near the TE, and a high amount of curvature in the tangential direction since the vane is one of 23 in a full wheel when tested in the AFRL TRF. The cooled RTV has a total of 648 holes, 282 of which are on the PS. Figure 11 is a diagram of the internal cooling plenums inside the cooled RTV. The vane has two internal coolant plenums, in which during testing the plenum near the LE is fed cooling air from the hub (ID), while the rear plenum is fed from the outer shroud (OD). The rear plenum feeds the four downstream PS hole rows of cooling holes while the front plenum feeds all remaining holes on the airfoil. There is no impingement cooling beneath the surface of the RTV, just the simple plenums shown in Figure 11. The baseline cooling design of the RTV is modern in terms of the amount of holes and the way the plenums are fed cooling air but basic in the way cooling hole rows are placed on the surface. Especially on the PS, repeated PS rows are evenly spaced such that a certain level of surface temperature is not exceeded.

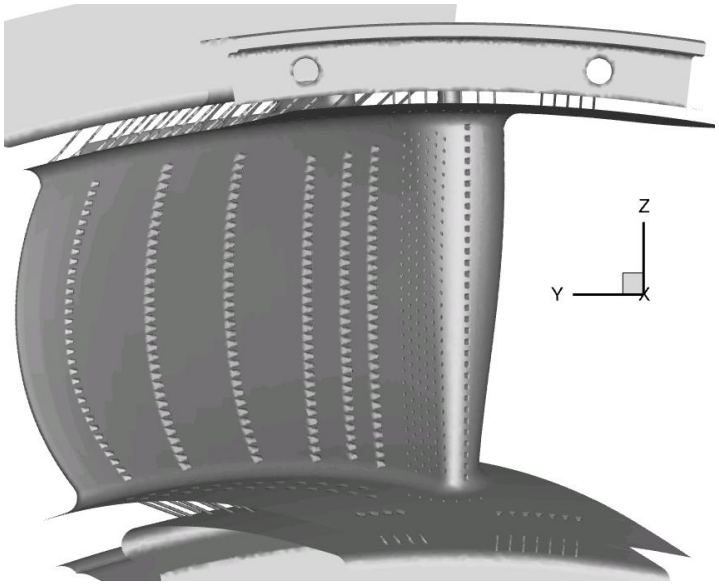

Figure 10 – 3-D CAD rendering of the fully cooled RTV viewing the pressure side.

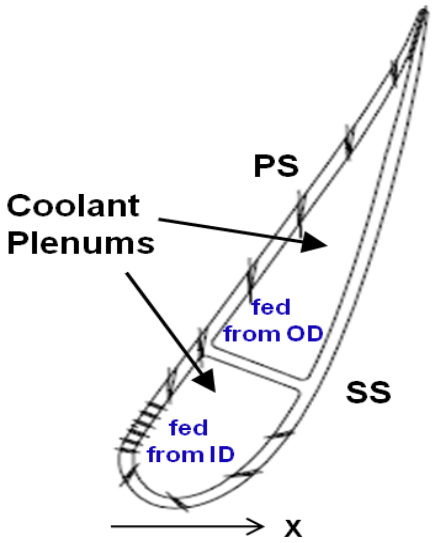

Figure 11 – Midspan cross-section of RTV showing two internal plenums fed from different radial directions.

CFD Simulations

Within this body of research, CFD was conducted for a number of purposes:

- To ensure that data on the RTV is taken at the right flow settings and design conditions in TRF tests by evaluating the 3-D vane in a full length test facility flowpath without cooling (see Appendix A).
- To provide 3-D cooling estimated external flow (CEEF) CFD simulations of the vane for use in simulations that will evaluate candidate RTV PS film cooling array designs within the optimization.
- To provide rigorous 3-D full grid conjugate heat transfer CFD simulations of the fully cooled RTV and flat plate geometry to justify the use of infrared thermography experiments in comparing the baseline and optimized cooling designs.

To ensure a proper level of accuracy in the simulations, the two types of CFD used in the current work were validated against experimental data from the Turbine Research Facility for the RTV. Documentation of the CEEF CFD validation can be found in Appendix B. It should be noted here that in terms of accuracy of the CEEF CFD for the optimization, heat flux is better predicted than temperature when compared to experimental data in the TRF. For the temperature itself, the PS levels are better predicted than on the SS. One weakness of the CEEF CFD is under-prediction of PS temperatures with film cooling, which were off by at most 10% of the experimental magnitudes. As the optimization here concerns the pressure side only, since heat flux in the presence of film cooling is predicted well, and temperatures with film cooling are predicted well on the PS near the LE, the CEEF CFD solver, associated turbulence model, and proposed use of near wall gas temperature and near-wall heat flux in making comparisons between the baseline and optimized cooling designs is deemed adequate for discerning major changes between cooling designs within the optimization. Ultimately, since only external flow CFD is available for an optimization to be completed in a reasonable amount of time, this type of CFD clearly distinguishes relative heat transfer characteristics between cooling designs, and the *Leo* CEEF CFD code is one of the newest turbomachinery codes available, it was deemed an appropriate choice for this work.

Documentation of the CHT CFD validation effort and other findings is given in Appendix C, where it is found that the CHT CFD is clearly not modeling everything in the experiments as predictions are well below experimental levels for temperature. For example, the kapton used for heat flux gauges in experiments is not modeled by the CFD.

While just like the CEEF CFD, conjugate heat flux is in general is predicted better than temperature even with film cooling, more work is necessary to mature the conjugate heat transfer code. Temperature predictions on the suction side can be off by as much as 12% of experimental magnitudes. The CHT CFD simulations in this work are intended to compare in a more rigorous simulation than the CFD feasible for the optimization the similarities and differences between the flat plate and vane geometries for the same baseline film cooling array. This provides added confidence that the relative experimental flat plate results between the baseline and optimized cooling designs represent what would be expected if the two designs were to be tested on a vane in the TRF.

3-D Cooling Estimation External Flow (CEEF) CFD

The 3-D CFD analyses used in the optimization of the RTV PS cooling array assume an axially-shortened 1/23rd tangential sector of the annular TRF passage centered on the vane, as there are 23 vanes in the full wheel. Simulations of the half-stage vane-only configuration of the TRF are reported on here. There are no rotating components simulated. The computational domain simulated here starts approximately 10 cm axially upstream of the vane and ends 10 cm downstream of the vane trailing edge. This corresponds to 2-¼ axial chord lengths in front of and behind the vane. The inlet and outlet locations also correspond with positions of upstream and downstream pressure and temperature instrumentation rakes in the TRF experiments. Concerning boundary conditions, the hub wall, shroud wall, are vane surface are set to solid no-slip surfaces,

the sides of the domain are periodic, and the inlet and outlet are a pressure inlet and outlet, respectively. Figure 12 is the computational domain used for all CEEF CFD runs.

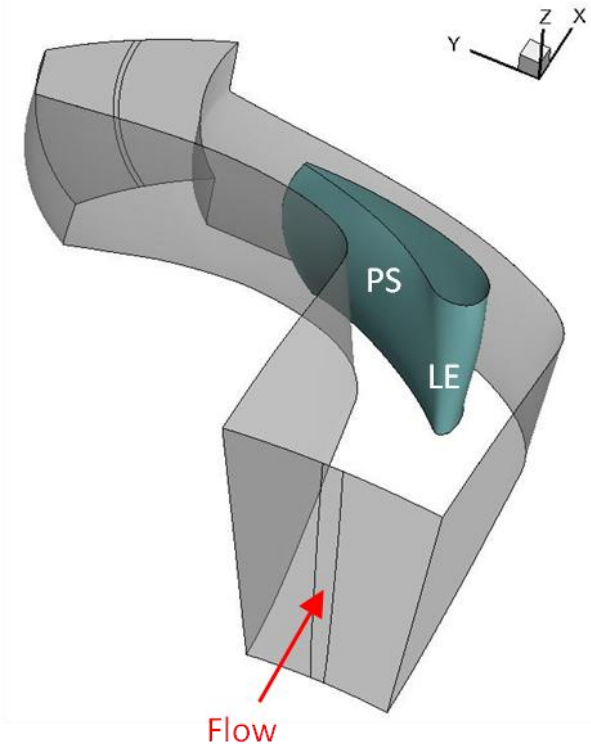

Figure 12 – CEEF CFD computational domain for the RTV shown here without cooling holes.

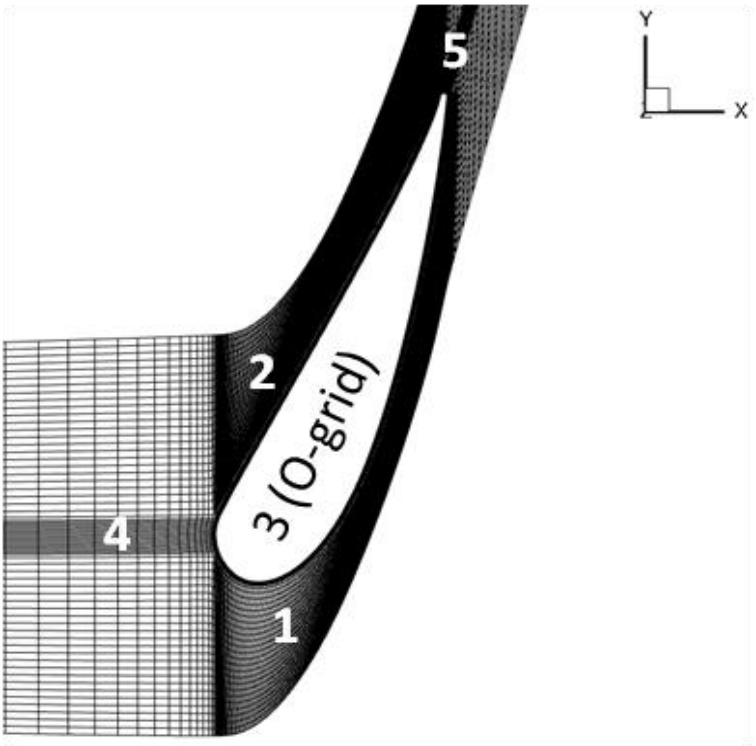

Figure 13 - Midspan slice of computational domain showing five grid blocks for vane CEEF CFD simulations.

All grids were generated using a program called WAND created by Aerodynamic Solutions, Inc. which is used by AFRL for turbomachinery applications. Only structured meshes were used for CEEF CFD in this work. WAND is a text-based grid generator that forms structured grids from a given 3-D geometry. An O-mesh was generated around the airfoil close to the surface with dense H-meshes created for the upstream and downstream passage centerline, and in the remainder of the passage between the vane PS and SS and the periodic boundaries. The meshes do not overlap—there are no overset grids. The five grid blocks around the vane at midspan for the highest grid resolution in the grid independence study is given in Figure 13. Figure 14 is a pressure-side view of RTV solid surface and the grid resolution used for simulations of the vane. WAND gives the user the ability to vary the dimensions of the structured grid created for the 3-D TRF

flow passage. Dimensions are defined in the axial i-direction, the tangential j-direction for pitch, and the radial k-direction. The i-direction nodes are split into three parts consisting of the upstream component, on-vane component (for the O-mesh and the H-mesh), and downstream component. The upstream axial nodes set the upstream dimension for grid blocks 1, 2, and 4. The on-vane axial nodes set the on-vane dimension for the O-mesh and grid blocks 1 and 2. The downstream axial nodes set the downstream dimension for grid blocks 1, 2, and 5. The tangential grid span is split into three regions with a concentrated grid around the passage centerline in the upstream region and in the wake downstream. The total amount of grid cells across the three domains in the j-direction upstream of the vane is preserved and distributed to the two free stream domains at the vane. The wall-normal dimension of the O-mesh as well as the initial grid cell height around the airfoil was also specified.

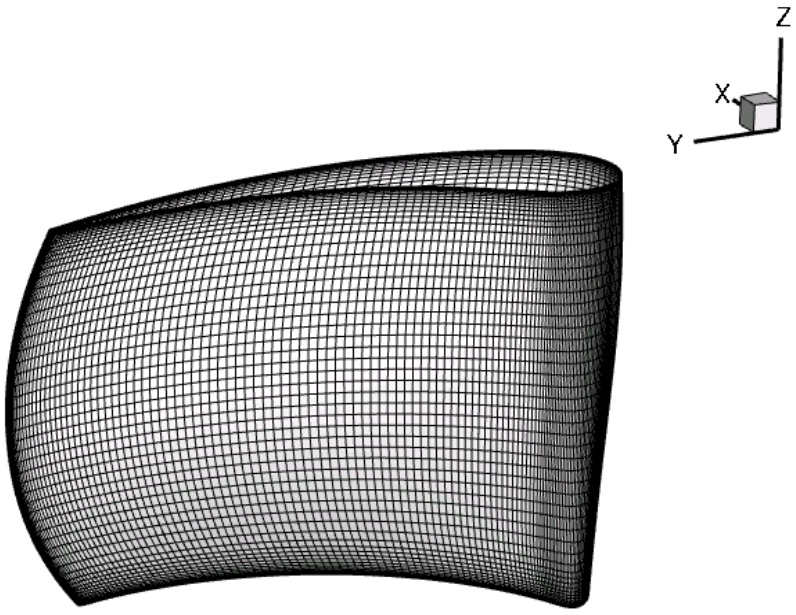

Figure 14 - Grid 2 resolution as seen on the pressure surface of the RTV.

Table 2 - Grid dimensions (nodes) for grid independence study.

	Grid 1	Grid 2
Tangential (pitch)	33	33
Radial	49	65
Axial	161	225
Wall-Normal in O-Grid	21	25
y^+	2.22	2.18
Computational Time [hrs]	13	25
TOTAL CELLS (millions)	*0.640*	*1.146*

Table 3 - Inlet and outlet mass flow rates [kg/s] for the grids studied.

	Inlet	Outlet
Grid 1 (No cooling)	1.569	1.568
Grid 2 (No cooling)	1.572	1.572
Grid 1 (Cooling)	1.512	1.619
Grid 2 (Cooling)	1.448	1.624

Two grids were considered in order to ensure the proper level of solution grid independence. Both of these grids are preset grids within WAND that are optimized to give accurate solutions on airfoils. The dimensions, initial cell height, CPU time for a single Intel Xeon 2.67 GHz processor, and the total number of cells for each grid is given in Table 2. No automatic local refinement of the mesh was performed near any of the cooling holes on the vane surface, as it is not currently a capability in the grid generator WAND. Therefore, it was desirable to choose a final grid that had adequate coverage and resolution as seen in Figure 14, especially in the axial flow direction, to ensure the characteristics of film-cooling were best modeled. The resulting mass flow rates at the

inlet and outlet of the domain for both grids is given in Table 3, showing levels of error. Naturally, with vane film cooling there is additional mass flow expected at the outlet. With cooling, the difference between the inlet and outlet mass flow rates tends to decrease as resolution of the grid increases and the magnitude of the difference agrees with the total added cooling flow. Summing the cooling hole mass flow rates on the vane and the inner and outer endwalls gives a number only 5% less than the current difference seen in Table 3. Therefore, there is little error in the mass flow rates and further resolution is unnecessary.

The results of the grid independence study for the midspan vane surface pressure distribution with film cooling is given in Figure 15. It can be seen that the results for the two grids are very close. The denser grid results in more oscillations in pressure mostly at the LE. The oscillations are a common result for surface pressure and a by-product of the film cooling mass injection by this form of CFD. Elsewhere, pressure spikes due to film cooling effects are very close in magnitude. For this reason, a third, higher density grid was not investigated. Higher density grids would only increase design cycle time for the optimization as well. Thus, either of the two grids were appropriate for cooled pressure interrogation. To maximize efficiency, the final grid chosen for the optimization has 1,146,880 total grid cells in the computational domain. There are 177 grid cells in the axial direction from LE to TE on the vane and 65 cells spanning from ID to OD on each the PS and SS.

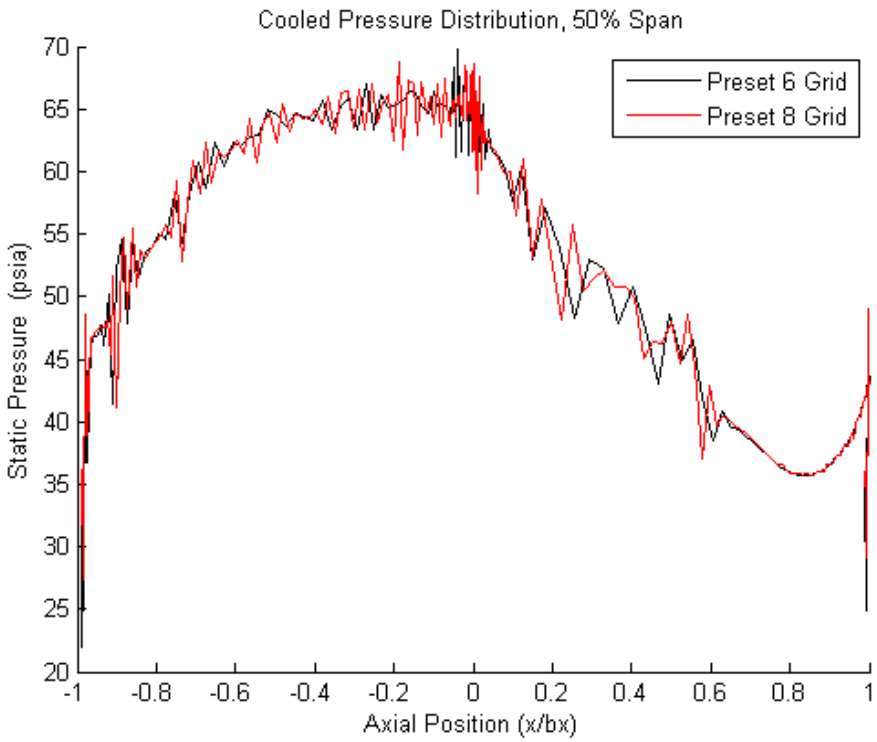

Figure 15 - Grid independence study surface pressure results for the RTV with film cooling.

The 3-D RANS solver used for all CEEF CFD predictions is called *Leo* [166]. It is used by AFRL's Turbine Division specifically for flows inside gas turbine engines. The discretization scheme is called the Ni scheme, based on the Lax-Wendroff scheme [167], and is second order in space and time. It is an explicit finite-volume solver for the structured RTV grids that uses implicit residual smoothing to speed up convergence, implicit dual time-stepping, and the Wilcox 1998 k-ω turbulence model [168]. All simulations are steady flow. All flow cases were run to 12,000 iterations which provided sufficient convergence of residuals of density, momentum and energy to 10e-3 or less. The fluid in the simulations is air and it is assumed to be an ideal gas.

The resulting simulated boundary conditions for the CFD required special consideration in order to accurately model the flow phenomena around the vane in the TRF. Starting with the inlet total pressure (P_t) and temperature (T_t), initial conditions were derived from upstream instrumentation rake data. Two rakes traversed 120 degrees clockwise around the vane wheel upstream of the test section measuring data over the 2.5 second main flow blowdown time, creating a map of T_t and P_t values. Each rake consisted of nine equally-spaced radial measurements, or sensors, resulting in a profile. In general, pressure profiles were approximately the same reading at a given radial and tangential location on the vane annulus while the temperature profiles typically showed the highest temperatures at the midspan radial location and the lowest temperatures at the hub (ID) and shroud (OD). One of the rakes was shown to have potentially errant data, so it was ignored. The inlet temperature profiles were modeled for CFD purposes by taking an average over the full 2.5 seconds of 120-degree traversing time for each of the nine sensors. Since the rake traversed in front of multiple vane passages over the run time, other considerations are necessary to factor in the conditions while the rake passed over the particular instrumented cooled vane of interest. Hence, in order to get a final profile, the normalized T_t value from the entire run time was scaled by the area-averaged sensor value from just the 1/23 annulus area directly in front of the vane of interest. Details regarding the full run time of the rig relative to the time of interest at which flow conditions were taken for the CFD are fond in Appendix A. The same process was used to find a good inlet P_t profile, although the profile was naturally more uniform than that for temperature. The static pressure at the vane passage exit was set to a value from the downstream rake measurements.

All TRF simulations used an isothermal vane surface boundary condition. As the TRF, and other typical high pressure turbines, are is not designed to run adiabatically, this governed the choice of wall boundary condition for the CEEF CFD. Initial vane test data from top and bottom gauges within various heat flux gauges in the TRF also clearly show that during the steady state portions of the facility operation, vane surface temperature varies very little with time, justifying the choice for an isothermal condition for all walls in the domain. The wall temperature initial condition was set for CFD runs by taking the reading from a single flush-mounted thermocouple from both the uncooled and cooled vanes of interest at a time just before mainstream flow initiation in a given run. These values were not the same between the two cases since cooling flow was started in experiments before the main flow and the cooled vanes experienced a much more significant temperature drop than the uncooled vane. Thus for a cooled simulation, the temperature from the cooled vane was used and for the uncooled simulation, its corresponding vane metal temperature was used. Table 4 is the CFD boundary conditions derived from TRF experimental measurements of the main and cooling flows for simulations of the cooled vane. CFD conditions used for the uncooled vane were different since it lies on the opposite side of the vane wheel in TRF tests. Those conditions are not given in Table 4 in order to focus on the design level RTV conditions that were held constant within the optimization.

Table 4 – Matched TRF experimental conditions for all 3-D CFD evaluations in the optimization for the RTV with film cooling.

Profile-averaged main flow $T_{t,in}$	442.78 K
Profile-averaged main flow $P_{t,in}$	4.57 atm
Profile-averaged main flow $P_{s,ex}$	2.65 atm
Main flow M_{in}	0.12
ID cooling flow $T_{t,in}$	258.68 K
ID cooling flow $P_{t,in}$	4.71 atm
OD cooling flow $T_{t,in}$	246.93 K
OD cooling flow $P_{t,in}$	4.90 atm
Wall temperature (isothermal cond.)	314.85 K

The coolant temperature at the exit plane was modeled by taking average value of three time-averaged (over the half-second duration of interest mentioned in the previous section) temperature measurements from sensors spaced equally over the vane wheel in the coolant chain closest to the vane internal plenums (seen in Figure 11). Since cooling hole exit temperatures are hard to measure in a full scale full annulus blowdown rig, this is the best estimate available of cooling temperatures entering the main flow. Each vane has two plenums separated by a vane spar, whereas the six showerhead cooling-hole rows, all four SS rows, and first two PS rows are supplied by the front plenum and the second plenum provides coolant to the four remaining downstream PS cooling-hole rows. This resulted in two different temperatures to be assigned to the each cooling hole exit in the boundary conditions, depending on which plenum they belonged to. This is seen in Table 4 where values of ID-fed and OD-fed cooling temperature and pressure conditions are specified.

Film-cooling on the surface of the vane and its endwalls were modeled by adding a source term to the governing equations on grid cells in the vicinity of injection locations. This technique is simple as it requires no grid adaptation at the site of cooling holes. Also, this method is requires much less computational time relative to full-grid CFD or conjugate heat transfer modeling. Equation 19 shows the general relation between the viscous fluxes (*F*) on the left and the source term (*Q*) on the right hand side for mass continuity. Equations 20 through 23 give the remaining Navier-Stokes equations for momentum, energy, and due to the turbulence model used, *k* and ω as well.

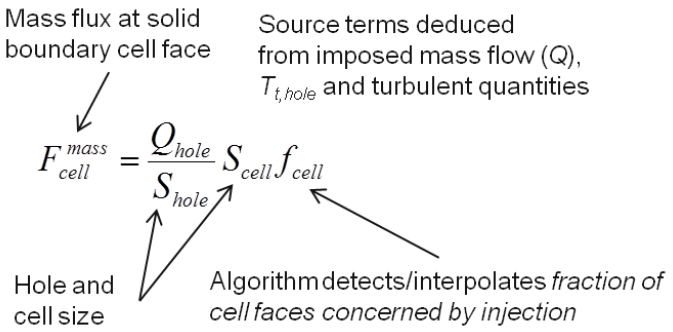

(19)

$$F_{(x,y,z)cell}^{mom} = \frac{Q_{hole}}{S_{hole}} S_{cell} f_{cell} V_{(x,y,z)hole,cell} \tag{20}$$

$$F_{cell}^{energy} = \frac{Q_{hole}}{S_{hole}} S_{cell} f_{cell} E_{hole,cell} \tag{21}$$

$$F_{cell}^{k} = \frac{Q_{hole}}{S_{hole}} S_{cell} f_{cell} k_{hole} \tag{22}$$

$$F_{cell}^{\omega} = \frac{Q_{hole}}{S_{hole}} S_{cell} f_{cell} \omega_{hole} \tag{23}$$

Based on the coarse surface grid used in the current work, only two to four grid cells will have added source terms for a given cooling hole, depending on hole size. This is based on the fact that the grid used only has 65 cells in the radial direction across the span. For example on the baseline cooling design, with 32 or 33 holes across the span and a lateral spacing of 3*D* between hole centers, then the resulting resolution of the cooling flux represents that seen in Figure 16. Therefore, in the radial direction, which has little room in the lateral direction to move on the surface within the optimization, cooling hole exit flux for a single will typically only be represented by one grid cell. There is more surface gird resolution in the axial direction relative to the radial direction, as seen in Figure 16, however, wall-normal grid resolution is very dense to capture all effects in the boundary layer as seen previously in Figure 13. Clearly this cooling estimation method will not resolve the different exit velocity profile due to different cooling hole shapes, such as the differences between a cylindrical and fan-shaped hole. However, as stated before, this optimization does not incorporate hole shape as a design variable. There is no local refinement of the surface mesh near cooling holes, making all grid cells on the vane surface at the sites of cooling injection the same size. This transpiration boundary treatment of the cooling injection means there is only an external flowfield mesh. Individual hole passages are not gridded, nor are internal coolant plenums. Despite this level of surface grid coarseness, the primary design variables, including hole size, hole location, injection angle, and compound angle can still be accounted for in the optimization.

WAND allows the user to specify the gas conditions, mass flow, location, size, and coolant injection orientation of all cooling holes for a given vane or blade being

interrogated. The advantage of this method is that it is robust and can be applied independently of the flow regime in the main stream outside of the cooling hole. Tartanville and Hirsch [50] have used the transpiration boundary condition technique outlined above and illustrated in Figure 16 for similar applications in which they also showed the advantages of not having to simulate the flow inside cooling passages, or worse, for the optimization, having to recreate 3-D geometries and generate new CFD meshes every time in the design loop. Having to simulate flow inside the passages and other internal cooling channels would add orders of magnitude of processing time in the optimization. In addition, as this is a cooling estimation technique, naturally this type of CFD will not resolve small-scale physical effects of cooling in the flow. It is adequate, however, for providing an assessment of cooling air distribution and the effects on temperature over the surface for this type of optimization.

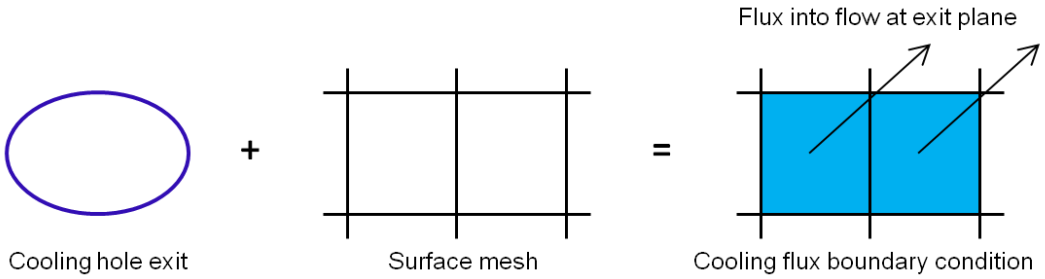

Figure 16 – Source-term cooling flux injection estimation at surface grid cells.

For the CEEF CFD, Figure 17 is a sample surface temperature contour using an adiabatic surface condition (this figure only) showing how the surface cells with the cooling flux estimation appear on the entire RTV pressure side. Cooling hole fluxes on the endwalls and suction side are simulated in the optimization. Clearly, it can be seen that cooling holes are only represented by 2 or 3 grid cells on the surface. The LE

showerhead array of smaller holes and multiple rows of larger holes are evident in the figure as well.

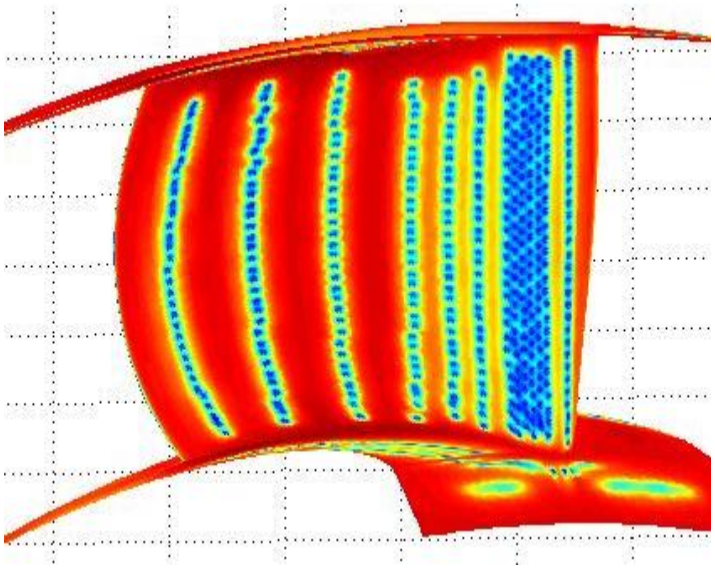

Figure 17 - 3-D CEEF CFD general surface temperature contour showing cooling hole locations.

During the development of the CFD assessment within the optimization, it was found that attempting to evaluate relative cooling array designs using the surface temperature and overall effectiveness calculated right at the surface created contours with little or no discernible features. This makes sense as an isothermal wall boundary condition was enforced in the CFD. This wall condition was chosen since it was more representative of what experimental data shows in the TRF. Data show quasi-steady levels of temperature at the surface over the run time, as seen in Appendix A. Data did not show levels of zero heat flux over the surface of the vane. Therefore an adiabatic surface condition was not considered here.

Instead of using the heat transfer properties from the first fluid cell next to the no-slip surface, the properties were calculated at the 10th cell from the surface, or the j=10 location, which gives a near-wall gas temperature ($T_{\infty,nw}$) and near-wall heat flux if the

temperature difference is accounted for between the 10th and 11th grid cell from the wall. Since an isothermal wall condition was chosen for the CEEF CFD, at the wall there is no variation in temperature characteristics since only the level set for the isothermal condition would be observed. Just outside of the boundary layer, there is little or no variation seen over the surface because only the main stream gas heat transfer levels would be observed. Therefore, some grid level away from the wall between these two extremes must be chosen. Thus, heat transfer characteristics in all CEEF CFD runs within the optimization were assessed 10 grid cells away from the wall. This provides the maximum amount of surface variation in heat transfer characteristics while still lying inside the viscous sublayer ($y^+ \leq 10$). The left half of Figure 18 is a plot of the number of grid cells away from the wall and the resulting near-wall grid thickness Reynolds number, y^+, for a sample location downstream of a cooling hole and the same location for the uncooled case. The right half of Figure 18 shows the differences in the temperature profiles the uncooled and cooled case, which clearly shows an 80+ K difference at 10 cells from the wall. In addition, the uncooled profile shows that the j=10 location is out of the linear range of heat flux, as there is a change in slope at j=7. This makes the temperature at this location, $T_{\infty,nw}$, a unique parameter relative to heat flux. At j=10, the feature variation provided heat transfer contours, as seen in the results, with adequately detailed temperature variation between cooling designs for proper enforcement of fitness functions. The j=10 location physically lies only 2.79e-5 meters from the surface in the boundary layer cells in the domain, making it a sensible representation of simulated surface heat transfer characteristics with film cooling for all genomes in the optimization. All plots in the results section for CEEF CFD are for this grid level away from the wall.

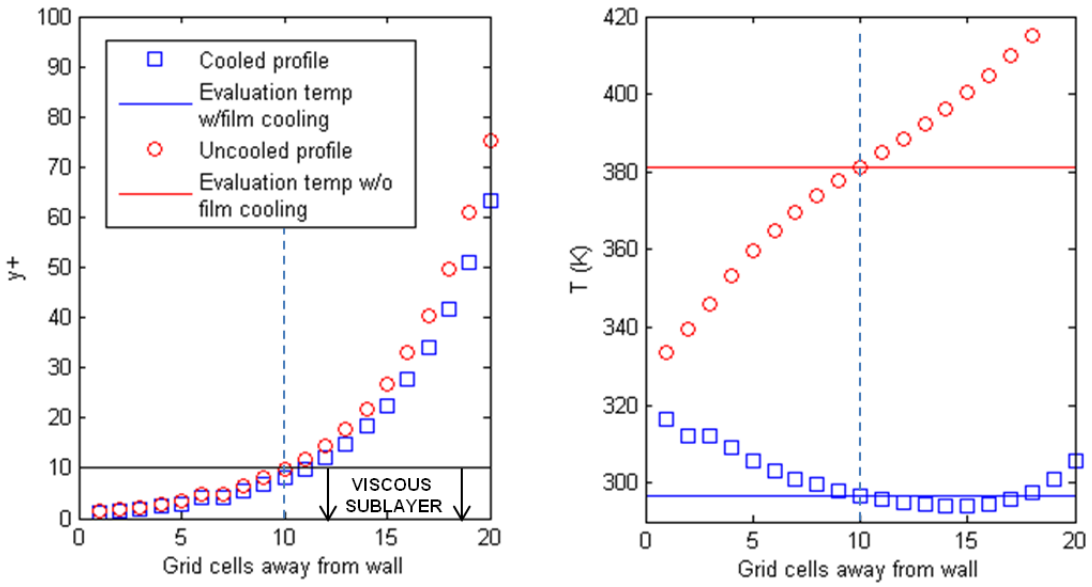

Figure 18 - Justification for use of *j*=10 grid location for CEEF CFD assessments in the optimization.

Presuming that the second type of CFD used in this work, CHT CFD, involves simulations with more realism, comparing this to the CEEF CFD used in the optimizations would only be problematic. Since the two approximations of surface heat transfer, the prescribed wall boundary conditions, and grid types are fundamentally different, a comparison would not provide a measure of relative accuracy for the CEEF CFD. In addition, depending on where on the vane surface the comparison is made, whether near a cooling hole or not, whether in an area of high curvature or not, the similarities and differences would vary significantly. Therefore, no such comparison is given.

3-D Full Grid Conjugate Heat Transfer CFD on the RTV

A new 3-D RANS CHT finite volume full-grid CFD solver, also called *Leo* [72], is used here to accurately evaluate the combined aero-thermal effects of the external hot

main flow, film cooling passage flow, internal fluid flow, and the vane solid material. This conjugate method factors in conductions effects from the solid when assessing fluid flow fields. The fully-cooled, 648-film-hole HIT RTV interrogated here is designed to an engine cycle consistent with future Air Force products. While the CFD used here can readily find detailed attributes such as flow momentum in all directions, counter-rotating vortex pairs, and adiabatic effectiveness in and around a single hole or hole-row, those results are put aside in favor of more meaningful comprehensive results which directly affect overall cooling effectiveness of the entire part.

The 3-D CHT CFD analyses assume an axially-shortened 1/23rd tangential sector of the annular vane-only TRF blowdown rig passage that is centered on the vane, as there are 23 total in the full wheel. It should be noted that the length of the domain is shorter than for the previously described CEEF CFD analyses in order to limit run times. The computational domain begins approximately one axial chord upstream from the vane LE and ends one-half axial chord downstream of the vane TE. Figure 19 is two views of the computational domain. The first view starts upstream of the vane and looks aft. It shows only the fluid mesh and how it was broken up into seven blocks with equal numbers of grid cells per CPU for the simulations. It also uses a temperature contour to show where the hot main flow goes through the domain and how the cooling flow enters from both the hub inner diameter (ID) and shroud outer diameter (OD). The second view is a top-down two-dimensional view of the domain which is actually a skewed rectangle. This also shows how the fluid mesh is broken up axially as well as the orientation of endwall and vane surface cooling holes. From the first view, it is seen that the domain width

decreases with decreasing radius, as the flowpath is really part of a whole wheel. These images emphasize the 3-D nature of the flowfield.

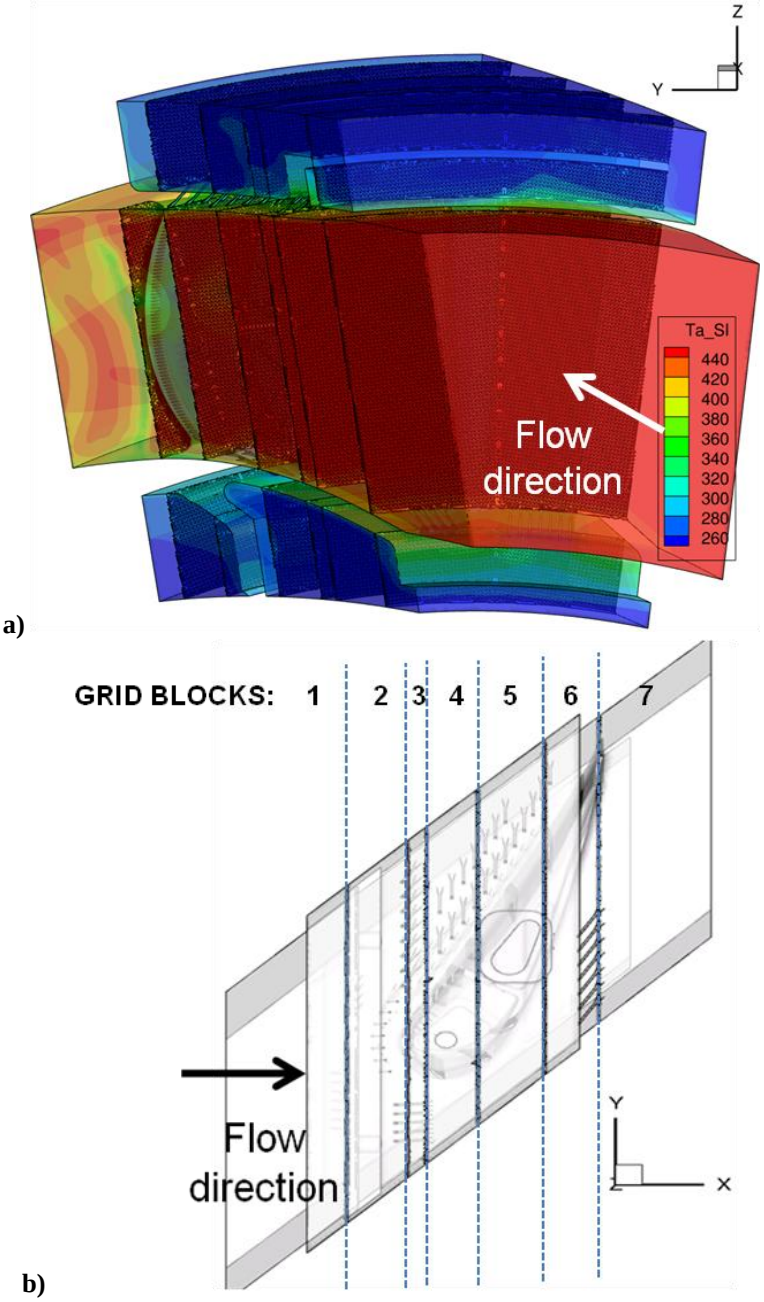

Figure 19 – CHT CFD fluid domain views from a) upstream of the vane looking aft with temperature [deg K] contours for cooling and main flows and b) top looking down.

Meshes were originally generated by Aerodynamic Solutions, Inc. from a CAD-modified geometry that was transformed from a manufactured version to a truly periodic shape using the meshing tool ICEM^{TM}. An unstructured mesh was used on the RTV to properly characterize the 3-D airfoil shape and intricate cooling passages for both the fluid and solid. Local grid cell refinement was prescribed in the vicinity of cooling hole features and areas of high curvature. More details of the mesh generation process are given in the work of Ni et al. [72].

Two grids, a medium and a fine grid, were evaluated in the current study for the RTV with film cooling holes. Figure 20 is the fine grid looking at the PS as well as a close-up of the LE of the vane at the outer endwall indicating the extent of the local unstructured grid refinement in the presence of film cooling holes. The medium grid consisted of 16.2 million fluid domain cells and 8.0 million solid domain cells, while the fine grid has 28.7 million fluid cells and 23.1 million cells for the vane solid. A wall function was used in all simulations. In comparing the two grids, Figure 21 is a surface pressure plot with film cooling on the medium and fine grids at 50% span and 5% span locations. It can be seen for either span location, the medium and fine grid surface pressure traces lie directly on top of each other, indicating that the 24-million-cell medium grid is sufficient for the CHT CFD simulations of the RTV. The surface heat flux contours for both grids were identical as well, which supports the adequacy of the medium grid in simulating cases with film cooling. A third, less-refined unstructured grid was used for the RTV without film cooling which has 2.6 million fluid elements and 1.3 million solid domain elements. Clearly, the presence of many cooling holes adds significant complexity to solid and fluid meshes. The uncooled vane mesh was generated

to determine the benefit of film cooling using CHT CFD on the vane. As a result, the uncooled vane cases required much less CPU time.

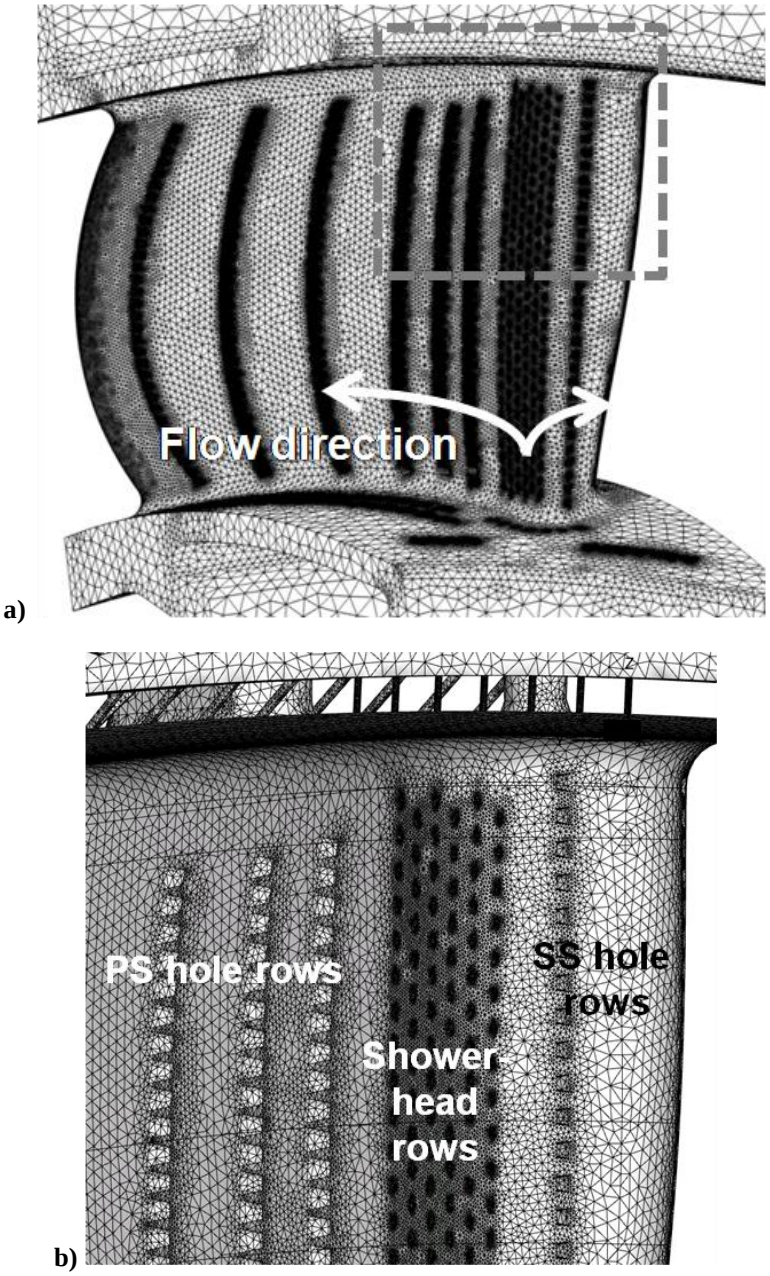

Figure 20 – RTV a) fine solid mesh and b) surface mesh close-up at the LE near the OD showing cylindrical showerhead and downstream fan shaped film cooling holes.

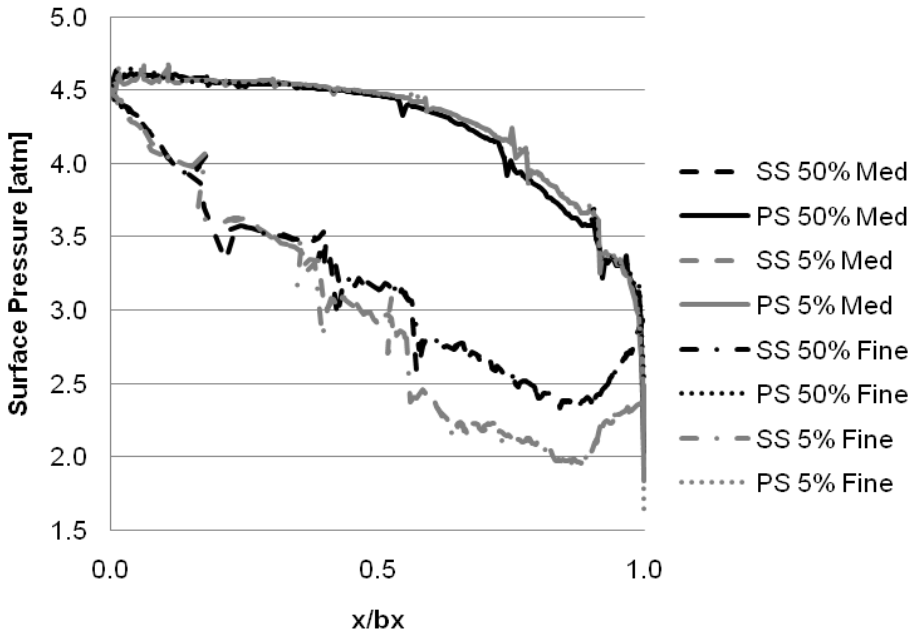

Figure 21 – Surface pressure plots with film cooling at two span locations for the medium and fine grid levels.

The 3-D Reynolds-Averaged Navier Stokes CHT CFD solver used for all predictions is called *Leo*, just like the CEEF CFD, by Aerodynamic Solutions, Inc. It is used by AFRL specifically for flows inside gas turbine engines. The CHT method used in the current work is a coupled solid-fluid solution technique for increased computational accuracy. The discretization scheme is called the Ni scheme, based on the Lax-Wendroff scheme, and is second order in space and time. It is an explicit cell vertex-centered, finite-volume solver for accurate and efficient modeling of conservation laws of mass, momentum, and energy within the unstructured RTV grids. *Leo* is a density-based code and uses an explicit time-marching scheme. The Wilcox 1998 two-equation k-ω turbulence model [168] is used in all simulations. All simulations in this work are assumed to be steady state. All flow cases were run to 30,000 iterations which provided sufficient convergence of residuals of density down to 1.0e-4, momentum down to 1.0e-

3, and energy down to 1.0e-3. The fluid in the simulations is air and it is assumed to be an ideal gas.

The solid conduction is solved using an approach that is first order accurate in time and second order in space and uses time-marching as the fluid does. The temperature-dependent thermal conductivity of the vane is incorporated into the solver, in which $k \approx 11.4$ W/(m^2-K) for Inconel 718, the true RTV material, at room temperature conditions. The solid-fluid interface takes into account heat flux contributions from both domains. To reduce computational time, the overall mesh was broken up into seven fluid domain parts with an equal amount of grid cells and one solid domain part and executed in parallel. The hub and shroud solid attachments are assigned adiabatic boundaries for the edges of the domain and the tangential sides of the simulated vane domain are periodic. Using eight Intel Xeon 2.67 GHz processors, the cooled medium grid case took approximately 100 hours to complete while the uncooled case required around 15 hours. The resulting simulated boundary conditions for the CFD required special consideration in order to accurately model the flow phenomena in the TRF. The same main and cooling flow conditions and methods for obtaining these for the cooled and uncooled vane CEEF CFD cases are used for the CHT CFD cases (see Table 4).

3-D Full Grid Conjugate Heat Transfer CFD on the Flat Plate PS Model

Since the current work involves a flat plate experimental model of pressure side cooling arrays and a thorough comparison using this type of CFD of this geometry relative to the vane, CHT CFD at design free stream and film cooling hole blowing conditions was conducted. All flat plate runs model the environment of the infrared

thermography experiments. The CHT solver uses high-density unstructured assessment which grids the hot flow, the cooling plenum, as well as each individual cooling hole, and solves the Fourier conduction equation for solid regions which are also meshed. The same Reynolds-Averaged Navier Stokes (RANS) solver as the vane case is utilized with the Wilcox k-ω turbulence model in the fluid domain near the surface of the plate. Full grid computational domains used include the cooling plenum fluid, cooling hole fluid, hot main stream flow, and the plate solid.

In order to analyze the relative benefits of film cooling, an uncooled plate model is used. It has no cooling holes but, like the experiments, it instead has three large circular coolant discharge holes near the downstream end of the computational domain. Figure 22 is the CFD uncooled plate model with a closer view of the discharge holes. The holes set up the same back-side conditions since in the cooled case coolant air is constantly supplied and released into the hot main flow. The discharge holes allow the upstream surfaces of the uncooled surface to be directly compared to a surface with film cooling. In other words, for example, an uncooled vane in a ground turbine test would have no holes but still have coolant on the back side surface influencing the conduction on the hot surface. Also, to maintain the same coolant plenum pressure condition, the combined area of the three coolant discharge holes equals the combined area of all the film cooling holes on the cooled plate. Finally, to compare the cooled and uncooled simulations at the site of the cooling holes, the areas on the uncooled plate where the cooling holes would be have a higher level of grid refinement. This is also true because these areas are the same recessed thickness areas to match the vane metal thickness as on the cooled plate. This, together with the matched back side coolant conditions ensures

the only difference between cooled and uncooled case is the absence of film cooling holes.

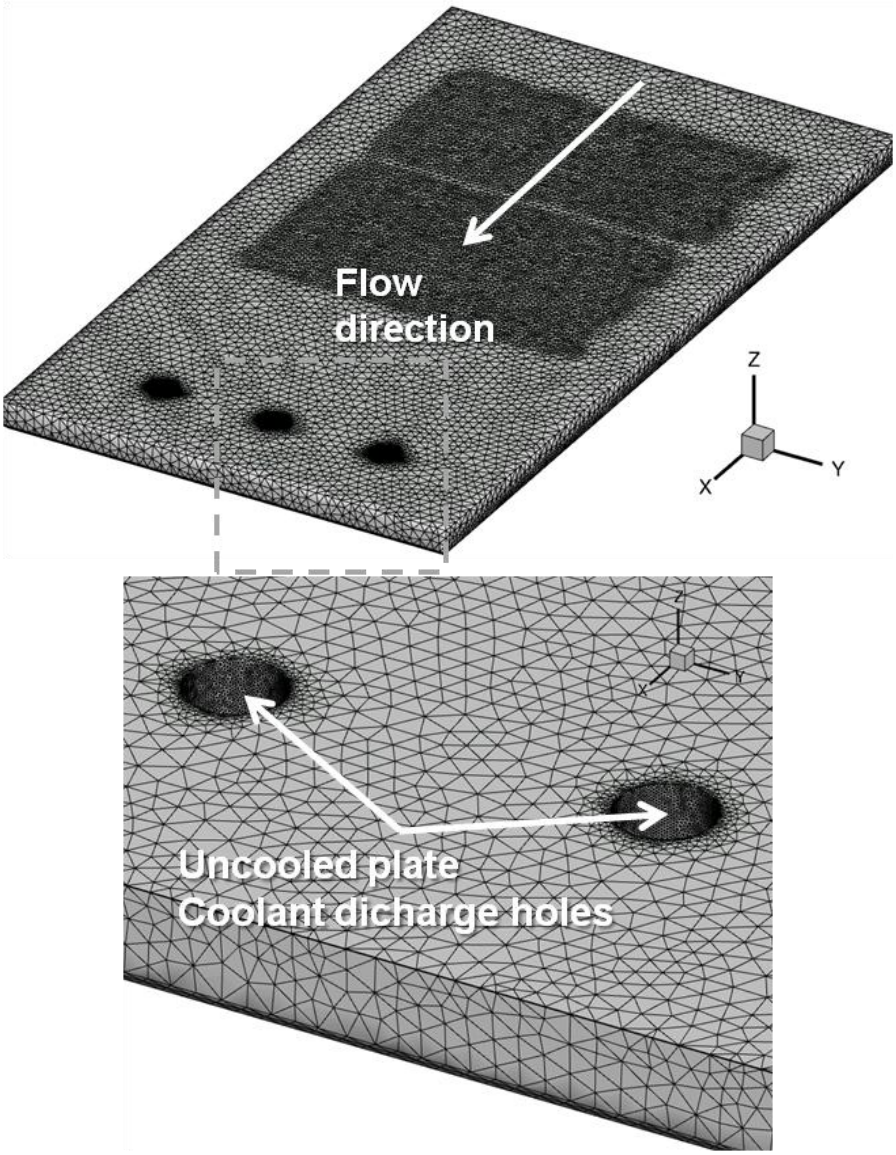

Figure 22 – Uncooled flat plate CFD model solid surface mesh (top) and close-up of discharge hole grid cell refinement (bottom).

The flat plate PS model with film cooling is modeled by 3-D CHT CFD analyses with a computational domain that mimics the full-scale geometry and environment of the infrared thermography experiments. The fluid domain includes a large hot main flow

section, a smaller cool air plenum section adjacent to the back side of the plate, and all fluid passages for all 282 film cooling holes. The experiments and therefore the hot main flow portion of the fluid domain do not have curved endwalls opposite the plate to match pressure gradients seen by the RTV PS. The hot main flow sees no change in area in the axial direction. The solid domain assumes the size, shape and material of the flat plate model. Figure 23 is the theoretical and actual computational domains for the flat plate CHT CFD simulations. It can be seen that the actual domain has a larger hot main flow region and smaller cooling air region, which better represents the actual dimensions of the experiments being simulated. The width and length of the domain are such that the cooled area of the plate is fully captured. How the boundaries of the domain were tagged is also given in Figure 23. The hot main flow is at a much higher Mach number than the cooling air from the plenum which flows through film cooling holes in the plate and mixes with the main flow due to the higher pressure relative to the mainstream. The fluid meshes are axially broken up into seven blocks. The flat plate models the pressure side of the 3-D RTV by maintaining the size, relative orientation, and type of film cooling holes.

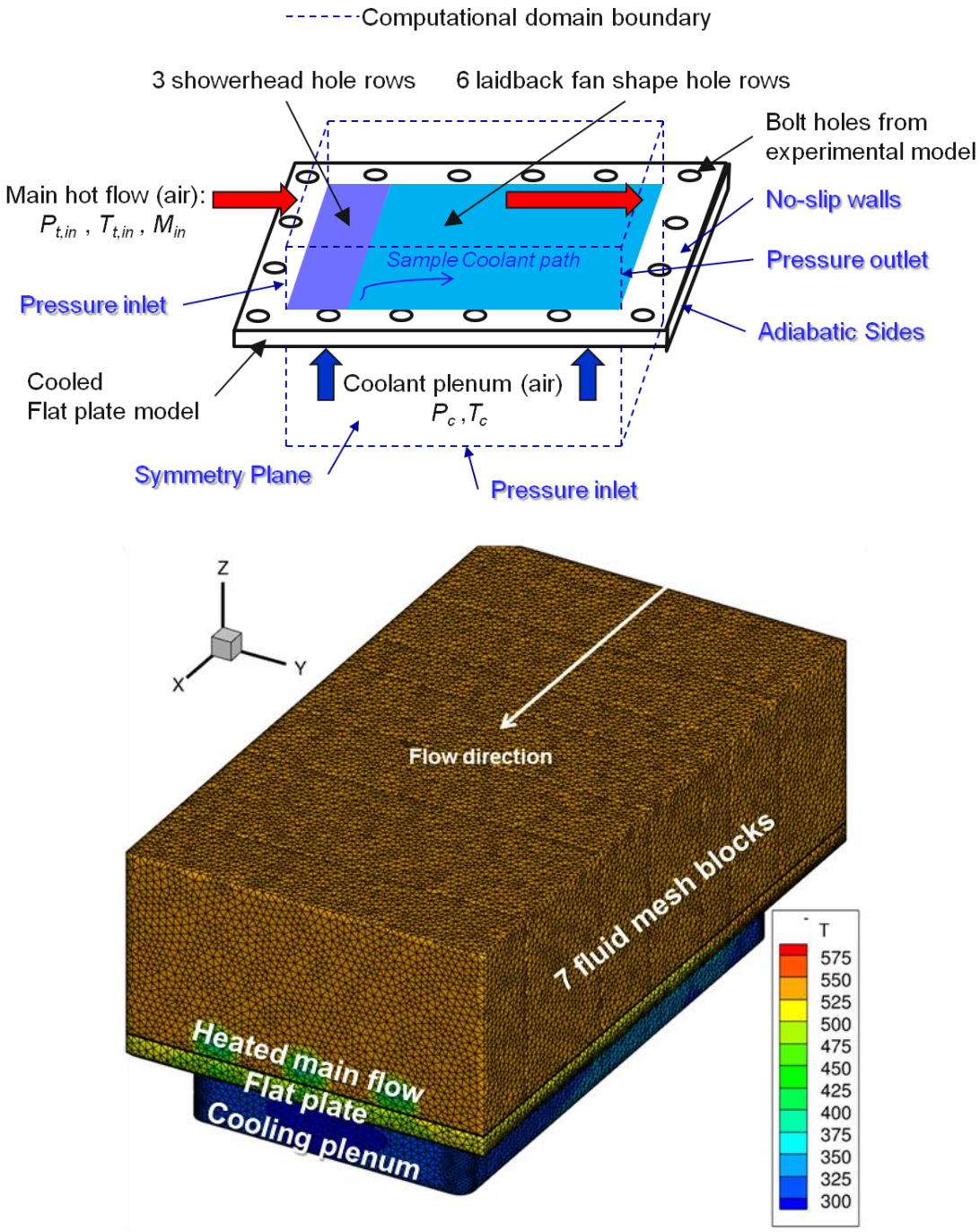

Figure 23 – Flat plate 3-D CHT CFD theoretical and actual computational domain extents featuring boundary condition tagging (top) and basic temperature contours [K] (bottom).

The full-scale film-cooled flat plate model mesh includes three of the six showerhead cylindrical cooling hole rows and all six PS fan-shaped hole rows that lie

further downstream. In transferring the rows of holes from the vane to the plate, they are straightened in the spanwise sense to conserve axial location of each hole. To increase the accuracy of the CFD, there is a great amount of grid cell refinement in the vicinity of each cooling hole both on the surface and inside the cooling hole passage as well as in the boundary layer. Figure 24 is the structured solid mesh with a close-up of the flat plate model showing both types of holes and their orientations, which matches the PS cooling array on the 3-D vane.

On both the plate and vane, all showerhead holes have a compound angle (β) of 90º oriented towards midspan and the laidback fan-shaped holes are axially-oriented. All holes have an injection angle (α) of 30º. The fan-shaped holes diffuse bi-laterally 10º and diffuse forward 10º in the injection plane. The plate thickness matches the vane thickness. The plate grid used here consisted of 7.8 million fluid domain cells and 5.8 million solid domain cells, for a total of over 13 million elements. Like for the vane simulations, a wall function was used for the plate simulations.

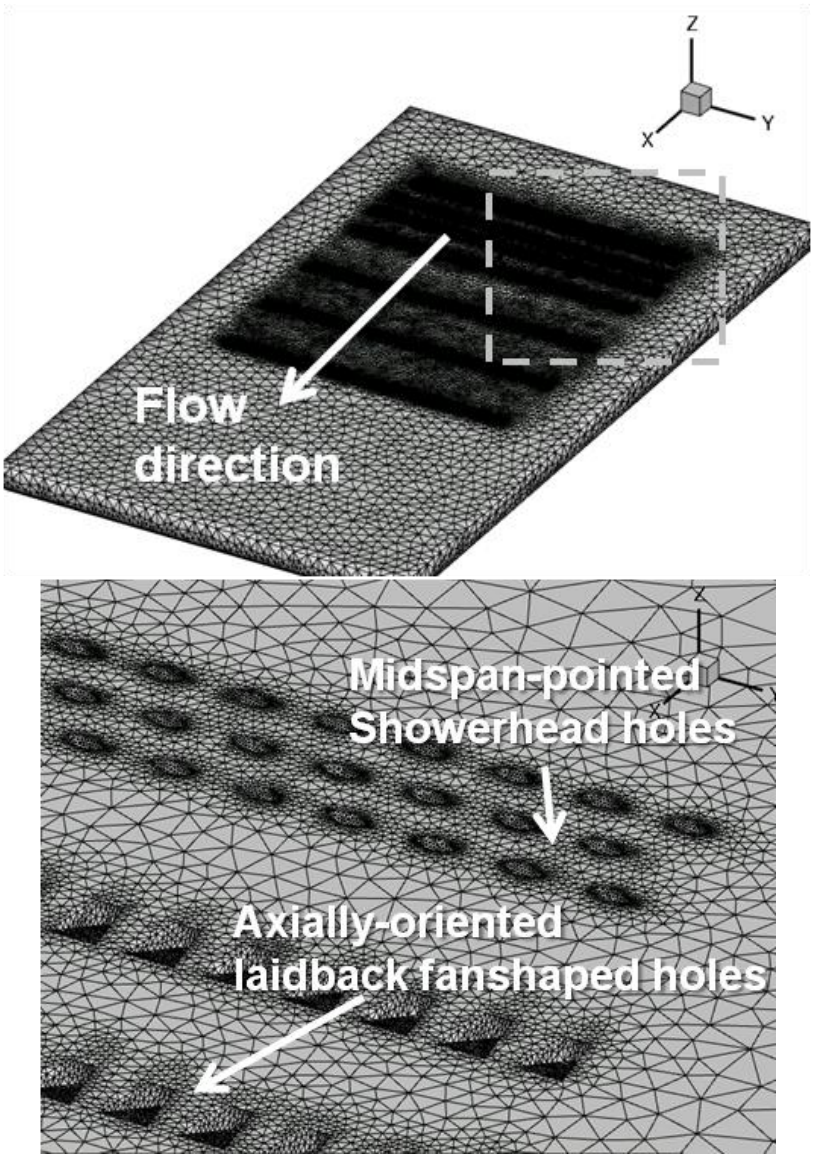

Figure 24 – Cooled flat plate solid surface unstructured mesh (top) and close-up of film cooling hole grid cell refinement in the leading edge region (bottom).

Table 5 – Grid cell count (millions) for the unstructured meshes in the CHT CFD flat plate study.

	Uncooled	Coarse	Med	Fine
Solid Mesh	0.68	1.47	5.75	12.01
Fluid Mesh	1.97	3.11	7.83	13.13
Total Cells	*2.65*	*4.58*	*13.58*	*25.14*

Two different flat plate solid mesh geometries were generated to represent the cooled and uncooled plates from the experiments. In the case of the cooled plate, three meshes with varying levels of refinement which are referred to as the coarse, medium, and fine grids, were created for the grid independence study. In each level of refinement, both the solid and fluid meshes were changed so that the grid cells at the solid-fluid interface were of matching local size. The solid, fluid and total grid cell count for the different unstructured meshes in the CFD study is given in Table 5. After comparing midspan surface pressure distributions like that in Figure 25, the similar surface temperature distributions of Figure 26, as well as inspection of various contours of heat flux and surface temperature, it was decided that since all grids gave similar results, the medium grid was rigorous enough and appropriate for comparison to experiments and the vane CHT CFD results.

Figure 27 is a side view of the fluid domain only for the medium grid and a detail view at a location that includes both types of film cooling holes. The fluid domain shows how the plate is recessed on the back side where cooling holes lie in order to match the thickness of the vane wall (0.002 m) and in turn match the L/D for all cooling holes. Since the coolant plenum in the experiments is a slightly smaller length and width relative to the entire plate size, this is also modeled in the domain. The depth of the coolant plenum side of the domain in the plate normal direction is matched in order to properly model the migration of coolant into the main flow through holes in the plate while the hot main flow side section matches the size of the rectangular hot gas flowpath in the IRT experiments.

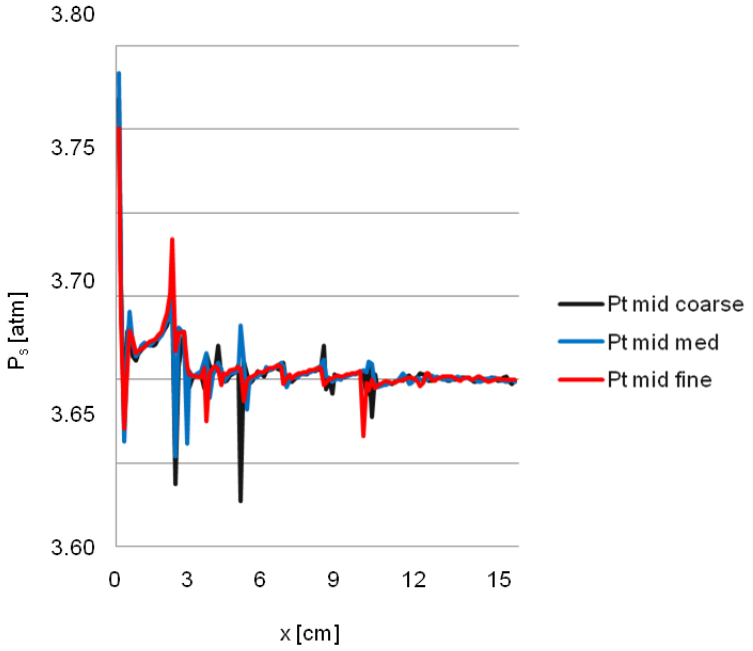

Figure 25 – Plate surface pressure comparison between the three cooled meshes.

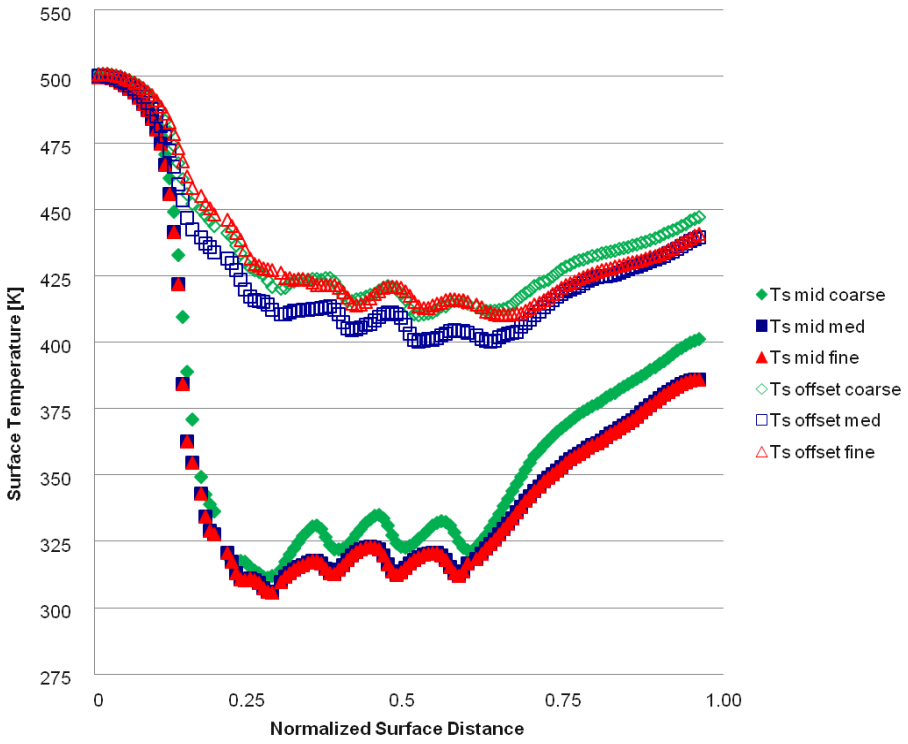

Figure 26 – Plate surface temperature comparison at two span locations between the three unstructured meshes with film cooling.

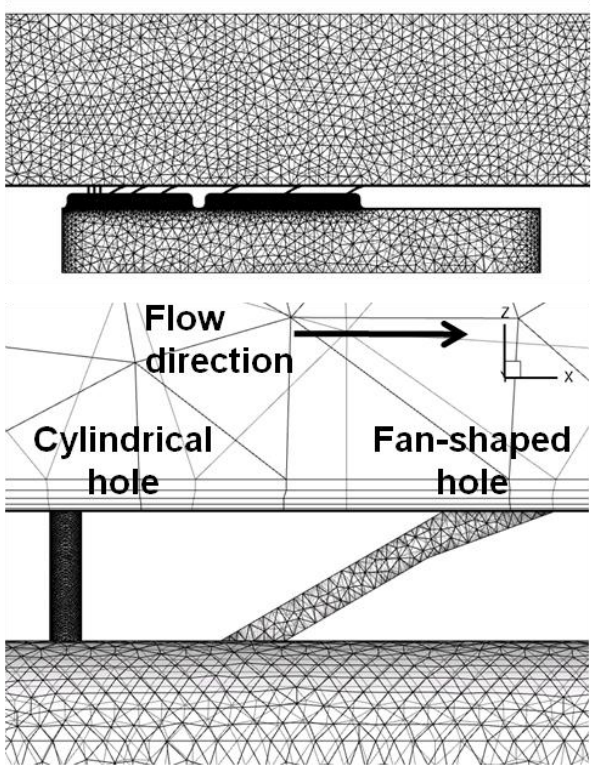

Figure 27 – Side views of the overall cooled plate domain (top) and a detail view showing mesh refinement in the hot flow, cooling passages, and coolant plenum of the medium grid (bottom).

Naturally, the same solver as for the Research Turbine Vane geometry was used for the flat plate geometry. Simulations in this work are steady state. All flow cases were run to 30,000 iterations which provided sufficient convergence of residuals of density down to less than 1.0e-5, momentum down to 1.0e-4, and energy down to 1.0e-4. The fluid in the simulations is air and it is assumed to be an ideal gas. Solid conduction is solved using an approach that is first order accurate in time and second order in space and uses time-marching as the fluid does. The temperature-dependent thermal conductivity of the vane is incorporated into the solver, in which $k \approx 11.4$ W/(m^2-K) for Inconel 718 at room temperature conditions. To reduce computational time, the overall mesh was broken up into seven fluid domain parts with an equal amount of grid cells and

one solid domain part and executed in parallel. Using eight Intel Xeon 2.67 GHz processors, the cooled plate medium grid case took approximately 130 hours to complete while the uncooled plate case only required 14 hours.

The resulting simulated conditions for the CHT CFD on the flat plate required special consideration in order to accurately model the flow phenomena in the IRT experiments. Primary design flow conditions are outlined in Table 6. Other initial conditions were set at or near boundary condition levels.

Table 6 – Matched IRT experimental conditions for the CHT CFD flat plate simulations.

Hot main flow $P_{t,in}$	3.98 atm
Hot main flow $P_{s,ex}$	2.79 atm
Hot main flow $T_{t,in}$	533.33 K
Hot main flow M_{in}	0.24
Cooling plenum flow $T_{t,in}$	295.37 K
Cooling plenum flow $P_{t,in}$	4.12 atm
Cooling plenum flow M_{in}	0.001
Wall temperature (initial cond.)	300.00 K

Film Cooling Array Optimization Methodology

Optimization Parameters

Here a means to improve current turbine component durability design methods is proposed by using 3-D physics-based analysis techniques coupled with heuristic optimization techniques to achieve a highly improved full coverage vane PS film cooling design. Using PS maps of near-wall overall film cooling effectiveness (ϕ_{nw}) and near-

wall gas temperature ($T_{\infty,nw}$), previously defined in the methodology, as evaluated by a 3-D Reynolds-Averaged Navier-Stokes (RANS) CEEF CFD solver, film holes modeled as discrete sources of mass flow, and a set of user-specified fitness functions, the genetic algorithm can progress through successively improved cooling designs with each new population of designs. Since the CFD in the optimization use an isothermal boundary condition, $T_{\infty,nw}$ is as a substitute for T_s. Near-wall overall effectiveness (ϕ_{nw}) is defined by a ratio of the hot freestream flow temperature (T_∞) to the newly defined $T_{\infty,nw}$ and the freestream flow-to-coolant air temperature (T_c) difference as shown before in Equation 7. Since the developing film on the surface has increased in temperature relative to when it entered the cooling hole, this number is usually less than one. However, on top of a cooling hole, $\phi_{nw} = 1$ and this level decreases steadily with surface distance until the next coolant injection location is reached. Naturally, the higher this value is over the surface of the vane, the better.

Most comprehensive technical investigations typically start with some kind of design-of-experiments (DOE) methodology. Here, however, a DOE-type plan is staged for realistic comprehensive CFD simulations instead of experiments. In experiments, there are variables measured as output (responses) that are affected by changing one or more of the process variables. Process variables are those which are intentionally changed to produce some change in the output variables. Control variables are those that do not change between tests and have no effect on response variables. Noise variables, like turbulence in an experiment, introduce uncertainty into the results and their effects to response variables are not readily to process variables and as such their effects should be minimized. Each variable must be identified so that their interdependence can be studied.

The response variables (ϕ_{nw}, $T_{\infty,nw}$) are those whose output is calculated in the simulation as a result of the assigned boundary conditions and cooling configuration for a given run. It is these variables that are essential to calculating each intermediate design's fitness. In an experiment, these would be the variables that are measured or observed.

In a recent comprehensive gas turbine film cooling literature survey, Bogard and Thole [3] cite certain fluid flow variables and physical hole attributes that affect film cooling performance significantly more than others. According to their review, among these variables are mass flux ratio, momentum flux ratio, 3-D hole shape, injection angle, compound angle, *Tu*, and surface curvature. Since the current study only assesses the external flow field in the CFD and since the vane has certain design flow conditions, it was decided to keep the external flow conditions and the combines mass injection of the film cooling constant for the optimization. Due to the estimation of cooling flux in the CFD, it is similar to having a simple cylindrical cooling hole shape with symmetrical exit velocity profiles, even though the real vane has fan shaped holes downstream of the showerhead region. Nevertheless, all holes are subject to this change, allowing valid comparisons between designs. The blowing ratio does change spatially over the vane PS due to the fact that coolant is fed by two different plenums with different measured conditions, and this is simulated in the CFD as well. The 3-D shape of the vane is constant for the optimization as well—there is no shape-changing in this work, and that is the essence of the efficiency of this method. The other primary control variable in the optimization is the combined PS cooling mass flow rate, which is managed by maintaining the total cross-sectional cooling hole area for the entire surface as cooling

hole sizes change. This is handled by conserving the combined area of cooling holes by row. Table 7 summarizes the control variables for this study.

Table 7 – Film cooling control variables for the optimization.

1) Main flow conditions
2) Simulated cooling hole exit velocity profiles
3) 3-D surface shape of the vane
4) Cooling mass flow rate (combined area of PS holes)

As a result of the control variables, the chosen process variables in the current optimization for individual film cooling holes include: injection angle, compound angle, two-dimensional surface hole location on the vane PS, row pattern, and cooling hole size. Table 8 summarizes the process variables and variable ranges prescribed for the optimization. Injection angle is the angle of cooling relative to the surface, or the lift-off angle. Compound angle is the angle from the axial direction in the surface plane that the cooling injection is turned. There are eight options for available in the optimization for injection and compound angle in the showerhead (first three rows) as well as the pressure side region downstream. A negative compound angle means the cooling flow is directed towards the ID. A fan compound angle means a gradual change in β laterally across a row that is symmetrical about midspan. This can be directed inward at the ID and OD and axial at midspan for "fan in" or directed outward at the lateral edges and axial at midspan for the "fan out" effect. Paired crossover means every pair of holes in a row has a compound angle of 45 degrees angled toward each other creating an "X" pattern. Some rows in given designs during the optimization have an uneven amount of holes, causing one hole at the ID or OD to be left without a partner. As mentioned above, hole size is

allowed change in the optimization only as long as total mass flow rate of cooling for a given row (and thus over the PS) is kept constant. Thus, the area variability is given in the table rather than the diameter variability. There are four options for hole size available in the optimization due to the three size options plus the option to have two different hole sizes in a row.

Table 8 – Film cooling process variables and their possibilities for the optimization.

Showerhead Injection angle, α (deg)	50º, 55º, 60º, 65º, 70º, 75º, 80º, or 85º
Downstream PS Injection angle, α (deg)	15º, 20º, 25º, 30º, 35º, 40º, 45º, or 50º
Compound Angle, β (deg)	-60º, -30º, 0º (axial), 30º, 60º, fan out 30º, fan in 30º, paired crossover at 45º
Cooling hole area	2.027e-7 m^2 times 1.0, 1.5 or 2.0; up to 2 different sizes in a row
Row patterns	32 (see Figure 30)

The ranges imposed on the variables are partly based on lessons learned from film cooling open literature and values that are very common in practice with limits assigned that make physical sense as well. Regarding the physical basis, for example, α is typically around 30°, and this is allowed to vary between 15° and 50°. Anything less than α = 15°, and the injection angle becomes close to being parallel with the flow which makes it difficult to manufacture, creates highly sharp edges, and undesirable structural shapes. Regarding lessons learned from works of film cooling, the following ideas are fairly well-known by avid gas turbine durability engineers that helps direct the focus of an optimization of PS film cooling:

- There are reasonable ranges of injection angle, compound angle, hole spacing within a row, row spacing, hole length-to-diameter ratio (irrelevant for CEEF CFD), and blowing ratio that should be adhered to.
- Shaped holes perform far better than cylindrical holes in most arrangements and should be placed in the region downstream of the leading edge.
- At the leading edge, cooling performance is based mostly on high injection angles for mixing with the stagnated head-on flow, thus the term showerhead.
- Downstream of the leading edge, compound angle cooling provides better lateral coverage than axial cooling.
- Double rows, especially staggered with respect to each other, perform better than single rows for cooling effectiveness.
- Taylor-Gortler vortices often disrupt film cooling near the hub and shroud of the vane PS, causing hot streaks and deterioration of film cooling.

The scope of film cooling parameter variation should be constrained to limits that can get results in a fairly reasonable amount of time, thus the effort expended choosing proper variables and limits.

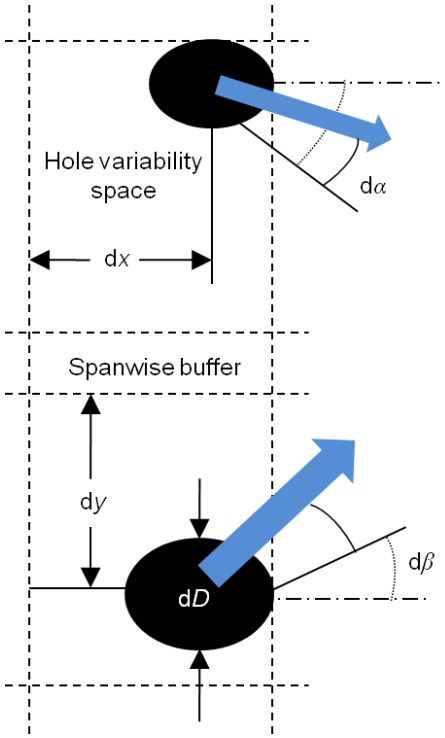

Figure 28 – Close-up example of two neighboring PS cooling holes showing potential for variability in the optimization.

The potential variability due to the chosen process variables for two neighboring cooling holes within a row on the PS is shown in Figure 28. The spanwise buffer serves to ensure as the hole locations vary, they do not overlap or touch, nor do they create an unrealistically close pair. How this is done is seen in Figure 29 as well as the streamwise buffers that appear on the entire PS of the vane. The streamwise buffers serve the same purpose as the spanwise buffers. After calculating the spatial locations of these buffers based on the available area, the axial and radial potential hole locations were checked to be sure they lie within these limits. It can be noticed from images of the RTV PS that the baseline film cooling configuration has six rows of holes in the region downstream from the showerhead. Since the static pressure can vary slightly over the pressure surface, the optimized cooling array redesign was allowed six main streamwise sectors that are

centered on the locations of the baseline configuration's rows. This allows the freestream static pressure seen by exiting cooling air to vary only a small amount as a cooling hole's or row's surface locations are changed in the optimization process. Clearly, there is less variability in the radial direction for a hole relative to axial changes due to space constraints. The six sectors seen in Figure 29 each have approximately the same amount of space to work within the optimization.

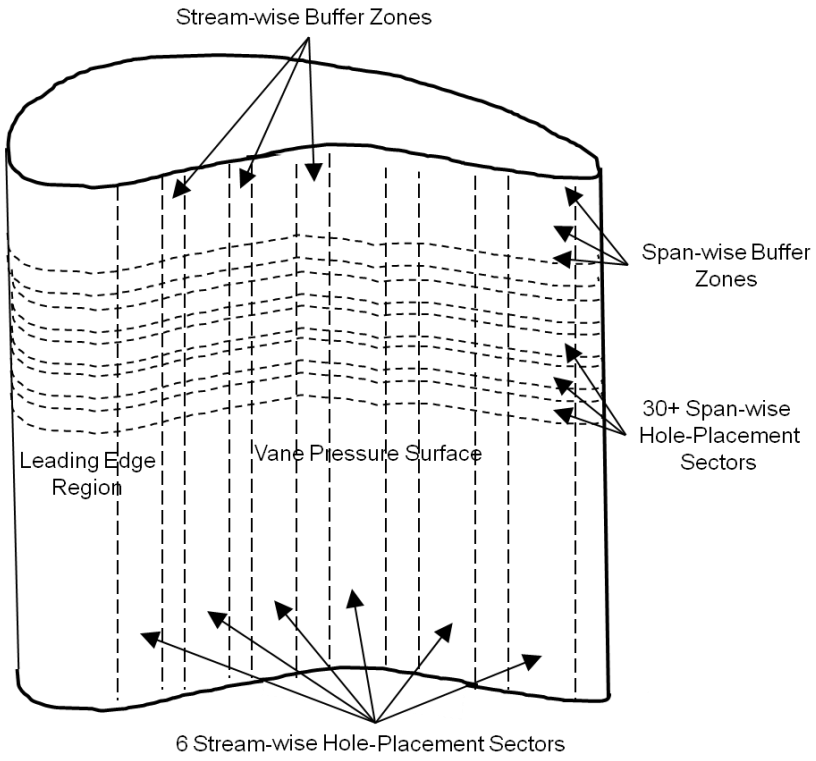

Figure 29 – RTV PS cooling hole location streamwise and spanwise variability plan for the array optimization problem.

The patterns available with this durability design method are one of the keys to its success. Placed in any one of the six sectors seen in Figure 29, these patterns allow a high number of different combined PS cooling arrays due to the combined effects of multiple patterns over surface. In addition, within each pattern, there is axial and radial

hole location variability that can change a given pattern dramatically. This means each pattern can stretch in the axial direction in discrete increments up to the limits of its placement sector. Certain patterns also have hole size variability as well. All patterns use injection and compound angle variability. The compound angle variability available to the patterns is unique in that all hole in a pattern can have the same parallel angle, or they can have a gradual inward-fan or outward-fan orientation. Some patterns have the ability to implement a paired-crossover compound angle orientation where every pair of holes has injection that intersects. Also, a few patterns had custom-designed β variability, like numbers 11 and 27, where every local group of holes has their own fan-out, fan-in, or fan-to-one-side orientation.

Figure 30 is a compilation of all 32 patterns implemented in the optimization, where flow is assumed to be from left to right. There are three discrete hole size changes used in this study: 1.0, 1.5 and 2.0 times the original size. Only some patterns use hole size changes. Most of the patterns were designed based on the prior-mentioned lessons learned from literature, such as the fact that staggered double rows and sister holes tend to perform very well. Some patterns focus cooling towards the outer edges of the vane, some focus cooling at midspan. There are other patterns, like number 10 called bulge or number 27 called flameholders that were simply created to test their viability in the optimization. The number of holes in a row pattern is conserved relative to the baseline cooling configuration, however with larger holes present, depending on how many, smaller holes are subtracted in order to conserve the combined row cooling hole area (i.e. combined mass flow rate). Figure 30 is not meant to show all holes in an implemented

pattern, it just shows enough holes to recognize the pattern intended and which ones have the options for larger hole sizes.

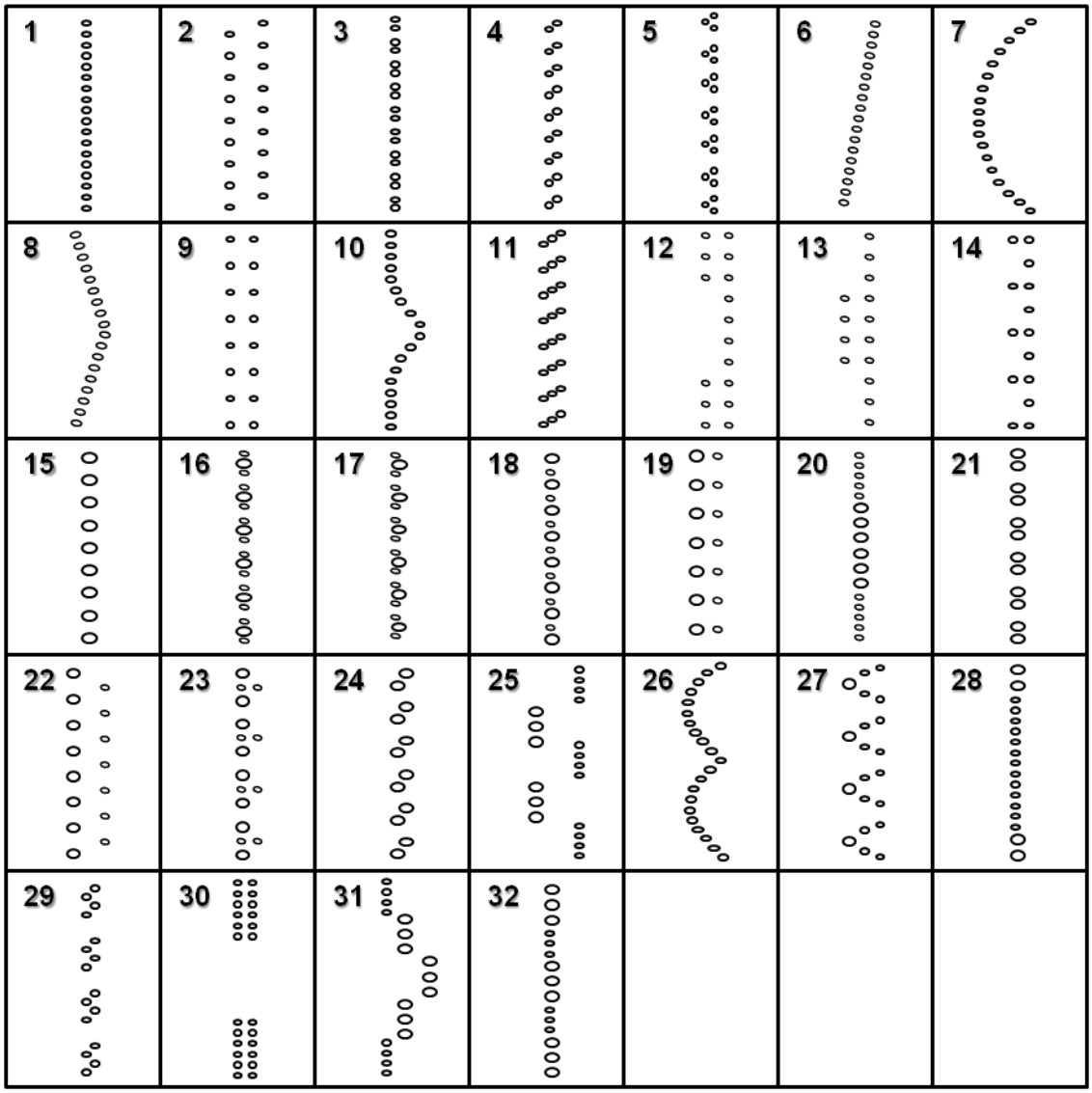

Figure 30 – 32 film cooling row patterns considered in the optimization process.

Optimization Process

Genetic algorithms (GAs) are at the core of the cooling design optimization in this work. GAs are a process for function optimization that mimics the genetic reproduction process experienced by biological organisms [169]. The goal of the GA process is to find

the best global design available. Figure 31 is a flow chart of the optimization process used. The optimization starts after the process variables are chosen, the ranges or discrete possibilities of those variables are assigned, and the boundary conditions of the CFD fitness-evaluation are set. Latin hypersquare sampling (LHS) occurs next to provide a random initial parent population of 600 highly-varying designs, or *genomes*, that have attributes that vary dramatically from across the design space. The first 100-genome population in generation one were randomly selected from the initial LHS pool. Each genome is represented by a binary digit bit string. Each new population of 100 genomes is a generation. Next, every genome and its unique cooling design in the original population is evaluated using many thousands of iterations of converged 3-D RANS CFD. From this, PS maps of ϕ_{nw} and $T_{\infty,nw}$ are obtained to determine the overall cooling performance of each genome.

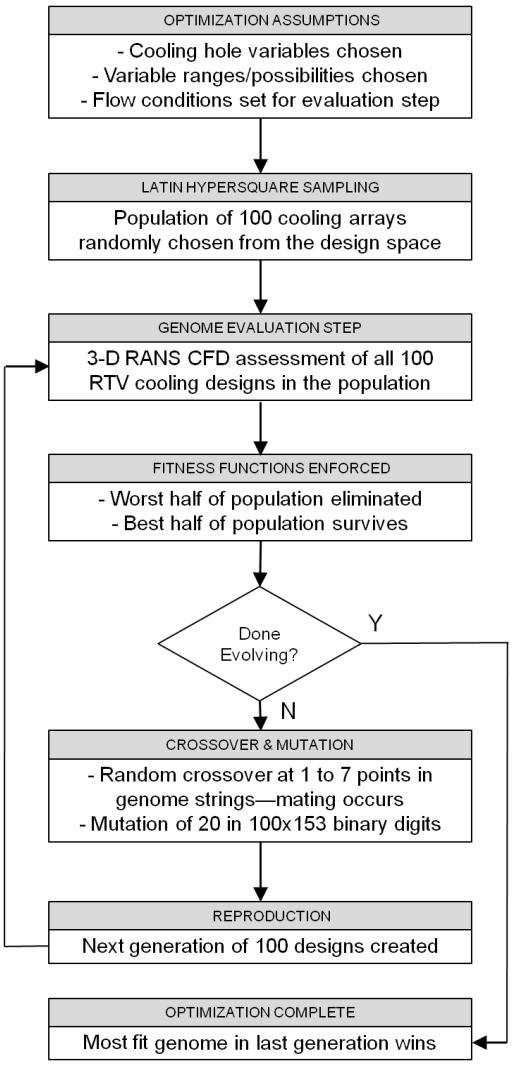

Figure 31 – Genetic algorithm optimization flow chart.

The fitness functions can be enforced based on the performance of each genome. From this, the best half of the genomes with the highest fitness values are kept and the worst half of the pool is eliminated. This is the feedback function of the process. Then, the crossover, or mating step occurs. Mating happens by copying the first genome in randomly paired genomes up to a random crossover point in its binary string and filling in the remaining digits with the binary identifiers from the second genome in the pair and vice versa, making two brand new genomes. Because it occurs in nature as well,

mutation is allowed to occur in the form of a bit string digit flip from 0 to 1 or vice versa. Mutation occurs randomly for 20 binary digits in every generation. The probability of mutation is low (0.13%) since there are 100 genomes in each new generation and a total of 153 binary digits in every genome. Once a new generation is created from the parents and respective children produced by crossover are in turn evaluated, the fitness functions are again enforced and genomes with the worst 100 fitness values are eliminated after assessing all 100 parents and all 100 children. Genomes that survive elimination become the parents of the next generation. Once the last generation of children is created and assigned fitness values, based on user preferences, the optimization comes to an end. The current optimization ended based on diminishing returns in fitness value improvements. Therefore, in the flow chart, for only the last generation, the optimization completes directly after the fitness values are calculated based on the CEEF CFD. Assuming the average fitness of every new generation has increased, which is an essential sign of a working GA and good fitness function, the best genome in the last generation is chosen as the optimized cooling array design.

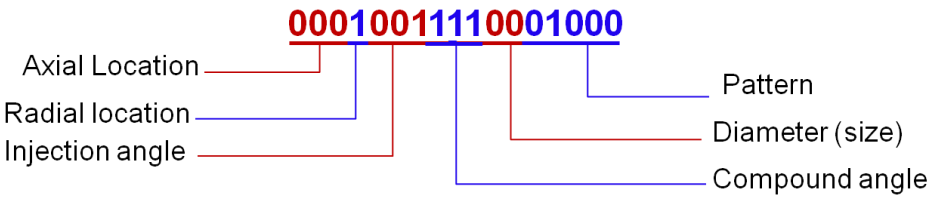

Figure 32 – Sample bit string for a single row of cooling holes with an implemented pattern in the vane PS optimization study.

Each genome is 153 binary digits because the variable of nine total cooling hole rows on the vane PS are combined to represent one cooling design. Three showerhead

rows and six downstream PS rows are optimized in this work. The showerhead rows only vary in terms of injection and compound angle, and the row patterns do not affect these holes. The downstream PS rows can vary through all process variables available. Each row has 17 binary digits assigned to it, thus with nine total rows on the PS, there are 153 digits for every RTV PS film cooling design genome. How a cooling hole row is identified as a bit string and broken up into its process variables is seen in Figure 32. By calculating two to the exponent of the number of digit places represented by a variable, it can be found how many discrete possibilities are available in the optimization. For example, five digits represent the row patterns, so $2^5 = 32$ available patterns. Injection angle, compound angle, and axial location can vary for $2^3 = 8$ possibilities in every row. Hole size, or diameter, can vary for $2^2 = 4$ possibilities in every row and radial (spanwise) location can vary for $2^1 = 2$ discrete possibilities. This can be cross-referenced with Table 8. Table 9 summarizes the primary specifications for the optimization.

Table 9 – Summary of optimization specifications.

Digits in each genome	153
Genomes in each new generation	100
Number of generations	13
Mutation probability	0.0013
Initialization method	LHS
Type of coding	binary
Recombination method	Random—1, 3, 5, or 7 points in a string
Maximum number of potential cooling array designs	0.32×10^{552}

Careful implementation of a user-specified fitness function in evaluating designs will result in a significantly improved cooling design in minimum time by using the process of natural selection to improve the set of parameters, or genes, that describe the PS cooling array. As mentioned before, the GA is not perfect, as it is susceptible to mutations and elitism, which makes the nature of the fitness function critical to its success. The main idea of the particular fitness functions enforced in this study was to minimize near-wall gas temperature over as much of the PS of the vane as possible. Another objective was to spread out the cooling by taking cooling away from over-cooled areas and redistributing it to hot areas as indicated by the performance of the baseline cooling configuration. Using turbine durability engineering experience and judgment, the equations considered in every genome's fitness evaluation from the CEEF CFD are:

$$fitness_1 = \phi_{nw,aavg} \tag{24}$$

$$fitness_2 = 1 - (T_{\infty,nw,max} - T_{\infty,nw,min})/(T_\infty - T_c) \tag{25}$$

$$fitness_3 = 1 - (T_{\infty,nw,aavg} - T_{\infty,nw,min})/(T_{\infty,nw,max} - T_{\infty,nw,min}) \tag{26}$$

$$overall\ fitness = (fitness_1 + 2 * fitness_2 + fitness_3)/4 \tag{27}$$

The first equation means the higher the value of ϕ_{nw}, the better. The second part of the fitness considers the difference between the maximum and minimum near-wall gas temperatures as found by the CFD on the vane for the particular cooling design considered, divided by the difference between freestream and coolant air temperatures. This is intended to decrease the maximum temperature close to the surface. The third fitness equation is intended to lower the average near-wall gas temperature on the vane PS. After a cross-correlation check for sensitivity, it was found that the first and third equations for fitness correlate very closely. For the overall fitness score, despite their

correlation, it was still desired to keep both of these. So in order to not drown out the relative effects of the second equation for the fitness, it was decided to multiply the second fitness by a factor of two in Equation 27. Subsequently, the average is taken by dividing by four since the fitness from the second fitness is counted twice in the equation.

Infrared Thermography Assessment of Flat Plate Pressure Side Models

Experimental Apparatus

The IRT facility used in this work to test the uncooled pate, baseline and optimized cooling array designs belongs to the Turbine Division within the Aerospace Systems Directorate of AFRL. It is a steady-state facility using air as a working fluid that is capable of a wide range of temperatures with test section pressure controlled by an orifice installed downstream of the test section and just before the exhaust line of the facility. Cooling air at a limited range of mass flow rates is conditioned at room temperature and pumped into a plenum behind the test plate so that the air is injected into the flow through the cooling hole passages of the test plate being interrogated. The main flow air is heated to the proper level in order to achieve the desired gas-to-coolant temperature ratio for a given trial. The test plate specimens are readily interchangeable and setup times and costs to run experiments are much less relative to full annulus blowdown rigs such as the AFRL TRF. This is the primary reason for choosing to run experiments of the RTV PS film cooling using flat plate models.

The flat plate rig is oriented with the test plate in a vertical position with the easily-adjusted IR imaging camera placed on a horizontal surface approximately 25 cm from the test surface outside the rig. Figure 33 s a top view of the test section

configuration for the experiments. It can be seen how the heated main flow passes through the test section over a low-pressure boundary layer bleed, across a boundary layer trip wire and over the flat plate specimen through which cooling air is injected. On the surface of the test plate the cooling air and main flow air mix to create a film which lowers the resulting external material temperature. The cooling air is supplied by the plenum on the back side of the test article due to an increased pressure relative to the freestream. Optical access to IR measurement of surface temperatures is provided by a 8.9 cm wide, 16.5 cm long, 0.95 cm thick ZnSe window installed in the flow channel wall opposite the specimen surface. The window has a high transmittance and high temperature resistance, however it is cooled with a film of injected air at room temperature. The IR camera is tilted slightly, as shown in Figure 33, to avoid reflection of the cryogenic detector off the window and back into the camera, creating an artificial cold spot on the IR images. This phenomenon can be seen on a few of the IR images in the results. Naturally, any temperature changes due to this effect are ignored.

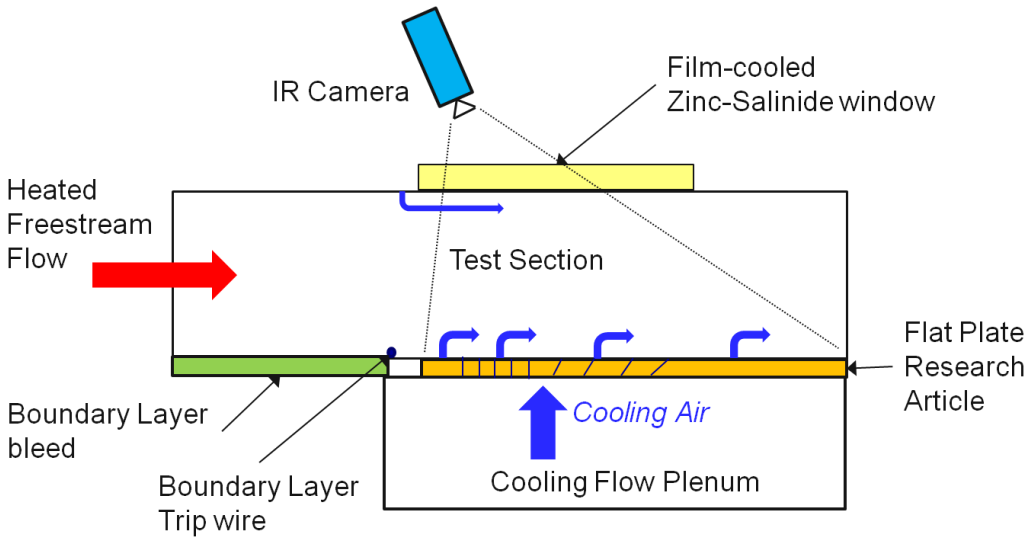

Figure 33 - Diagram of the flat plate IR thermography experimental test setup (top view).

Figure 34 is an image of the outside of the flat plate rig looking downstream from the camera viewing side where it can be seen how the cooling air enters the main stream perpendicularly through the test article which is bolted between the test section and the plenum housing. The cooling plenum housing holds a rake for total temperature and pressure measurement which is averaged for the observations. All pressure and temperature leads connect to a National Instruments analog-to-digital data acquisition system linked to LabView software providing a real-time graphical output of rig flow properties such as pressure, temperature, and mass flow for various locations. Figure 35 is the same rig from the other side looking upstream. Here, the upstream and downstream rakes of pressure transducers and thermocouples that measure total pressure and temperature are seen. All thermocouples used were type K. For the IR camera setting (373 to 773 K) based on temperature ranges assessed in this work (400 to 550 K), the error in temperature readings did not exceed ±2.2 K. All pressure readings were obtained using tube leads connected to a NetScanner Model 9116 module which gave a maximum error of ±6.8E-4 atm (0.01 psi). The pressure readings on the rakes were referenced to atmosphere using a Ruska controller which itself has an error of ±6.8E-5 atm. The IR camera can also be seen positioned in front of the test section window pointed at an angle. The rig has the capability to house turbulence-generating grids; however none were used in the current study. The ambient turbulence intensity in the test section is estimated to be between 1 and 2%.

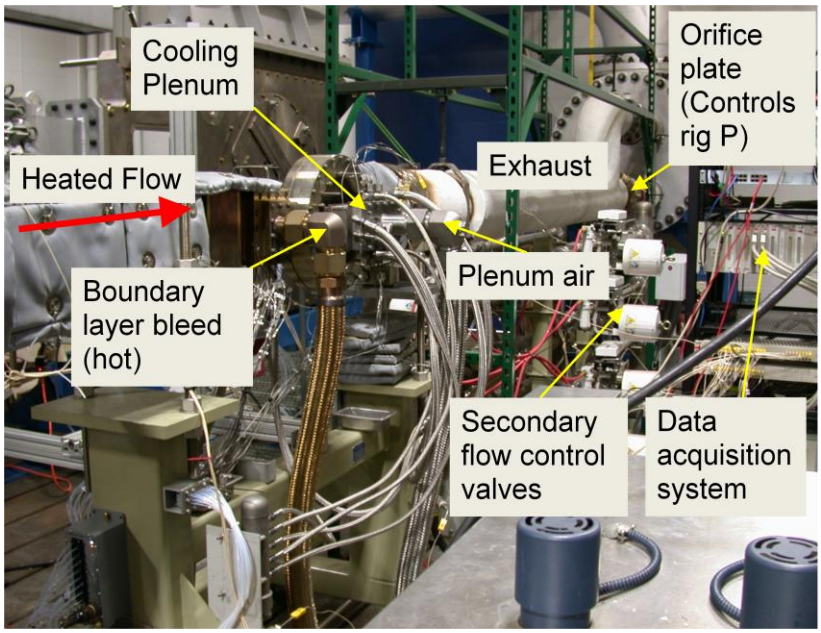

Figure 34 - Image of the AFRL Aerothermal Research Laboratory setup looking downstream.

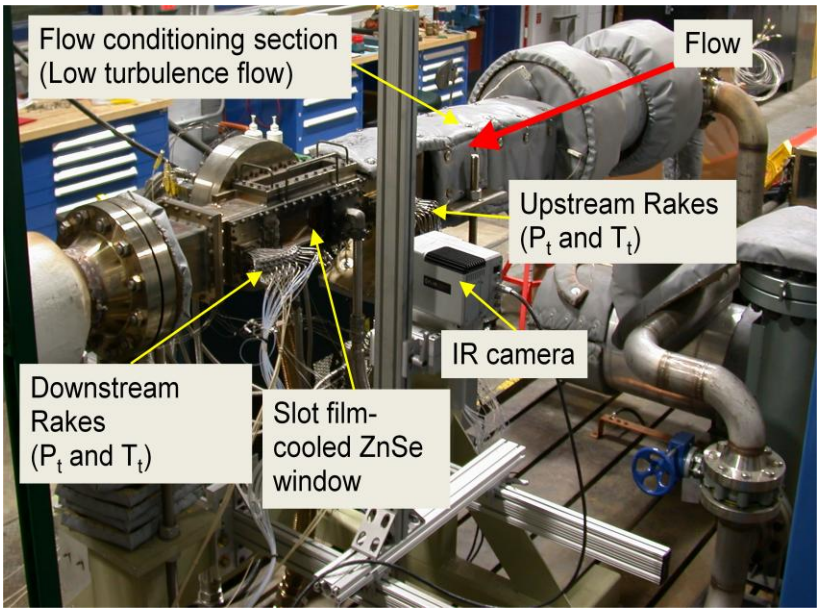

Figure 35 - Image of the AFRL Aerothermal Research Laboratory rig looking upstream.

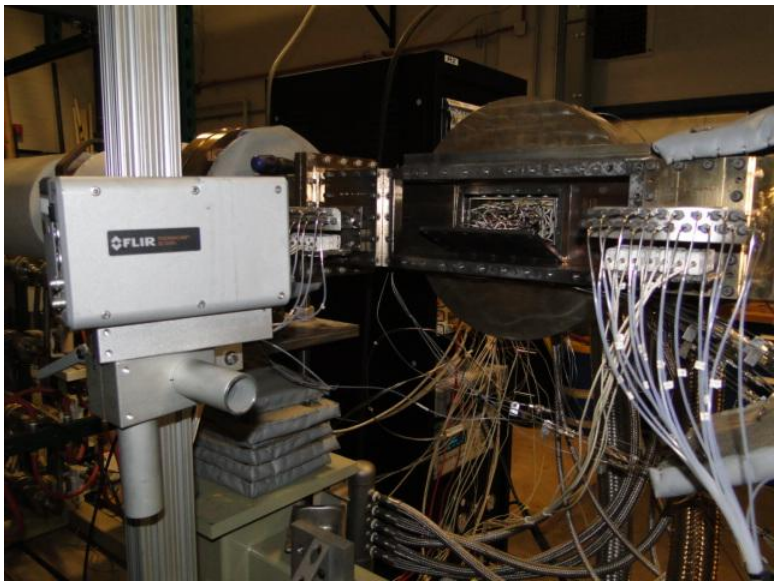

Figure 36 - Image of the IR camera aimed at the open test section.

The surface temperature is obtained using a FLIR ThermaCAM SC3000 infrared thermography camera. This is the same camera used in the work of Ekkad et al. [126]. An image of the camera with a view looking inside the test section with a test plate ready for final installation is shown in Figure 36. It can be seen that the cooling plenum can be crowded with wires and tubes for temperature and pressure instrumentation. The system provides a high-quality, nonintrusive method for obtaining real-time thermal data for analysis. IR temperature measurements are observed using commercially available software including LabView, and these are accessed in the same graphical suite that displays facility air temperature and pressure data. The system allows for direct pixel-by-pixel temperature measurements without the difficulties of recording a video image, grabbing frames, or converting gray scale levels to temperatures in separate processes. The system has a quantum well infrared photon detector which receives and records the thermal electromagnetic radiation between 8 μm and 9 μm in a 320 by 240 pixel field.

The system is internally cooled down to 70 K with a Stirling cycle and has several temperature ranges between 253 K and 1773 K. The stated system accuracy is ±2% of the chosen measurement range or ±2 K, whichever is larger. A temperature range of 478 K to 589 K is used for the current study.

All flat plates had a 15.24 by 7.62 cm testable area. They were fabricated using Inconel 718, the same material used in the 3-D RTV tested in the TRF. Any film cooling holes in the flat plates were created using EDM drilling. The hot side of all plates are spray painted with a thin layer of high-emissivity flat black paint so the IR camera can accurately read surface temperatures. For calibration, each plate had three flush-mounted pressure taps and three flush-mounted thermocouples. All plates had two identical recessed material regions that matched the material thickness of the Inconel 718 on the 3-D vane. All cooling hole features fit within these regions and thus, cooling hole *L*/*D* is matched. The cooled plates had 12 back-side thermocouples welded to the back surface and arranged in a straight line along the midspan to allow the measurement of heat flux across the material thickness. Six different plates were tested in all.

Uncooled Flat Plate Model

An uncooled blank test plate was used to compare temperatures of the same material without a cooling array. This allows for an understanding of the absolute benefits of the cooling holes on the tested film cooling designs. As seen in Figure 37, the uncooled plate has three evenly-spaced small coolant discharge holes near the downstream end of the test section whose combined area matches the combined area of all the film cooling holes in the cooled plates. This provides the same back-side cooling

condition on the uncooled plate as the cooled plate, since the flow is moving slowly behind the cooled plate before it is forced through the cooling holes. This migration of cooling is mimicked in the uncooled case by allowing flow to escape through the discharge holes near the downstream end. Despite the fact that the cooling air comes in slowly, without these discharge holes, the plenum would continue to fill up with cool air with nowhere to go, causing an undesired impingement effect. The back side of the discharge holes are chamfered to preserve the effective hole areas due to coolant fluid shear layers. Figure 38 is the back side of the uncooled plate. Thermocouple and pressure line leads can be seen attached to the plate. The holes around the edges of the plate are for screws to hold the test plate in the test section. The heads of these screws can be seen in the IR images.

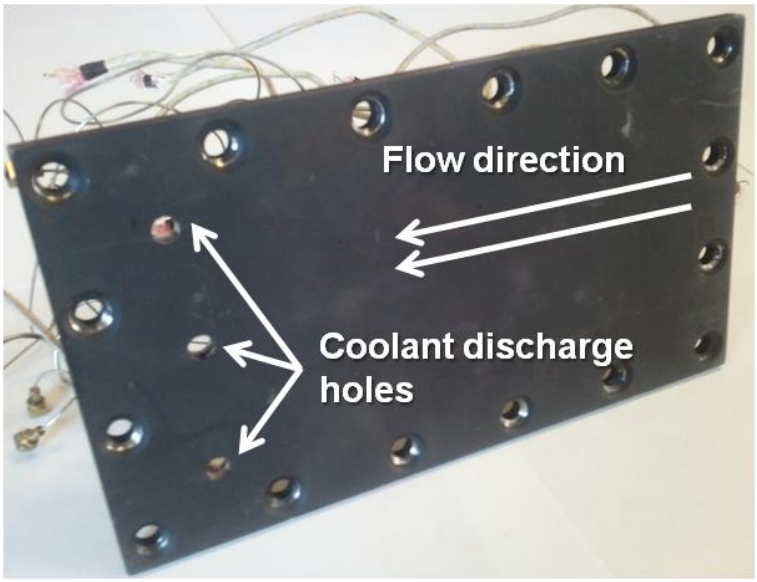

Figure 37 – Hot side image of the uncooled flat plate with three downstream discharge holes.

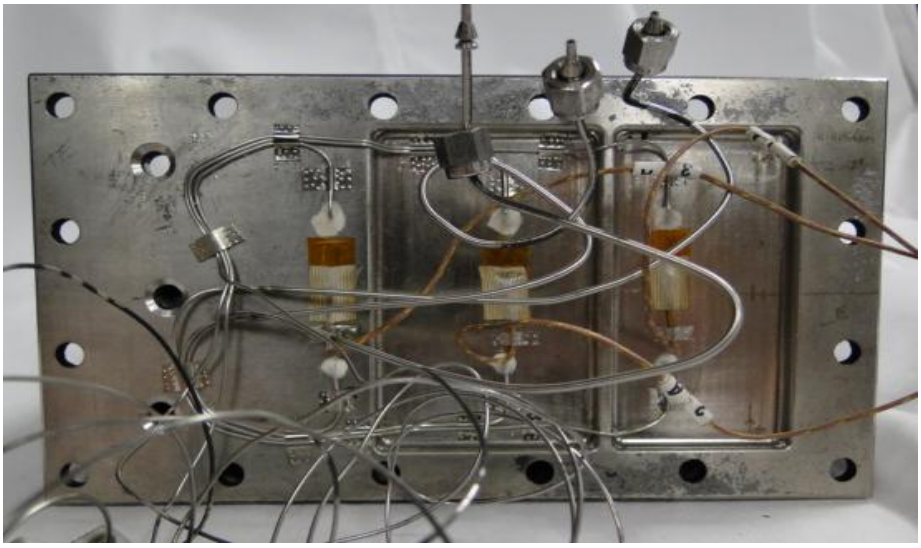

Figure 38 - Image of the back side of the uncooled flat plate with three downstream discharge holes and pressure and temperature instrumentation.

Baseline Cooling Design Flat Plate Model

The RTV pressure side (PS) film cooling array includes three rows of showerhead holes near the leading edge and six rows of laidback fan-shaped holes moving towards the trailing edge. All holes have a 30º injection angle. The showerhead holes are oriented with a compound angle of 90º towards midspan. These are all accounted for on the baseline PS film cooled plate. The cooling features on the flat PS of the RTV that become the cooling features on the plate are given in Figure 39.

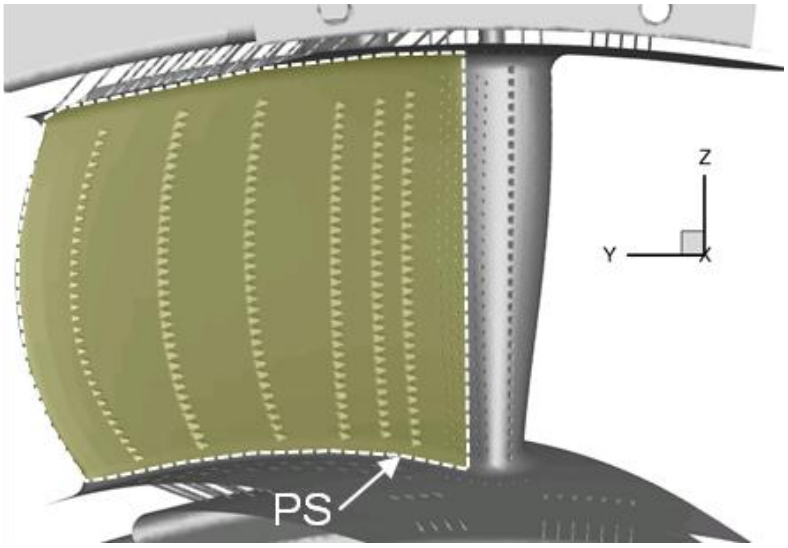

Figure 39 - 3-D CAD rendering of the HIT RTV highlighting the baseline pressure side film cooling array that is translated to the cooled plate.

Figure 40 is the baseline PS film cooled plate as viewed on the hot side with flow going from right to left. Naturally, the cooled plate does not have discharge holes like the uncooled plate. It can be seen that the 3-D nature of the vane with its curved trailing edge causes slight differences in stream-wise spacing near midspan and adds a slight bow to the cooling hole rows in the spanwise direction. This is analogous to clamping a deck of cards and pushing only the cards in the middle of the stack in one direction creating symmetrical curvature from the bottom to the top of the stack. However, near the hub and shroud, both the vane and plate have the same stream-wise spacing. The only major difference between experiments using flat plates and TRF blowdown tests on the 3-D vane, besides the plates being flat, is that the IRT facility has one cooling plenum the size of the plate while the RTV installed in the TRF has two small internal cooling plenums, fed from different radial ends. Material, flow conditions, and cooling hole sizes and configuration are all the same between the cooled plate and the cooled vane PS in the

TRF. Again, the basic nature of the baseline film cooling design can be seen as the last four repeating shaped hole rows are evenly spaced and all holes across a row are evenly spaced with the same injection and compound angles.

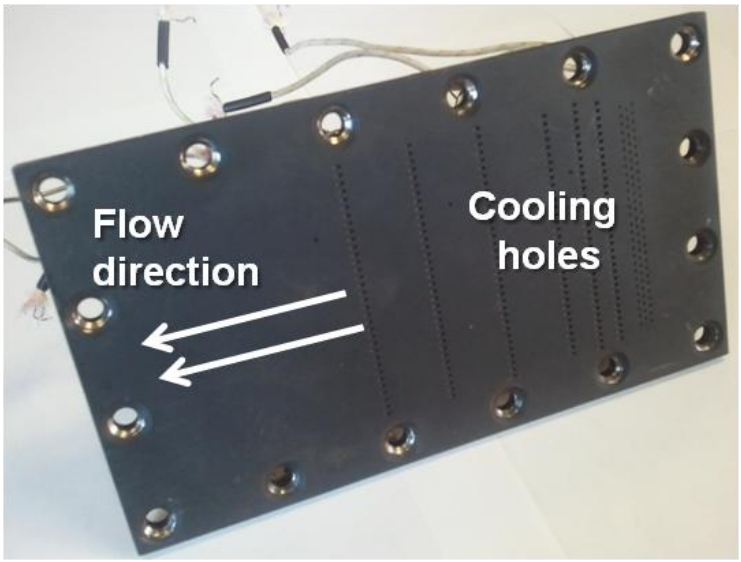

Figure 40 – Image of the baseline cooled flat plate hot flow side.

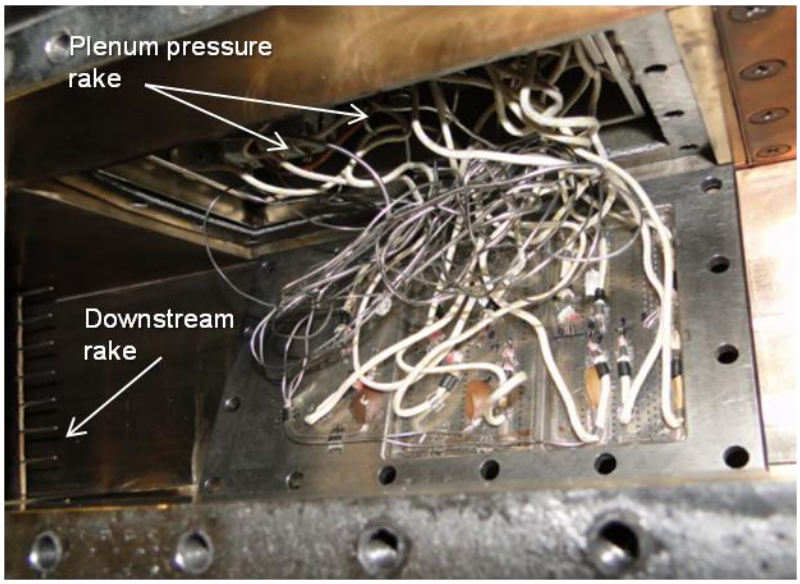

Figure 41 - Image of the back side of the cooled test plate as installed in the test section.

Figure 41 is like Figure 36, but a closer view of the cooled plate in the test section. The recessed areas to match vane *L/D* are seen along with the thermocouples welded to the back side between cooling hole rows to obtain heat flux. The heated main flow goes from right to left in the image. After the pressure and temperature instrumentation is carefully placed in the cooling plenum, the flat plate can be screwed in flush with the side wall and be ready to test. The downstream flow rake and cooling plenum rake can be seen. While the instrumentation is extensive coming off the back side of the plate, cooling flow is conditioned based on readings on the rake.

Optimized Cooling Design Flat Plate Models

The last four of six plates tested in the IRT facility have the optimized RTV PS cooling design each with a different cooling hole shape for the six rows of holes downstream of the three showerhead cylindrical-hole rows. The showerhead hole shapes were unchanged between the four plates and had the optimized injection orientations. Flat plates with cylindrical, fan-shaped holes just like that on the RTV, Vehr holes [158], and mini-trench shaped (MTS) holes were tested [159]. Since the computational optimization was not conducive to optimizing for 3-D hole shape, it was decided that the optimized cooling configuration could be tested using IRT with four different hole shapes in a trial and error format to see which hole shape worked best for the optimized cooling array. In order to not give away the optimized cooling design here, an image of the optimized cooling design on the flat plate are given in the IRT experiment results section.

The fourth film cooling hole shape tested on a flat plate for the optimized cooling array is the MTS hole. Many of the experimental studies on trenched cooling hole

configurations such as that by Waye and Bogard [20] use shaped holes embedded within large trenches, which can be hard to manufacture. Depending on the depth and width of the trench, EDM drilling of a laidback fan-shaped hole lying inside a trench can be difficult to do without disturbing the front edge of the trench. More importantly, it is undoubtedly more expensive. The MTS hole attempts to solve this problem by embedding a miniature trench inside a standard shaped hole as seen in Figure 42. This is easy to manufacture since the shaped holes can be fabricated as usual followed by a small trench aligned with the upstream edge of the shaped hole. The axial length of the trench is determined by the amount of forward diffusion of shaped hole. Knowing the unconventional nature of the optimized cooling array, and that some rows are shorter than others (not full span), the lateral expanse of the trench is only as long as a given row of holes. Figure 43 is what a straight row of MTS holes looks like on a flat plate.

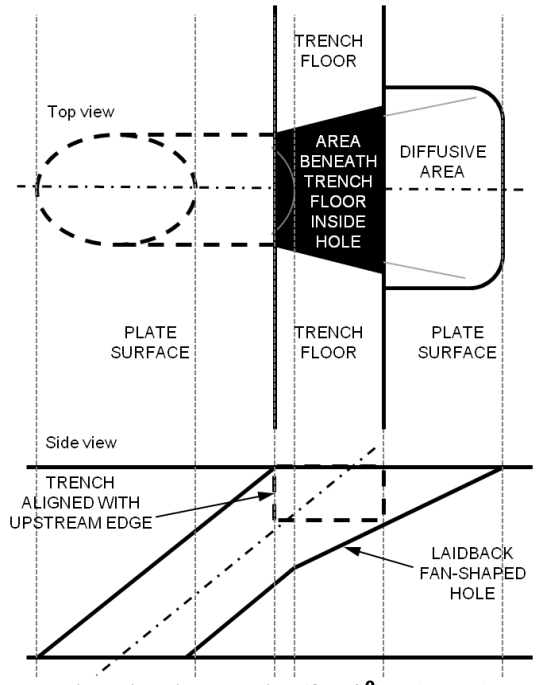

Figure 42 - MTS hole top-down and side view in an axial ($\beta = 0^0$) orientation and a nominal injection angle (α). Flow is left to right in this image.

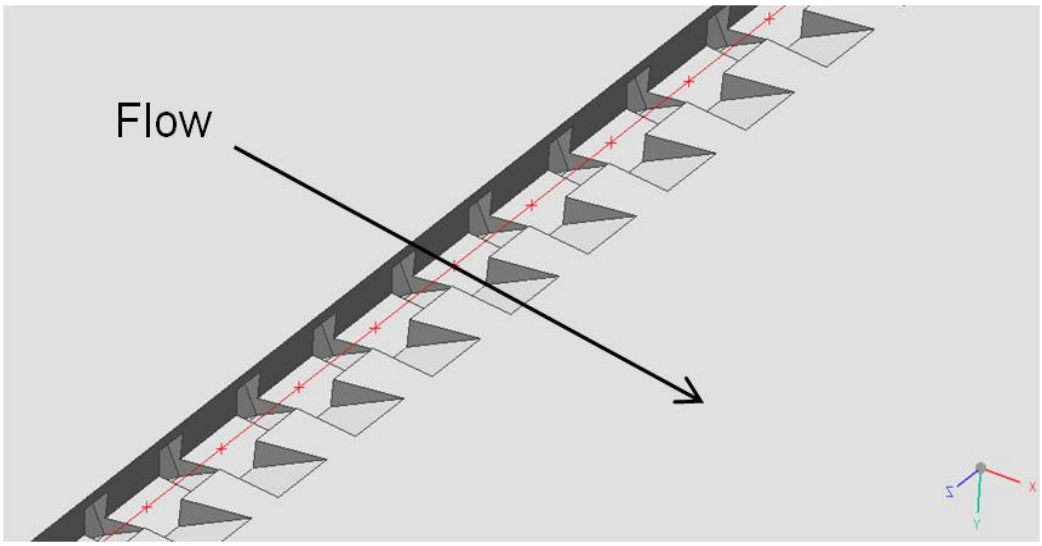

Figure 43 – CAD image of MTS holes as they would appear in a basic straight row.

Experimental Procedure

A near perfect blackbody with a known emissivity very close to unity was accomplished by spraying the flat plates black. Prior to the actual thermal measurements, calibration of the entire thermography system and IR signal was required. The test specimen surface was heated with the hot air supplied by the blower through the facility mainstream air heater. Once steady state is reached, the temperature of the thermocouple is compared to that measured by the IR system at that location. The position of the thermocouple is known relative to the center of one of the X-shaped screw heads also captured in each of the IR images (whose coordinates can be found using MATLAB image tools), so the proper pixel coordinates can be found to get the IR temperature at the location of a thermocouple. For a broad set of varying temperatures over the range of experimental operation, the temperatures measured by the thermocouple were plotted against the IR temperature readings creating a straight line and an equation of slope an intercept which can be used to correct the IR data. For thermocouple-base temperature

corrections such as this, the question of the thermocouple's accuracy arises—which is determined by the calibration curve, its exact position on the surface, and its orientation with respect to temperature gradients [114]. Therefore, only thermocouples in a uniform temperature area on an uncooled flat plate can be used. This procedure corrects for the emissivity of the flat black paint, the transmissivity of the viewing window, the humidity in the air, as well as for the overall radiative environment unique to a particular setup [113].

Following the suggestion of Schulz [114], the calibration was performed using three equally axially-spaced thermocouples on the uncooled flat plate surface since using the cooled plate creates unreliable non-linear curves due to high local temperature gradients. Figure 44 is a curve-fit plot of the calibration data. Since most tests on flat plates would involve increasing the main flow temperature first, followed by changing the plenum pressure at a design level temperature, the calibration was conducted on the uncooled plate in the same way. The scatter towards the top of the plot is explained by changes in cooling plenum pressure, which ultimately changes blowing ratio for the film cooling. The magnitude of scatter is the least for sensor two, and the offset in for the pressure-changing values is not far off from the temperature-changing values. Sensor two also exhibits temperature levels between the other two three thermocouples in terms of output, since as is seen in the results section, surface temperature rises with axial distance on the plate. So the correction for the IR camera was derived from those readings. All temperatures were taken as facility set points were increased to avoid the adverse thermal inertia and soaking effects that would be encountered if data were taken as temperature decreased after being at a higher level for an extended period of time.

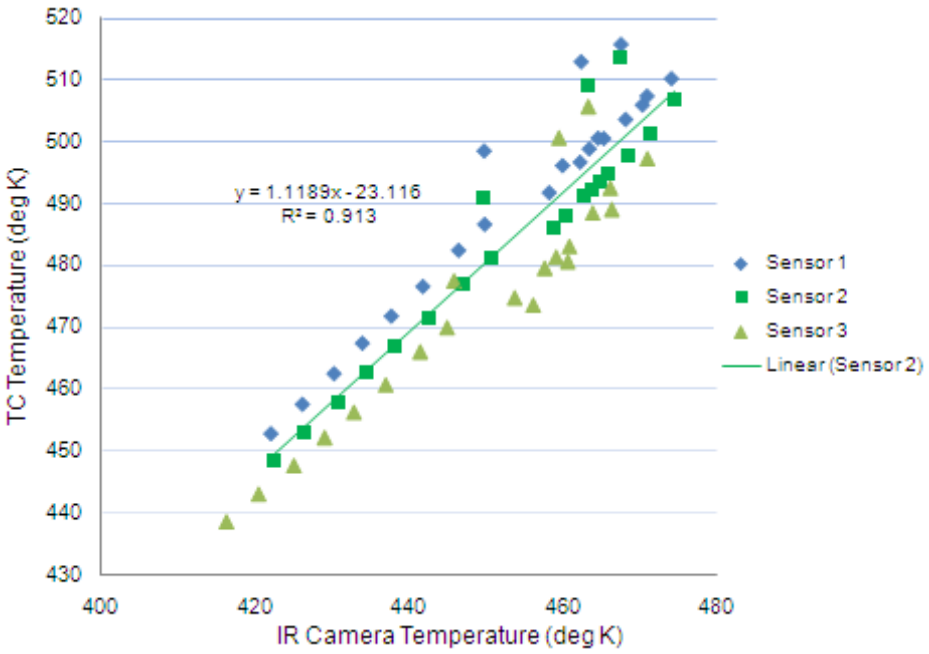

Figure 44 - IR camera calibration data and curve fit from three hot-surface thermocouples.

In the current work, coolant-to-mainstream total pressure ratio will be used rather than blowing ratio. During testing, this ratio is varied while density ratio based on changes in the mainstream flow temperature changes varies only slightly. Flow property ranges were chosen that encompass the design conditions for the RTV. The temperature of the test section air was set by a facility air flow heater. The set point of the heater is typically higher than the test section temperature since there is a lag due to heat transfer to the piping between the heater and test section. IR images were typically taken for total mainstream flow temperatures ranging from 478 K (400º F) to 561 K (550º F) at 8.3 K (10º F) intervals, at 1 Hz for 15 seconds. The final IR images are obtained by taking the average surface temperature pixel values from the set of 15 images. When the temperature in the test section reached 533 K, the coolant-to-mainstream pressure ratio was changed by varying the mass flow to the cooling plenum. It was found that after

adjusting the valves to the cooling plenum, the desired steady-state coolant-to-mainstream pressure ratio was reached within 30 seconds.

Some of the key considerations for matching conditions to both operational engine-representative levels and to data in the short-duration blowdown 3-D vane annulus TRF tests included matching the cooling passage L/D (as seen before with the reduced-thickness areas on the test articles), matching the total coolant-to-hot mainstream pressure and temperature ratios ($P_{t,c}/P_{t,\infty}$ and $T_{t,c}/T_{t,\infty}$, respectively) between the rigs, and matching the high-temperature levels expected. According to Han et al. [146], these figures of merit are some of the most useful measures in quantifying film cooling effectiveness, since they provide the ratio of coolant to hot mainstream thermal capacitance. Typically, for a given pressure ratio, the lower the temperature ratio, the better the film cooling protection will be. Likewise, for a given temperature ratio, the higher the pressure ratio, the better the resulting film coverage. For these reasons, effort was made to match these values to design levels as well as off-design conditions in runs of the Turbine Research Facility blowdown rig.

The pressure capability of the current IR flat plate rig (3.74 atm) is not nearly as high as that of the TRF (6.8 atm), however the TRF (at 444 K) cannot achieve the design temperature levels of the IR flat plate rig (533 K). In addition, coolant in the TRF can be sustained at a much lower temperature (250 K) and higher pressure (7.12 atm) than for the IR flat plate rig which maintains cooling air at room temperature (300 K) and a lower pressure (3.91 atm). Thus, taking all this into consideration, appropriate values for total pressure ratio and temperature ratio are: $P_{t,c}/P_{t,\infty} = 1.046$ and $T_{t,c}/T_{t,\infty} = 0.563$, which are constant between the two facilities.

V. CEEF CFD PS Film Cooling Optimization Results and Discussion

3-D CEEF CFD on RTV

Uncooled Case

CEEF CFD predictions of uncooled vane case at design flow conditions as outlined in the methodology is presented first. Most contours will focus on the RTV PS as it is the focus of the cooling optimization. Since these simulations had isothermal boundary conditions, and temperatures at the wall shows little or no variation, the temperature distribution had to be investigated for some number of grid cells from the wall in the structured grid. This is explained in detail in the optimization results. Temperature at the wall-normal grid location for which the cooling array optimization was performed, previously defined in the methodology as $T_{\infty,nw}$, is reported here. The plots in Figure 45 for simulated surface pressure and near-wall gas temperature on the vane without film cooling shows that the LE area and just downstream is the hottest area on the PS. Basic correlations used in typical durability design practices are likely to be able to pick up on this, as the baseline cooled vane concentrates most of its cooling hole rows near the LE flow stagnation area in order to cool this area down. The temperature decreases over 60 K from LE to TE as the flow becomes less stagnated, picks up velocity, and becomes parallel with the surface. Comparing the two plots, the hot areas on the surface are primarily an axial function of the pressure loading. Looking across the lateral direction, the near-wall gas temperature distribution is somewhat dependent on the span location. It appears that endwall secondary flow is potentially causing an increase in temperature close to the hub. This cooler area at midspan is simply due to the 3-D shape

of the vane and the curved TE. This runs counter-intuitive to the baseline cooling design that directs shower head film cooling towards midspan, creating a pileup of coolant. If designers had accounted for this, film cooling at the showerhead would be directed towards the endwalls instead in order to cool the higher temperature zones. Knowing that EDM drilling would be difficult due to the endwalls being in the way, at least the holes near midpsan could be drilled with an endwall-directed orientation to solve this problem, keeping the showerhead injection near the endwalls at 90 degrees. It will be seen that the optimized cooling design takes the cooler area at midspan into account as the resulting array removes cooling holes near midspan. Overall, the contours show that the 3-D nature of the vane creates a lot of variation in the axial and radial direction that must be accounted for in film cooling designs.

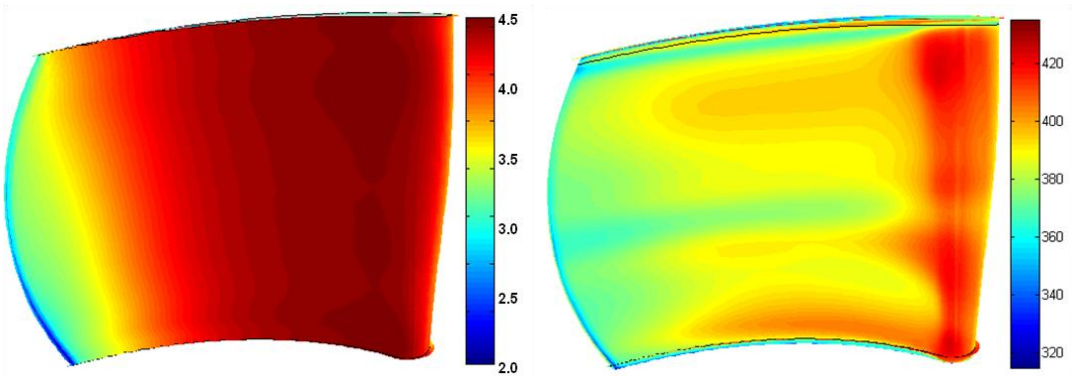

Figure 45 – Surface pressure [atm] contour (left) and $T_{\infty,nw}$ [K] contour (right) for the uncooled vane PS at design conditions.

Figure 46 and Figure 47 are the uncooled $T_{\infty,nw}$ distributions for midspan and 90% span, respectively. Each plot includes predictions for laminar flow, transitional flow, and turbulent flow. Since the environment in the Turbine Research Facility being simulated is a relatively low turbulence intensity flowpath, all three plots are given here as well as the validation in Appendix B. In these plots, like many others in the results, pressure side

is on the left half and the suction side is on the right, with the LE in the center. At midspan, with fully turbulent and transitional flow, the LE temperature is about 10 K higher than for laminar flow. Trends between the different flow regimes are similar, with PS and SS levels being as much as 30 K lower for laminar flow. This temperature difference between regimes is much greater for the PS. Transition appears to occur on the SS near the LE. At 90% span in Figure 47, overall temperature levels are higher and there is much less temperature difference at the LE. On the SS, transition occurs farther upstream as well. In both Figure 46 and Figure 47, it can be seen that the LE to TE temperature range on the PS is less than for the SS, making it a logical starting point for cooling optimization.

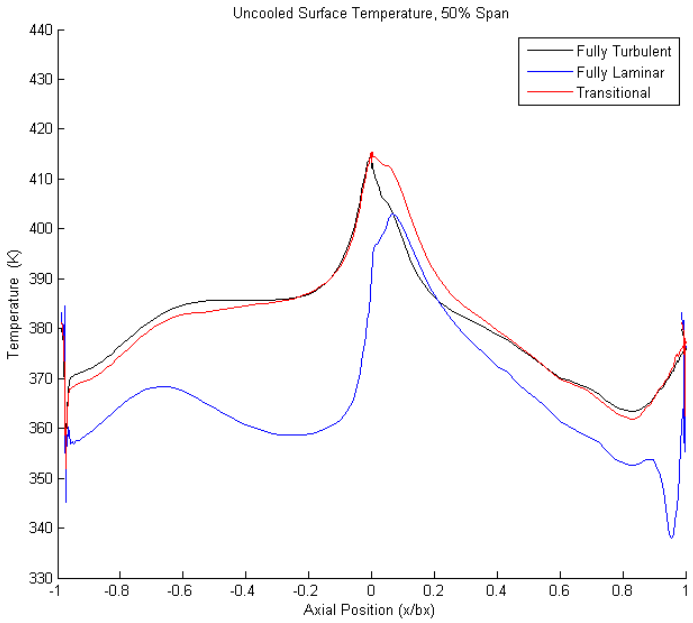

Figure 46 - $T_{\infty,nw}$ [K] at midspan for the uncooled vane at design conditions.

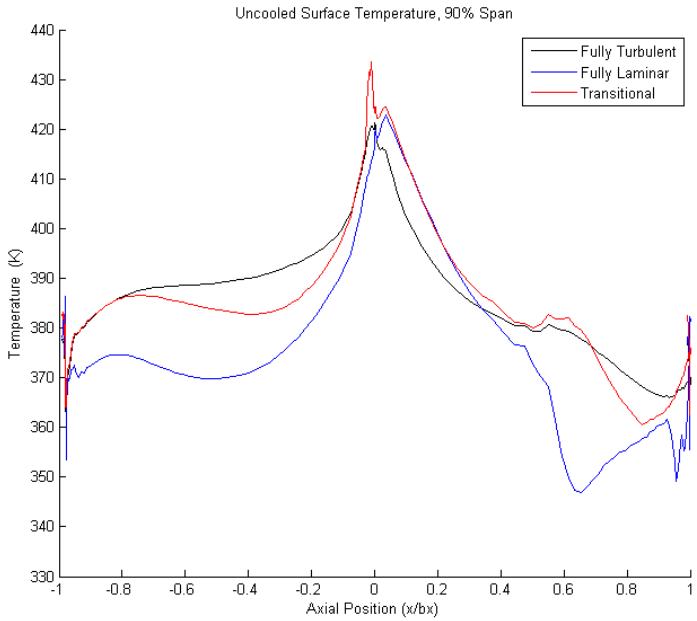

Figure 47 - $T_{\infty,nw}$ [K] at 90% span for the uncooled vane at design conditions.

Baseline Cooled Case

Next, showing near-wall heat transfer contour plots for just the baseline cooling scheme, it can be seen in Figure 48, Figure 49, and Figure 50, how the elementary cooling pattern on the PS with its simple straight repeating rows causes cyclic increases and decreases in near-wall gas temperature and heat flux. As is discussed in the optimization results, all plots shown here are the results at the wall-normal grid cell location at which the optimization was performed. This cooling pattern causes repeating cool areas that run the length of the span but this also results in hot spots that are generated between rows. Ideally, these differences in heat flux and temperature can be reduced.

Figure 48 is the near-wall gas temperature contour for the PS which shows that the coolest area does not arise until far downstream past the 5^{th} and 6^{th} rows of

downstream (excluding the showerhead) film cooling holes. Hot spots are repeated near the hub and at about 80% span just before cooling holes. The midspan pileup of cooling due to the unique showerhead hole injection angles is evident. Only near the LE is cooling spread out enough to keep temperature the same over the pressure surface. This plot also shows that there is a hot streak at the shroud over most of the axial length, even with endwall film cooling simulated in the optimization. The hottest part of the vane PS was the LE at the hub, which lies out of the physical boundaries of the optimization and ultimately was not alleviated.

Figure 49 is a plot of the near-wall heat flux for the baseline cooled case. Heat flux is an indicator of temperature gradients in the direction normal to the surface. It can be seen that with film cooling the results are very similar to the near-wall gas temperature. This is largely because heat flux is highly dependent on the simulated temperature at the grid location away from the wall. Like the temperature results, as observed in many past works, repeated cooling rows cause cyclic changes in heat flux in the axial direction. High heat flux is observed in the shroud region as well as just upstream of cooling hole rows. The lowest heat flux is observed at midspan and just downstream of cooling holes. One small difference is that the hot spots for heat flux are slightly smaller than that for temperature. This would indicate that the hot spots are decreasing in size and heat flux is becoming more uniform away from the wall. Figure 50 is the near-wall overall effectiveness for the PS where higher values of ϕ_{nw} are colored red. The patterns observed are the same as for the temperature which is to be expected knowing how it is calculated and referenced to mainstream and cooling flow temperatures. Unlike near-wall heat flux, which reaches a maximum just before a

cooling hole row, ϕ_{nw} typically is a maximum at the location of the cooling holes and decreases with downstream distance.

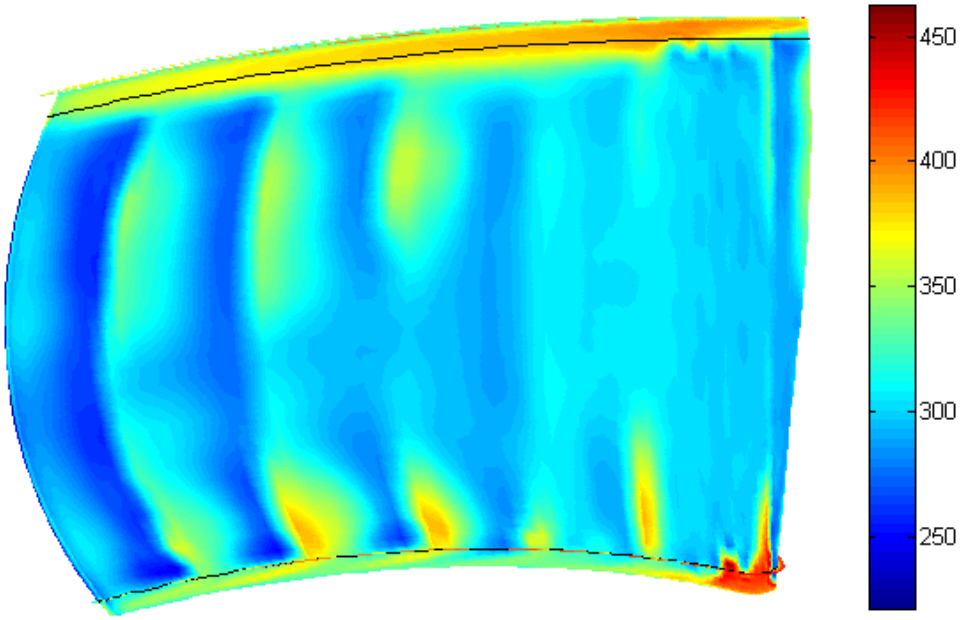

Figure 48 - $T_{\infty,nw}$ [K] contours with film-cooling for the RTV PS.

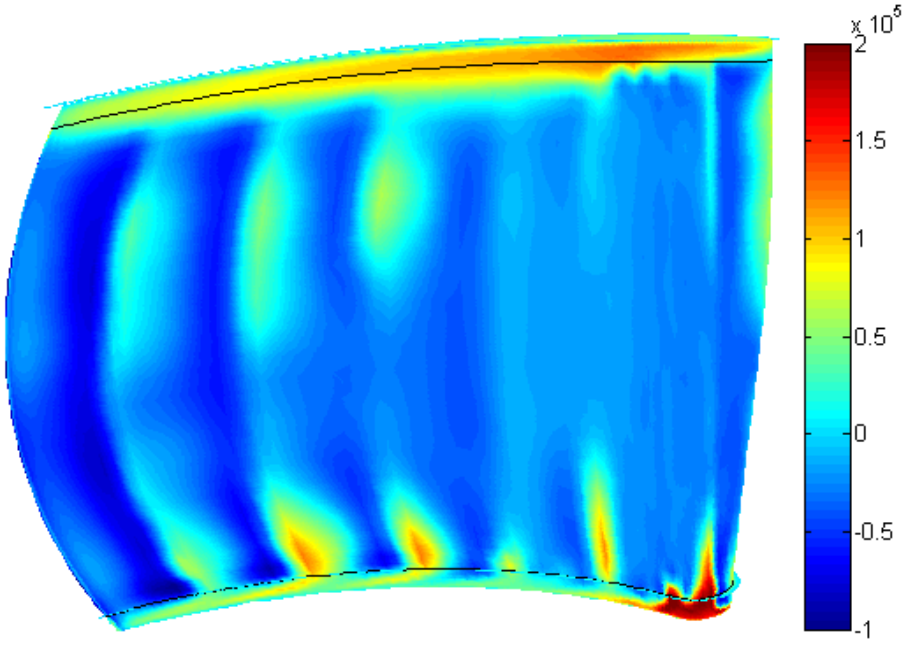

Figure 49 – Near-wall heat flux [W/m^2] contours with film cooling for the RTV PS.

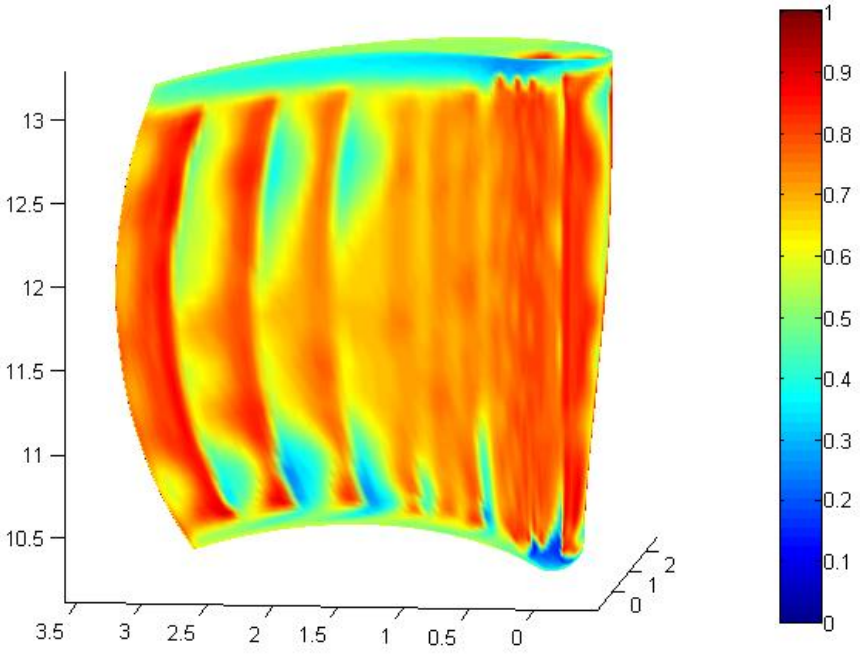

Figure 50 – Near-wall overall effectiveness contours with film-cooling for the RTV PS.

Cooled vs. Uncooled RTV Comparison

Now the results of the CEEF CFD heat transfer predictions on the RTV PS with and without film cooling are directly compared to provide an idea of the benefit of cooling due to a baseline design. The first four plots, Figure 51 through 56, are comparisons of near-wall gas temperature. Figure 51 is a contour plot of the near-wall gas temperature difference with and without film cooling. This illustrates how film cooling changed the temperature of the uncooled vane. Naturally, most of the PS temperature is reduced approximately 80 K. In fact, there are only few small areas where temperature actually increases. Some locations just downstream of cooling holes are reduced up to 120 K. Although, the addition of standard film cooling rows appears to cause very small increases in temperature just upstream of film cooling features past mid-

chord near the hub. This is due to combined 3-D cooling and secondary flow effects that did not exist in the uncooled case. It can be seen that the addition of film cooling, mostly due to its common axial compound angle, aligned with the freestream and parallel with the endwalls, does little to reduce near-wall gas temperature near the shroud. Due to the design, the cooling holes are also rather far from the wall. It will be seen that the optimization results that redistributed cooling flow is necessary to cool this area.

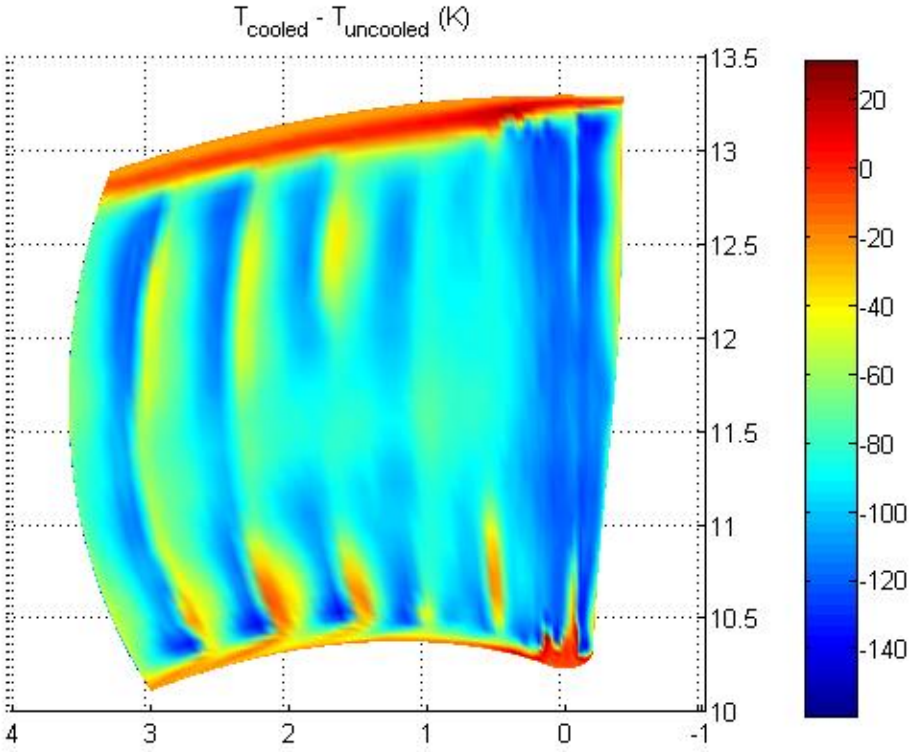

Figure 51 – Contour of $T_{\infty,nw}$ difference [K] between cooled and uncooled vane.

The PS (left half) and SS (right half) near-wall gas temperature distributions with and without film cooling at the 10% span location near the hub is given in Figure 52. The PS hot spots near the hub can be seen in this plot. Clearly, the dramatic changes in $T_{\infty,nw}$ due to film cooling are greater on the PS than the SS. However, at all levels across both surfaces, temperature has dropped an average of about 50 K with cooling. The

magnitude of the cyclic increases and decreases in temperature is reduced in Figure 53 for midspan, most likely due to the lack of secondary flow and the addition of midspan-oriented cooling from the showerhead. Here again, relative to the uncooled case, near-wall gas temperature is reduced 50 K over most of the PS and SS. Han et al. [1] have noted that a 50 K reduction in part surface temperature can lead to double the life span of the part. It can be seen in Figure 54, for the 90% span location, similar trends as midspan, with slightly higher jumps in temperature between cooling hole rows.

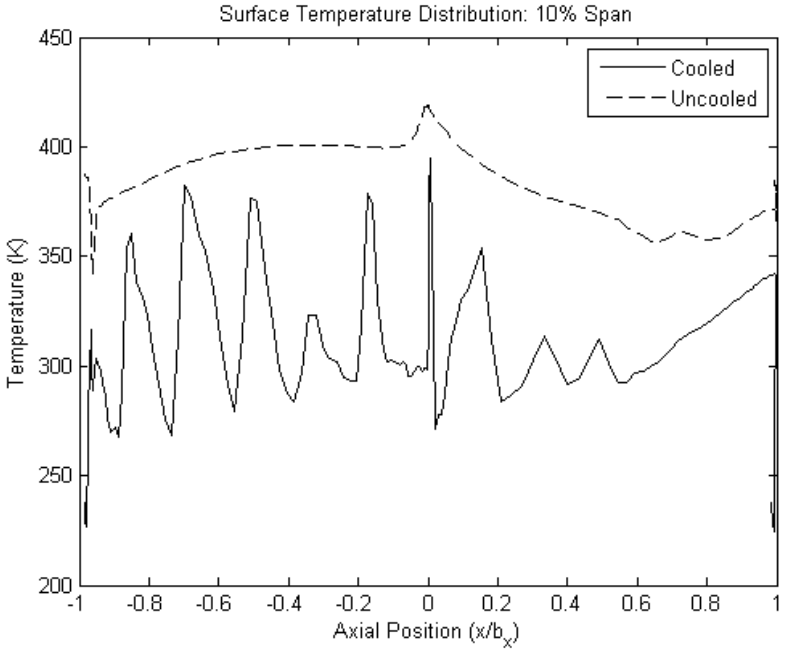

Figure 52 – $T_{\infty,nw}$ [K] distribution comparison with and without film cooling at 10% span.

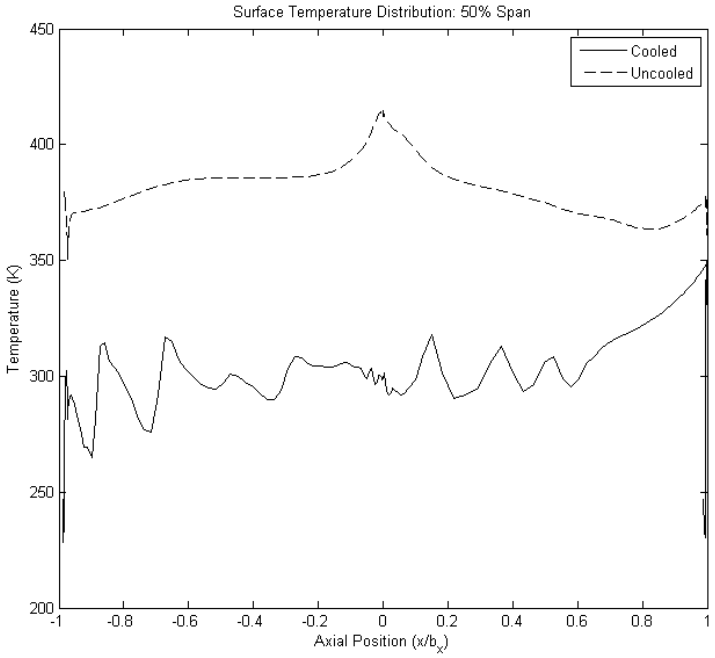

Figure 53 - $T_{\infty,nw}$ [K] distribution comparison with and without film cooling at 50% span.

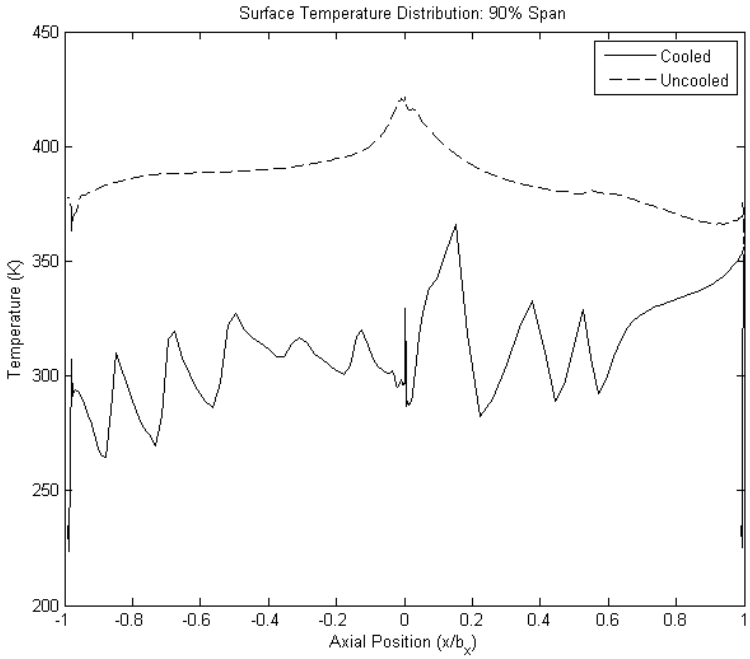

Figure 54 - $T_{\infty,nw}$ [K] distribution comparison with and without film cooling at 90% span.

The difference between the cooled and uncooled predicted near-wall heat flux is plotted as a contour in Figure 55. Most of the heat flux was reduced due to the baseline cooling scheme at the LE between midspan and the shroud. Over most of the PS, heat flux is reduced with the addition of film cooling. However, unlike for temperature, addition of film cooling features actually increases heat flux a very small amount right at the location of holes. This is especially evident past mid chord for the last three rows of holes. This makes sense as most of the mixing and resulting temperature gradients normal to the wall occur where cooling holes lie. This has been observed in many past works in open literature such as that by Schmidt et al. [144]. As mentioned for temperature, film cooling was not able to reduce heat flux in the shroud region.

10% span near-wall heat flux distributions with and without film cooling are given in Figure 56. In the left half of the plot for the PS, the small increases in heat flux due to addition of film cooling can clearly be seen. It is highly likely that the favorable pressure gradient, as its magnitude decreases, is not enough to overcome the effects of injection of film cooling into the flow just above the pressure surface. As a result, past mid-chord, where the vane PS is fairly flat, film cooling performance is more like that on a flat plate. This combined with a thickening boundary layer that is becoming turbulent, allows greater interaction of cooling flow into the mainstream away from the surface of the vane, causing increases in wall-normal gradients.

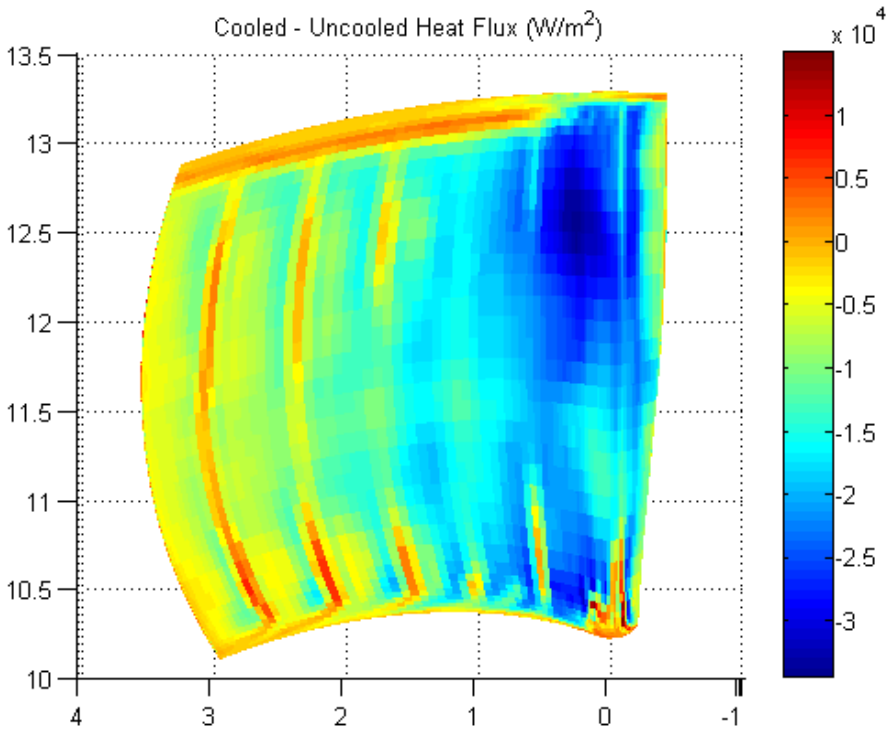

Figure 55 - Contour of near-wall heat flux difference [W/m^2] between cooled and uncooled vane.

At midspan and 90% span locations, in Figure 57 and Figure 58, respectively, near-wall heat flux is reduced over the entirety of the vane surface. Reductions in temperature are greater on the PS relative to the SS, which is afforded by the fact the film cooling performance is generally better in favorable rather than adverse pressure gradients. The spikes in heat flux are much less relative to the hub at these locations. On the PS, even with midspan-oriented showerhead holes, the magnitude of the local change in heat flux due to film cooling is about the same between midspan and 90% span. Overall, the addition of the baseline film cooling design to the uncooled vane has reduced both near-wall temperature and heat flux considerably over both surfaces of the vane, but more so for the PS, where the cooling configuration is optimized.

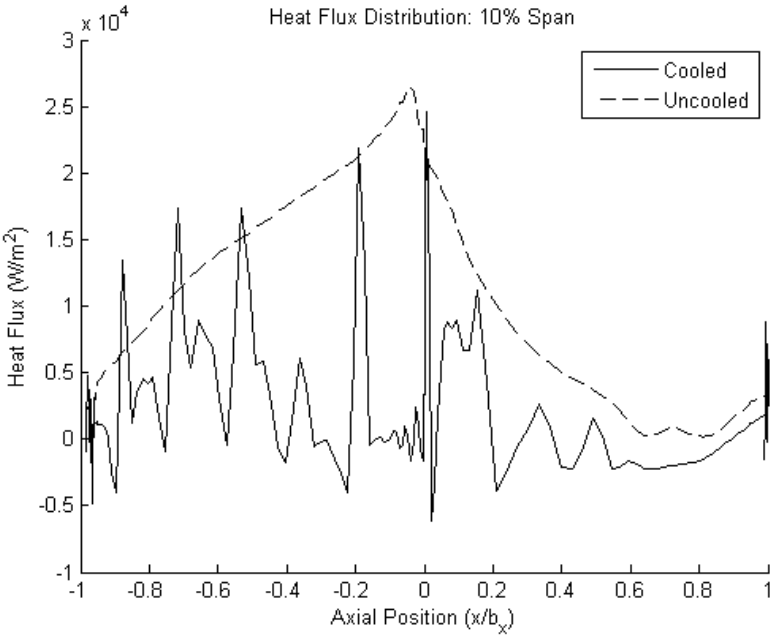

Figure 56 – Near-wall heat flux [W/m^2] distribution comparison with and without film cooling at 10% span.

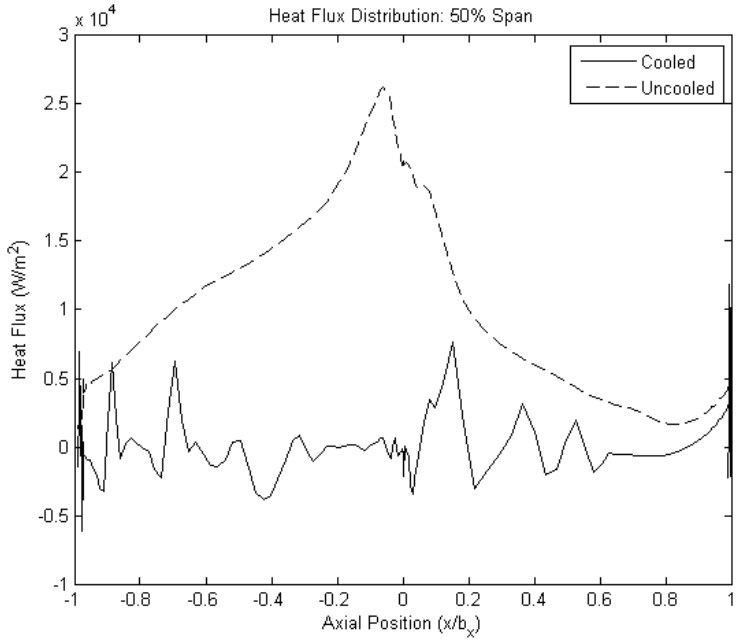

Figure 57 – Near-wall heat flux [W/m^2] distribution comparison with and without film cooling at 50% span.

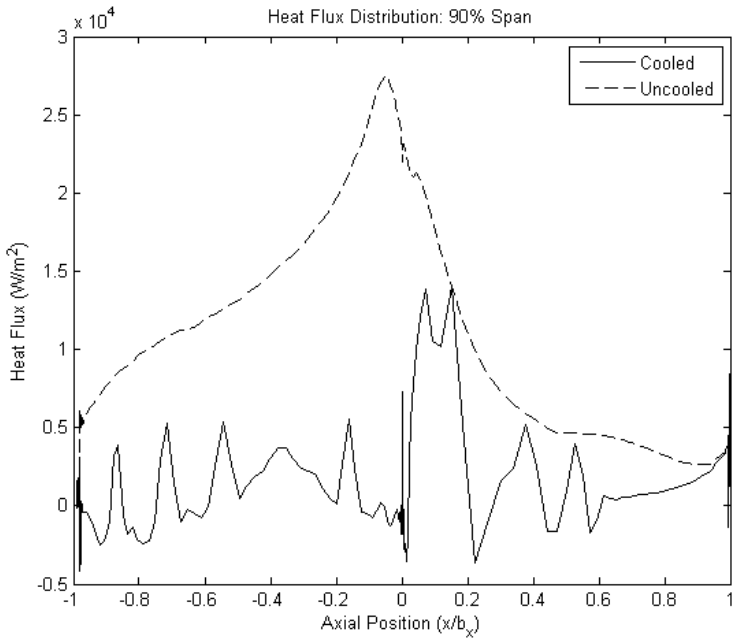

Figure 58 – Near-wall heat flux [W/m2] distribution comparison with and without film cooling at 90% span.

RTV PS Film Cooling Array Optimization

Optimization Results

Baseline Cooling Array Configuration

The transpiration boundary condition treatment for the film cooling flux at the surface and how it interpolates the locations of cooling holes at the surface is given in Figure 59. The figure shows how the CFD views the cooling holes at the surface grid cells. As explained in the methodology, due to the high level of surface grid coarseness, while the wall-normal grid density is very high, discrete cooling holes on the pressure surface cannot be distinguished for the most part with only 2 or 3 grid cells per cooling hole, but the orientation of injection, locations, patterns and sizes of cooling features are still captured.

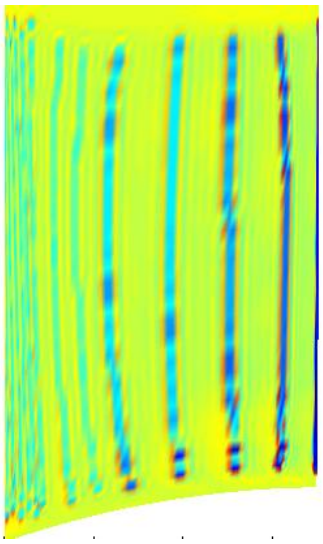

Figure 59 – Locations of cooling holes for baseline configuration as determined by transpiration boundary condition interpolation. The LE is on the left and TE is on the right.

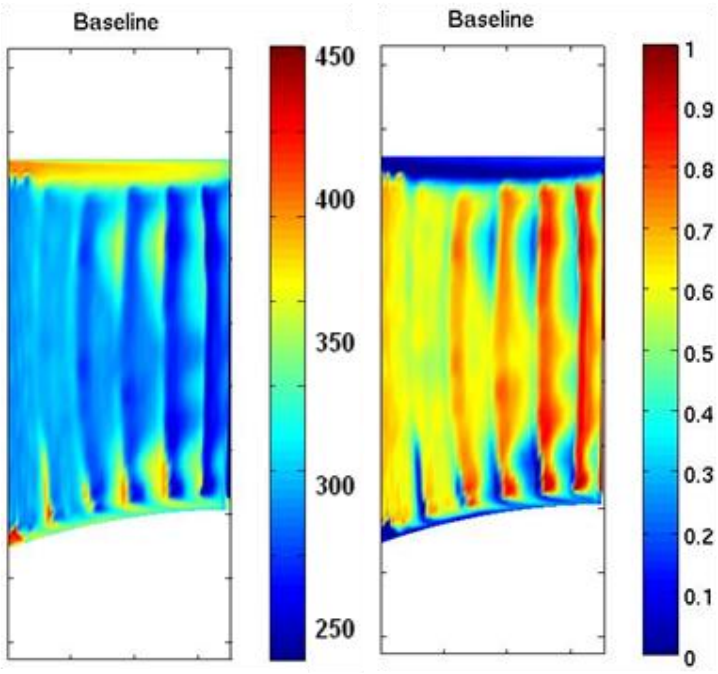

Figure 60 – Contour plots of near-wall gas temperature [K] (left) and local near-wall overall effectiveness (right) due to a baseline cooling design. Flow goes from left to right.

Contour plots of $T_{\infty,nw}$ as defined in the methodology (left) and near-wall overall effectiveness (right) for the RTV baseline cooling configuration as a result of the 3-D RANS CFD simulation with the design flow conditions is given in Figure 60. These are the same contour plots with film cooling as seen before, except these simplified views were used to conduct fitness calculations in the optimization process. One difference is that flow goes from left to right, instead of right to left. With near-wall gas temperature ($T_{\infty,nw}$), blue is cooler. With the near-wall overall effectiveness plot, red is cooler. The 3-D nature of the flow over the PS of the vane can be seen in the features captured near the ID and OD, which are both very hot relative to the rest of the surface. The OD region is the biggest problem area in terms of near-wall gas temperatures and received a lot of attention in the optimization. The design process did not allow for the addition of cooling holes outside the lateral extents of the baseline design. That is one lesson to take towards a second effort at the optimization, although the optimization still accounts for necessary cooling array changes between the hub and about 90% span. Hot spots in the temperature contour also appear just upstream of cooling hole rows from about mid-chord to the TE. This phenomena of hot spots just upstream of cooling hole rows that grow towards midspan getting closer to the TE is also regularly seen in conjugate heat transfer full-grid CFD simulations of the cooled the RTV. This lends credibility to the use of the j=10 grid cell level in the fitness evaluation process. Clearly, the overall effectiveness is very close to unity at the location of cooling air injection with decreases on the surface farther downstream until another row of cooling holes is reached. It can be seen that $T_{\infty,nw}$ characteristics are generally the opposite of near-wall overall effectiveness, as seen in the OD region where the temperatures are high and the cooling effectiveness is low.

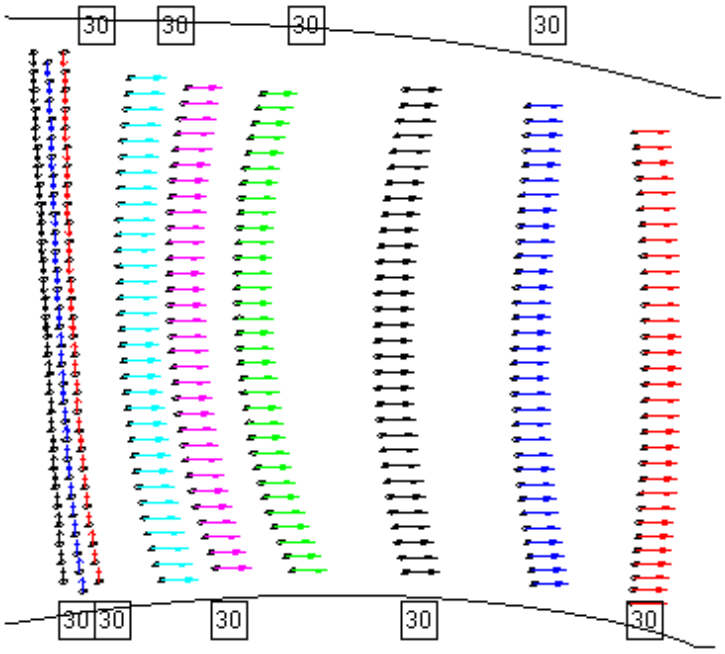

Figure 61 – Vector plot for RTV the baseline cooling array configuration showing axial compound angles, constant injection angles, and midpsan-oriented showerhead injection (flow is left to right).

Vector plots were used between generations for visual assurance that cooling configurations generated from the optimizer were realistic and lie fully within the pressure surface of the vane. These plots also indicate the direction of cooling injection in the surface plane, or the compound angle, for each cooling hole. Figure 61 is the vector plot for the RTV baseline cooling configuration. The numbers in boxes on the plot indicate the injection angle in degrees for each of the nine rows on the PS. If the numbers in boxes is 55 or greater (not the case for Figure 61), this number represents the injection angle in degrees for the outer half of the span, then subtract 35 degrees to get the injection angle for the inner half of the cooling hole row. The inner half is the area between 25% and 75% span locations on the vane. The reason for this option in the optimization is the knowledge that the baseline array has high temperature regions at the

ID and OD, and that higher injection angles will best cool these areas. The baseline cooling design does not vary injection angle over the span, as seen in the plot, and all compound angles are oriented axially, making it a simple design. The baseline cooling design is obviously a function of a simple correlation to predict heat transfer on the surface as cooling features do not change over the span of the PS and rows of holes are evenly spaced in the axial direction.

Optimized Cooling Array Configuration

After 13 generations of cooling array designs for the RTV surface geometry and design-level flow conditions, the optimized design was chosen. Figure 62 is a vector plot of the optimized cooling design and Figure 63 are the contour plots for near-wall gas temperature and cooling effectiveness. The optimized cooling array has a number of unique features. Many of the nine rows (three showerhead and six downstream rows) employ the use of paired-crossover ("X"-shaped) compound angle injection. Many of the rows use compound angles toward the OD. Referencing Figure 30, the six row patterns determined by the optimization include: pattern 7 (1^{st} and 3^{rd} rows), pattern 28 (2^{nd} row), pattern 30 (4^{th} row), a mirror image of pattern 12 (5^{th} row), and finally pattern 6 (6^{th} row), which is a slanted row, but only very slightly. It does not appear to be so in Figure 62 because the slanted row is placed on a curved surface.

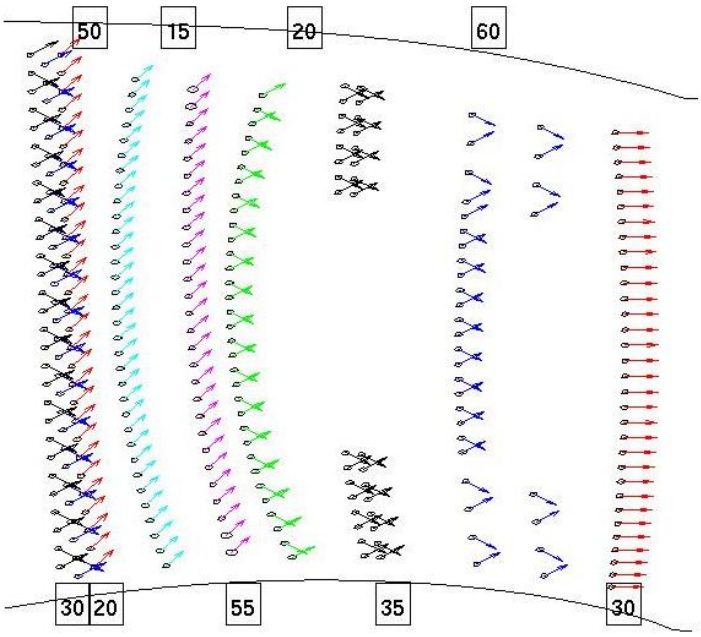

Figure 62 – Vector plot for the optimized cooling array showing the use of patterns, varying injection and compound angles in the GA optimization.

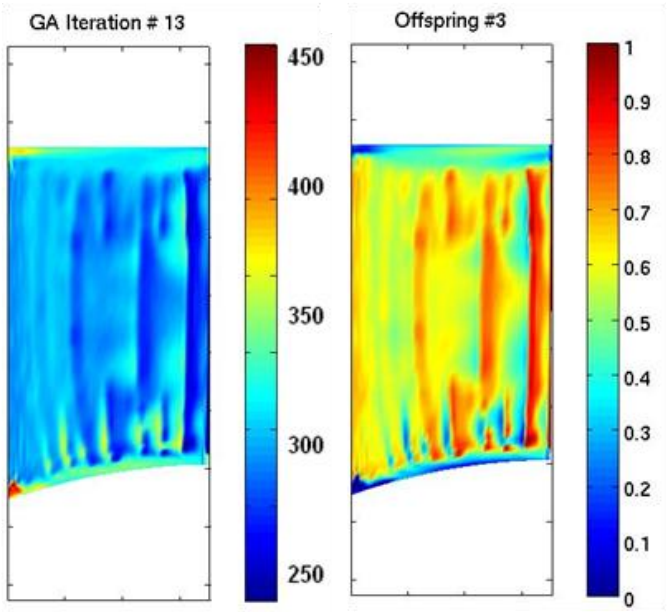

Figure 63 – Contour plots of $T_{\infty,nw}$ [K] and local near-wall overall effectiveness due to an optimized cooling design.

Clearly, the optimization resulted in a redistribution of cooling away from the midspan region where on the baseline vane cooling air accumulates due to the midspan-oriented showerhead array. The optimized cooling array in includes a number of unique features: paired-crossover compound angles for the 1st showerhead row, 3rd, 4th, and 5th downstream rows; high α injection at the ID and OD for the 2nd showerhead row (50º), 2nd downstream row (55º), and 5th downstream row (60º); compound angles directed towards the OD for the 2nd and 3rd showerhead rows and the 1st and 2nd downstream rows; and a limited need for cooling in general for the middle half of the span after the 50% axial chord. The injection of cooling flow toward the OD to counter the uncooled hot streak can be seen in Figure 63. Comparing Figure 60 and Figure 63, these trends are also apparent. The optimized cooling array used five different patterns for the six downstream rows, each with their own amount of axial and radial variation based on the allowable dimensions for the optimization. Rows also appear to alternate axially between high and low α, which is likely an added benefit. The optimized design spreads out the film cooling coverage over the vane PS and avoids large hot areas. The overall hot-to-cold near-wall gas temperature extremes are significantly reduced through optimization as well. Lastly, even with the 4th row of cooling holes on the PS lacking midspan holes, the existing cooling is sufficient to outperform the baseline array. The midspan area of the baseline design was therefore over-cooled. The traditional turbine durability engineer or designer might see an optimized design like this and say that such a design would never work in an engine because, perhaps, it does not look right. However, a 3-D inverse design optimization using RANS CFD shows that the optimized design is the best

available for the RTV PS. It seems reasonable based on what is known about the baseline design that a flow-governed cooling configuration would be so different.

Histograms showing the distribution of pattern selection by row are provided in Figure 64 and Figure 65 for the start and the end of the optimization, respectively. Pattern numbers can be referenced from Figure 30. Row 1 is just downstream of the leading edge cylindrical showerhead holes and Row 6 in near the trailing edge. In other words, increasing row number in the figures is closer to the leading edge. Figure 64 represents the pool of 100 parents in the first generation and Figure 65 represents the 100 children in the last generation. At the start, it can be seen that there is a very even distribution of patterns to work with in the first generation and there is no clear bias towards any pattern in particular. By the end of the optimization, it is clear that the optimization process has narrowed each vane PS cooling hole row to a handful of patterns that are useful in achieving proper prescribed fitness objectives based on the unique fluid physics at each location as simulated by the 3-D RANS CFD. Some rows, such as row 4, exhibited a tighter preference towards certain patterns than other rows.

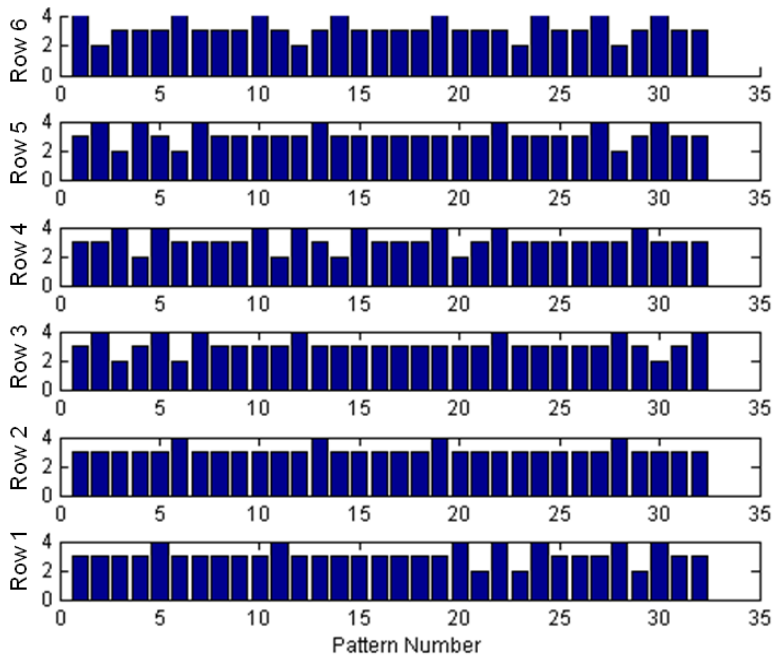

Figure 64 – Histograms showing the distribution of the 32 film cooling row patterns for the six modified rows on the vane PS at the start of the optimization.

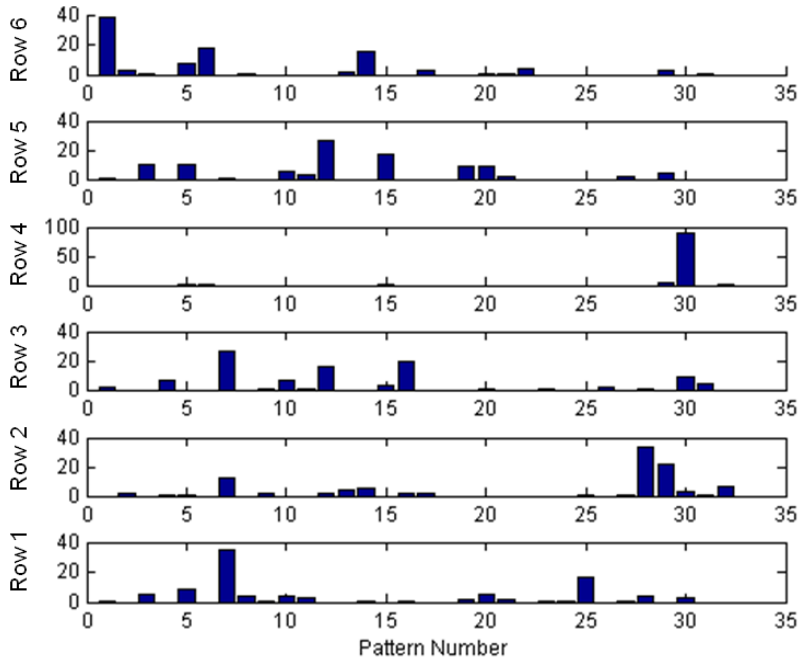

Figure 65 – Histograms showing the distribution of the 32 film cooling row patterns for the six modified rows on the vane PS at the end of the optimization.

The last result of interest is the behavior of all genomes in each generation in terms of fitness values. Figure 66 is the relative ordered fitness for all 13 generations in

the optimizations normalized by the first population. The obvious trend is that given more generations, the fitness levels will asymptote towards some maximum relative fitness level. The variation between genomes in a generation decreases with every new generation. So, as mentioned before, genomes become more alike as the optimization progresses. This is a phenomenon called elitism common to GAs. However, with more optimization, there are diminishing returns. For this reason, the process was terminated after 13 generations. This plot is intended to show the successful optimization, as there was a continual increase in average fitness, from 0.511 to 1.21, an improvement of 237% from start to finish. The fitness value of the optimized cooling design is 1.33, which is a 257% improvement over the baseline RTV cooling design fitness level of 0.518.

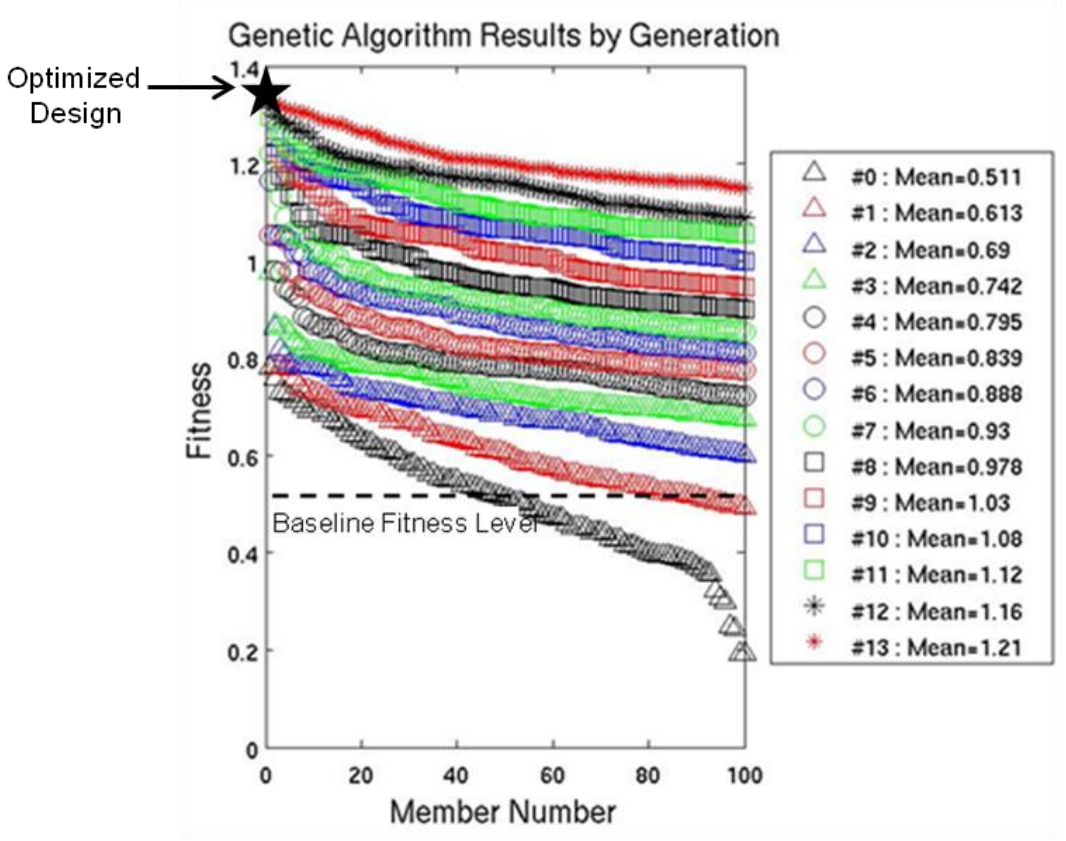

Figure 66 – Ordered fitness values of cooling design populations by generation with the pre-optimization baseline RTV fitness level highlighted.

Optimized vs. Baseline Cooling Comparison

Streamwise distributions of PS near-wall gas temperature (flow goes from left to right) are given in Figure 67 through 74 for the optimized and baseline cooling arrays. Looking at these plots, it can be seen how the optimization resulted in lower $T_{\infty,nw}$ at many PS locations and where it was determined that temperature could stay the same or even be allowed to increase. At 10% span, Figure 67, temperature spikes at approximately 20%, 50%, and 70% axial chord are decreased significantly. At 30% span, in Figure 68, the near-wall gas temperatures are overall cooler than the hub and the axial temperature changes are smaller in magnitude. This is one of the only locations that the optimization actually increased the magnitude of two high-temperature spikes by approximately 20 K. This is likely an area that was calculated to have an excess of cooling relative to the rest of the PS. At midspan, Figure 69, it appears that upstream of 50% axial chord, there is an excess of cooling as the optimized cooling case allows for an increase in temperature. Meanwhile, farther downstream, high-temperature spikes are suppressed. The same trend as for midspan can be seen for 70% span in Figure 70, except the reduction in $T_{\infty,nw}$ downstream of mid-chord is greater in magnitude. At 90% span, Figure 71, $T_{\infty,nw}$ is reduced in the optimized cooling array over most of the chord. Finally, at 95%, in Figure 72, it is obvious that film cooling has little effect here since cooling holes do not exist at this span location. However, due to the optimized cooling pattern that emphasizes OD-directed film cooling, there is a large drop of 50 K over most of the axial length. At most span locations, the local peak near-wall gas temperatures are reduced between cooling hole rows, while the local minimums are either maintained or increased. This is a result of a more even spreading of film cooling over the PS.

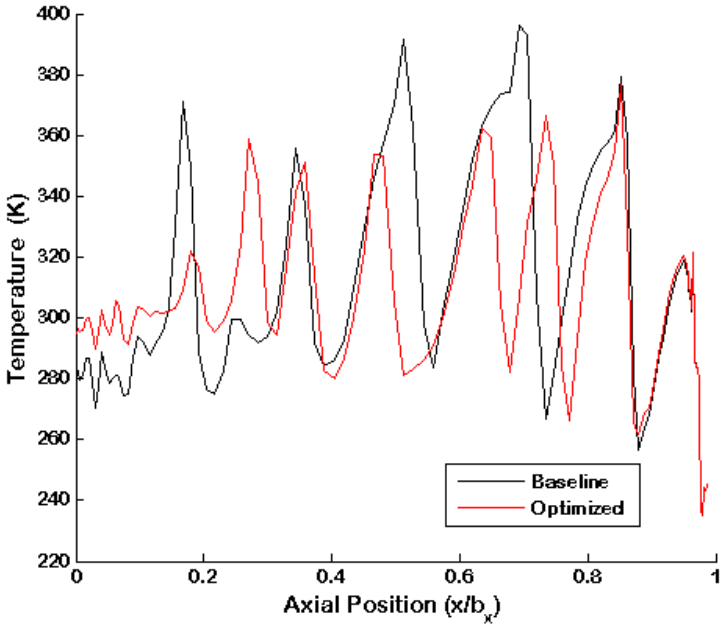

Figure 67 - Streamwise $T_{\infty,nw}$ comparison between optimized and baseline PS cooling arrays at 10% span.

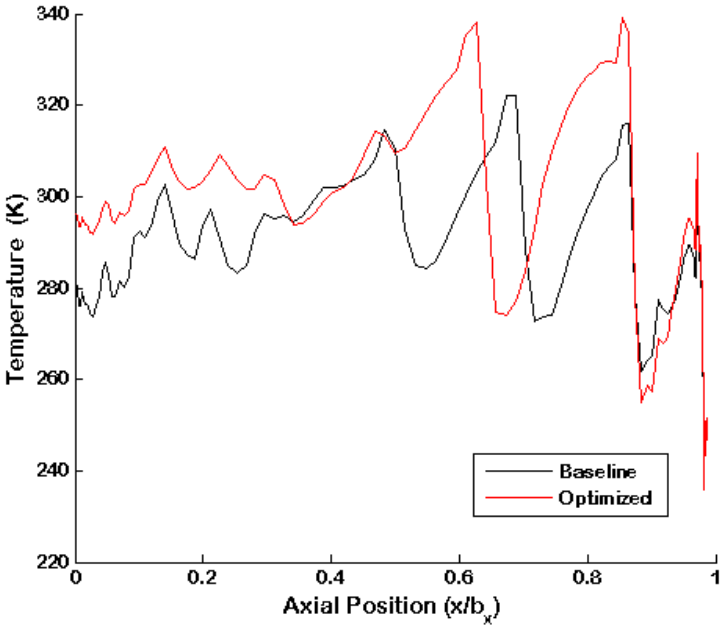

Figure 68 - Streamwise $T_{\infty,nw}$ comparison between optimized and baseline PS cooling arrays at 30% span.

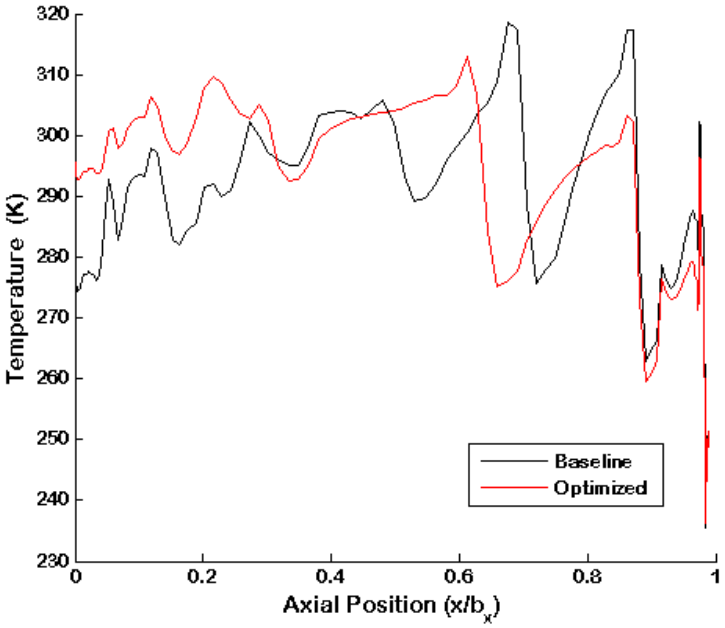

Figure 69 - Streamwise $T_{\infty,nw}$ comparison between optimized and baseline PS cooling arrays at 50% span.

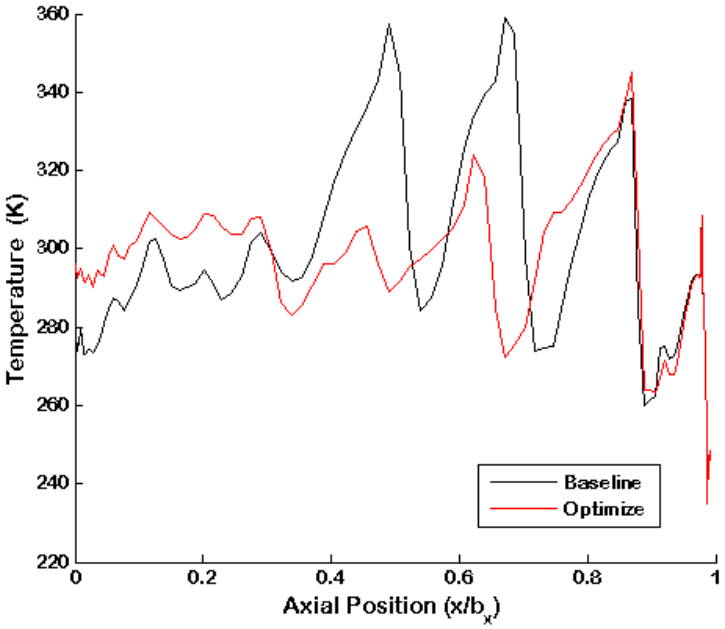

Figure 70 - Streamwise $T_{\infty,nw}$ comparison between optimized and baseline PS cooling arrays at 70% span.

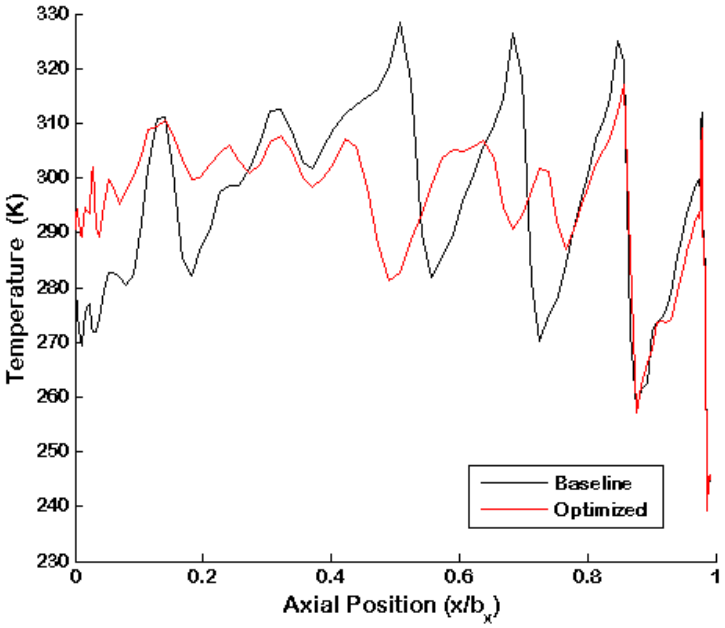

Figure 71 - Streamwise $T_{\infty,nw}$ comparison between optimized and baseline PS cooling arrays at 90% span.

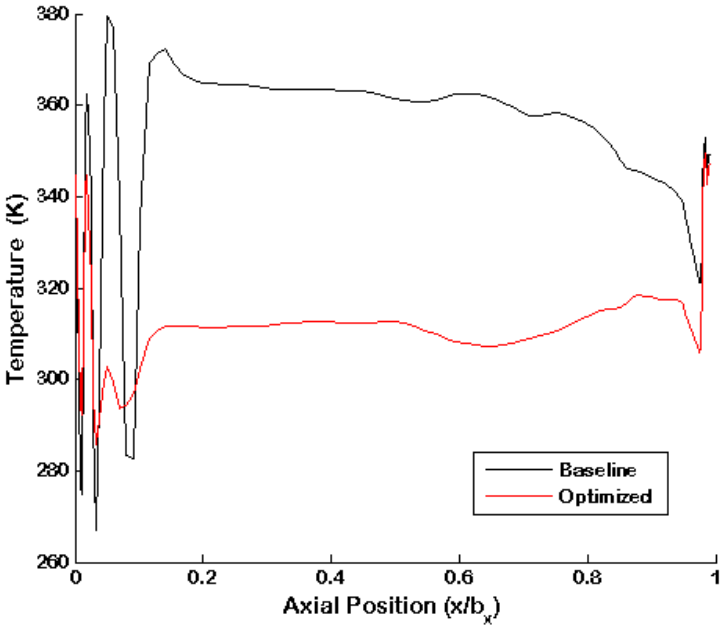

Figure 72 - Streamwise $T_{\infty,nw}$ comparison between optimized and baseline PS cooling arrays at 95% span.

Figure 73 is a contour of the near-wall gas temperature difference between the optimized film cooling array and the baseline cooling array. This kind of plot is useful as it takes into account contributions of both designs. Here, flow goes from right to left. This means the darker blue and black areas (negative values) underwent the greatest drop in temperature. Clearly these areas were at about 50% and 70% axial chord across the span, as well as nearly the entire shroud (OD) region. These areas are coincident with hot spots seen in Figure 60. Meanwhile, small increases in $T_{\infty,nw}$ are exhibited by the optimized cooling array mostly near the leading edge across the majority of the span length. Other small increases in $T_{\infty,nw}$ were a result of the redistribution of cooling past mid-chord just downstream of film cooling hole rows. Interestingly, much of the surface exhibited no change in near-wall gas temperature due to the optimized design.

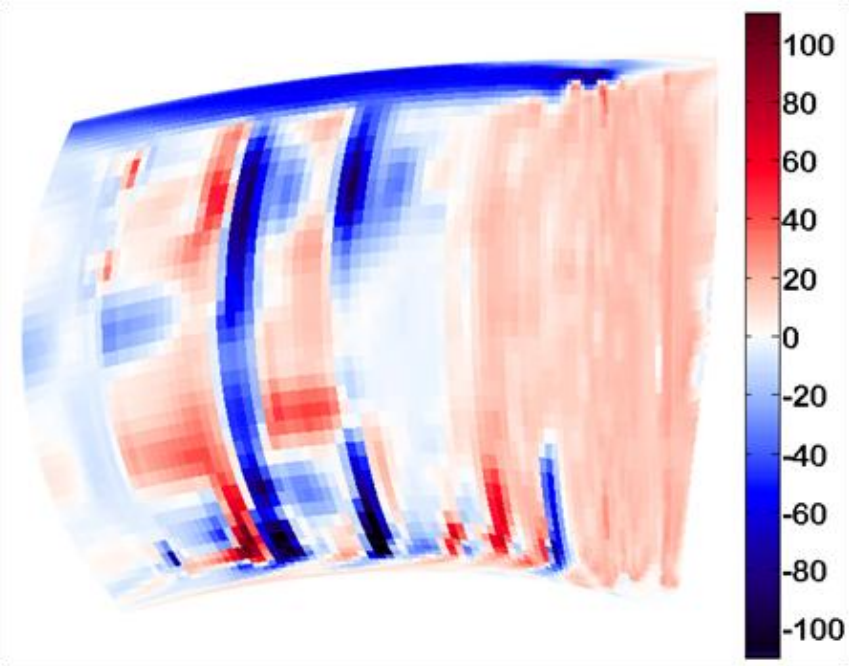

Figure 73 - PS contour of $T_{\infty,nw,\text{optimized}} - T_{\infty,nw,\text{baseline}}$ [K]. Flow goes from right to left.

Figure 74 through Figure 79 are streamwise distributions of near-wall heat flux, *q"*, for the baseline and optimized cooling arrays. This value is calculated using the difference in temperatures between the 10^{th} and 11^{th} grid cells normal to the vane surface in the CEEF CFD, along with the thermal conductivity of air due to the average of the temperatures. As stated in the methodology, using this grid location (2.79e-5 meters from the vane wall) for assessment of heat transfer characteristics is effective for distinguishing near-wall gas temperature for isothermal CFD cases. The near-wall gas temperatures in Figure 67 through 74 are also obtained at this 10^{th} wall-normal cell location, which is the location at which temperature characteristics were optimized.

First, it can be seen in comparing these plots to the near-wall gas temperature plots, the trends are very similar, but there are some subtle differences. One of the differences is that *q"* between the two designs near the leading edge for 30%, 50%, and 70% span locations are at about the same level, unlike $T_{\infty,nw}$, which is slightly higher for the optimized array. This is possible by having a higher temperature closer to the freestream for the optimized relative to the baseline design. So, for the optimized design, $T_{\infty,nw}$ increases, but heat flux is kept at the same level. For the 95% location, reduction in heat flux decreases with axial distance while the $T_{\infty,nw}$ reduction is fairly constant, meaning that with the baseline design, there is less cooling and a higher driving temperature towards the freestream compared to the optimized design. Overall for heat flux, the same general streamwise cooling improvements seen for temperature are seen at 10%, 50%, 70%, 90%, and 95% percent span locations.

Second, the values of *q"* are centered at zero and can be negative due to the isothermal condition set in the CEEF CFD. With cooler air being injected over surfaces

set at higher temperatures, naturally, *q"* can be negative. Additionally, in blowdown rig tests, depending on the part of the airfoil, there is not always a well-behaved wall-normal temperature gradient from hot gas to cold walls. Past work has shown that negative *q"* can be measured experimentally and is physically accurate [170]. While these particular values of *q"* from the CFD at 10 grid cells from the wall are not intended for direct validation with experiments, they are sufficient in showing relative simulated heat flux trends between the baseline and optimized cooling designs.

Lastly, unlike for temperature comparisons, local heat flux maximums are mostly reduced, while local minimums are either maintained or decreased. This is especially true at 70% and 90% span locations. Therefore, not only are average heat flux levels reduced for some span locations, but also the magnitude of the change in heat flux between cooling rows with respect to the axial direction.

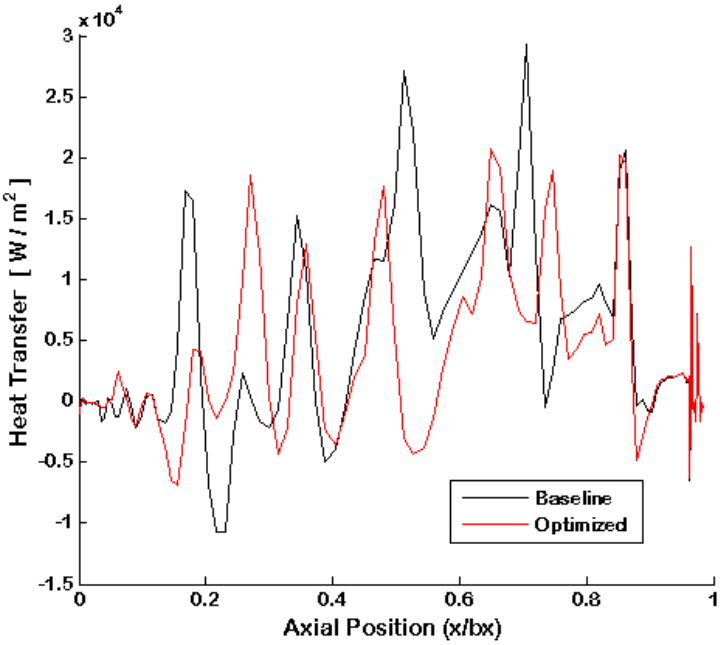

Figure 74 - Streamwise near-wall heat transfer comparison between optimized and baseline PS cooling arrays at 10% span.

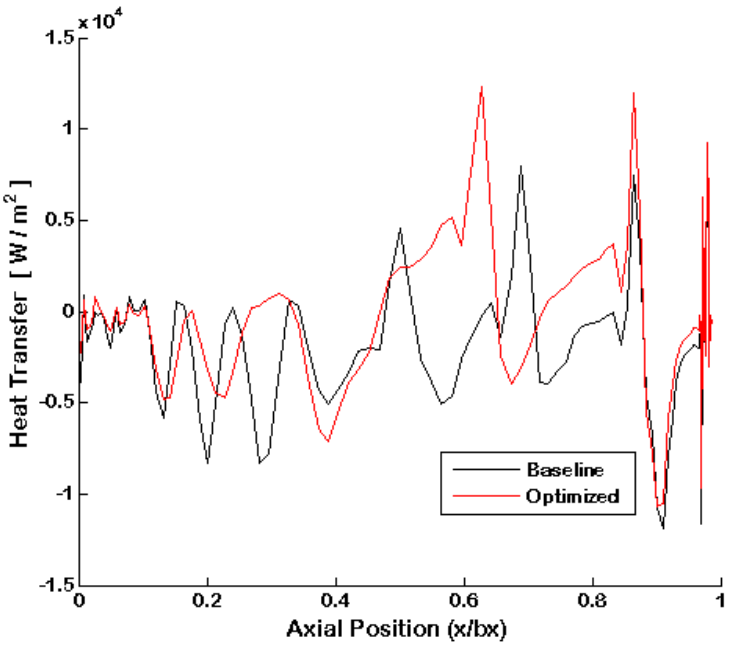

Figure 75 - Streamwise near-wall heat transfer comparison between optimized and baseline PS cooling arrays at 30% span.

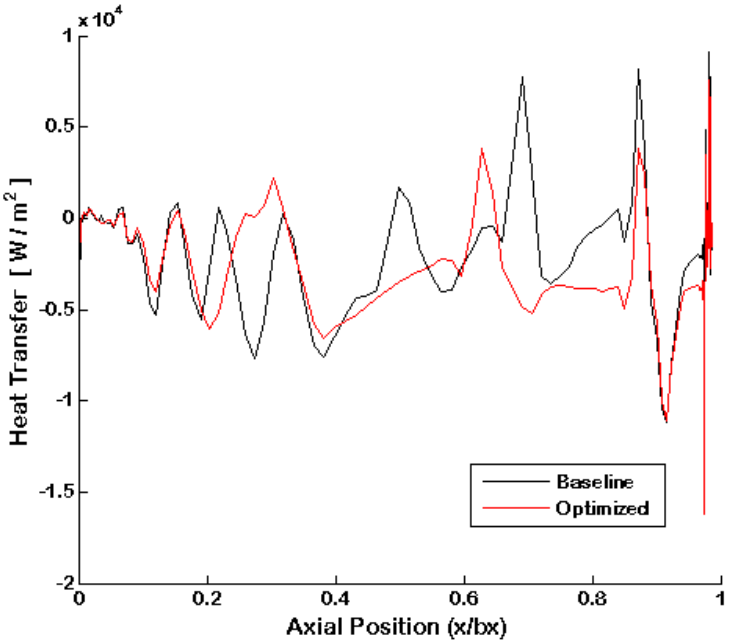

Figure 76 - Streamwise near-wall heat transfer comparison between optimized and baseline PS cooling arrays at 50% span.

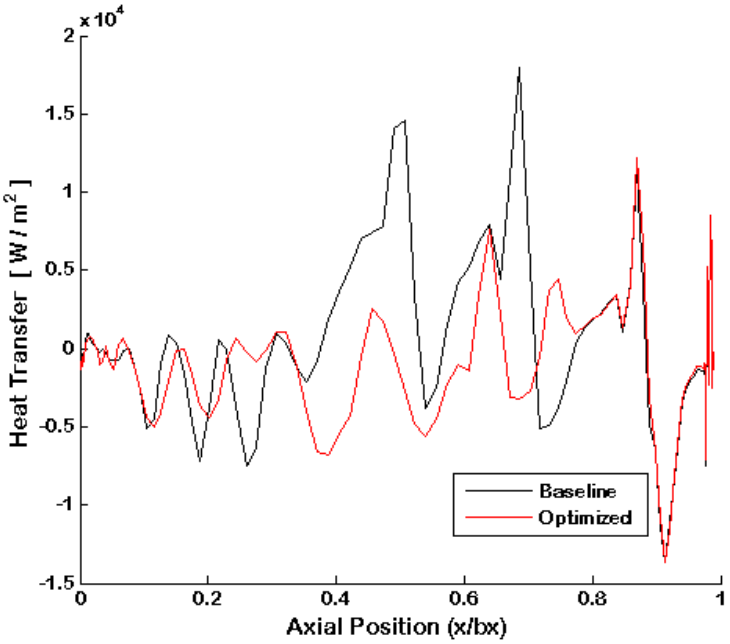

Figure 77 - Streamwise near-wall heat transfer comparison between optimized and baseline PS cooling arrays at 70% span.

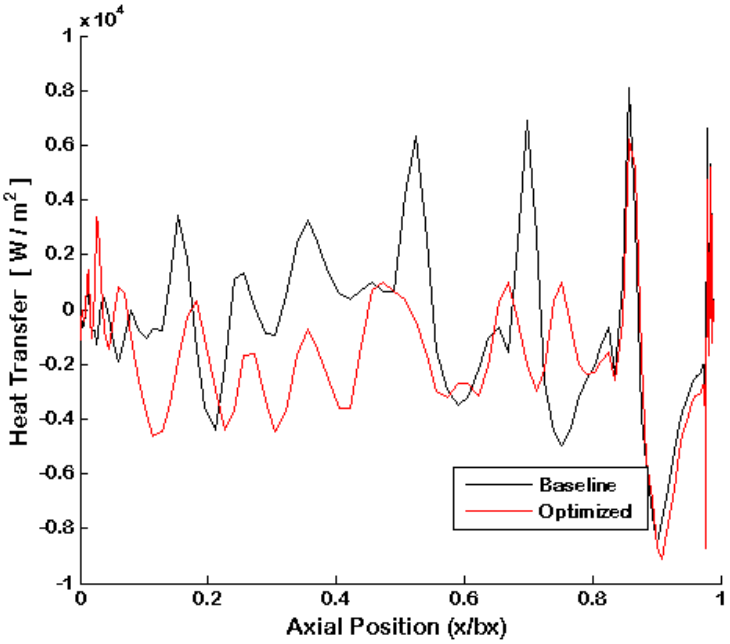

Figure 78 - Streamwise near-wall heat transfer comparison between optimized and baseline PS cooling arrays at 90% span.

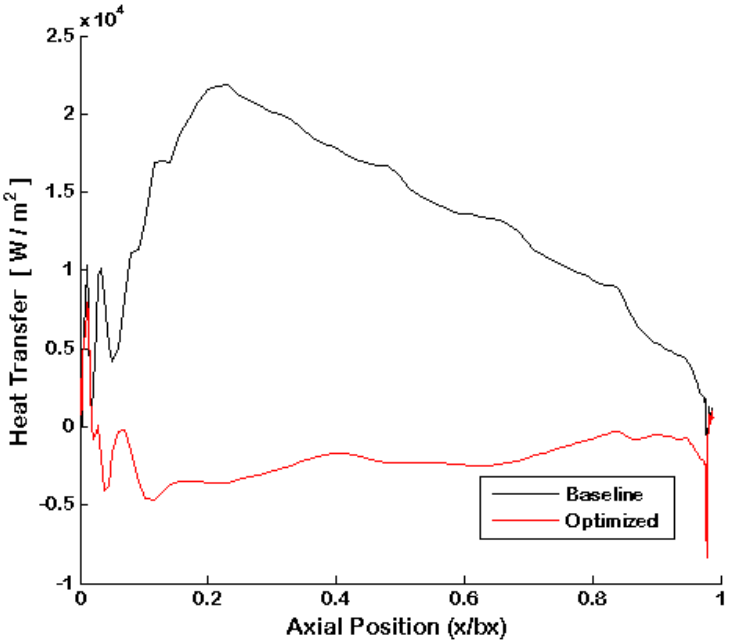

Figure 79 - Streamwise near-wall heat transfer comparison between optimized and baseline PS cooling arrays at 95% span.

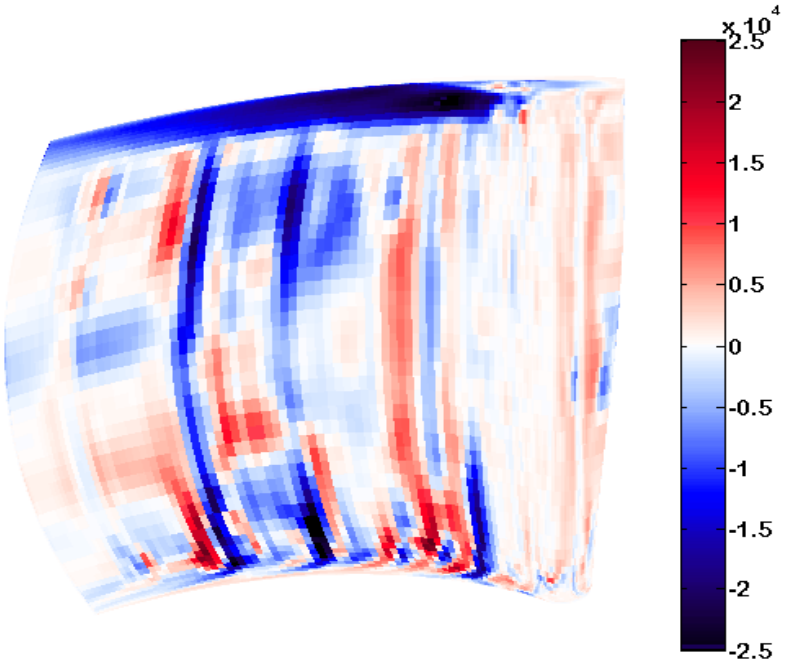

Figure 80 - PS contour of near-wall ($q''_{optimized} - q''_{baseline}$) [$W/m^2$]. Flow goes from right to left.

Figure 80 is a contour plot for every PS grid cell of the heat flux difference between the optimized and baseline film cooling arrays. Like Figure 73, the darker blue and black areas signify improved cooling performance. The beneficial *q"* differences appear to mostly match $T_{\infty,nw}$ differences in Figure 73, except for in the leading edge area. There is little change in *q"* for the first 25% of axial chord up to a point where heat flux is allowed in the optimized case to increase over most of the span, especially near the hub. This area is therefore deemed to have an excess of cooling for the baseline design. The area downstream of 75% axial chord also appears to be neutral in terms of *q"* changes as well. Most heat flux changes occurred near midchord and, like near-wall gas temperature, at the shroud (OD).

Figure 81 through Figure 83 are streamwise distributions of near-wall overall effectiveness based on $T_{\infty,nw}$ representing T_s at 10%, 50%, and 95% span locations, respectively. The improvements in ϕ_{nw} are not as dramatic as they are across the surface for near-wall heat flux and temperature. Most improvement in ϕ_{nw} is seen near the leading edge, with little change at mid-chord and farther downstream, where peaks in this value are moved upstream, due to the new cooling geometry, rather than increased or decreased. As is observed by the other CEEF CFD trends, the overall effectiveness is increased dramatically near the shroud over most of the surface. In fact, ϕ_{nw} is nearly doubled. Since the area over which the optimization evaluated the fitness (cooling performance) over the PS was larger than the area covered by cooling holes in both cases, a lot of potential cooling benefit was expended in the optimization to cool this outer shroud region of the vane surface where cooling holes did not exist (and could not be placed outside of the extents of the baseline design). In future optimizations, with more

variability in cooling hole row radial placement limits, less effort can be expended in focusing on the OD region and more gains could potentially be seen in the midspan regions. Here, however, the optimization was still successful in improving overall cooling despite vast redistribution of cooling to the shroud. In span locations that exhibited reduced cooling performance, it likely means there was an excess of cooling for the baseline design, not that the optimized design is necessarily worse. Figure 84 is a contour plot of the percent change in ϕ_{nw} from the baseline to the optimized cooling array designs. It can be seen that this plot follows the trends seen in Figure 73 for $T_{\infty,nw}$, a substitute here for T_s, which is in turn part of the calculation for ϕ_{nw}.

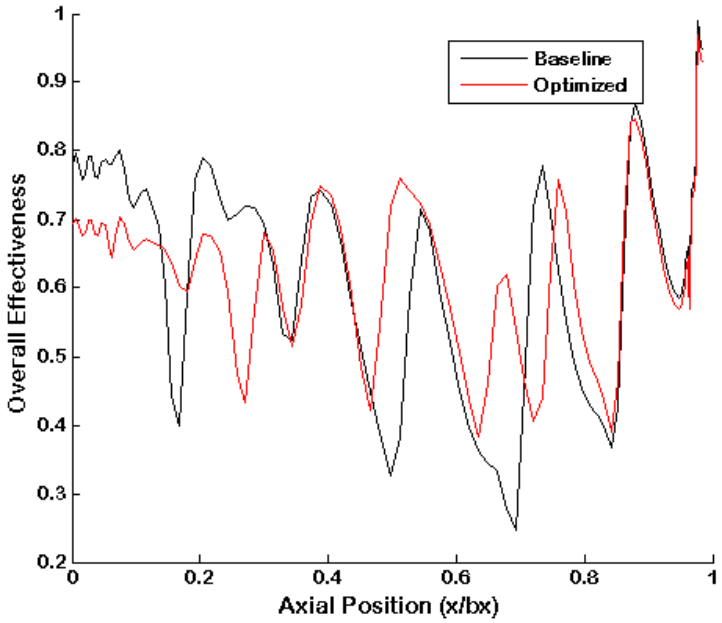

Figure 81 - Streamwise near-wall overall effectiveness comparison between optimized and baseline PS cooling arrays at 10% span.

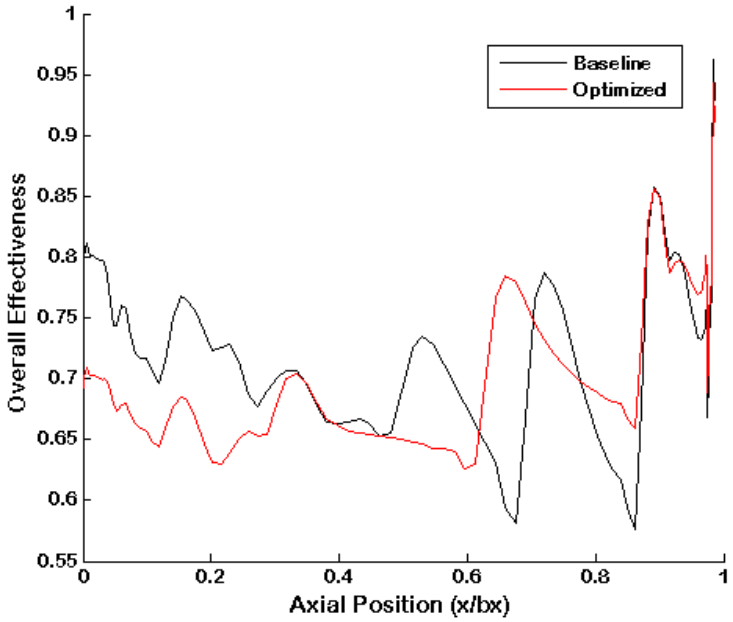

Figure 82 - Streamwise near-wall overall effectiveness comparison between optimized and baseline PS cooling arrays at 50% span.

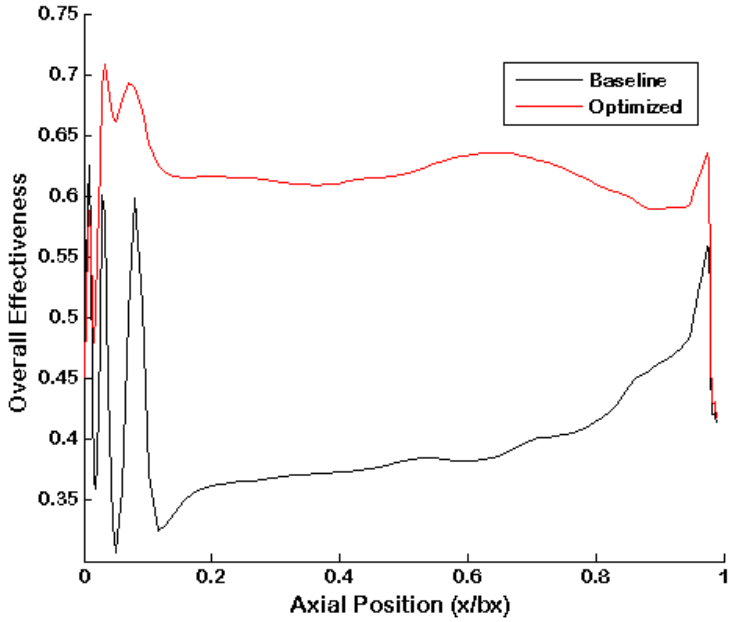

Figure 83 - Streamwise near-wall overall effectiveness comparison between optimized and baseline PS cooling arrays at 95% span.

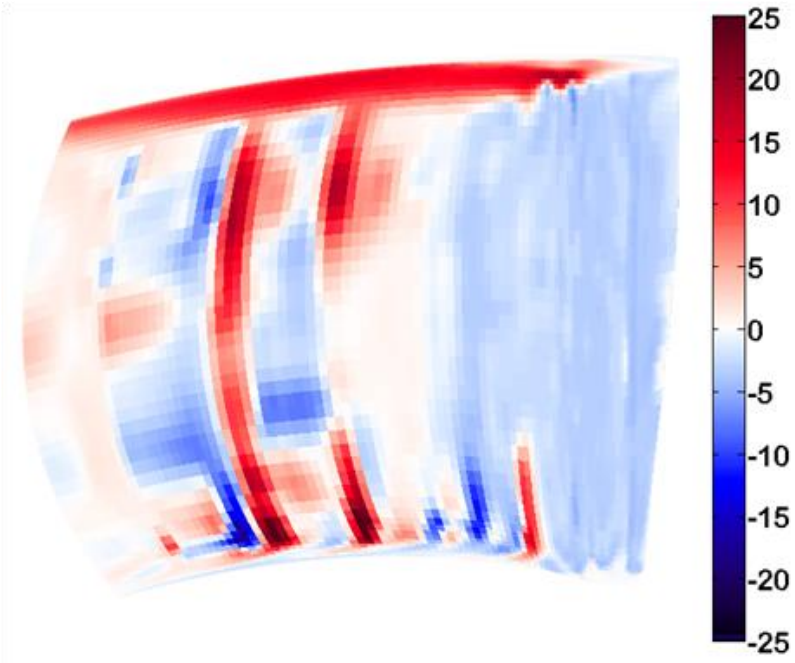

Figure 84 - PS contour of percent change in near-wall overall effectiveness between the optimized and baseline cooling arrays.

Finally, Table 10 is a list of values of near-wall heat transfer (q''), near-wall gas temperature ($T_{\infty,nw}$), and cooling effectiveness parameters for the baseline and optimized cooling designs. The area-averaged reduction in q'' is fairly significant. Minimum q'' increases and maximum q'' is reduced over the surface. The optimization decreased the overall amplitude of q'' spikes between local minimum to local maximum levels. $T_{\infty,nw}$ was decreased more so than ϕ_{nw} between designs as seen in the plots, however, the new cooling array worked well in redistributing cooling where it was needed most—in the shroud region. Surface-averaged ϕ_{nw} stayed fairly constant while maximum ϕ_{nw} actually decreased slightly. Knowing that pressure loss is important, the optimized cooling array allowed a slight decrease in loss from 4.887% for the baseline cooling array to 4.841% for the optimized array. The optimized cooling array ultimately resulted in a reduction of average near-wall gas temperature of 2 K, a reduction in the maximum near-wall gas

temperature of 3 K, a reduction in maximum heat flux of 2 kW/m^2 and a slight reduction in pressure loss over the vane, all while maintaining a constant level of area-averaged overall effectiveness. The optimization required approximately 12 hours of computational time per generation using 100 2.67 GHz CPUs, for a total of 156 hours, or just under one week.

Table 10 - Comparison of PS near-wall heat transfer parameters between the baseline and optimized cooling arrays.

	Units	Baseline	Optimized	Difference	% Change
q''_{aavg}	W/m^2	1,008.50	-620.10	1,628.60	-
q''_{min}	W/m^2	-26,411.00	-21,770.00	4,641.00	17.57%
q''_{max}	W/m^2	71,327.00	69,156.00	2,171.00	-3.04%
$T_{\infty,nw,aavg}$	K	304.37	302.08	2.29	-0.75%
$T_{\infty,nw,min}$	K	231.73	231.68	0.05	-0.02%
$T_{\infty,nw,max}$	K	438.09	435.28	2.81	-0.64%
$\phi_{nw,aavg}$	-	0.663	0.662	0.001	-0.11%
$\phi_{nw,min}$	-	0.128	0.124	0.004	-3.05%
$\phi_{nw,max}$	-	0.993	0.973	0.019	-1.93%

Implications of an Improved Film Cooling Array

Assuming the modern RTV baseline cooling scheme is acceptable, the use of the optimized cooling array at the same cooling performance level can result in the use of less cooling mass flow from the compressor in the operational environment. At the same cooling mass flow, the optimized cooling array reduced overall temperature over most of the surface of the vane, which would increase part life. This work assumes that simulated $T_{\infty,nw}$ fairly represents T_s. If higher engine thermal efficiency is desired, then decreasing cooling mass flow with the optimized cooling design is necessary. This is especially true

considering the combined effects of a full wheel of vanes with optimized cooling. Any engine efficiency gains become more profound if similar studies are performed for the blade wheel and second vane wheel.

For the current case, with a known proprietary RTV-specific level of cooling mass flow (m_{cool}) to the vane wheel, the design level of inlet temperature ($T_{t,4}$) and using the relation of Equation 28, a cooling mass flow savings can be calculated based on the improvement in average surface temperature for the optimized cooling array relative to the baseline.

$$m_{cool,opt} = Q_b / (c_{p,avg}(T_{t,4} - T_{surf,opt})) \tag{28}$$

Q_b is the baseline level of heat removal from the surface due to film cooling. Equation 28 can be used for the baseline levels as well in order to get a savings value. Since at different spans, the optimized cooling array resulted in different levels of improvement, there exists best case and more typical case levels of cooling mass flow savings. The best case occurs at 95% span where the OD-oriented flow in the optimized array was able to cool the shroud significantly. Assuming such a large temperature drop due to the optimized array, this would result in a savings of 40%. A more typical case for the whole vane PS as in this case is a savings of 2% cooling mass flow into the vane. Since the physical PS area of fitness evaluation was larger than the area on which cooling holes could be placed or moved, a limitation was put on the optimization. This was done in order to keep the lateral span of coverage of holes constant between the baseline and optimized arrays. In the case where the area where cooling features can be placed were equal to the area over which average values of surface temperature were taken, the surface-averaged cooling savings is expected to increase beyond 2%. With more spread

out film cooling due to increased freedom for hole placement and less OD-directed cooling, it is likely that the surface temperature over the remaining PS (not the shroud) would decrease slightly in an optimization. This would be one lesson learned from this work.

Assuming no changes to cooling mass flow requirements, and again assuming $T_{\infty,nw}$ fairly represents T_s, a reduction in average surface temperature as seen in Table 10 of a few degrees Kelvin would certainly increase part life. If a reduction of temperature of 50 K doubles part life [1], then even a small reduction 2 or 3 K is beneficial. Again, without the penalty of fitness evaluation area being larger than the area where holes can be placed, especially in the hot shroud region, this temperature drop would be larger over the PS. Also, an extra digit in the bit string could have handled more variability for compound angle such that only holes very close to endwalls direct cooling air toward the wall, rather than having the same compound angle for all the holes in a given row. Perhaps more importantly, the in-plane surface temperature gradients were reduced due to the more even spreading of cooling as seen in temperature contours. Also, the wall-normal temperature gradients are reduced as seen by the improvements for heat flux. Bunker [9] has stated that not only is the level of temperature important when considering the fatigue on a component, but also the thermal gradients as well. The effect of thermal gradients combined with structural fatigue is a well documented phenomenon. In application, combining an optimized cooling array with more complex internal impingement cooling, thermal barrier coatings and temperature resistant materials would further increase part life.

VI. Results of Flat Plate and RTV Comparison Using CHT CFD

Before going into the results of the film cooling experiments using infrared thermography, the use of a flat plate to model pressure side cooling performance in experiments will be justified. First, in terms of experiments, IRT flat plate runs are less expensive and more repeatable than full scale blowdown rig runs on the 3-D Research Turbine Vane in the AFRL Turbine Research Facility. While the testing the RTV cooling performance in the TRF allows for discrete data points of heat flux and certain span locations and axial locations, infrared thermography provides full-map surface temperature distributions. As outlined in the methodology, as long as coolant-to-mainstream total temperature and pressure ratios are matched between the rigs, IRT experiments are sufficient in assessing PS film cooling heat transfer characteristics.

Preliminary CHT CFD Studies

Prior to relying fully on the CHT CFD results, much had been accomplished with the authors of the *Leo* code at Aerodynamic Solutions (ADS), Inc. The Turbine Branch of the Aerospace Systems Directorate was charged with the responsibility of maturing the new code as well as perform stress tests to ensure its accuracy and robustness. Most of this preliminary work was done using the RTV geometry; however, results from the flat plate geometry for the PS film cooling models were shared with ADS as well. Initially, work was done to ensure proper boundary condition tagging for the RTV domain. A core flow inlet, hub cooling inlet, core flow outlet, and a shroud cooling inlet were generated to establish flow coming in and out of the RTV domain for the cooled case.

Another study was conducted on the actual vane geometry itself, in which it was found when the hub and shroud attachments were geometrically simplified, the computational time was greatly reduced. Naturally, with more complex shapes, many more grid cells are necessary in the fluid and solid to accommodate them. These attachments were ultimately assigned adiabatic boundary conditions. This also helped isolate the cooling flow inlets, since the real vane has more holes for instrumentation and bolts, etc. The fact that the fabrication-ready RTV shapes generated by Florida Turbine Technologies, Inc. were much more complex and different than what needed to be simulated in CHT CFD was a source of particular effort by ADS and AFRL. Not only were the attachment features very different, but the fabrication-ready part was not periodic in shape. One tangential side of the real physical vane is not exactly the same size as the other, which would restrict truly periodic tangential conditions. Lastly, the CAD drawings showed a slight twist inside film cooling holes between the constant diameter portion and the expanded portion for all (hundreds of) shaped holes. These each had to be adjusted in order to ensure a smooth surface inside each film cooling passage. The shaped cooling holes in the CAD drawings also exhibited a square cross section, which was done in order to save file memory. The EDM drill would recognize the extents of these squares as the preferred diameter of the circles to be drilled out on the physical part. For CFD purposes, all of these square-cross-section holes were rounded out to ensure proper simulation accuracy, which led to significantly large mesh file sizes (over 1 GB per file).

Looking at thermal response times, the fluid response times was five orders of magnitude different from the solid response times. While this is expected knowing the

relative thermal conductivity, this is important when considering convergence for each case as well as the initial temperatures to set the solid to for each run. Both hot and cold metal initiation temperatures were tested and confirmed to run to a steady level of exit mass flow and exit main flow temperature after 30,000 iterations. In addition, a study found that heat flux was highly sensitive to initial wall temperature and inlet turbulence settings. The best heat flux match with data was achieved using the top gauge from a heat flux gauge pair (Appendix C) rather than embedded thermocouples. It was also found that TRF conditions on the vane surface are more laminar than turbulent, with some transition near the TE.

Concerning convergence, it was found that the simpler uncooled case would not converge as quickly as the case with film cooling holes. In experiments, cooling flow is pumped into the plenums of the uncooled vane and then allowed to leak out at various locations including holes for instrument access. At first, the uncooled cases would not converge at all, even after 80,000 iterations. This is because there was no cooling outlet assigned to the uncooled vane. This caused the buildup of cooling inside the uncooled vane which allowed no escape for cooling air. Surface temperatures would continue to decrease without a lower limit. To alleviate this, seepage at the level observed by cooling flow measurements in the TRF blowdown rig was assigned as a cooling outlet condition. This allowed the cooling flow to cycle through and the solution to converge. Interestingly, the more complex case with 648 film cooling holes converged more readily at 30,000 iterations due to the outlet of cooling flow forming a steady state problem. Ultimately, this number of iterations was deemed appropriate for all CHT CFD runs.

As most of the runs presented here use a wall function, resulting in a y^+ value of ~20 and about 10 prism layers for the boundary layer, work by ADS found that another term must be introduced to make wall functions more accurate. In most CFD, resolution of pressure phenomena and turbulent eddies near the wall are of importance at the expense of heat transfer gradients. To enforce accurate heat transfer gradients, a non-dimensional T^+ term was assigned as seen in Equation 31 to calculate near wall temperature and heat flux. Since y^+ and u^+ are a part of the overall formulation, these are given in Equations 29 and 30, respectively.

$$y^+ = \rho * y * u_\tau/\mu \tag{29}$$

$$u^+ = u/u_\tau \tag{30}$$

$$T^+ = (T_w - T) * \rho * c_p * u_\tau/q" \tag{31}$$

The term u_τ is the friction velocity (equal to $\sqrt{(\tau_{wall}/\rho)}$), while ρ is density, τ_{wall} is shear, c_p is heat capacity at constant pressure, y is the normal distance of the first node away from the wall, μ is dynamic viscosity, q'' is the near wall heat flux, T is the near wall temperature, and u is the near wall velocity. Log-layer equations for y^+ between 15 and 300 were used to get values of u and T. After accounting for T^+, it was found that heat flux spikes were reduced by a factor of three and running a wall function as specified above against a wall integration case (y^+ = 2, prism layers = 20) shows very similar results for the same number of iterations. Ultimately, using a wall function requires less computational time. Other studies perfected the TRF measurements used as boundary conditions for cooling, but overall, due to these studies, the CHT CFD simulations were deemed to be reliable for the intended purposes.

Uncooled RTV

Looking at vane without film cooling, surface temperature and heat flux contours are given in Figure 85 through Figure 88 for both the PS and SS surfaces. The contour limits are set such that they are the same as future contour plots with film cooling so they could be directly compared. The temperature contours show high temperature areas on the PS near the LE downstream closer to the TE. While not of interest to the optimization, SS temperatures are fairly constant over the whole uncooled surface. On both the PS and SS, a low temperature region emanates from both endwalls which is attributed to the build-up of secondary flow that is typical of vane flows. The lateral encroachment of secondary flow grows slightly with axial distance on the SS, while on the PS it appears to have less of an effect towards the TE. This is likely due to the difference in axial pressure gradients across the length of the vane. Except at the endwalls, the PS temperatures are fairly constant across the lateral span.

Figure 85 is not meant to match the CEEF CFD results for the vane PS. As previously seen in Figure 45, near-wall gas temperature was given for the uncooled vane PS as it was the primary driver for the optimization. Here, true surface temperature is given and naturally with a full-grid solid conduction simulation, the result is going to be quite different. Since these two figures show fundamentally different results ($T_{\infty,nw}$ versus T_s), assuming conjugate simulations are more accurate, it also cannot be said that the CEEF CFD cannot accurately approximate temperature on the PS. Results in Appendix B show the CEEF CFD matches most uncooled experimental data on the PS.

SS temperatures are generally higher and very close to freestream temperatures. The location of the spar that separates the two cooling plenums inside the vane can be

seen on the SS where there are distinct points of lower temperature at the same axial location stemming from the endwalls. This is due to the increased metal thickness and thus added conduction at these locations. Closer to midspan, the main flow temperatures become too high for this effect to be seen. This is one of the major advantages of CHT CFD, being able to see what lies beneath the surface of interrogated objects, much like an x-ray. It also shows the necessity for CHT CFD assessments and the effect of adding solid conduction to a given CFD problem.

The heat flux contours in Figure 87 and Figure 88 indicate less surface variation relative to the surface temperature. Heat flux is slightly increased at the endwalls where more mixing is present. Clearly, there is a large positive value of heat flux into the vane due to the high temperature freestream and an adiabatic surface condition is irrelevant for realistic turbomachinery problems.

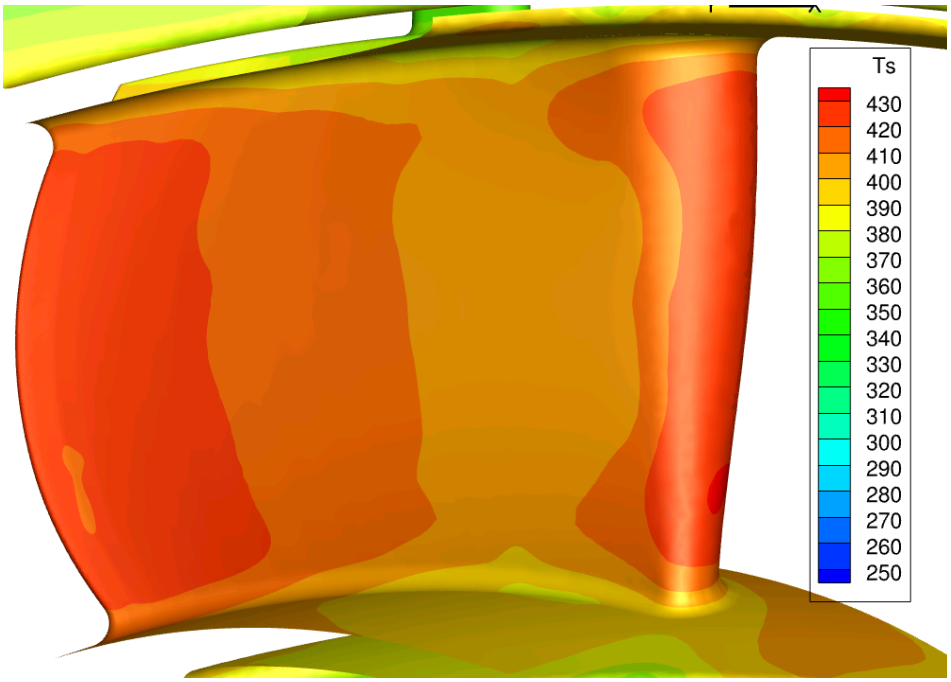

Figure 85 – Uncooled RTV surface temperature [K] contour for the PS.

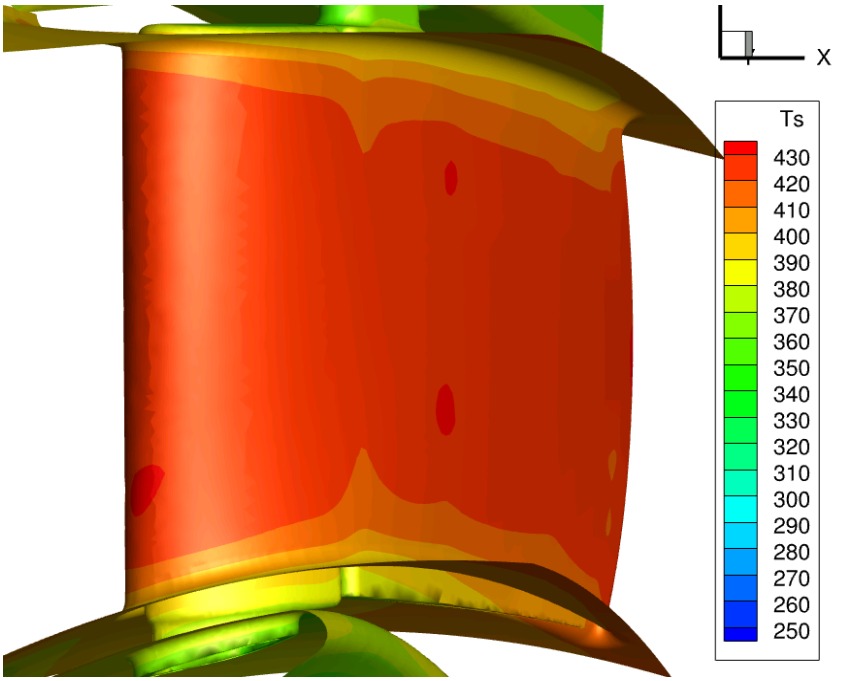

Figure 86 – Uncooled RTV surface temperature [K] contour for the SS.

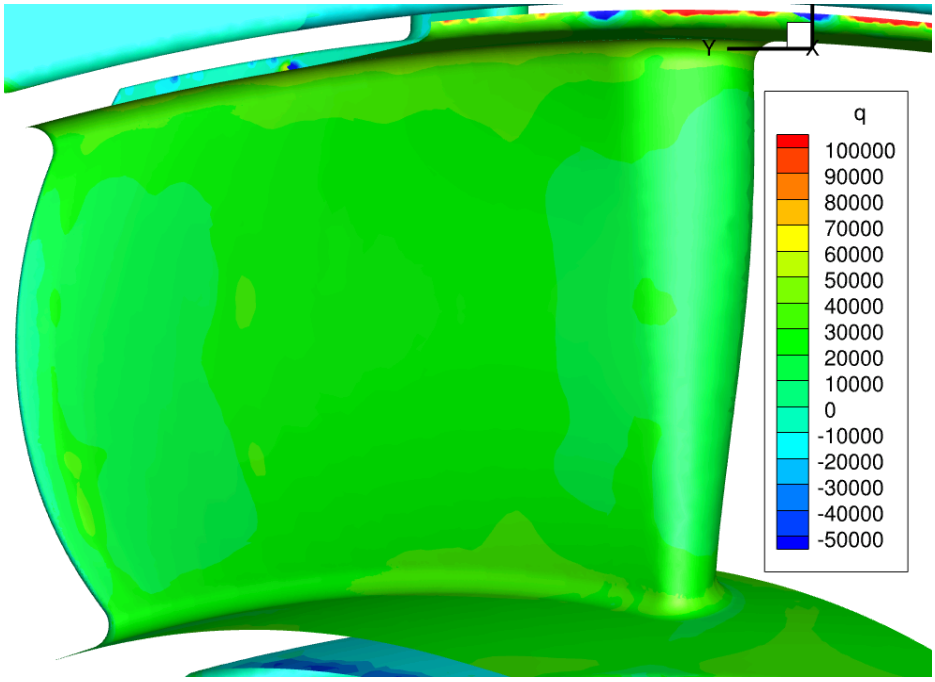

Figure 87 – Uncooled RTV surface heat flux [W/m^2] contour for the PS.

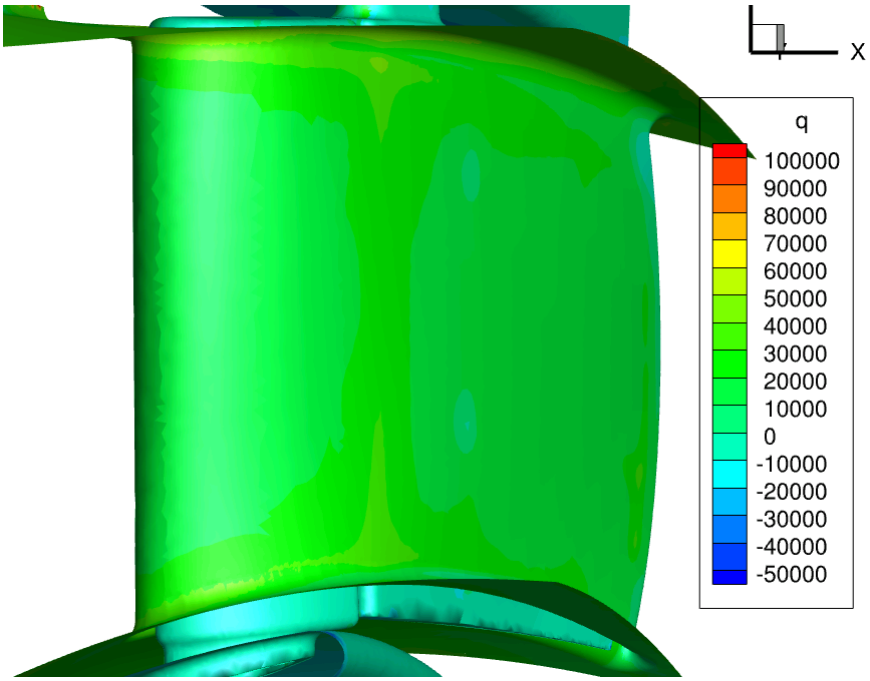

Figure 88 – Uncooled RTV surface heat flux [W/m^2] contour for the SS.

Uncooled Flat Plate

Figure 89 is a contour plot of surface temperature at design flow conditions for the uncooled flat plate in CHT CFD where flow from right to left. The cooling air discharge holes described in the methodology can be seen on the left. This plot, just like the experimental case, displays one of the major advantages of CHT CFD, being able to see what lies beneath the surface of interrogated objects, much like an x-ray. The two recessed rectangular areas in the plate that are intended to match the actual 3-D vane thickness can be seen. The surface temperature is greater where the plate metal is thinner and vice versa. This shows the necessity for CHT CFD assessments and the effect of adding solid conduction to a given CFD problem. As expected, there is a reduction in surface temperature near the coolant discharge holes. Since absolute temperatures are higher in IRT tests compared to the TRF, these temperatures are higher than for the vane

PS simulations. Ultimately, these uncooled results will help with future validation work. The result from the cooled plate with the baseline cooling design is reserved for the comparison in a later section.

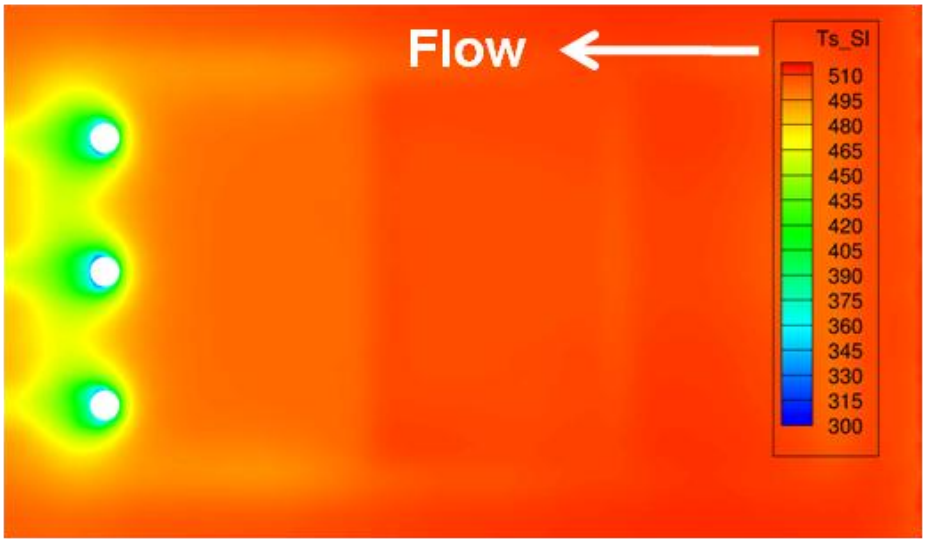

Figure 89 – Uncooled plate surface temperature contour [deg K] from CHT CFD simulations.

RTV Baseline Film Cooling Design

Figure 90 through Figure 93 are surface temperature and heat flux, respectively, for both sides of the RTV with all 648 film cooling holes on the endwalls and both the PS and SS. Looking at surface temperature first in Figure 90, compared to the uncooled vane, a majority of the surface is at least 100 K lower with film cooling. The cooling flow mixing with the main flow causes cooler temperatures on the ID half of the vane, especially downstream of the showerhead. The cool streak at midpsan on the PS is due to the showerhead cooling array of holes pointing towards midspan (with a compound angle of 90º). This array of holes is fed from the ID endwall, which increases discharge coefficient for the holes near the hub and effectively lowers the discharge coefficient for

the showerhead holes above 50% span closer to the OD endwall. This is because the ID-fed cooling flow in the plenum for holes on the OD-half has to turn around and change direction to exit onto the vane surface because of its midspan-directed orientation as explained in the work of Ni et al. [72]. Since the downstream cooling effectiveness is highly dependent on the film cooling injected from the LE, this is likely causing the higher temperatures downstream relative to the ID-half of the surface. Hot spots can be seen at the LE and TE near the endwalls where cooling is not being injected. On the SS in Figure 91, low temperatures are seen just downstream of cooling rows however the remaining axial distance on the vane across the span is fairly constant at a level approximately 80 K lower than the main stream.

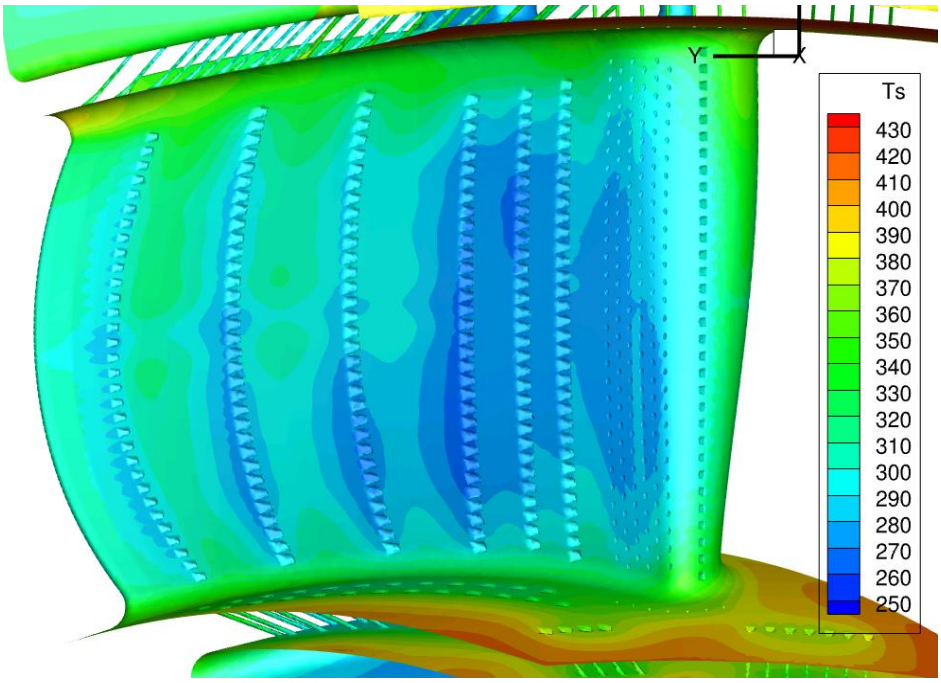

Figure 90 – Cooled RTV surface temperature [K] contour for the PS.

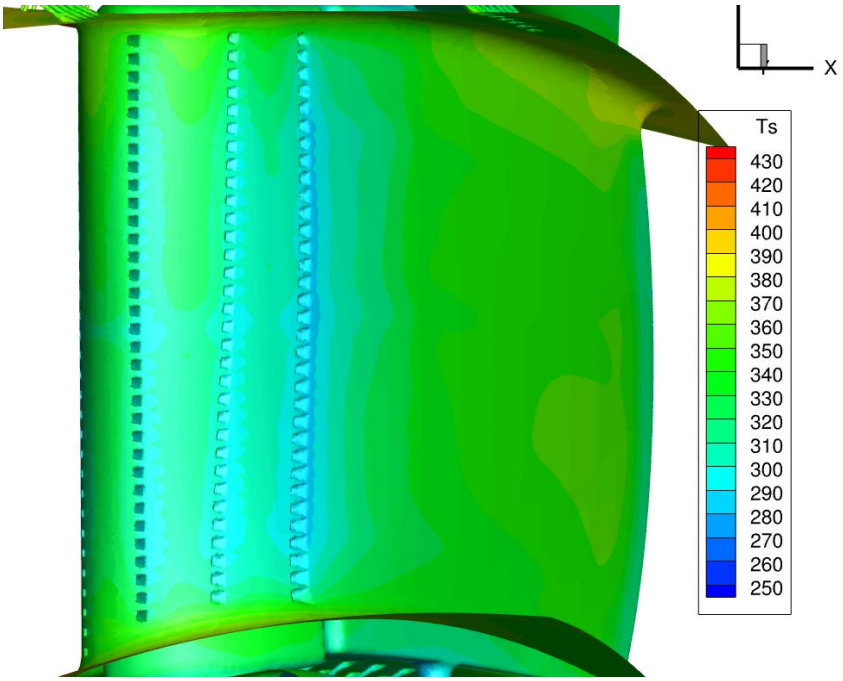

Figure 91 – Cooled RTV surface temperature [K] contour for the SS.

Looking at the PS heat flux contour with film cooling in Figure 92, in general, the areas of high heat flux match many of the areas of high temperature, especially near the LE. The same LE hot spots and PS cool streaks can be seen as in Figure 90. However, high temperature does not always mean high heat flux. For example, the half of the vane PS near the ID is relatively low in temperature but displays repeating areas of high heat flux just like the OD-half does. In fact, this peak in heat transfer just before a film cooling row is seen over most of the vane, especially farther downstream. This increase in heat flux would not exist if the cooling row was not there, as seen in Figure 87. Higher heat flux is also caused by increased mixing which starts at cooling hole injection sites, and is more amplified when the difference between the direction of the cooling and main flows are a maximum, such as at the LE. At the LE, the hot main flow has not picked up

any axial velocity due to the location at the vane stagnation point, and as a result almost directly opposes the film cooling flow and this is where heat flux is a maximum. High injection angles downstream also produce this effect. Lastly, looking at the PS near the TE, the CHT x-ray effect can be seen due to the cooling channels which line up directly with the streaks of high heat flux, where there is a greater change in temperature at the surface due to TE cooling channels that exit right at the vane edge.

Downstream of the LE, abrupt drops in heat flux are seen right at the location of cooling holes followed by a gradual increase leading up to the next successive row of cooling holes where the cycle is repeated. This cyclic phenomenon is also seen in the less rigorous CEEF CFD cooled heat flux distributions shown in previous sections. This is unlike the behavior of surface temperature between cooling hole rows which rises at first, reaches a peak as cooling flow is established, and decreases as the cooling flow cools the surface and the next row of cooling holes is encountered. Recalling Figure 90, it can be seen especially on the ID-half of the PS that cooler areas reside on both sides of cooling hole rows rather than just the downstream side. It is also believed that there is lower temperatures leading up to a row of cooling holes because via conduction, since the shaped cooling holes at a low injection angle effectively reduce the thickness of the vane at these locations and due to the cooling flow beneath the tapered vane thickness, the effects of cooling by conduction affects surface flow before it reaches a row of cooling holes. Heat flux, on the other hand, increases steadily upstream of a cooling hole row which means while the surface temperatures are decreasing, the wall-normal gradients are increasing. This trend of high heat flux just upstream of cooling holes has also been observed by Heidmann et al. [59] and Na et al. [54].

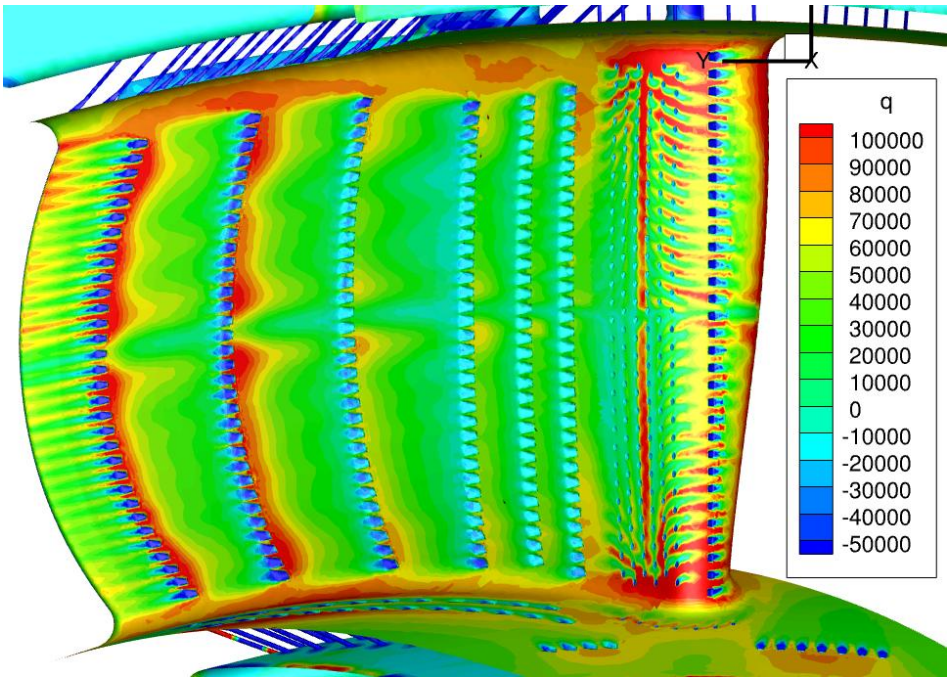

Figure 92 – Cooled RTV surface heat flux [W/m^2] contour for the PS.

On the SS in Figure 93, the same high heat flux trend just upstream of cooling holes is seen along with the midspan cool streak due to the showerhead injection orientation. Farther downstream, the heat flux is fairly constant across the span at a level slightly higher than the cooled areas on the PS. This trend of SS heat flux being higher than PS heat flux is observed in the CEEF CFD as well.

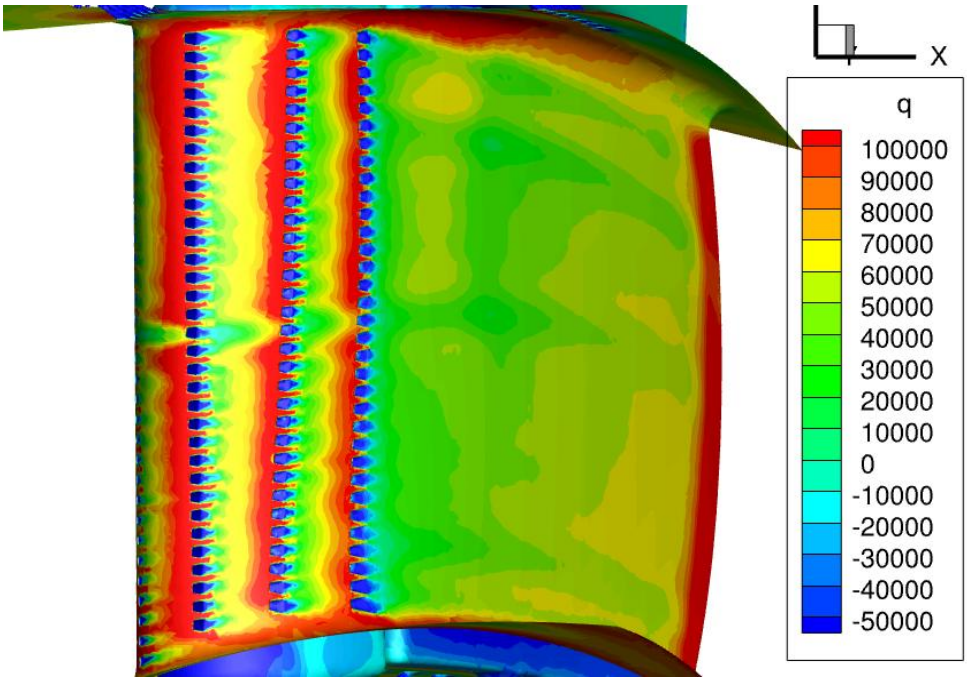

Figure 93 – Cooled RTV surface heat flux [W/m^2] contour for the SS.

Comparison of Flat Plate and Vane Geometries

In order to determine the appropriateness of using a flat plate to model in modeling the film cooling on the fairly flat PS of the 3-D RTV, a number of things can be done to explore this. With two types of CFD (CEEF and CHT) and two different geometries (vane and flat plate) at hand, along with experimental data from the IRT rig as well as from the TRF for the baseline cooling configuration on the RTV, there are clearly many combinations possible for comparison. For example, the CEEF CFD on the 3-D vane could be compared to the CHT CFD on the vane. This is not the best option though, since the solid surface boundary conditions between the two types of CFD are very different. In the case of CEEF CFD, there are isothermal wall conditions and in the CHT there is a more realistic heat flux balance incorporating solid conduction. This presents

the issue of what wall-normal grid location in the CEEF CFD to compare to the CHT CFD. Another option might be to run the IRT experimental domain in CEEF CFD using the conditions from these experiments. Unfortunately, this would be not be a fair comparison since the plate would be simulated with a transpiration conditions for cooling injection and an isothermal or adiabatic wall condition, while the experiments involve a large plenum of cooling air on the back side of the plate that drive conduction effects. Lastly, the TRF and IRT experiments could be compared but since the two rigs run at different overall temperature levels and one provides mainly heat flux and the other mainly surface temperature maps, this is also not the best option.

In order to simplify the problem and provide the best option for comparison, it was decided that using CHT CFD to compare the vane and flat plate in their respective experimental environments would give the most comprehensive results. This way, the CFD would model all conduction effects, cooling hole flows and cooling plenum effects for the IRT and TRF rigs. As the plate and vane are the same material, k was matched between the simulations. It should be noted that both experiments were intended to run at the HIT RTV design-level coolant-to-freestream total pressure and temperature ratio: $P_{t,c}/P_{t,\infty} = 1.046$ and $T_{t,c}/T_{t,\infty} = 0.563$. However, due to the difficulty in obtaining these exact conditions in the two different experiments, the flat plate IRT experimental values were ultimately $P_{t,c}/P_{t,\infty} = 1.035$ and $T_{t,c}/T_{t,\infty} = 0.563$. Meanwhile, using a simple average for the OD and ID cooling flows, the conditions from the TRF runs with the RTV installed turned out to be $P_{t,c}/P_{t,\infty} = 1.051$ and $T_{t,c}/T_{t,\infty} = 0.571$. Hence, the total temperature ratio difference in between the vane and flat plate simulations is 3%.

To assess the appropriateness of using flat plates to represent 3-D vane PS thermal chracteristics in the presence of film cooling, a comparison of the pressure side contours of heat flux and overall effectiveness are given in Figure 94 and Figure 95, respectively. Comparing the heat flux on the same scale shows remarkable similarites between the 3-D vane case and the flat plate. Both exhibit the same general heat flux levels over most of the PS, especially between cooling hole rows. Both have an area of high heat flux near the leading edge. This area is smaller on the vane due to the angle of the cooling injection relative to the flow, which is less for the flat plate configuration. On the vane, the flow interacts head on with showerhead injection. Farther downstream on the vane, the injection angle relative to the main flow becomes more like that of the flat plate. On the flat plate, the showerhead holes have an injection angle of 90 degrees, or perpendicular to the hot flow, which causes increased mixing and heat flux relative to the vane LE. Both geometries exhibit small areas of high heat flux just upstream of a cooling hole row with localized lowered heat flux at the site of cooling holes. Both indicate the effects of the midpsan-oriented showerhead array in creating a cool streak extending to the TE. By matching the coolant-to-mainstream total temperature and pressure ratios between the experimental rigs that these CFD results rspectively represent, except at the leateral edges where endwalls lie on the vane, it appears that major trends in heat flux are matched quite well.

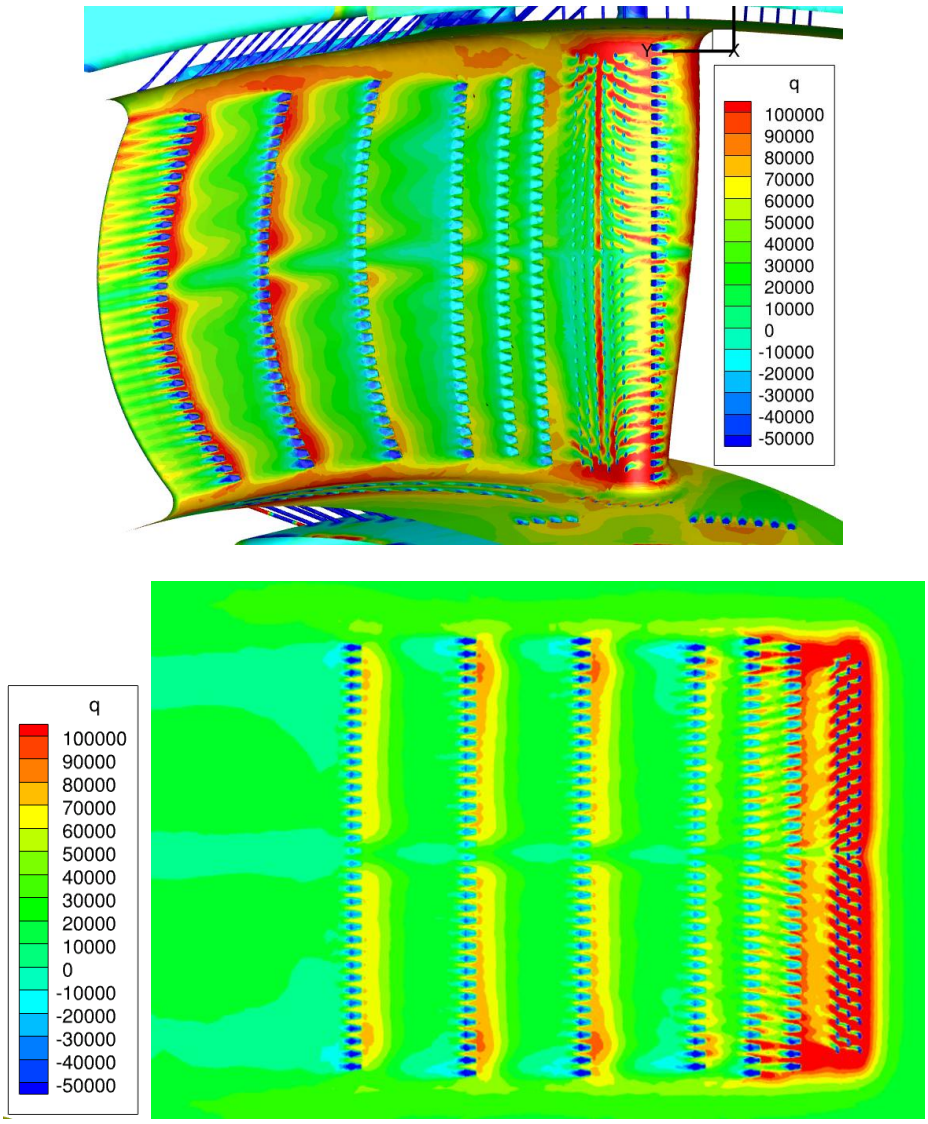

Figure 94 - Cooled PS CHT CFD heat flux contours [W/m2] for the 3-D RTV (top) and flat plate (bottom).

Contour plots of overall effectiveness in Figure 95 show similar trends between the geometries. In general, both contours have values of ϕ = 0.8 for a majority of the area between cooling hole rows and ϕ = 0.5 at the edges of the rows. Both also have lower values around ϕ = 0.2 at the high-temperature leading edge, with a higher concentration for the plate due to the fact that the plate again has different relative injection angle to the

main flow at this part of the surface. Finally, the effect of the cool streak from the showerhead causing an increase in ϕ is seen in both plots. From two pairs of contours, the use of a flat plate in modeling the heat transfer characteristics of the PS of a modern 3-D vane appears to be appropriate, especially downstream of the LE.

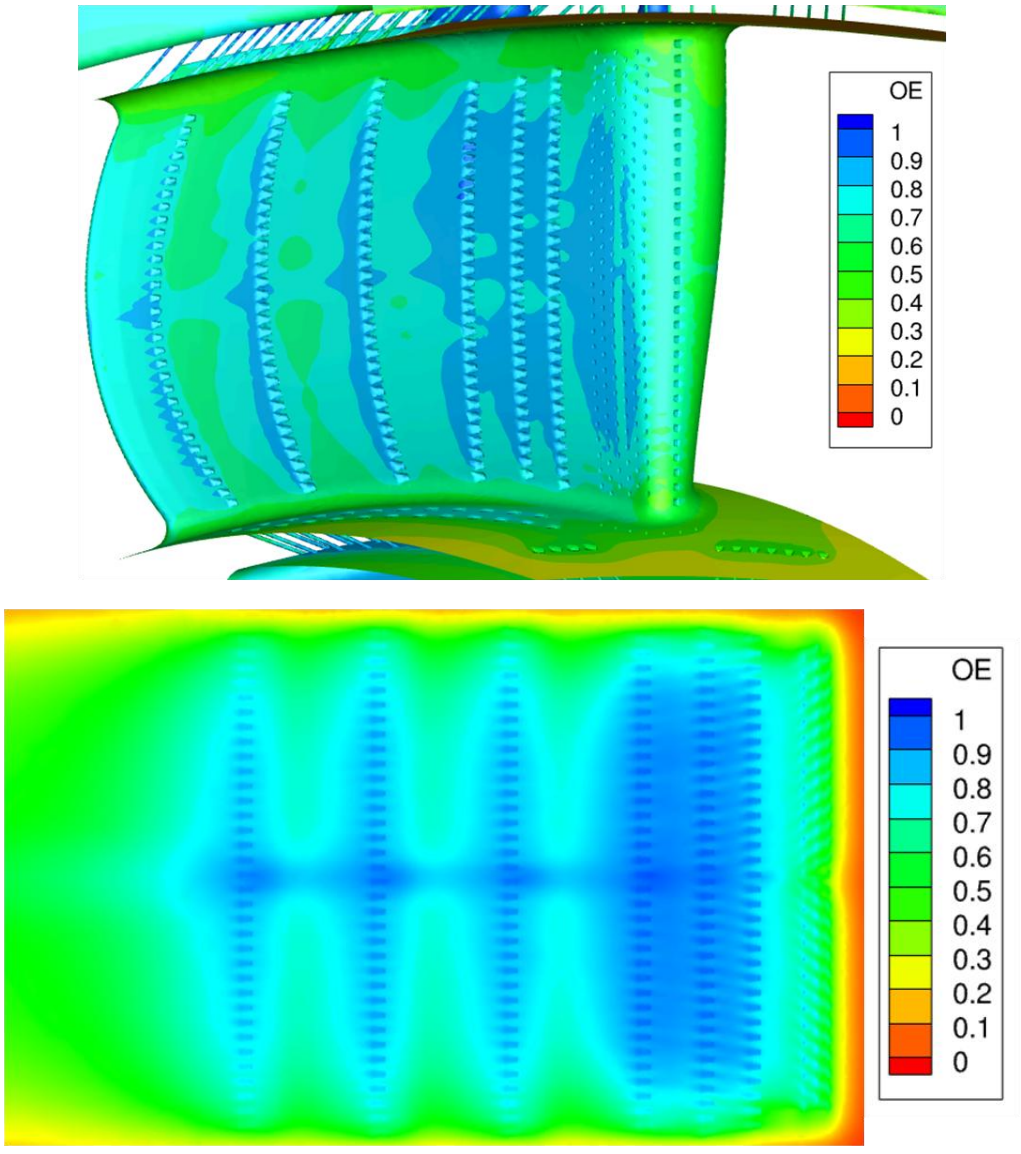

Figure 95 – Cooled PS CHT CFD overall effectiveness contours for the 3-D RTV (top) and flat plate (bottom).

Comparing the CHT CFD results from the two geometries in more depth, temperature contours are given at midspan for the flat plate for each of the six shaped holes as labeled in Figure 96. Flow is from left to right in this figure, as well as the next three. Just like the experiments, the cooling air comes from one plenum for the plate, as opposed to two small plenums in the case of the vane. While the solid material temperature was simulated in the CHT CFD cases, the plate thickness (and vane thickness in later figures) is shown as white space in order to emphasize the effects of conduction on only the fluid temperatures.

Progressing from the 1st to the 6th hole, moving axially downstream, it can be seen that the hot flow has less influence in the area of the hole as the cooling film develops. The air exiting the cooling holes generally does not increase in total temperature until just above the surface. Each hole clearly does an adequate job at creating a film for the next hole lying downstream as a fan-shaped hole should. Figure 96 also shows that the film upstream of hole 2 and 3 is stronger than for holes 4, 5, and 6, which makes sense since the latter are spaced farther apart downstream. For the 6th hole, it can be seen that the plate becomes thicker just downstream as indicated by the fillet in the material. It appears that despite the simulated conduction effects, the cooling air passing through the holes picks up very little heat as no temperature increase is detected until just above the surface. Upstream of holes 2 and 3, cooler surface temperatures are seen due to the gradually reduced thickness of the angled cooling hole combined with the conduction of the cooling flow in the hole reducing the temperature in the main flow.

Comparing the previous contours to Figure 97 for the six shaped holes on the vane PS, the features are generally similar. The temperature range for the vane is

different than for the flat plate due to the different operational temperature levels of each experiment, but it should be reiterated that the coolant-to-freestream total pressure and temperature ratios are matched between the two. Cooling air in the simulations here match reality in that it is fed from two different internal plenums for the vane and from different radial directions as explained in the methodology. It appears that the temperature gradients at the exit of each film cooling hole are pushed closer to the surface for the vane case. This is due to the strong favorable pressure gradient and the turning flow around the vane. The boundary layer is thinner over the surface of the vane relative to the flat plate, too. The flow passing over the plate is not turned and thus the injected cooling air has more of an influence farther from the surface. Unlike the plate case, the temperature of the injected air for the vane PS is observed to dramatically change just before the exit plane, especially farther downstream toward the trailing edge. However, the vane does show the same trend as the plate in terms of the strength and temperature of the approaching cooling film due to axial hole spacing. There are subtle differences between the two geometries, but nothing to suggest that in terms of temperature, it is unreasonable to use a flat plate model to represent film cooling on a 3-D vane pressure side.

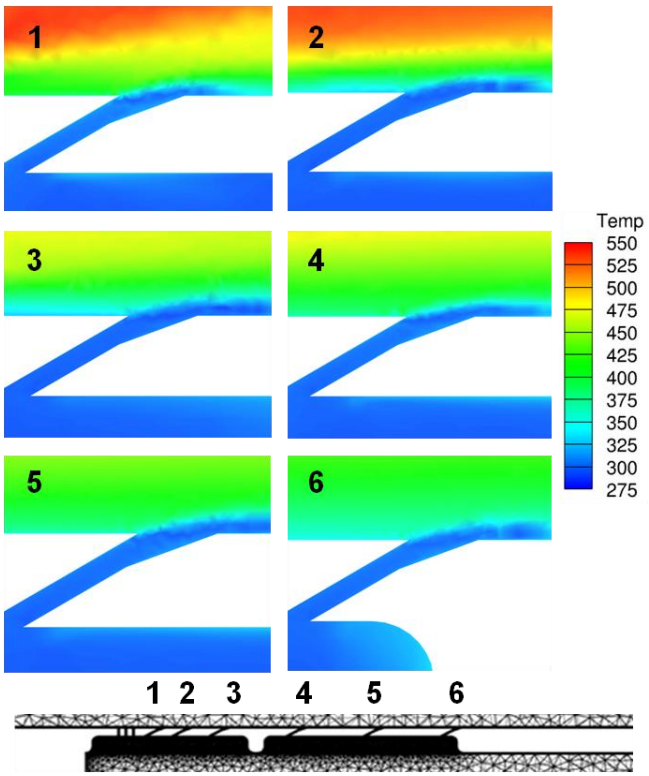

Figure 96 - Flat plate temperature [deg K] contours at midspan.

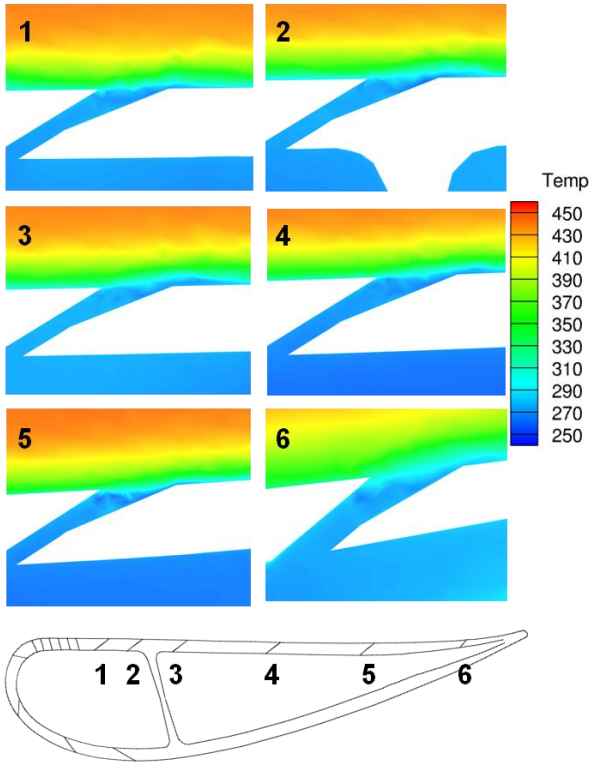

Figure 97 - Vane temperature [deg K] contours at midspan.

Static pressure contours with velocity vectors for each of the shaped holes in the plate at midspan are given in Figure 98. They show that pressure is changing throughout most of the cooling passage, although most of the change in each hole occurs at the entrance on the plenum side. For all holes, the change in pressure through the hole is just under 1 atm. From hole to hole, the pressure gradients as well as the velocity characteristics are essentially the same. This is expected as there is no pressure gradient on the plate and no contoured opposite wall in the experiments. Lastly, with one large plenum, there is no change for each hole in cooling pressure.

Meanwhile, in Figure 99 for the vane, the external static pressure clearly decreases axially with each hole. In addition, it can be seen that the velocity inside and outside of the hole increases with downstream distance. Unlike the flat plate shaped holes, the vane exhibits very high pressure gradients isolated to the entrance of the cooling passages on the plenum side. The plate holes show pressure changes that are spread more evenly throughout the cooling passages. The slight difference in the plenum temperatures, based on TRF pressure measurements, can also be seen. The through-hole pressure change is much higher for the rear cooling plenum than for the front plenum. This is attributed to the fact that the rear plenum only supplies four rows of holes, while the front plenum supplies the remaining five rows of PS holes as well as all seven SS rows of showerhead and shaped holes. While the static pressure and velocity changes between the plate and vane are quite different, more so than for temperature, both flow geometries display the same general trends for flow exiting a shaped cooling hole.

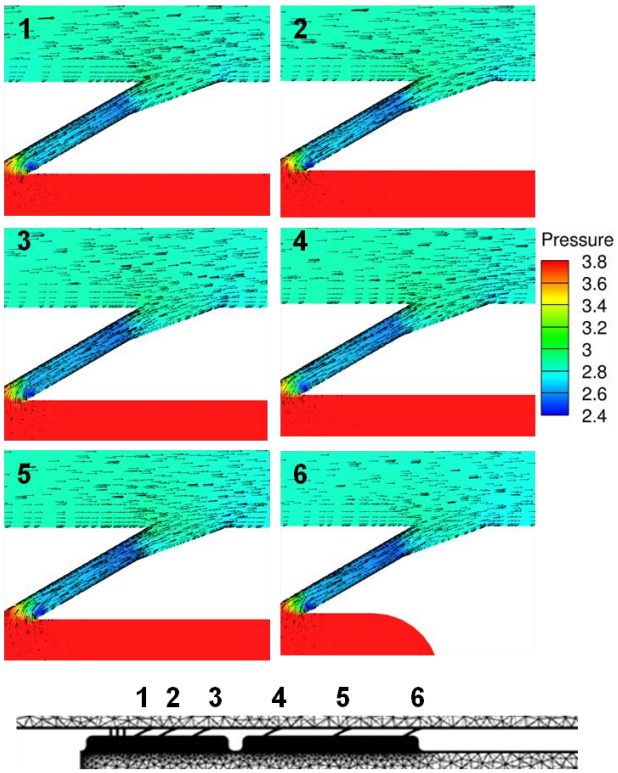

Figure 98 - Flat plate static pressure [atm] contours at midspan with velocity vectors.

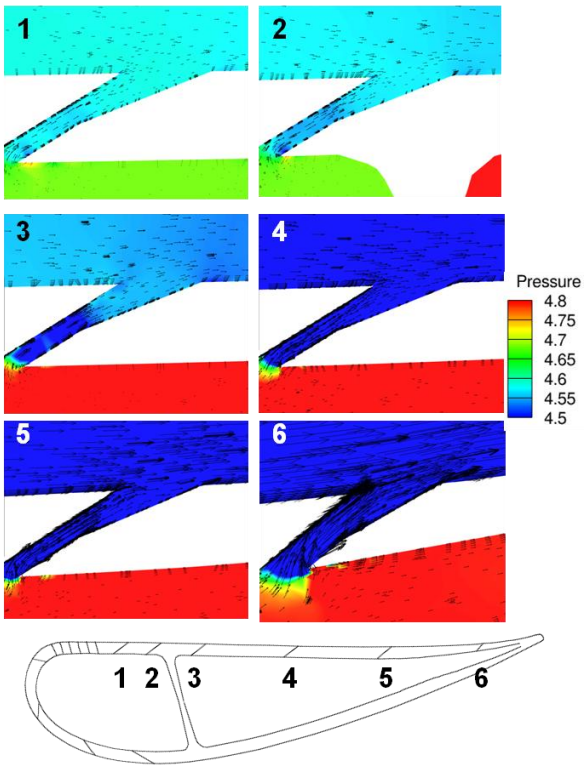

Figure 99 - Vane static pressure [atm] contours at midspan with velocity vectors.

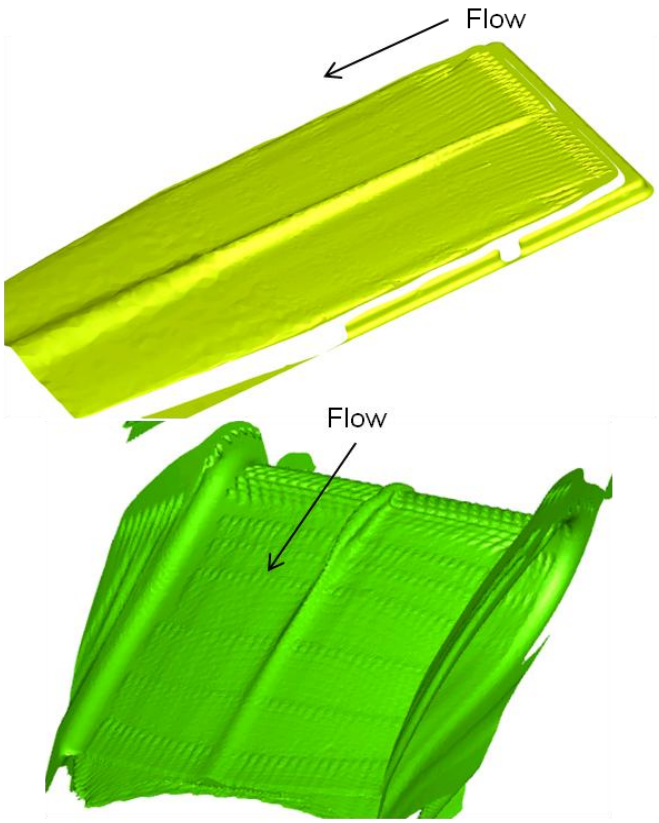

Figure 100 - Comparison of flat plate (top) and vane (bottom) PS temperature isosurfaces just above the surface temperature level.

Temperature isosurfaces for levels just above the surface temperature showing film cooling flow surface patterns for the plate and vane are given in Figure 100. Both flowpath geometries show very similar surface flow patterns due to the showerhead and successive six rows of shaped holes. The pileup of cooling at midspan due to the orientation of the showerhead is clearly seen in both cases. The one major difference is how the flow is contracted toward midspan and pushed towards the surface on the vane. This is likely due to the endwall effects as well as the stronger vane pressure gradient that is absent on the plate.

The next sets of results include streamwise distributions of non-dimensional temperature at different span locations on the flat plate and vane. Flow is from left to right. From Figure 95 it can be seen that the streamwise spacing of cooling hole rows is the same at the ID and OD between the vane and plate. However, the 3-D nature of the vane with its curved LE causes slight differences in stream-wise spacing at span locations near midspan. Thus, the data for the vane was axially normalized to match locations of cooling hole rows on the plate.

Figure 101 is a comparison of distributions at the 25% and 50% spanwise locations. The plate case exhibits a large temperature drop from the freestream levels at the beginning of the plate. The vane, on the other hand, involves head-on, rather than perpendicular, main flow orientations relative to cooling flow as well as potential contributions from suction side LE cooling which keep temperature down relative to the plate. Both locations have very similar distributions in terms of the heat transfer characteristics between holes. Both show the characteristic rise and fall of temperature between cooling hole rows as seen in the surface contours. The overall level of temperature at both span locations only differs by approximately 5%. This difference is likely accounted for by the small differences in $P_{t,c}/P_{t,\infty}$ and $T_{t,c}/T_{t,\infty}$ for the boundary conditions matched. Recall that the difference in CHT CFD $T_{t,c}/T_{t,\infty}$ between the geometries was 3%. This difference also partly explains differences in temperature levels seen at other spanwise locations between the cases. The vane 75% span location distribution is added in order to show the asymmetry of the vane relative to the 25% spanwise location distribution, however, the differences are very small over the entire surface distance. The flat plate, as seen in experimental [171] and CFD [132] studies,

typically displays a symmetrical temperature distribution about midspan. Naturally, the vane, which exhibits changes in area from leading edge to trailing edge and from hub to shroud, along with endwall effects, will not exhibit symmetry about midspan in its heat transfer properties.

Figure 102 and Figure 103 are more detailed plots of the asymmetry of the vane non-dimensional temperature on the PS. Both figures give the 5% or 95% and the 10% or 90% spanwise locations for the flat plate, since the plate properties are symmetrical. The same LE characteristics can be seen in both figures between the vane and plate as seen in Figure 101. Figure 102 is vane results at 5% and 10% spanwise location near the hub. The difference in 5% and 10% spanwise location temperature levels is greater for the plate compared to the vane, whose levels are nearly the same. Unlike at the 25% and 50% spanwise locations, the flat plate temperature levels are generally higher than the vane levels. The 10% span location temperature levels between the vane and flat plate are very close with a maximum difference past the LE of about 3%. Meanwhile the 5% span location temperature differences are higher at around 7% which is a maximum between cooling hole rows. It is seen that successive shaped hole rows have clear effects on temperature for the vane while the temperature levels are not tamed into a repeating pattern until about the 3rd row of shaped holes on the plate. The difference between maximum and minimum temperature between cooling hole rows are also higher for the plate relative to the vane, likely due to the absence of a pressure gradient.

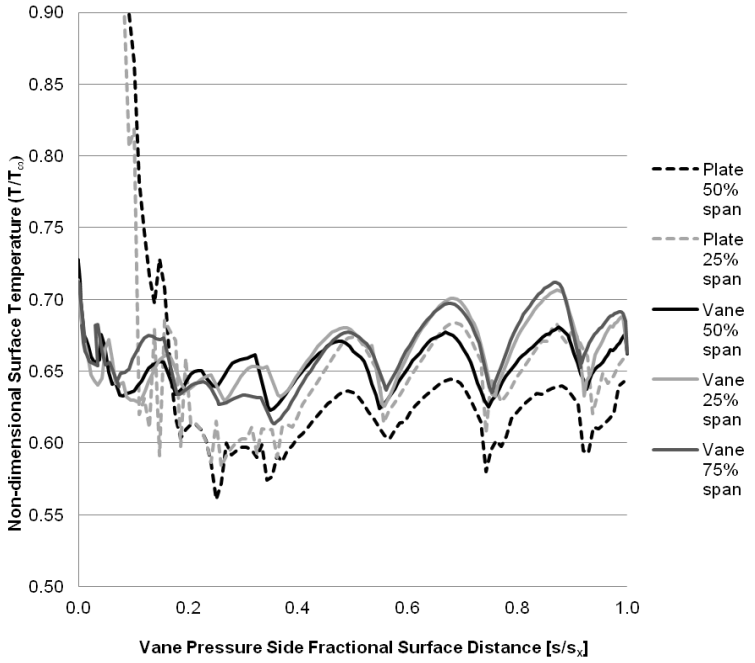

Figure 101 - Film-cooled pressure side streamwise non-dimensional temperature distributions at 25% and 50% spanwise location for the flat plate and vane CHT CFD cases.

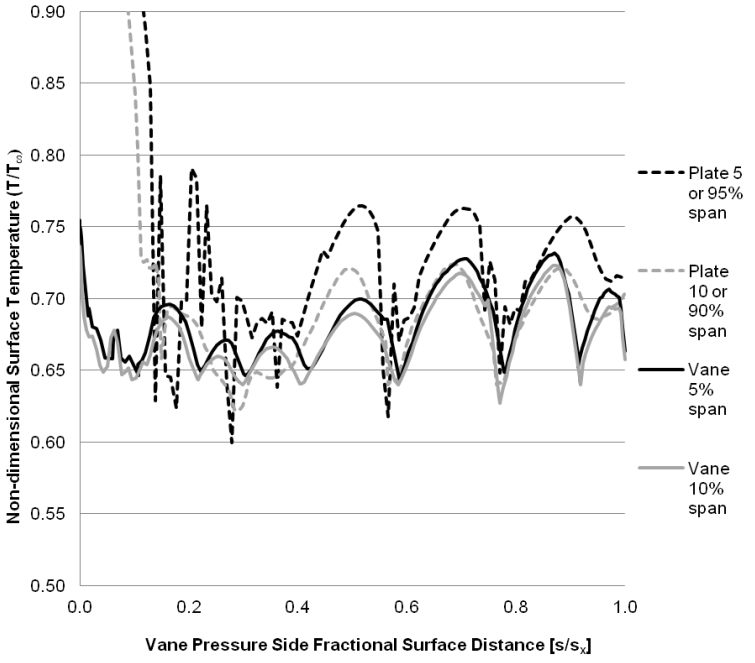

Figure 102 - Film-cooled pressure side streamwise non-dimensional temperature distributions at 5/95% and 10/90% spanwise locations for the flat plate and 5% and 10% locations for the vane.

Figure 103 is a comparison of the same plate locations to the 90% and 95% spanwise locations on the vane near the shroud. Clearly, for the vane, there is little effect of film cooling at 95% spanwise location, as rows of holes terminate just beyond 90% spanwise location. Unlike the vane geometry, the plate film cooling characteristics are symmetrical about midspan and thus the lack of cooling is not seen. Comparisons of the vane shroud region to the plate show the greatest differences for all spanwise locations, but even for 90% spanwise location, the difference in non-dimensional temperature is still only 4% on average over the pressure surface distance.

Figure 104 is the spanwise distributions in non-dimensional temperature at the leading edge of the 2nd, 4th, and 6th shaped hole rows on the PS for the plate and vane. Here, non-dimensional temperature is on the x-axis and fractional spanwise location is on the y-axis. Overall, the differences are quite small between the vane and plate where there is a maximum of 7% difference in temperature for all three rows over almost 80% of the span length. Again, this difference is would be reduced if the total pressure and temperature ratios between the cases were identical. Just as seen with the LE comparison in Figure 101, the lateral edges see much higher temperature gradients for the plate relative to the vane. The midspan pileup of film cooling due the showerhead orientation also reduces temperature on the vane more than the plate.

Finally, showing the results here in terms of overall effectiveness, while it can account for subtle differences in $T_{t,c}/T_{t,\infty}$ between the two cases, it does not account for the 1.5% difference in $P_{t,c}/P_{t,\infty}$, which is representative of blowing ratio. Thus, the results presented are comprehensive enough to draw conclusion from the similarities and differences observed.

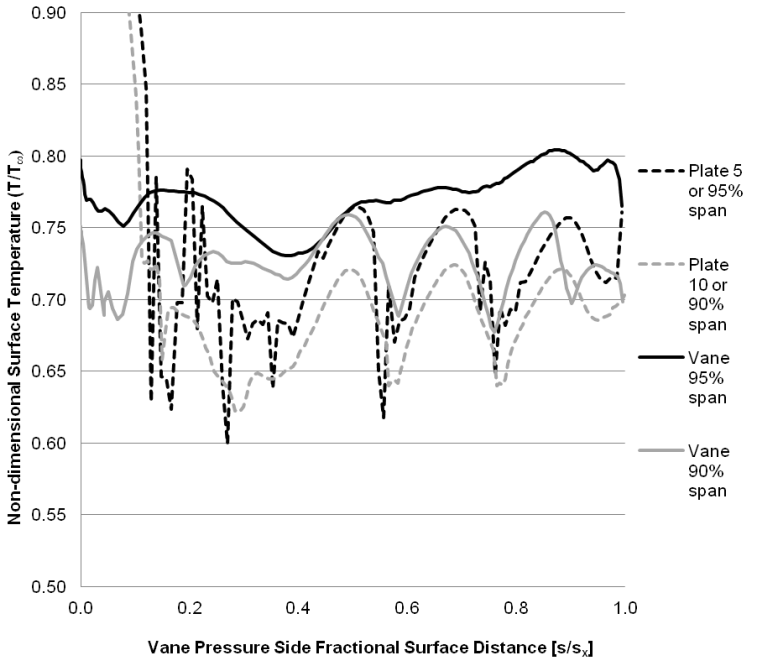

Figure 103 - Film-cooled pressure side streamwise non-dimensional temperature distributions at 5/95% and 10/90% spanwise locations for the flat plate and 90% and 95% locations for the vane.

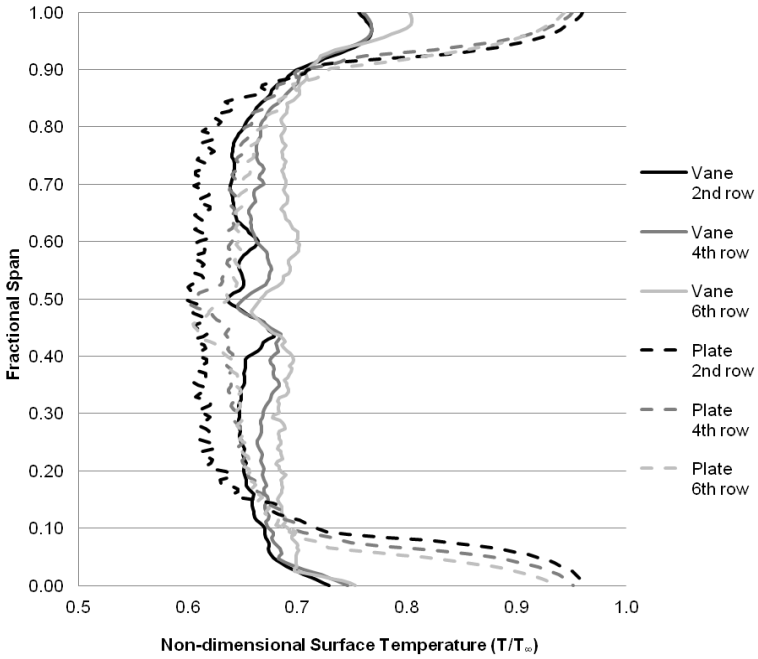

Figure 104 - Film-cooled pressure side spanwise non-dimensional temperature distributions at the leading edge of the 2nd, 4th, and 6th shaped cooling hole rows for the flat plate and vane cases.

As many past film cooling works have relied on the data and correlations found from flat plate models, this study to justify the use of modeling 3-D vane PS film cooling with a flat plate is intriguing. Average differences in non-dimensional surface temperature levels between the vane and plate geometries were very small at 25% and 50% spanwise locations, which is most likely explained by the difference in the coolant-to-freestream total pressure and temperature ratios assigned as boundary conditions in both cases. The cyclic increase and decrease of surface temperature due to film cooling rows between the geometries followed very closely, especially after approximately 30% axial surface distance. Differences in simulated temperature at spanwise locations toward the hub and shroud are greater between the vane and plate which is explained by the highly 3-D, asymmetric nature of flow in the vane case. Lastly, despite the stronger through-hole pressure changes in the rear plenum on the vane relative to the front plenum, the temperature distributions are very close to that of the flat plate which uses one large cooling plenum. This study has shown through CHT CFD that use of a flat plate with the same engine-representative cooling array in modeling vane PS heat transfer characteristics is accurate, especially for the middle half of the vane span downstream of the showerhead. Any discrepancies between the geometries in cooling performance can likely be made up by abandoning the precise experimental conditions of the respective simulations and directly matching the coolant-to-freestream total temperature and total pressure ratios between the CHT CFD cases.

VII. Flat Plate Infrared Thermography Experimental Results and Discussion

Baseline Cooled Plate

All results discussed from here on are IRT experimental results. To ensure the right conditions are being tested, a blowing ratio sensitivity study was done to see the isolated effects of both changing inlet total temperature and coolant plenum total pressure. There is a high sensitivity of blowing ratio to the controllable parameters in the IRT experiments as seen in Figure 105.

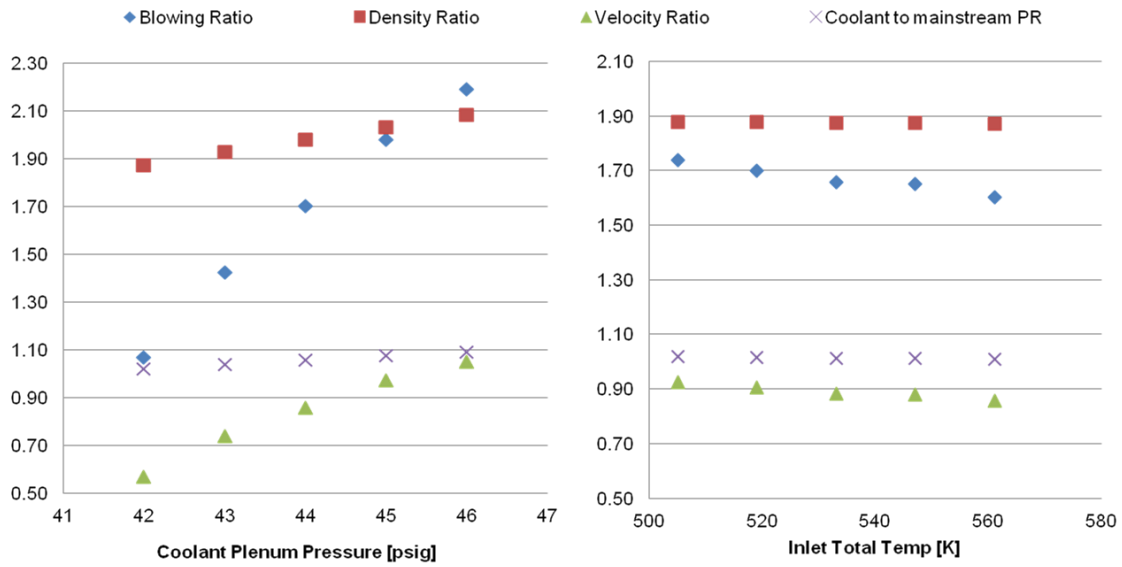

Figure 105 – Sensitivity of different parameters with respect to changes in cooling plenum total pressure (left) and inlet total temperature (right) spanning the design level $P_{t,c}/P_{t,\infty}$.

The results in Figure 106 are the streamwise variation of surface temperature according to IRT measurements at three mainstream total temperature levels at three span locations on the baseline cooled plate. In Figure 106, the right side is the leading edge of the vane and the left side is the trailing edge of the vane with the flow going from right to left. The distributions given include midspan and lateral offset locations ±15 mm from

the midspan. It can be seen that the surface temperatures increase over the entire length of the plate correspondingly with the test section inlet temperature. For each temperature level, the respective midspan lines (labeled center in the figure) are significantly cooler than the other two lines. The other two lines at each temperature level coincide since the baseline cooling hole array design on the RTV PS, and therefore the film cooling characteristic, is symmetric. The anomalies seen in the off-midspan distributions near the trailing edge can also be seen in the IR images. This is the effect of the "cold spot" due to the reflection of the cryogenic detector in the IR camera and can be ignored. Later IRT runs alleviated this effect by increasing the tilt of the IR camera relative to the access window.

The cooling hole rows on the baseline cooling design are arranged for maximum protection (lowest relative surface temperature) close to the leading edge, moderate protection from about ¼ to just after ½ chord, and limited protection near the trailing edge. This relationship is in accordance with the inverse relationship typical to heat transfer distribution seen on an uncooled vane profile. In other words, more cooling is provided to the parts of the PS on the vane expected to have the highest temperature. Naturally, in the presence of a pressure gradient, this trend appears different. Around mid-chord, the last three laidback fan-shaped cooling hole rows appear to be spaced such that the surface temperature is limited to a certain level. However, the level increases slightly with downstream distance. With a positive pressure gradient, this peak inter-row temperature levels are likely to be more similar as seen in CHT CFD results.

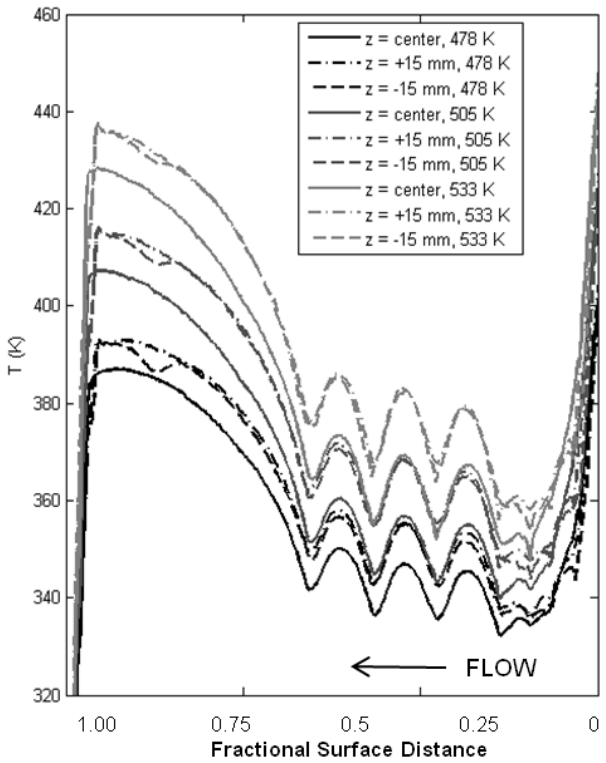

Figure 106 - Streamwise cooled plate surface temperature distributions for three span locations at three freestream gas temperatures.

Figure 107 is a plot of spanwise distributions of temperature at three axial locations on the cooled plate for the three different temperature levels from Figure 106. The surface temperature levels increase accordingly as the test section temperature increases and this incremental increase becomes slightly greater as the distributions move downstream. Due to the symmetric nature of the cooling design, each set of lines for a given downstream location bears the same shape. The dramatic dip at midspan is attributed to the effect of the showerhead holes having compound angles of 90º towards midspan and creating a low temperature streak. The temperature distribution at x = 30 mm shows oscillations because that location is directly on top of the closely spaced cooling hole rows whereas the other two locations are not.

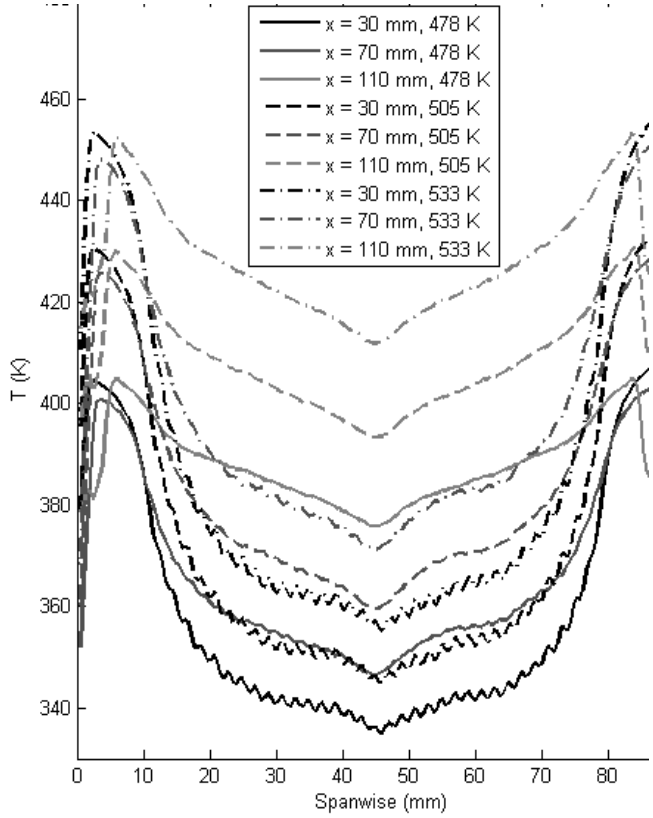

Figure 107 - Spanwise cooled plate surface temperature distributions for three axial locations at three freestream gas temperatures.

Surface temperature contours are given in Figure 108 for the cooled plate at the design main flow inlet total temperature of 533 K for five different coolant-to-mainstream total pressure ratios. Flow is from right to left in all IR images. The five pressure ratios span the design point value of 1.046. The screws that hold the test plates in place and that were used in the calibration procedure can be seen on the top and bottom of each image. Clearly, the surface temperatures decrease as the volume of cooling air is increased. As mentioned before, the IR camera cryogenic detector can be seen reflecting on the images on the left side near midspan creating a cold spot. The effect of the compound angles towards midspan in the showerhead cooling hole array can be seen in the form of a cool region that extends far downstream relative to cooling from

other parts of the vane PS span. At higher values of $P_{t,c}/P_{t,\infty}$, the combined effect of the midspan-oriented showerhead and the cooling hole rows makes a narrow diamond pattern on the vane surface.

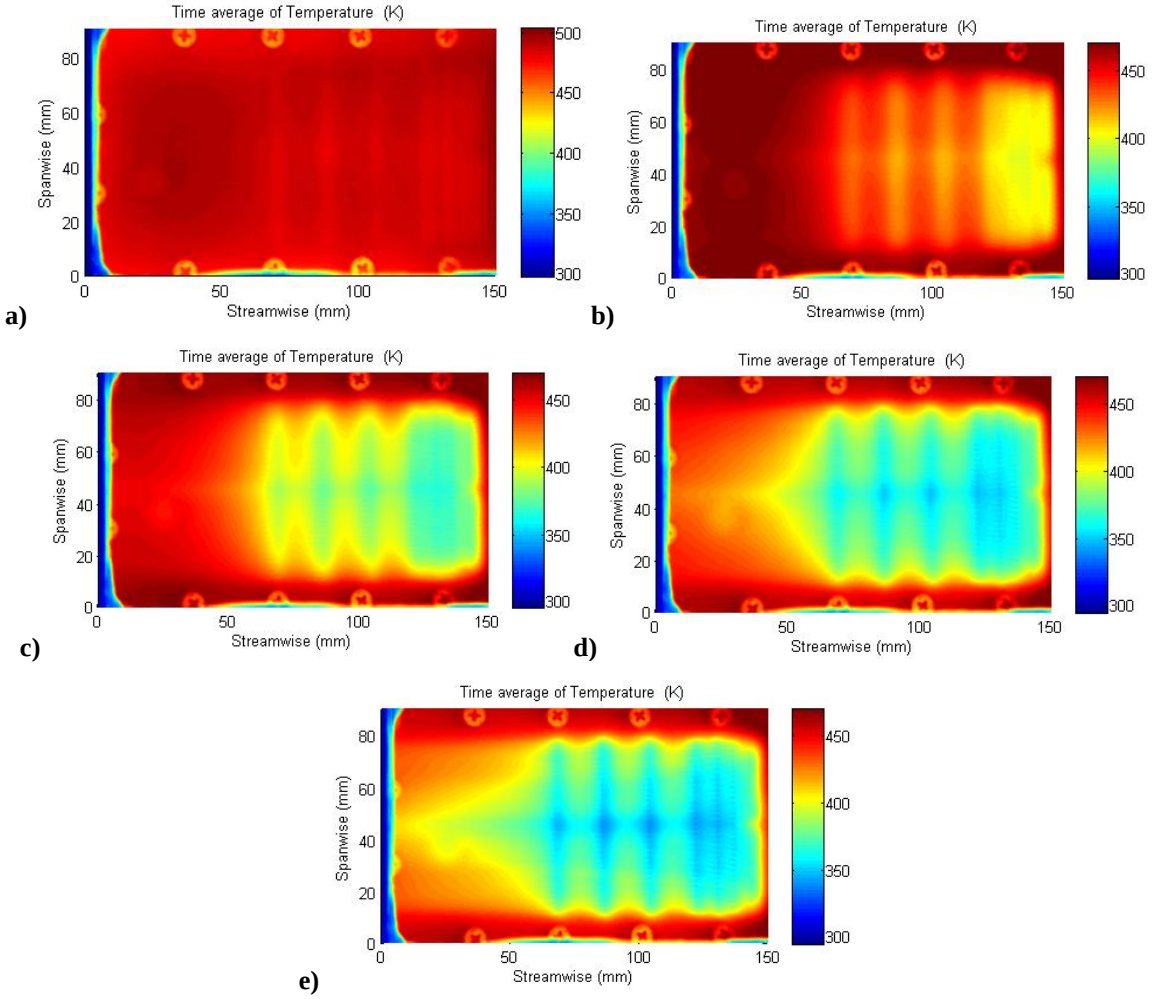

Figure 108 – Baseline cooled flat plate surface temperature contours at the vane design temperature for $P_{t,c}/P_{t,\infty}$ = a) 1.008, b) 1.017, c) 1.027, d) 1.072, and e) 1.144.

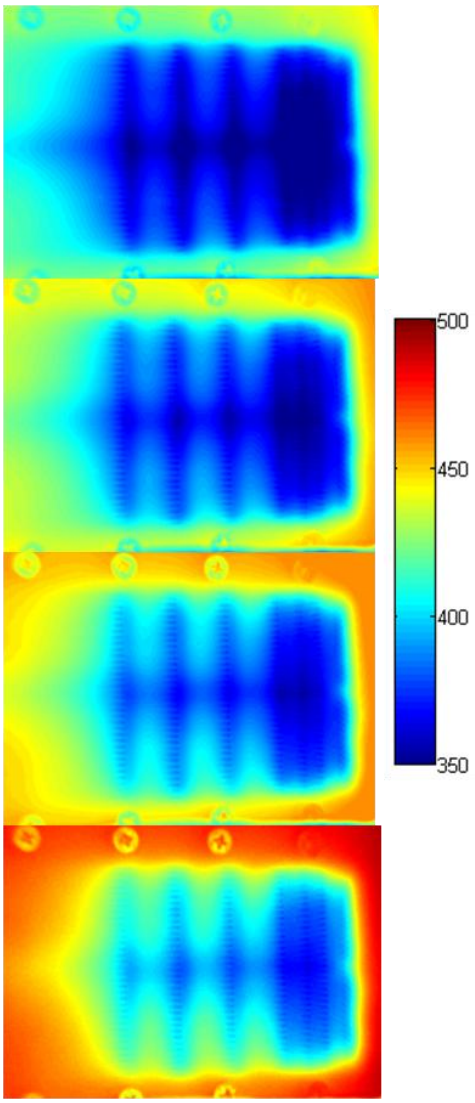

Figure 109 - Cooled flat plate surface temperature contours at design value of $P_{t,c}/P_{t,\infty}$ for (from top to bottom) $T_{t,\infty}$ = 506 K, 519 K, 533 K, and 547 K.

The next images in Figure 109 are surface temperature contours at the design coolant-to-mainstream total pressure ratio for four different test section inlet total temperatures. The coverage of the film cooling clearly becomes less as the inlet temperature increases, not only axially but laterally. The temperature of the outside edge of the flat plate is clearly increasing as well. In the range of temperatures tested, the relationship between the coolest and hottest surface temperatures and the freestream gas

temperature is fairly linear. The last few rows of cooling holes show the same cooling pattern up until the hottest temperature shown, where the last row appears to have less cooling coverage. This may mean the last cooling hole row on the baseline design needs to move farther upstream to handle higher temperatures.

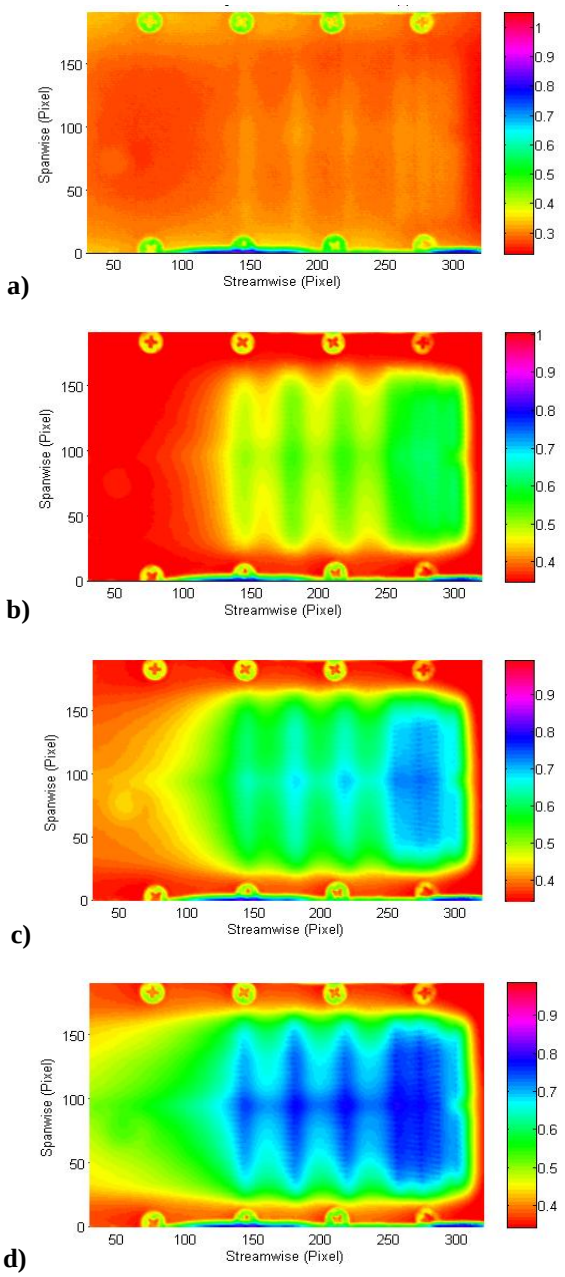

Figure 110 - Overall effectiveness contour plot for RTV PS design gas temperature for $P_{t,c}/P_{t,\infty}$ = a) **1.008, b) 1.017, c) 1.027, and d) 1.072.**

Overall effectiveness contours are given in Figure 110 for the four levels of coolant-to-mainstream total pressure ratio. In terms of film cooling patterns, these are very similar to that given by surface temperature data. The peak effectiveness in the images is approximately 0.3, 0.6, 0.75, and 0.8 for $P_{t,c}/P_{t,\infty}$ equal to 1.008, 1.017, 1.027, and 1.072, respectively. Therefore, with a non-linear increase in coolant-to-mainstream pressure ratio, the overall effectiveness may plateau at some peak value. Looking at coverage with $\phi \geq 0.5$, clearly the case with the greatest coolant blowing is the best result, but even for $P_{t,c}/P_{t,\infty} = 1.027$, less than the design level of 1.046, a large majority of the RTV PS surface meets this nominal cooling effectiveness.

Figure 111 is the overall effectiveness contour in grayscale for design temperature and pressure ratio conditions. In the plot, white areas are cooler. The lower effectiveness seen around the edges of the plate is attributed to heat conduction from the uncooled perimeter of the plate. As the extent of the cooled RTV PS flat plate model test surface does not overlap the area of the plate with the screws, over 95% of the PS surface has a value of $\phi > 0.5$. Thus, this baseline cooling design presents a fair challenge as a candidate for cooling coverage optimization.

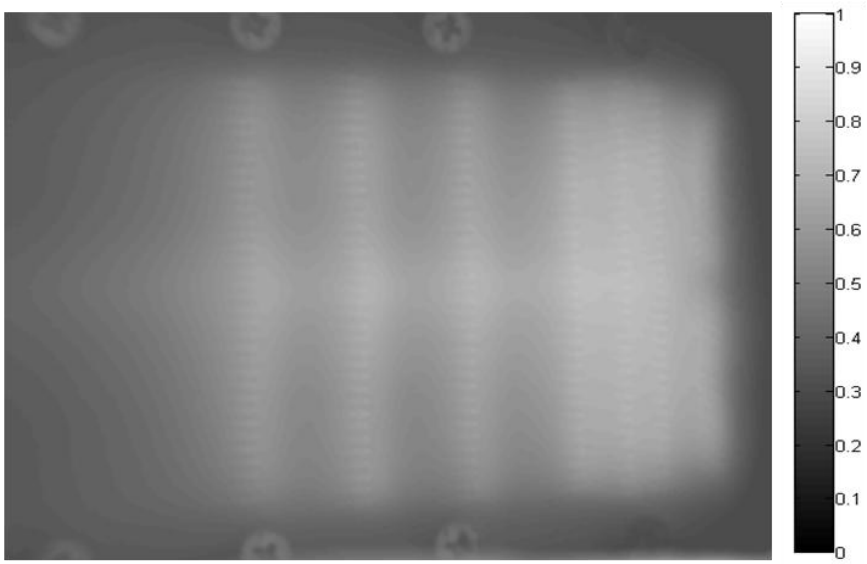

Figure 111 – IRT overall effectiveness contour for baseline cooled flat plate IRT for RTV design flow conditions.

Hot-surface temperatures for varying inlet total temperatures measured by three embedded thermocouples are given in Figure 112. The inlet temperatures span the design level of 533 K and flow goes from left to right in this figure. On the hot side in the left half of Figure 112, the thermocouples register an increase in temperature with axial distance, which is consistent with the streamwise surface temperature distributions shown previously. Data from 12 plenum-side surface-mounted thermocouples is given in the right side plot of the figure. A decrease in temperature can be seen at first as the showerhead cooling is established, followed by a area of low temperature, then an increase due to the increased cooling hole row spacing, and then a sudden jump down with continued increase at the same slope at thermocouple #9 due to the sudden increase in thickness of the plate at this location. This plot shows the effects of conduction of the hot flow through the plate to the cool side.

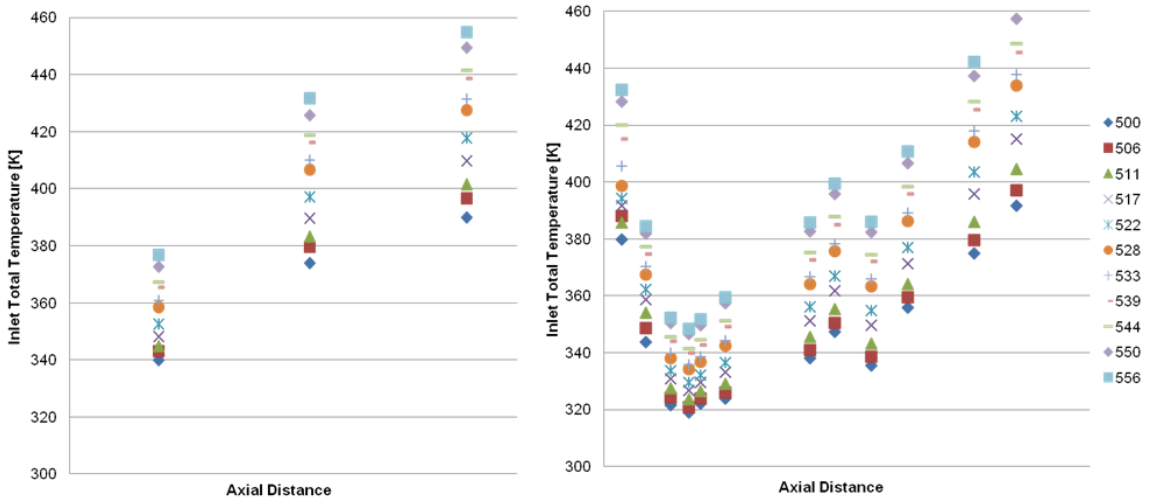

Figure 112 - Flat plate hot side (left) and plenum side (right) streamwise temperature distributions as a function of inlet total temperature.

Comparison of Optimized and Baseline Cooling

The next set of results incorporate the cooling performance of the optimized film cooling array flat plate as measured by IRT. Uncooled plate results are also given here. An image of the hot side of the optimized cooling array with shaped holes is provided in Figure 113. Figure 114 is an overall effectiveness contour at design conditions for the optimized cooling array, which can be compared to Figure 111. The effectiveness at the site of the holes appears to be higher at some locations but this may be due to the high injection angle relative to the baseline cooling configuration. Some of the blended hole shapes with high compound angles and paired crossover angles are also increasing the overall effectiveness. Downstream and lateral film cooling coverage appears to be comparable with the baseline cooling design. The lower half of Figure 114 is meant to model the OD part of the vane. Thus there is a relative abundance of cooling in this area. Also, as this array was optimized for a 3-D vane and it not symmetrical about midspan

like the baseline array. Therefore, it is expected that some span locations will be cooled more than others on the flat plate.

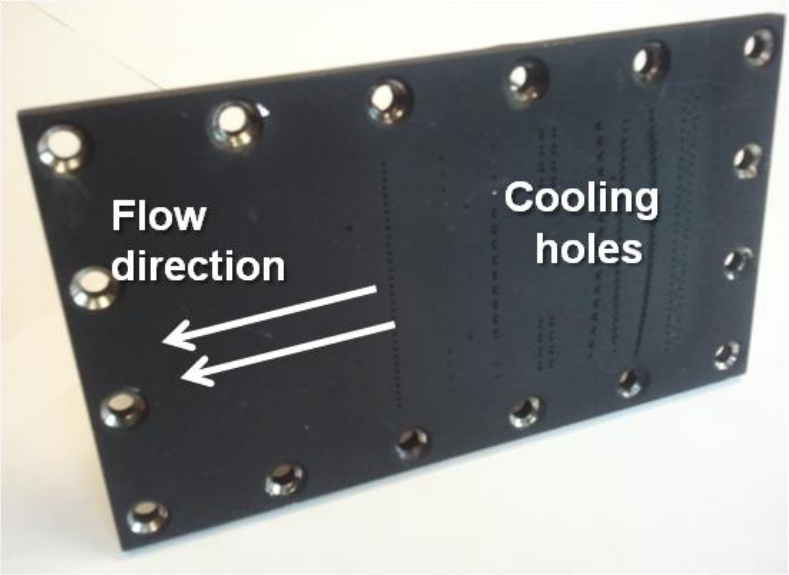

Figure 113 - Hot side image of the optimized cooling array flat plate with shaped holes.

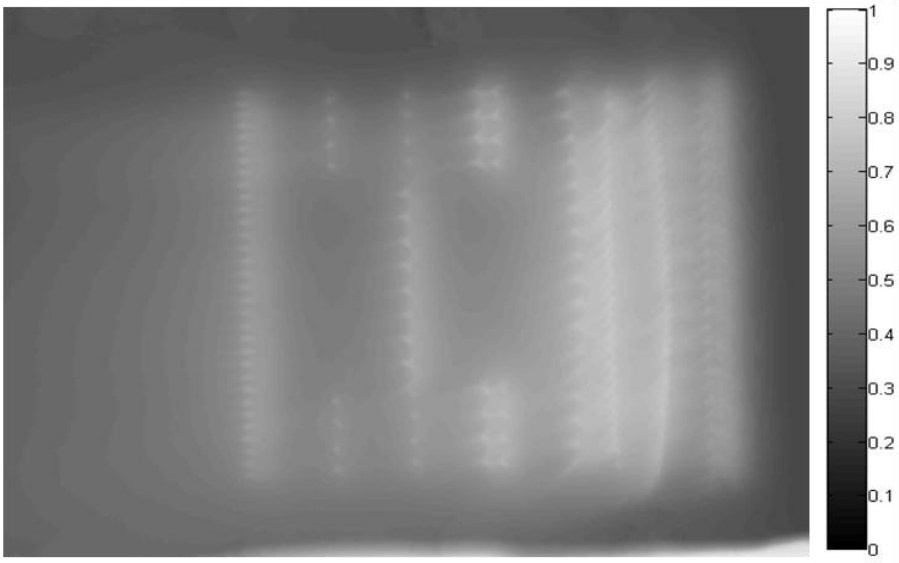

Figure 114 – IRT overall effectiveness contour for optimized cooling array flat plate for RTV design flow conditions. Air flow is from right to left.

Figure 115 is a more direct comparison of the baseline and optimized cooling array using a different color map. In this figure, it is clearer how asymmetrical the cooling distribution is for the optimized array. In the absence of a pressure gradient and 3-D secondary flow effects of the vane geometry, it is not surprising that there are large areas of low overall effectiveness in the midspan areas where the optimization resulted in the removal of midspan film cooling holes. The area downstream of the last row of holes appears to be cooler for the optimized array, despite the lack of cooling hole in the midspan region.

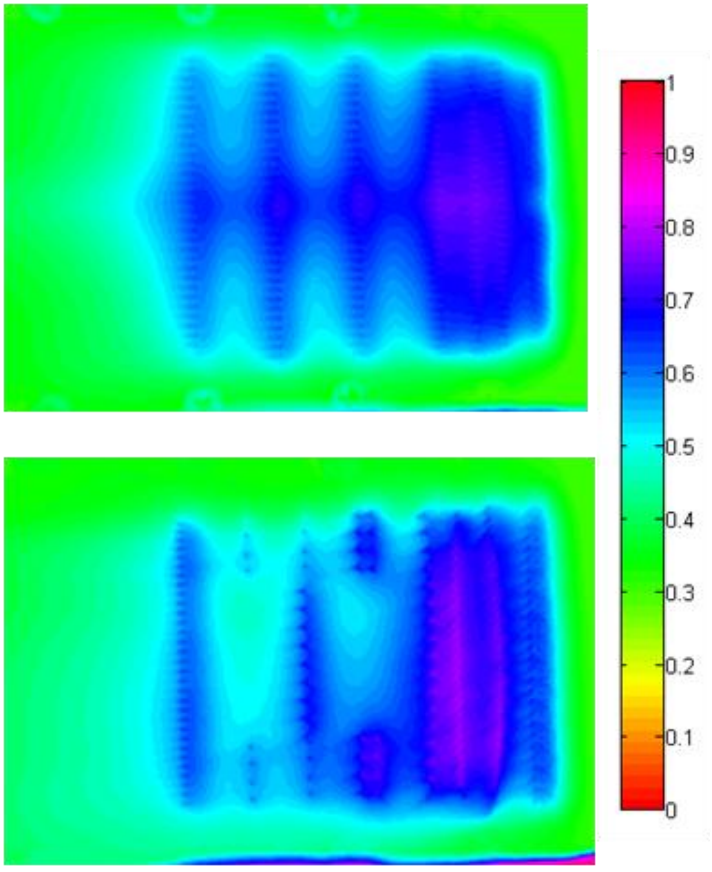

Figure 115 – IRT overall effectiveness comparison between the baseline and optimized cooling array flat plate at RTV design flow conditions. Air flow is from right to left.

Contours are merely qualitative comparisons. Therefore, the next sets of data look at streamwise and spanwise temperature distributions at different locations on the flat plates. In all of the streamwise plots shown, mainstream flow over the plate goes from right to left. In spanwise plots, the vane hub (ID) and shroud (OD) locations are labeled. Figure 116 through Figure 120 are comparisons of non-dimensional surface temperature distributions in Kelvin for the uncooled plate, baseline cooling array with shaped holes, and the optimized cooling array with shaped holes at five gradually increasing span locations. As temperature is a well-understood life-limiting parameter and of greatest concern for durability design, it is reported here in the results. In each figure the uncooled plate surface temperatures are clearly much higher over the length of the plate. The uncooled temperature distribution decreases with downstream distance due to the existence of the large coolant discharge holes described in the methodology. As the coolant flow migrates towards the discharge holes on the plenum side of the plate, the coolant velocity is increasing slightly. This combined with the plate material being thicker downstream causes the non-linear drop in hot-side temperature.

Comparing the baseline and optimized cooling arrays each with shaped holes, it can be seen that the new distribution of holes, hole sizes, injection angles and compound angles over the surface of the plate works well in reducing surface temperature as determined by IRT for many of the span locations. At the 5% span location, in Figure 116, most of the length of the plate has reduced surface temperature due to the optimized cooling array. On the other hand, at the 95% span location in Figure 120, the baseline array temperatures are lower, which is an unexpected result knowing that the optimization resulted in compound angle injection towards this edge of the plate,

especially for the first few rows of holes. The effects in lowering temperature due to the OD-directed compound angles for the optimized design can be seen up until mid-chord. Still, baseline array temperatures are lower. This is likely one of the most affected spans in terms of differences between the plate and vane geometry and flow characteristics due to the endwall. On the vane, as the CEEF CFD in the optimization showed, the OD-directed flow is effective relative to the standard baseline cooling. However, here on the plate, with no secondary endwall secondary flows in the problem, the baseline performs better. In addition, the CHT CFD comparison of geometries showed greater differences in film cooling trends near endwalls relative to spans between 25% and 75%. Naturally, without endwalls, flat plate data will likely not represent vane data at high and low span locations. Therefore, results in Figure 116 and Figure 120 are likely less reliable than results at other span locations.

At 25% and 75% span locations, in Figure 117 and Figure 119, respectively, the cooling performance is fairly similar between the two designs although the optimized causes lower minimum temperatures near the leading edge. Overall, at these span locations, the optimized cooling array resulted in similar surface temperature levels as the baseline cooling array, however the local minimum temperatures near cooling holes is at least 2% lower for the optimized array. In addition, there is a slight increase in temperature just downstream of mid-chord for the optimized array at these locations that matches the trends observed for both span locations in the optimization results.

At midspan in Figure 118, the baseline cooling array exhibits a lower temperature, mostly downstream of the quarter chord location, but this makes sense and agrees with computational results from the optimization because it was found that the baseline design

was over-cooled at midspan. The optimized cooling array still results in a lower surface temperature by 3% near the leading edge and limits the amount of temperature fluctuation relative to the baseline design. Overall, the optimized cooling design results in surface temperatures comparable with the baseline design, with improvements in local minimum temperatures at most span locations, especially closer to the showerhead.

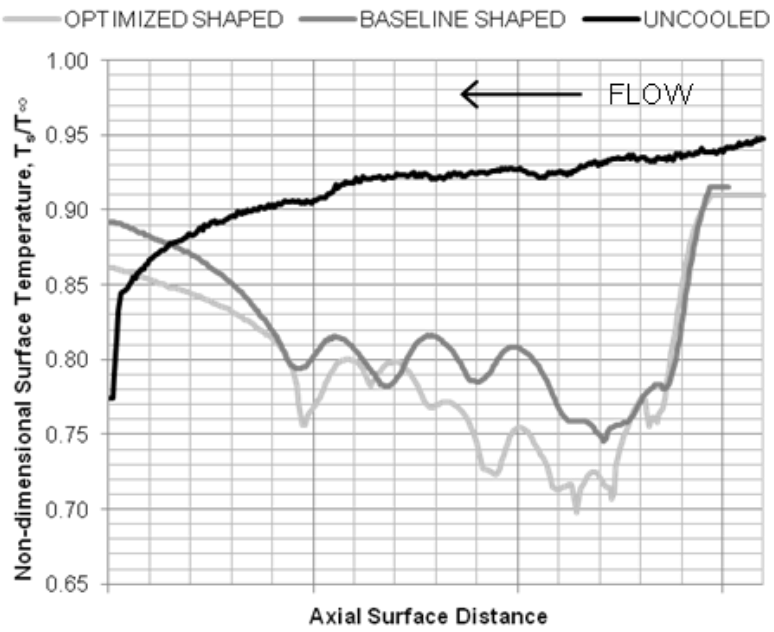

Figure 116 - Streamwise (axial) non-dimensional surface temperature on the uncooled, baseline, and optimized flat plate RTV PS cooling arrays at the 5% span location.

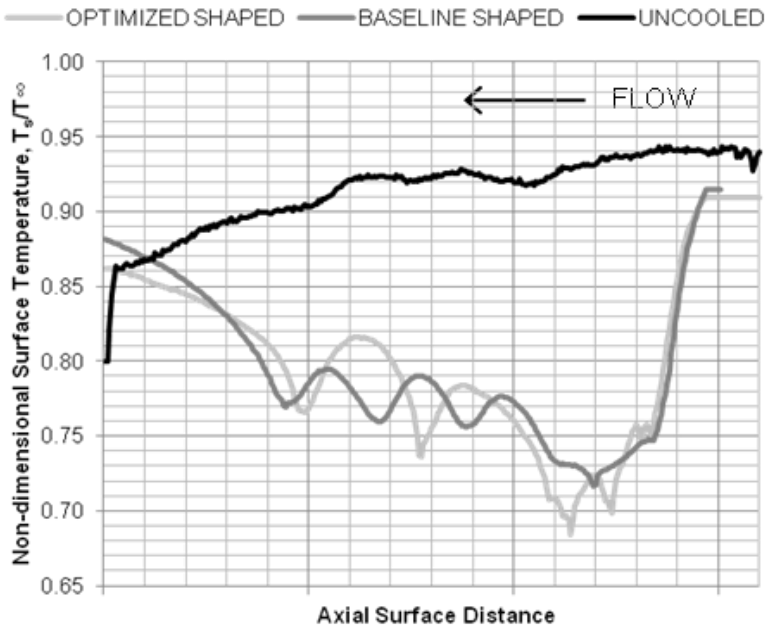

Figure 117 - Streamwise (axial) non-dimensional surface temperature on the uncooled, baseline, and optimized flat plate RTV PS cooling arrays at the 25% span location.

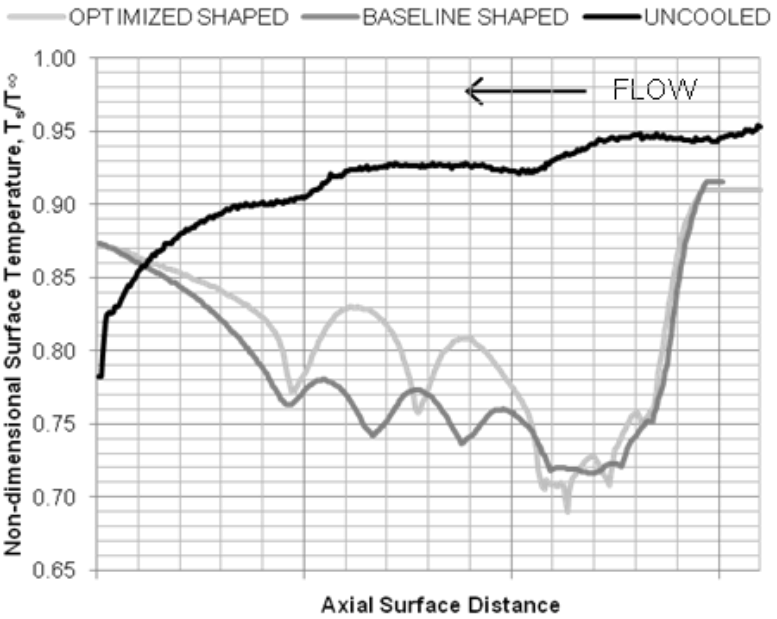

Figure 118 - Streamwise (axial) non-dimensional surface temperature on the uncooled, baseline, and optimized flat plate RTV PS cooling arrays at the 50% span location.

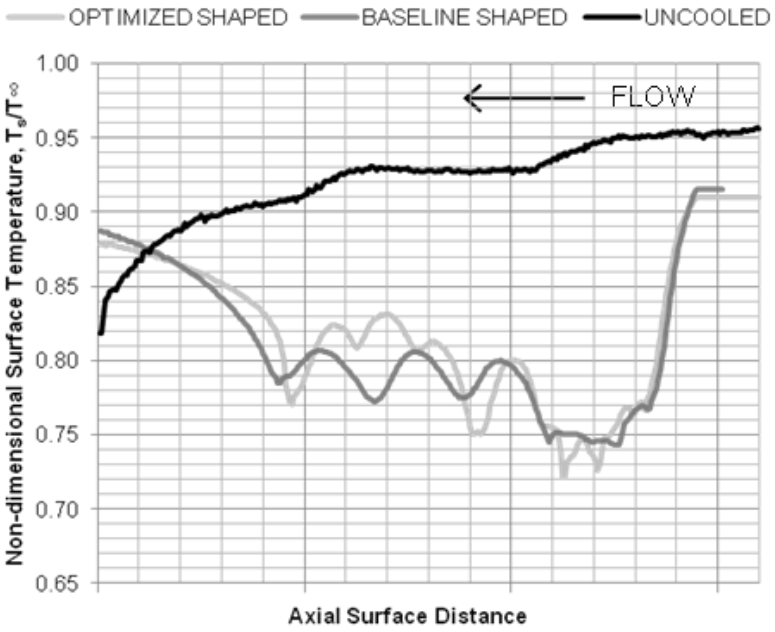

Figure 119 - Streamwise (axial) non-dimensional surface temperature on the uncooled, baseline, and optimized flat plate RTV PS cooling arrays at the 75% span location.

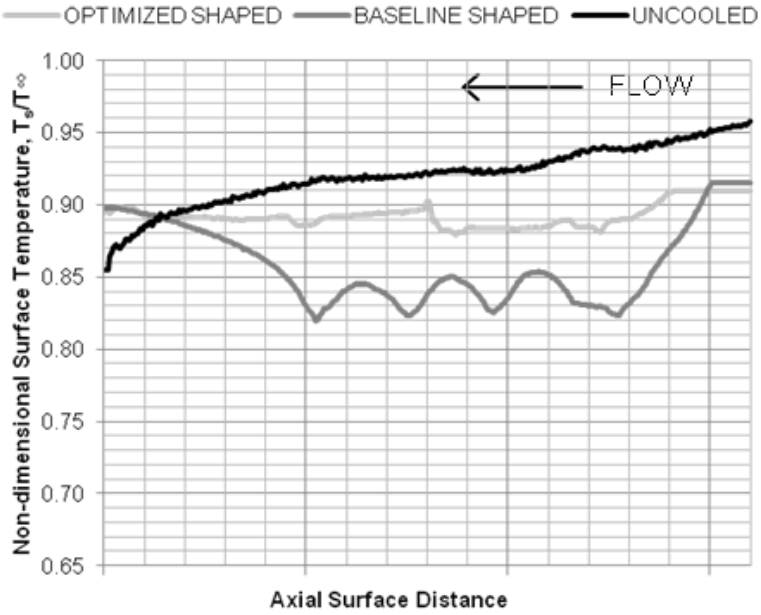

Figure 120 - Streamwise (axial) non-dimensional surface temperature on the uncooled, baseline, and optimized flat plate RTV PS cooling arrays at the 95% span location.

Figure 121, Figure 122, and Figure 123 are similar plots comparing overall effectiveness at the 25%, 50%, and 75% span locations, respectively. Overall effectiveness incorporates combined experimental effects of the mainstream flow, the surface temperature and the cooling flow temperature in the plenum. These span locations are shown since the cooling performance at these locations are more likely to model that on the vane surface, as the reasoning above explains. Overall, the same relative trends for the each span location can be seen for ϕ that was observed for T_s. In fact, the results appear to be an inverse of the temperature results. This is expected knowing that the experimental conditions, based on the Research Turbine Vane design levels, in the mainstream and cooling flow were closely monitored and the same between the three runs. The only small difference between the ϕ and T_s plots is that the percentage differences between baseline an optimized cooling array performance is slightly greater in the overall effectiveness comparisons. For example, at 25% span in Figure 117, the local minimum non-dimensional surface temperatures due to the first three cooling hole rows on the optimized array are 3% lower. This results in an increase in overall effectiveness of up to 0.06 as seen in Figure 121. Since overall effectiveness plots show similar relative (inverse) trends as non-dimensional temperature, these will be the only ϕ distribution plots given here in the results.

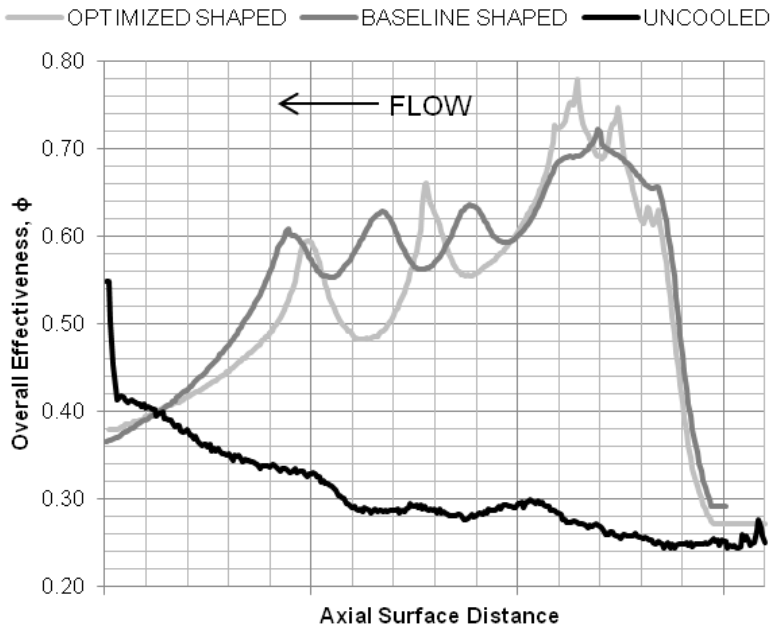

Figure 121 - Streamwise (axial) overall effectiveness on the uncooled, baseline, and optimized flat plate RTV PS cooling arrays at the 25% span location.

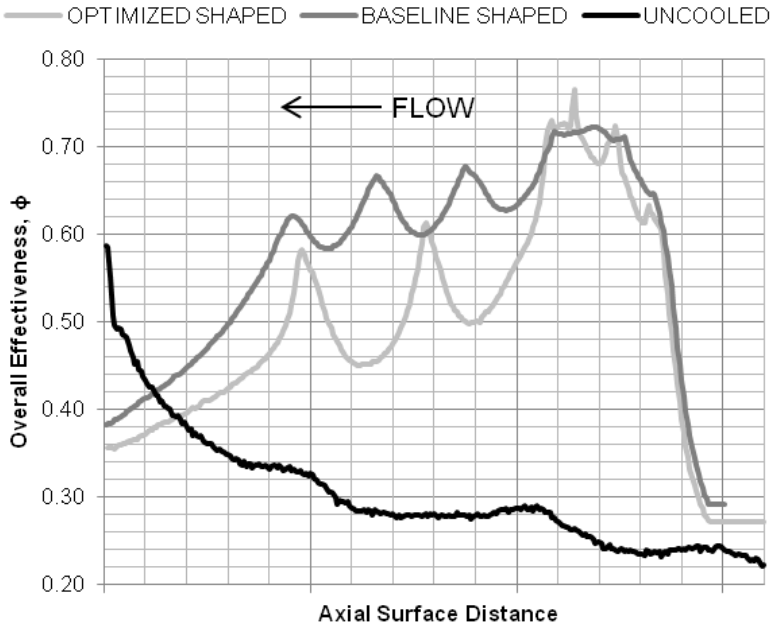

Figure 122 - Streamwise (axial) overall effectiveness on the uncooled, baseline, and optimized flat plate RTV PS cooling arrays at the 50% span location.

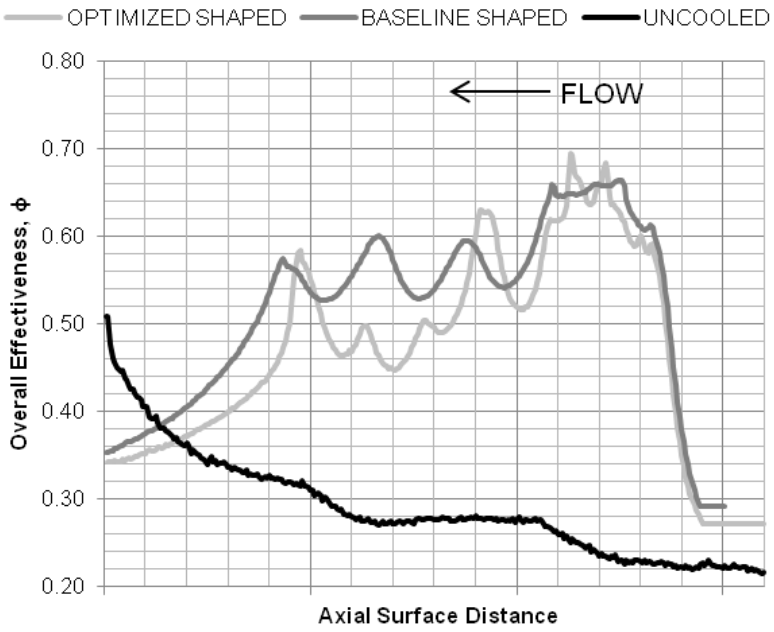

Figure 123 - Streamwise (axial) overall effectiveness on the uncooled, baseline, and optimized flat plate RTV PS cooling arrays at the 75% span location.

Figure 124 through Figure 127 are spanwise distributions of non-dimensional surface temperature at the leading edge, 25%, 50% and 75% vane pressure surface chord locations on the flat plate. In terms of how the cooling array lies on the vane, the hub (ID) is on the left side and the shroud (OD) is on the right, with midspan in the center. The optimized cooling array clearly results in lower temperature at the leading edge and at 25% chord. At 50% and 75% chord, it can be seen how the optimization redistributed the wasteful cooling pileup at midspan into two cooler areas at about 20% and 80% span. It is also seen how a cooling design optimized for a 3-D vane surface results in an asymmetric temperature distribution on a flat plate, unlike the symmetrical baseline design. For all chord locations, the uncooled plate temperatures are well above the cooled temperatures, showing the general benefit of film cooling.

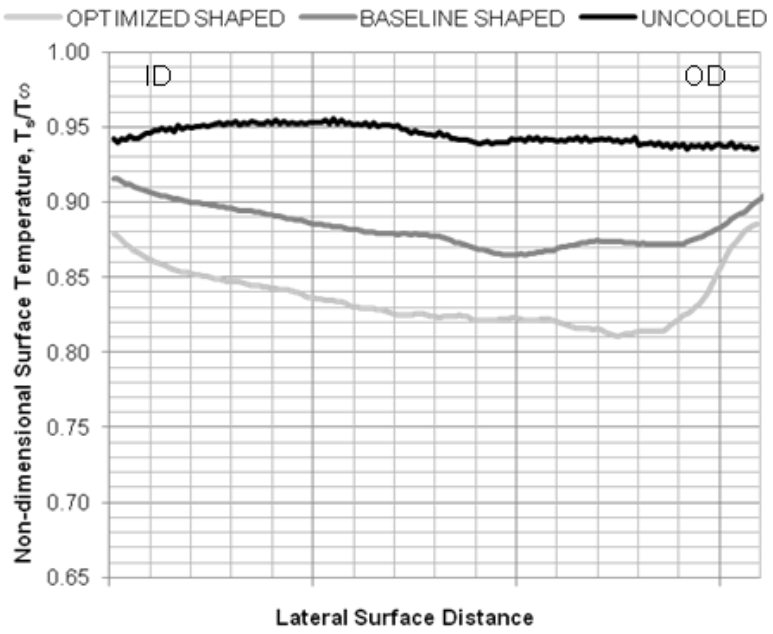

Figure 124 - Spanwise (lateral) non-dimensional surface temperature on the uncooled, baseline, and optimized flat plate RTV PS cooling arrays at the leading edge location.

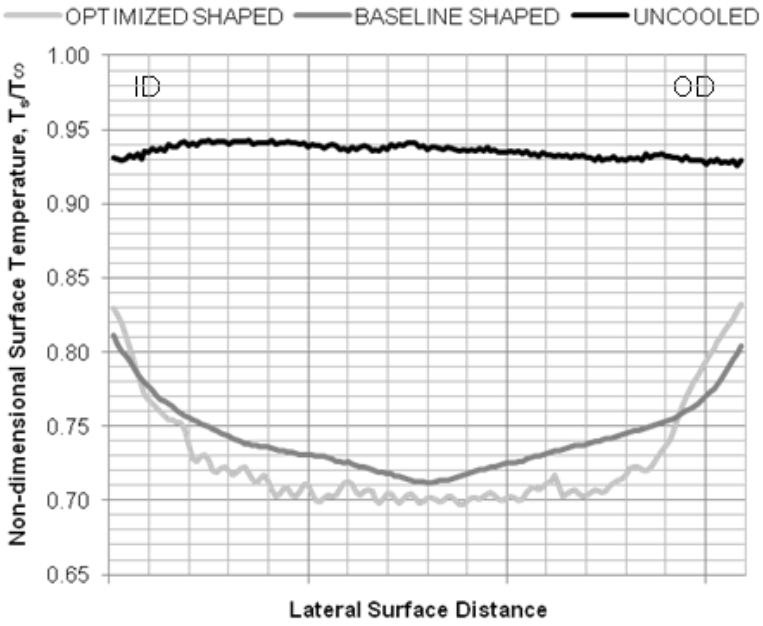

Figure 125 - Spanwise (lateral) non-dimensional surface temperature on the uncooled, baseline, and optimized flat plate RTV PS cooling arrays at the 25% surface chord location.

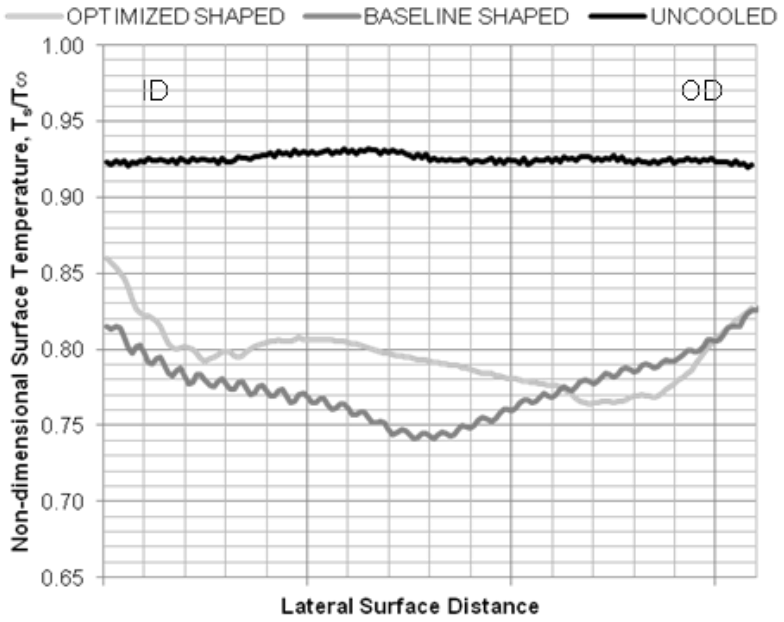

Figure 126 - Spanwise (lateral) non-dimensional surface temperature on the uncooled, baseline, and optimized flat plate RTV PS cooling arrays at the 50% surface chord location.

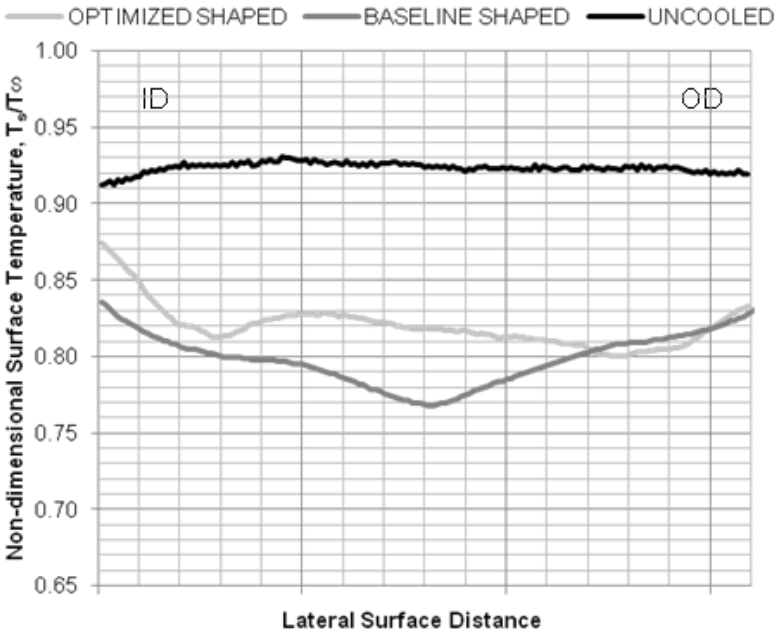

Figure 127 - Spanwise (lateral) non-dimensional surface temperature on the uncooled, baseline, and optimized flat plate RTV PS cooling arrays at the 75% surface chord location.

Comparison of Four Hole Shapes on Optimized Design

First, surface temperature contours from the IRT runs for all six flat plates at design flow and blowing conditions are given in Figure 128. Here, darker color indicates cooler surface temperatures. The flat plate cooling arrays were modeled to be mirror images of the vane about the leading edge, therefore the hub is at the top of the images and the shroud at the bottom. As explained in the methodology, to match the 3-D RTV cooling hole *L/D*, there are two rectangular areas of reduced thickness of reduced metal thickness on the plate which can be seen in the uncooled plate image. This x-ray effect can also be seen in CHT CFD simulations [132]. The coolant discharge holes can be seen on the far left side of the uncoooled plate. The second image in Figure 128 is the baseline cooling array with shaped holes. The cooling pileup at midspan due to the midspan-oriented showerhead cooling can be seen as well as the simple cooling characteristics of repeating symmetrical straight rows.

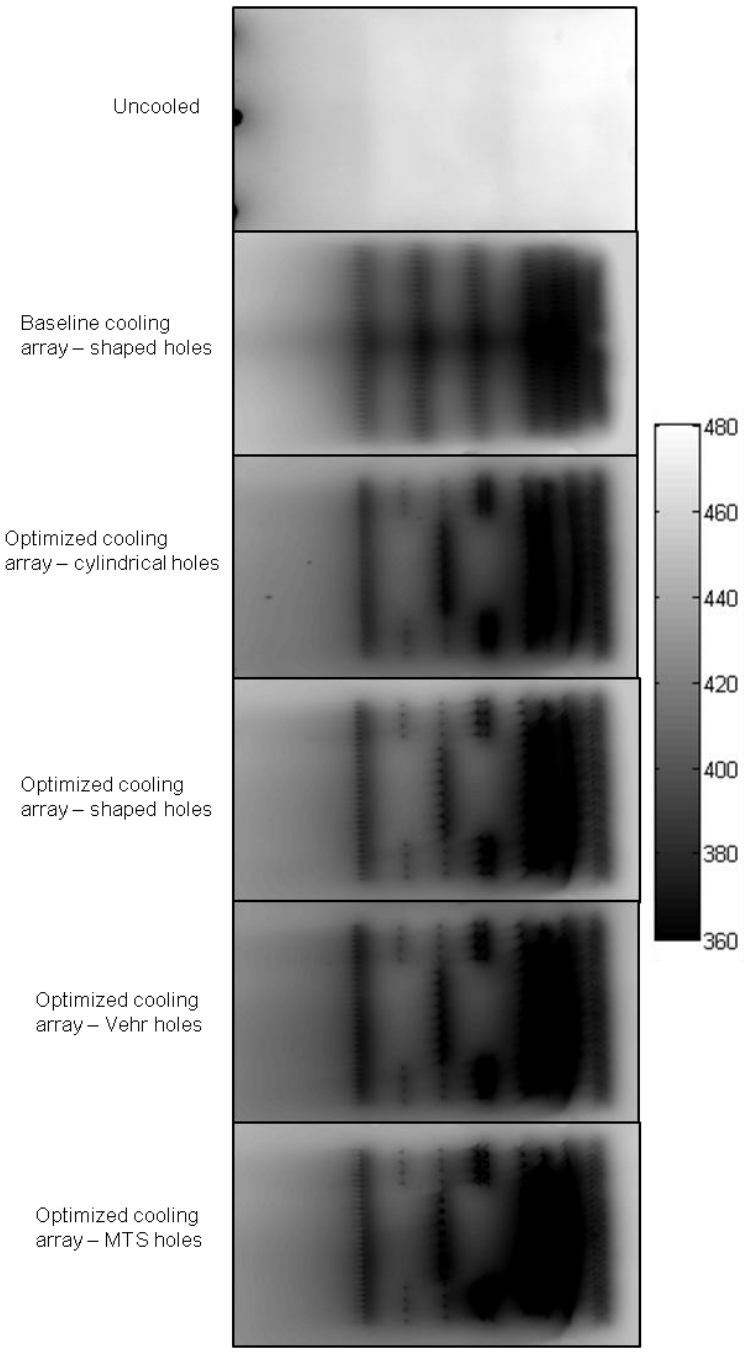

Figure 128 - Surface temperature contours [deg K] at design main flow and blowing conditions obtained by IRT for the six flat plates. Air flow is from right to left.

The third through sixth images in Figure 128 are results for the four different hole shapes tested for the optimized cooling array. The fan shaped holes are simply referred

to as shaped holes here. The shroud-oriented (directed towards the OD) holes in the upstream set of cooling hole rows clearly add more cooling to the lower portion of the image relative to the baseline cooling array. As seen in previous images, the optimized array also removes cooling from areas near midspan where cooling was wasted according to the optimization. Comparing the different hole shapes on the optimized array also shows improved cooling performance toward the shroud for the Vehr holes and MTS holes, especially between the leading edge of the array and mid-chord. The next sets of data look at spanwise and streamwise temperature distributions for the different hole types at different locations on the flat plates.

Figure 129 through Figure 133 are comparisons of streamwise distributions of non-dimensional surface temperature for four different cooling hole shapes of only the optimized cooling array at the same span locations as shown in Figure 116 through Figure 120. Hole locations are indicated by the vertical dotted lines in the plots. Due to the unique optimized design, it can be seen that at some span locations, especially closer to the lateral edges, there are more cooling hole rows than others. Overall, there are only minor differences, which makes sense since the only thing different between the plates is the specific shape of the cooling holes.

At the 5% span location in Figure 129, cylindrical holes are outdone by the other three hole types especially near the leading edge. This result is not surprising knowing the detrimental non-diffusive nature of cylindrical holes. The MTS hole performs well in this particular area and provides the lowest minimum temperature at this span location as well as at every other except 95%. At the 95% span location in Figure 133, shaped holes appear to be the worst option of the four while cylindrical holes are the best upstream and

Vehr holes the best farther downstream. The Vehr holes perform well here relative to their shaped counterparts at this location. Also, the cylindrical holes result in a highly different temperature distribution, perhaps due to the additional cooling flow and mixing typically induced by cylindrical holes. However, for the same reasons as stated for Figure 116 and Figure 120, the lack of endwalls makes relative trends between the hole types at these locations unreliable in terms of expected performance on the 3-D vane.

At the 25% span location in Figure 130, although not by much, the shaped holes perform the worst relative to the others with the MTS hole providing the lowest temperatures over most of the surface chord distance. At the 75% span location in Figure 132, cylindrical holes perform well over most of the length of the plate. Unlike the baseline cooling array, in terms of compound angle injection, the optimized cooling array is not symmetrical about midspan. Here, there is a lot of mixing due to the interaction of shroud-oriented upstream cooling holes with axially-oriented downstream holes which is likely causing cylindrical holes to perform better.

At 50% span location in Figure 131, the temperature levels are the closest between the hole types, with shaped holes again performing the worst and MTS holes providing the lowest temperatures except downstream of the last row. Vehr holes dominate downstream of the last row and appear provide lowest temperatures far downstream for most span locations.

Cylindrical holes, relative to the other hole types perform well, especially with respect to shaped holes at the more reliable span locations of 25%, 50%, and 75%. This is contrary to many well-known works in the past. However, most of the works in the past that compared various hole types used constrained conditions with the single hole,

multiple hole, or double row setups that do not model a typical full-map engine-ready cooling array. The major difference is that few, if any, works have incorporated combined effects of cooling hole rows downstream of a showerhead for different hole types on a realistic array. Without more instrumentation such as two-component hot-wires near the surface which were not used here, more information regarding this finding cannot be provided. It is hoped that planned CHT CFD analyses of the same four flat plates and hole types will provide more insights regarding the relatively poor performance of shaped holes.

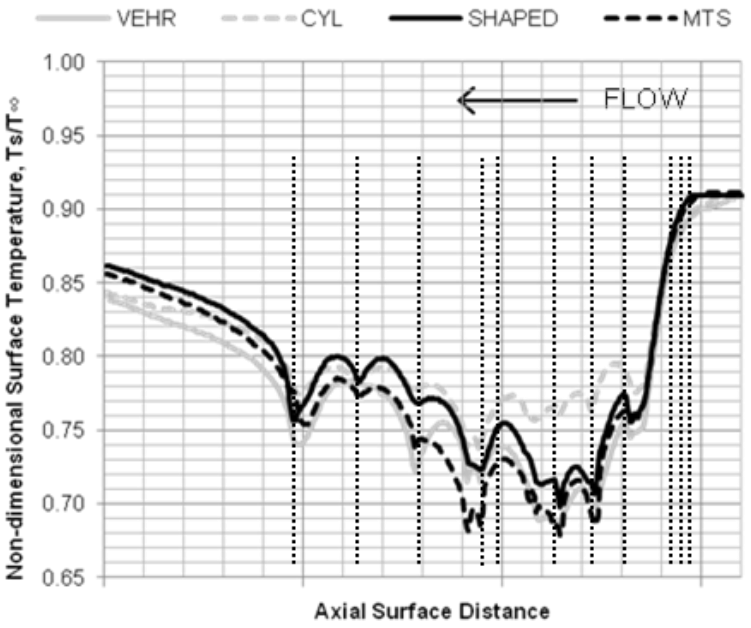

Figure 129 - Streamwise (axial) non-dimensional surface temperature for the four different hole shapes on the optimized flat plate RTV PS cooling array at the 5% span location.

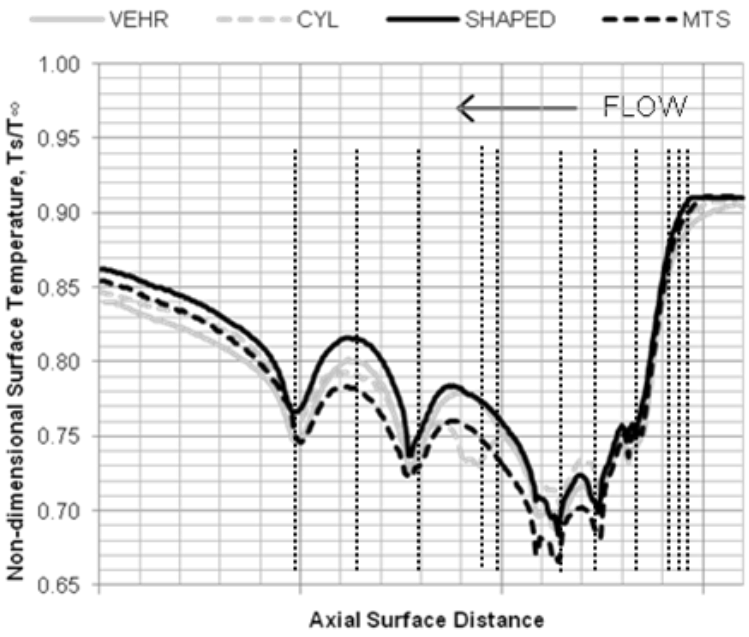

Figure 130 - Streamwise (axial) non-dimensional surface temperature for the four different hole shapes on the optimized flat plate RTV PS cooling array at the 25% span location.

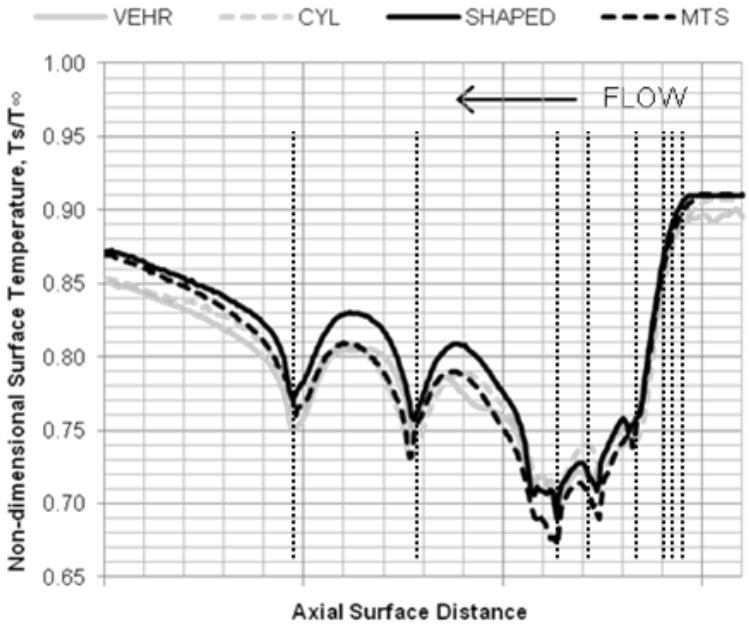

Figure 131 - Streamwise (axial) non-dimensional surface temperature for the four different hole shapes on the optimized flat plate RTV PS cooling array at the 50% span location.

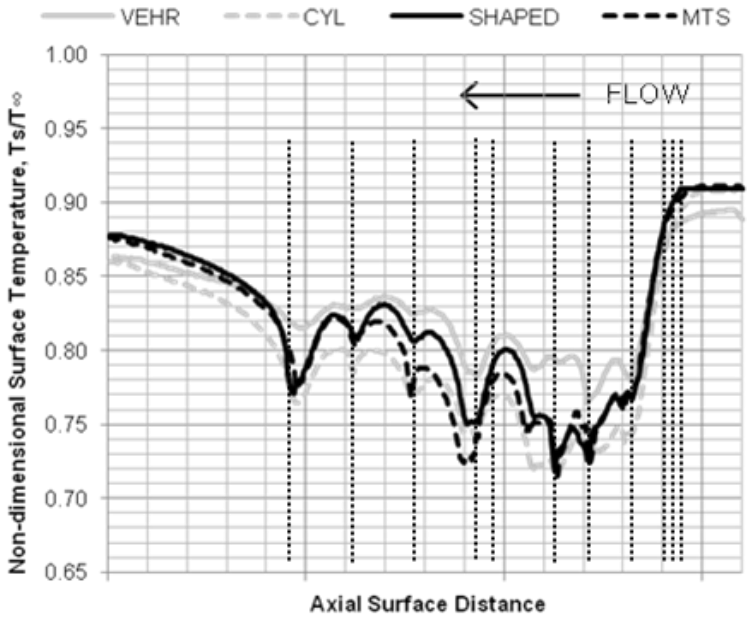

Figure 132 - Streamwise (axial) non-dimensional surface temperature for the four different hole shapes on the optimized flat plate RTV PS cooling array at the 75% span location.

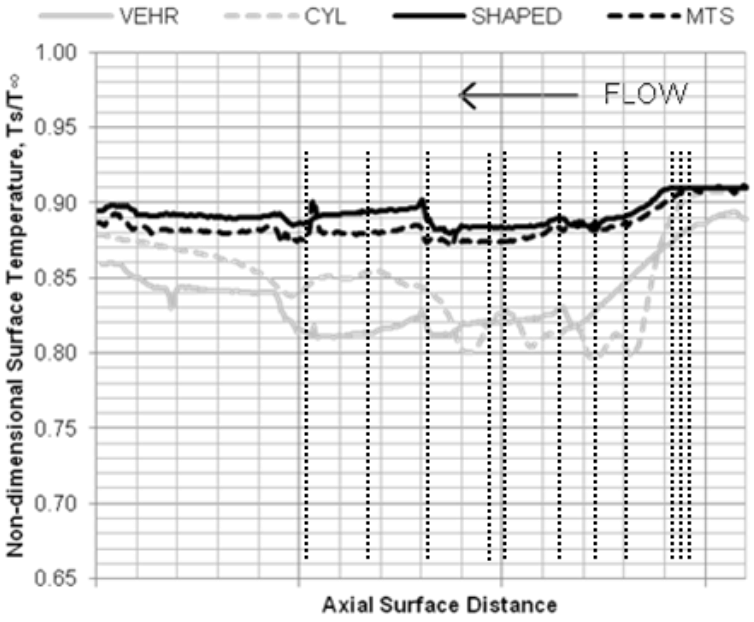

Figure 133 - Streamwise (axial) non-dimensional surface temperature for the four different hole shapes on the optimized flat plate RTV PS cooling array at the 95% span location.

Figure 134 through Figure 137 are spanwise surface temperature distributions for the four different hole types on the optimized cooling array at the leading edge, 25%, 50%, and 75% pressure surface chord locations. Again, midspan is at the center of these plots. There is little spanwise difference in these plots, again, since only the cooling hole type has changed between them. At the leading edge, the shroud-oriented showerhead and following cooling hole rows clearly reduce temperature on the right side of the plot. Also at the leading edge, Vehr holes provide the best cooling, but MTS holes appear to do relatively well at all other chord locations, especially at 25% chord. Relative to the baseline array, the spreading of cooling flow away from midspan in the optimization and the shroud-oriented cooling is clearly seen at the 50% chord location. Finally, at 75% chord, the MTS holes do well at midspan, while Vehr holes cause the lowest temperatures towards the outer edges.

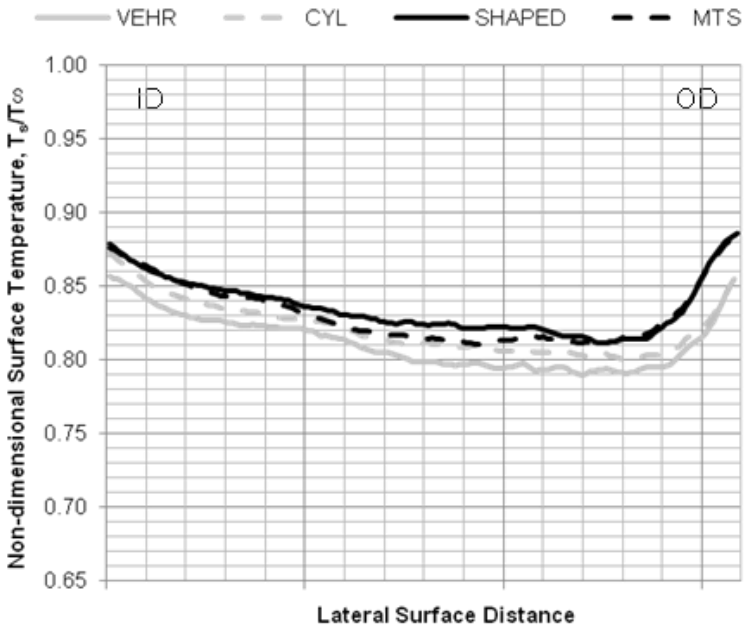

Figure 134 - Spanwise (lateral) non-dimensional surface temperature for the four different hole shapes on the optimized flat plate RTV PS cooling array at the leading edge location.

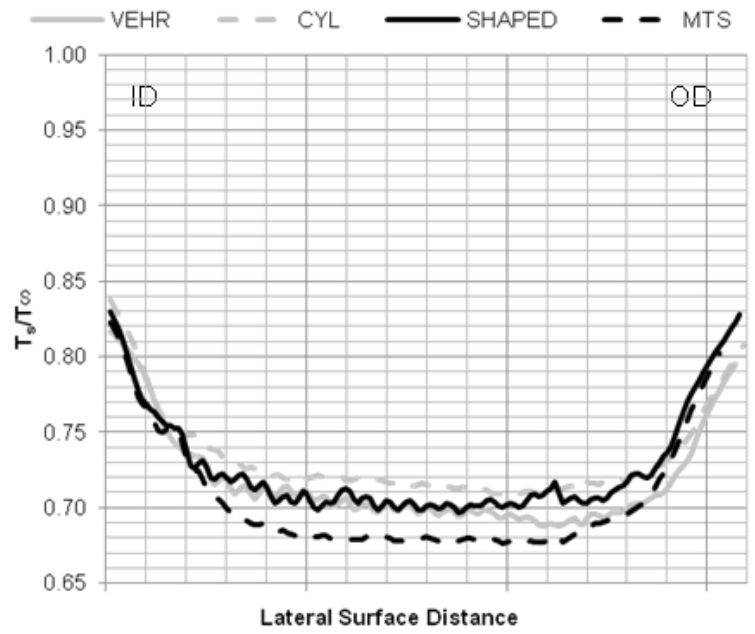

Figure 135 - Spanwise (lateral) non-dimensional surface temperature for the four different hole shapes on the optimized flat plate RTV PS cooling array at the 25% surface chord location.

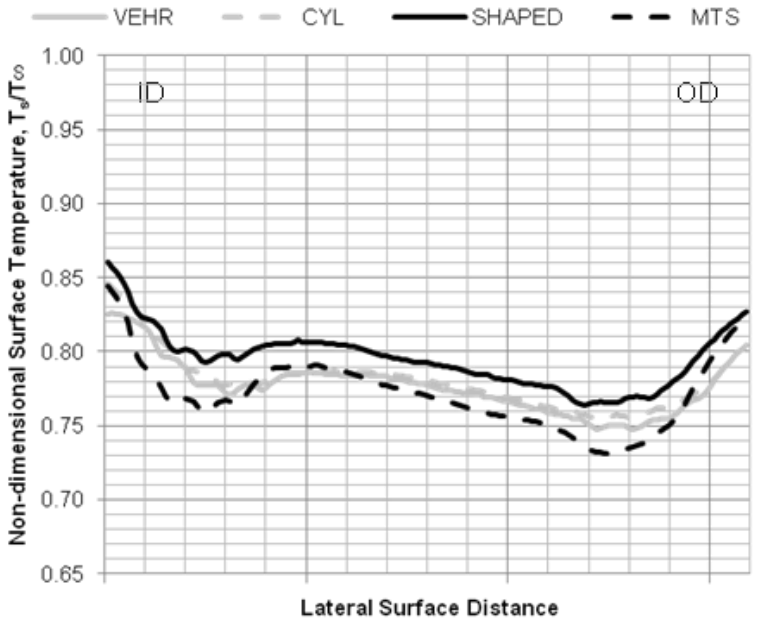

Figure 136 - Spanwise (lateral) non-dimensional surface temperature for the four different hole shapes on the optimized flat plate RTV PS cooling array at the 50% surface chord location.

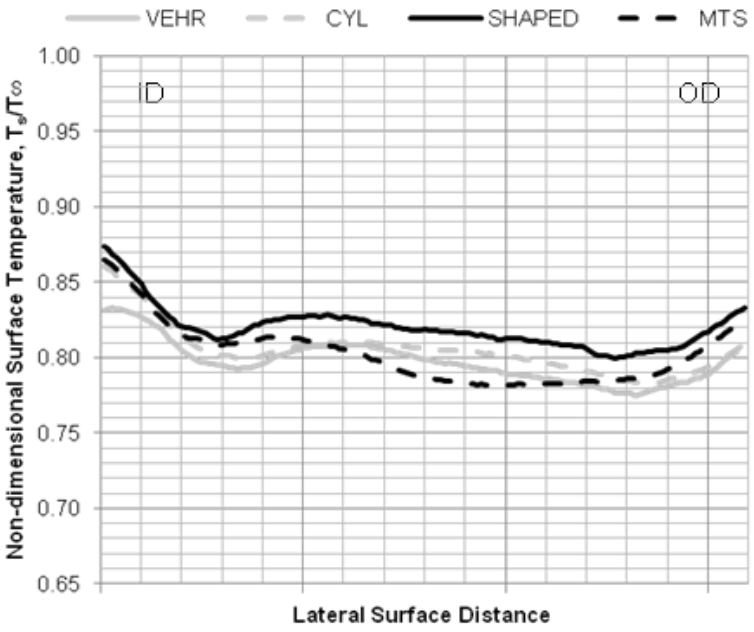

Figure 137 - Spanwise (lateral) non-dimensional surface temperature for the four different hole shapes on the optimized flat plate RTV PS cooling array at the 75% surface chord location.

The comparison of four different cooling hole shapes on the optimized film cooling array was conducted to determine which hole types performed the best on different areas of the flat plate surface in order to dictate the next vane design, keeping in mind that results near the lateral edges were deemed unreliable relative to what is expected on the vane pressure surface. The new mini-trench shaped (MTS) hole performed well at most span locations relative to the other hole types tested. IRT results suggest that for the optimized cooling array on the vane PS, Vehr holes are appropriate in the farthest downstream row, while MTS holes are appropriate between 25% and 75% span, especially for the first three rows of holes downstream of the showerhead array. The IRT experiments also showed notable improvements in film cooling performance for the optimized cooling array relative to the baseline, especially considering local minimum temperatures.

VIII. Conclusions and Future Work

Optimization of RTV PS Film Cooling Array

Research over the last several decades has resulted in much knowledge that is used in an ad hoc manner for turbine durability design. State-of-the-art durability designs such as that on the baseline RTV cooling array are often grounded in simple correlations from decades ago to allow for rapid analysis and turnaround times. They are not routinely grounded in the physics of the flowfield and do not allow for tailoring of a cooling design to the unique requirements of a modern 3-D turbine engine component in its expected operating conditions. For example, there is no three-dimensional, heat transfer prediction in-the-loop design method documented in open literature to design film cooling arrays. Instead, a number of assumptions about film cooling performance are typically made that do not take into account critical data from reliable heat transfer simulations and modern computing methods.

Given the same amount of cooling flow, the novel optimization method outlined here improved the PS film cooling performance of the Research Turbine Vane by spreading cooling flow out so that hot spots were mitigated and redistributing cooling away from over-cooled areas on the surface to areas that were in much greater need of cooling, such as the shroud in this case. While there are a few weaknesses in the accuracy of the CEEF CFD as indicated in Appendix B, the widely used turbomachinery CFD code performs well in general in other cases and for its primary purpose, which is to resolve differences in heat transfer characteristics between cooling designs with the optimization. According to CEEF CFD evaluations between the baseline and optimized

designs, decreases in near-wall gas temperature and near-wall heat flux are seen at most span locations. The optimized cooling array resulted in a reduction of average near-wall gas temperature of 2 K, a reduction in the maximum near-wall gas temperature of 3 K, a reduction in maximum heat flux of 2 kW/m^2 and a reduction in pressure loss over the vane, all while maintaining a constant level of surface-averaged overall effectiveness. Based on assigned criteria, the optimized design also resulted in a 257% increase in fitness compared to the baseline cooling design. Here, the area of CFD evaluation was larger than the area where holes could be placed. In a more ideal case, if less cooling air was required to cool the hot shroud and its lack of cooling holes, even larger performance improvements are expected. The optimization required approximately 12 hours of computational time per generation using 100 2.67 GHz CPUs, for a total of 156 hours, or just under one week.

Assuming the baseline level of cooling effectiveness is acceptable, and assuming optimized cooling arrays were employed for an entire wheel of vanes, this method could also be used to increase engine thermal efficiency. Using the optimized cooling array and decreasing cooling flow until surface-averaged film cooling performance decreases and temperatures increases to levels of the baseline cooling array, with less cooling flow diverted from the compressor core flow to stator components in the wheel, thermal efficiency gains could be realized. The relative increase in core flow allows more work to be extracted from the flow by the turbine. There may be other ways to parameterize film cooling designs that were not employed here, although the current method allows for effective design-space exploration for a large number of candidate designs. The optimization ultimately showed that an improved film cooling array could be redesigned

by changing only certain film cooling variables using an efficient form of CFD within a reasonable amount of time.

CHT CFD Comparison of Flat Plate and Vane

To justify the use of flat plate experiments in comparing film cooling designs for the Research Turbine Vane, conjugate heat transfer CFD cases were run for the vane and flat plate with the baseline cooling array where each were intended to model their respective experimental conditions. Due to the limited amount of instrumentation necessary and decreased cost of simplified test articles relative to full-annulus blowdown rigs like the TRF, flat plate experiments are less expensive and highly repeatable. In addition, much of the historical film cooling literature relies on data and correlations found from flat plate models and laboratory experiments.

Differences in non-dimensional surface temperature distributions between the vane and plate geometries, especially downstream of the showerhead array, only ranged between 3% and 7% at both the 25% and 50% span locations, which is explained by the difference in the coolant-to-freestream pressure and temperature ratios enforced in the boundary conditions between the cases. The pattern of surface temperature between film cooling rows on both geometries were closely matched at 25% and 50% span locations. Differences in streamwise temperature distributions at span locations toward the hub and shroud are greater between the vane and plate which is explained by the nature of flow near endwalls in the vane case. Therefore, it is suggested that any results in flat plate experiments near the lateral edges are less reliable in representing the vane than the results for the middle half of the lateral span. This study has shown, through full grid

CFD simulations that include the effects of solid conduction, that use of a flat plate with the same engine-representative cooling array to model vane PS heat transfer characteristics is accurate, especially for the middle half of the vane span just downstream of the showerhead.

Infrared Thermography Experiments

The IRT experimental study using flat plate models to represent the pressure side cooling array of a modern turbine inlet vane has shown the capability of obtaining abundant data in the form of 2-D full map surface temperature distributions. In comparisons of streamwise non-dimensional surface temperature distributions on the baseline and optimized plates, at the 5% span location, the optimized cooling array exhibited a lower temperature by 5% over most of the chord length. At the other lateral edge, at 95% span, the baseline cooling array exhibited a lower temperature than the optimized array. This result at 95% span does not match the result of the computational optimization for the vane, which clearly reduced temperature at this span due to the redirection of cooling flow toward the shroud. Also, since the CHT CFD comparisons of the two geometries were quite different near the endwall span locations, these results are considered unreliable regarding expected cooling performance on the vane. On the other hand, since the reported CHT CFD comparison of the geometries showed similar results at span locations between these, results for the middle half of the lateral span are considered reliable.

At 25% and 75% span locations, the optimized cooling array resulted in comparable surface temperature levels to the baseline cooling array. However, the local

minimum temperatures near cooling holes for the first three optimized rows is at least 3% lower for the optimized array. In addition, there is a slight increase in temperature just downstream of mid-chord for the optimized array at these locations that matches the trends observed in the optimization. The optimization also showed that less cooling, and hence fewer cooling holes, were required at midspan across most of the chord length. This resulted in IRT measurements for the optimized cooling array exhibiting higher surface temperatures at 50% span. Like for 25% and 75% span, minimum temperatures due to the first cooling hole three rows were also lower for the optimized design at midspan. In addition, distributions of overall effectiveness showed the same relative inverse trends as non-dimensional surface temperature.

The comparison of four different cooling hole shapes on the optimized film cooling array was conducted to determine which hole types performed the best on different areas of the flat plate surface in order to dictate the next vane design, keeping in mind as explained before, that results very close to the lateral edges are unreliable relative to what is expected on the vane pressure surface. The new mini-trench shaped hole performed well at most span locations relative to the other hole types tested. IRT results suggest that for the optimized cooling array on the vane PS, Vehr holes should be used in the farthest downstream row and near the edges, while MTS holes should be used mostly near midspan and for the first three entire rows of holes just downstream of the showerhead array. Ultimately, the IRT experiments showed notable improvements in film cooling performance for the computationally optimized cooling array.

Overall Summary

As a first effort to fundamentally change the way in which film cooling designs are generated, the computational optimization, which took into account the critical heat transfer effects of the 3-D external flow using the latest in external flow turbomachinery CFD and factored in the combined effects of multiple variables on film cooling arrays, was successful in assessing differences between 1,800 candidate designs using prescribed estimation techniques in relatively short order. This is an improvement upon the current state of the art for turbomachinery durability design. The IRT experimental comparison of the modern baseline and optimized design flat plate film cooling performance confirmed notable improvements were made due to the optimization and support the use of a brand new cooling hole shape. The CHT CFD comparisons of the flat plate and vane geometries justified the use of flat plate experimentation and gave insights into the relative performance to be expected of the baseline and optimized cooling design in experiments on the vane in the future. This process has also shown that there is potential for cooling mass flow to be saved for turbine components designed in this manner.

Recommendations for Future Work

The following is a list of work suggested as a logical follow-on to that reported in this dissertation. Ultimately, with flat plate IRT and full-wheel TRF blowdown experiments, the two types of CFD, the two geometries available for investigation using CHT CFD, and the baseline and optimized film cooling arrays, there is still much that can be studied in the future including:

- Comparing the baseline and optimized film cooling array performance using CHT CFD on the vane geometry to determine how the relative trends compare to that for the CEEF CFD on the vane.
- Comparing the baseline and optimized film cooling array performance using CHT CFD on the flat plate geometry to determine how the relative trends compare to that for the flat plate IRT experiments.
- Comparing using CHT CFD how well the flat plate and RTV geometry film cooling performance matches for solely the optimized array, just as was done for the baseline array.
- Simulating using CHT CFD the RTV with design conditions with a simulated kapton layer, since the experimental vanes have heat flux gauges with this extra layer, and compare with TRF vane heat flux and surface temperature data for further validation.
- Performing additional generations in the CEEF CFD RTV PS film cooling array optimization using local surface grid refinement or overset grids at the locations of holes to better resolve flow detail at the hole exits.
- Performing sensitivity studies of the effects of changing $P_{t,c}/P_{t,\infty}$ versus $T_{t,c}/T_{t,\infty}$ using various CHT CFD cases using the baseline cooling array on either the vane or plate geometry to determine which of the two variables have a greater impact on film cooling.
- Testing the optimized film cooling array on a 3-D vane (see Figure 138) in the Turbine Research Facility after assigning cooling hole types to the PS based on IRT experimental results and flat plate CHT CFD results to determine if the actual

turbine component with an optimized array performs better than the vane with the baseline cooling array.

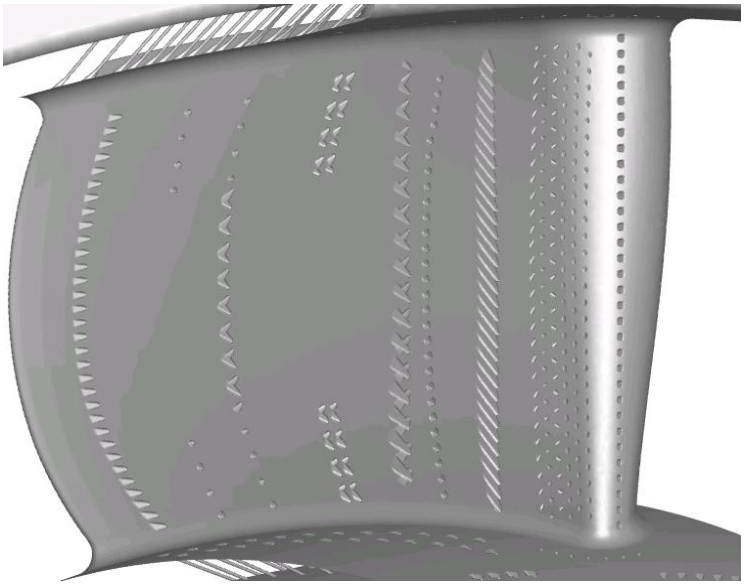

Figure 138 - CAD representation of 3-D RTV with optimized cooling array and shaped holes.

- Performing CHT CFD code *Leo* validation using the flat plate geometry and IRT experimental results.
- Comparing 3-D RANS CHT CFD simulations of the RTV using Bob Ni's *Leo* code to that using the 3-D LES CHT CFD code by Roger Davis to determine similarities and any advantages between the two.

All of these studies would be highly worthwhile in advancing the state-of-the-art in turbomachinery durability for the Research Turbine Vane and for the science of film cooling.

APPENDIX A: AFRL Turbine Research Facility (TRF) Details

Turbine Research Facility Flowpath Study

Abstract

The purpose of this investigation [172] is to model the 3-D flow field inside the AFRL Turbine Research Facility (TRF). Simulations here aided in preparation for short-duration vane-only tests with a novel turbine nozzle guide vane design installed. Subsequent experimental runs will obtain critical heat transfer data on the vane surfaces with and without cooling flow. The test hardware for experimentation is a 360-degree inlet vane annulus with 23 vanes. The computational fluid dynamics (CFD) domain used here models the flow in a 1/23rd sector of the annulus with periodic boundary conditions from a specified upstream distance, through the vane passage, past an isolation valve, to the end of the passage where flow exits to a dump tank. The primary objective is to assess how the variable area choked isolation valve located downstream of the test section changes the properties on the vane, downstream after the vane, in the nozzle at the valve location, and to see what other flow phenomena such as shocks or secondary flow potentially exist. These passage flow characteristics can vary depending upon the geometry of the vane design installed and the resulting swirl distribution. Thus, the flow resulting from different valve positions is assessed for the current hardware design at a gas turbine-representative set of initial conditions. Ultimately, after some modifications to the computational domain, the appropriate valve setting is found in simulations to provide design conditions for the vane in the experiments. Predictions are compared to

the same preliminary TRF experimental data for vane pressure loading. This study serves to help facility operators more expediently and accurately set the valve positions in future TRF runs and provides a comparison of simulated uncooled and cooled vane pressure results with initial experimental data.

Introduction

The objective of testing currently ongoing at the AFRL Propulsion Directorate is to assess the aerodynamic and thermal performance of the High-Impact Technologies (HIT) Research Turbine stage and one half in order to advance the state-of-the-art for high temperature, greater efficiency turbine engines. Before planned stage-and-one-half runs with the rotating hardware, tests were conducted with only the inlet guide vane hardware installed. CFD simulations of the flow passage in the Turbine Research Facility (TRF) rig aided in assessing the expected flow properties on the test article for the vane-only experimental configuration. By changing the computational domain to model flow in the rig with different downstream isolation valve settings, time and effort can be saved in order to find the proper settings that provide proper design conditions for the hardware being interrogated.

The Turbine Research Facility is a full-scale experimental blowdown rig designed to obtain pressure, surface temperature, and surface heat flux data from various installed single shaft turbine hardware designs [173]. In this rig, flow starts in the upstream pressurized tank, through the test section and into dump tanks. Surface temperature is monitored using surface mounted thermocouples on the vanes, static pressure data is gathered using taps leading to Kulite transducers on the surface at varying span locations,

and heat flux data is obtained using custom-designed double-sided thin film heat flux gauges. Heat flux data is obtained from vanes with film cooling holes as well as without. Sections of the vane annulus are designed and instrumented in such a way as to obtain separate measurements of both uncooled and cooled heat flux, surface temperature, and surface pressure. The TRF is capable of operating as a one-and-a-half stage, vane and rotor, or in the case of the current work, vane-only configuration. The TRF operates at flow conditions that are non-dimensionally consistent with the turbine environment. The vane design interrogated here is called the HIT Research Turbine Vane (RTV). An isolation valve located in the nozzle portion of the flow passage downstream of the test section can be set to varying flow area intervals which in turn sets the test duration, stage pressure ratio, and mass flow rate. The isolation valve displaces axially and is located in the middle of a converging-diverging (C-D) nozzle. Depending on the valve setting and the hardware design being tested, this may ultimately change the flow properties on the vane, at the vane outlet, and may force noteworthy flow phenomena in the passage itself.

Many fundamental CFD assessments have been completed in the past to predict outcomes in experiments and to reduce operational risks for high pressure turbomachinery components. CFD has been used to asses unsteady effects of vane-blade interactions in turbomachinery [174], to perform comprehensive aerodynamic assessment for multistage configurations [175], to assess airfoil scaling effects on unsteadiness in a stage-and-a-half turbine [176], and to reduce resonant stresses on turbine blades [177]. CFD methods can be used as a check prior to experiments to ensure proper conditions are tested. A simulation similar to this work was performed in 1996 by Pratt & Whitney [178] for the TRF, in which stage inlet and outlet properties were evaluated due to the

nozzle area changes from the closing valve. An Euler inviscid model was used with similar operating conditions in which relevant vane-only and full stage simulations were accomplished. Vane exit Mach number was plotted with varying flow area for both configurations. The current work using more advanced CFD methods may be used as a comparison to the original study.

The figures produced in previous work [178] had been used until recently it was decided with today's CFD computing power and repeatability, and with the knowledge that each new vane and/or blade design and flow path installed in the TRF produces slightly different flow property data, the simulation should be redone, ideally for increased accuracy. Thus for best results, this study can be efficiently repeated for all new hardware installed for reference to expected flow estimates. In addition to the quantitative vane property data, this new study may provide insight into qualitative data regarding secondary flows, separation, and shocks. This is advantageous as this reduces the experimental cost of establishing a matrix of run parameters for different valve positions by exercising the blowdown facility multiple times and recording the data. Attempting to perform by experimentation the same work done via simulation here, along with any new findings or roadblocks, may take anywhere from weeks to months to complete, not to mention a significant amount of labor and monetary cost. Therefore, the current simulations serve multiple purposes. They provide a thorough estimate of flow properties in the TRF passage which is ideally improved over the original study [178], help prepare proper isolation valve settings for the intended hardware design conditions within the experimental test matrix, and they may be used as a prediction tool for comparison with experimental pressure and temperature data taken in the rig.

It is originally expected that with the RTV which is designed to run with an inlet Mach number of 0.11 and outlet Mach number of 0.88, with additional flow-choking occurring at the C-D nozzle of the isolation valve, and that a proper flow property range will be set up for isolation valve positions starting at about 40% closed getting progressively better the more the downstream flow area is reduced. However, unlike the current transonic RTV design, the TRF has been run in the past in a vane-only configuration with only subsonic vane designs that had lower exit swirl and the flow in the TRF passage may behave differently as a result.

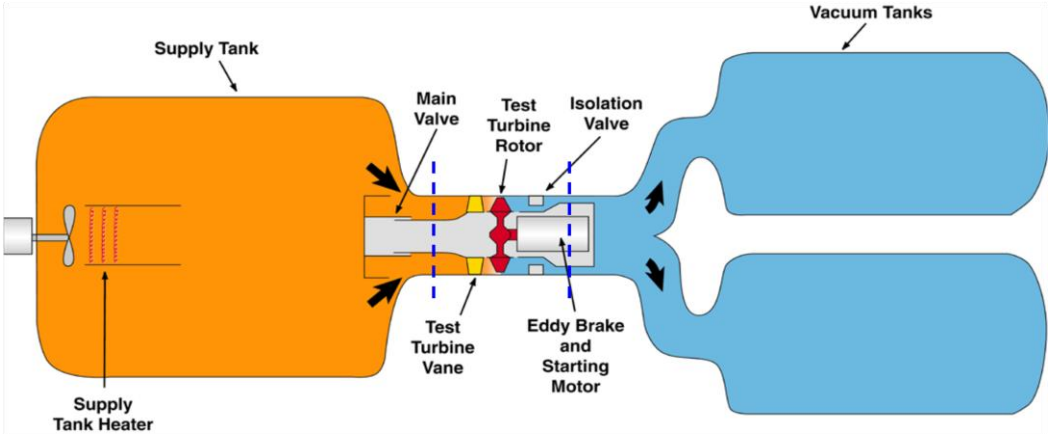

Figure A.1 – Diagram of the AFRL Turbine Research Facility (TRF) with CFD domain bounded by dashed lines.

Facility Details

Under typical operation, nitrogen in the upstream tank is pressurized and heated to the appropriate conditions for the installed hardware design for a given run, released by way of the main valve through the inlet vane wheel test section (and blade wheel when applicable), through the flow passage and the isolation valve, and into two downstream dump tanks initially at near-vacuum pressures. The back pressure in the dump tanks can be set between 0.68 atm and 4.76 atm. The typical run time from which steady state data

is taken is on the order of 2.5 seconds. The flow conditions for the RTV experiments are an initial total pressure of 6.8 atm (100 psia) and initial total temperature of 444 K (800 R), which will also serve as the initial conditions for the CFD simulations. A diagram of the TRF test stand with the simulated passage bounded by straight blue dashed lines is given in Figure A.1. The location of the isolation valve downstream of the test vane can be seen in the figure. The flow path to be interrogated begins 19.05 cm (7.5 in) upstream of the leading edge (LE) of the vane and ends 76.2 cm (30 in) downstream, for a total computational length of approximately 95 cm.

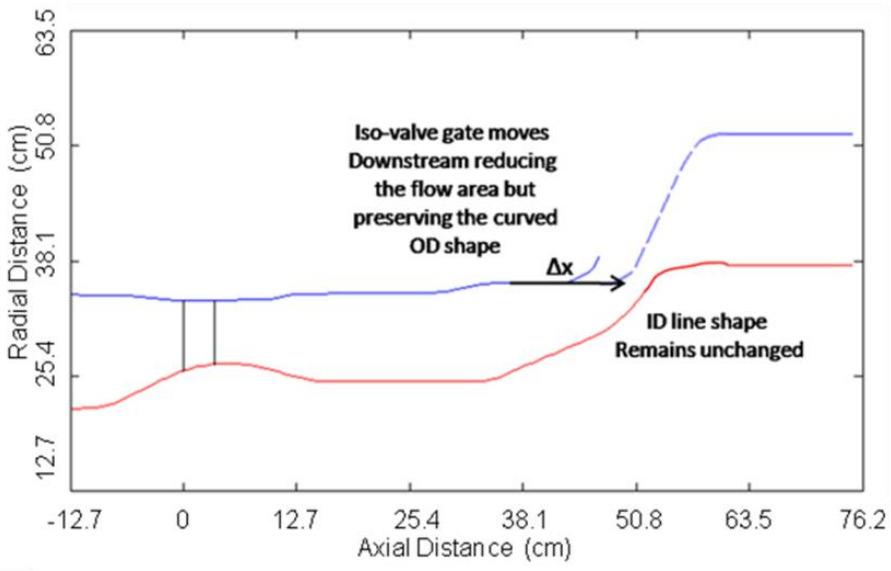

Figure A.2 – Diagram of the TRF passage and the translation of the OD wall for the isolation valve. Flow goes from left to right.

Computational Domain

The 3-D CFD analysis assumes a 1/23rd sector of the annular TRF passage since there are 23 vanes in the full annulus. The computational domain simulated here starts approximately 5.5 chords upstream of the vane and ends just upstream of the dump tank at the end of the passage. Flow starts in the positive axial direction (towards

downstream), turns through the vane passages, and continues to the end of the passage. With periodic boundary conditions on the walls of the sector, flow can be simulated for the entire annulus by combining the results for all 23 vane passages. The only varying boundary conditions will be the outer diameter (OD) geometry of the domain, as the isolation valve position will close to cause variations in resulting flow parameters upstream. The image in Figure A.2 shows how the isolation valve translates axially downstream to change the flow area and thus the outer domain near the end of the passage in the C-D nozzle. The throat area in the nozzle is taken at the point of minimum distance between the ID and OD walls. The valve position can be set to very fine intervals, to the fiftieth of a centimeter. The range of travel of the valve is 10 cm.

The flow domain geometry was initially created using the computer-aided drafting (CAD) program Solidworks^{TM}. Based on the inner diameter (ID) and OD line shapes as seen in Figure A.3, surfaces of revolution were created to define the 3-D flow passage. The ID wall varies with axial distance from 19.69 to 37.62 cm (7.75-14.81 in) radial, while the OD wall varies from 33.73 to 52.07 cm (13.28-20.5 in) radially.

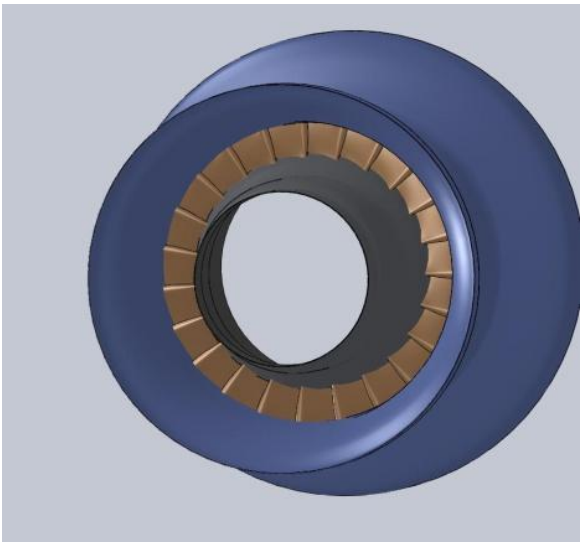

Figure A.3 – Solidworks rendering of the RTV HPT vane full annulus for CFD simulation.

Figure A.3 is a solid model of the entire annulus looking downstream into the passage. The flow domain geometry symmetrically models half a vane passage on the airfoil pressure and suction sides creating smooth constant side walls for the domain that turns with the flow through the vane test section. The domain is 15.652 degrees wide (1/23rd of 360 degrees). To simulate the flow downstream of the vane annulus, spiral geometry is used in which the flow stays turned 76.88 degrees (the turning of the inlet vane) and spirals around the 3-D annular passage until the downstream exit. This will be referred to as the "ribbon" geometry.

3-D Vane Geometry

The RTV design interrogated in the AFRL TRF is described in detail in the methodology section of this dissertation.

Grid Generation

Before grids could be created, the OD lines representing the varying isolation valve position had to be created and rendered in Solidworks™. Originally, the plan was to represent the changing isolation valve area at 0%, 20%, 40%, 60%, and 80% closed positions and plot the resulting vane flow properties. The OD geometry was changed by importing the text file of 201 coordinates for the OD line into a spreadsheet and adding points in the x-direction to simulate the sliding motion of the valve as seen in Figure A.2. The x-distribution of points was conserved for the length of the C-D nozzle shape to ensure the OD curvature did not change. Without more complex interpolation, the set of 201 coordinates were preserved and thus only discrete changes were made to the OD line.

This resulted in examined isolation valve settings of 0%, 23%, 38%, 53%, 76%, 84% and 91% closed.

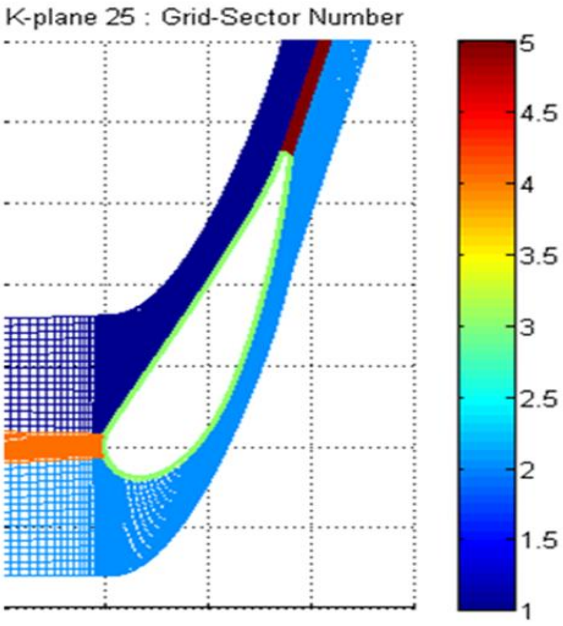

Figure A.4 – Grid sectors at the vane and within the TRF flow passage.

All grids were generated using a program called WAND by Dr. Bob Ni of Aerodynamic Solutions, Inc. used by AFRL for turbomachinery applications. WAND is a text-based grid generator that forms structured grids from a given 3-D geometry. A geometry file was exported from Solidworks™ and input into WAND for every OD geometry representing the different percent-closed cases. An O-mesh was generated around the airfoil with H-meshes created for the upstream and downstream passage centerline (wake area), and in the remainder of the passage. The meshes do not overlap. Figure A.4 is the different meshes created around the vane creating five different domains. The example given is at midspan for the third of four gradually refined grids created within the grid study of this work. This layout is the similar for every radial

location along the vane to create the 3-D grid. Also, from Figure A.4, grid sectors 1, 2 and 4 extend into the passage upstream while grid sectors 1, 2, and 5 extend all the way downstream.

WAND gives the user the ability to vary the dimensions of the structured grid created for the 3-D TRF flow passage. Dimensions are defined in the axial i-direction, the tangential j-direction, and the radial k-direction. The i-direction nodes are split into three parts consisting of the upstream component, on-vane component (for the O-mesh and the H-mesh), and downstream component. The upstream axial nodes set the upstream dimension for grid sectors 1, 2, and 4. The on-vane axial nodes set the on-vane dimension for the O-mesh and grid sectors 1 and 2. The downstream axial nodes set the downstream dimension for grid sectors 1, 2, and 5. The tangential span when not on the vane is split into three regions with a concentrated grid around the passage centerline in the upstream and in the wake downstream. The total amount of grid cells across the three domains in the j-direction upstream of the vane is preserved and distributed to the two free stream domains at the vane. The radial dimension of the O-mesh around the airfoil was also defined.

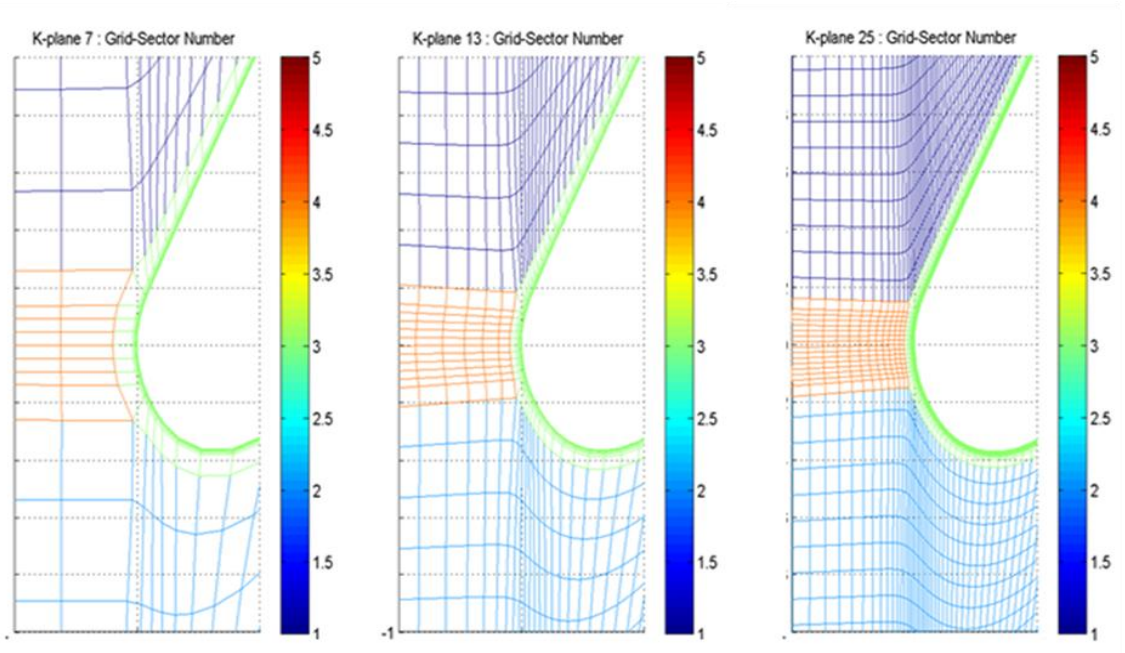

Figure A.5 – Three increasingly refined viable meshes from grid independence study. Final grid is on the right.

Four grids were originally considered for the TRF passage geometry. Since it was projected that it would take six days for grid 4 for the ribbon geometry to be run in the flow solver plus several hours for the grid to be created in WAND, it was decided to base the grid independence study on the first three grids. These grids have 32,000, 230,000, and 1.5 million cells, respectively. Additionally, upon constructing the grids for the varying flow geometry cases for the closing isolation valve, grid 4 was too refined for the small area in the C-D nozzle of the isolation valve. Images in Figure A.5 show grids 1, 2, and 3 from left to right at the leading edge, showing the progression of refinement. The gradual refinement in the grids can be seen along with the increased density of grid cells in the vicinity of the vane with a smooth transition from the upstream component to the vane passage. The axial and circumferential grid cell growth in the O-mesh can be seen for each grid. It can be seen that not only does grid 3 have a smaller O-mesh in the radial

dimension, but there are more grid cells in that dimension as well. This is important since the boundary layer of the viscous flow simulated will need to be sufficiently resolved.

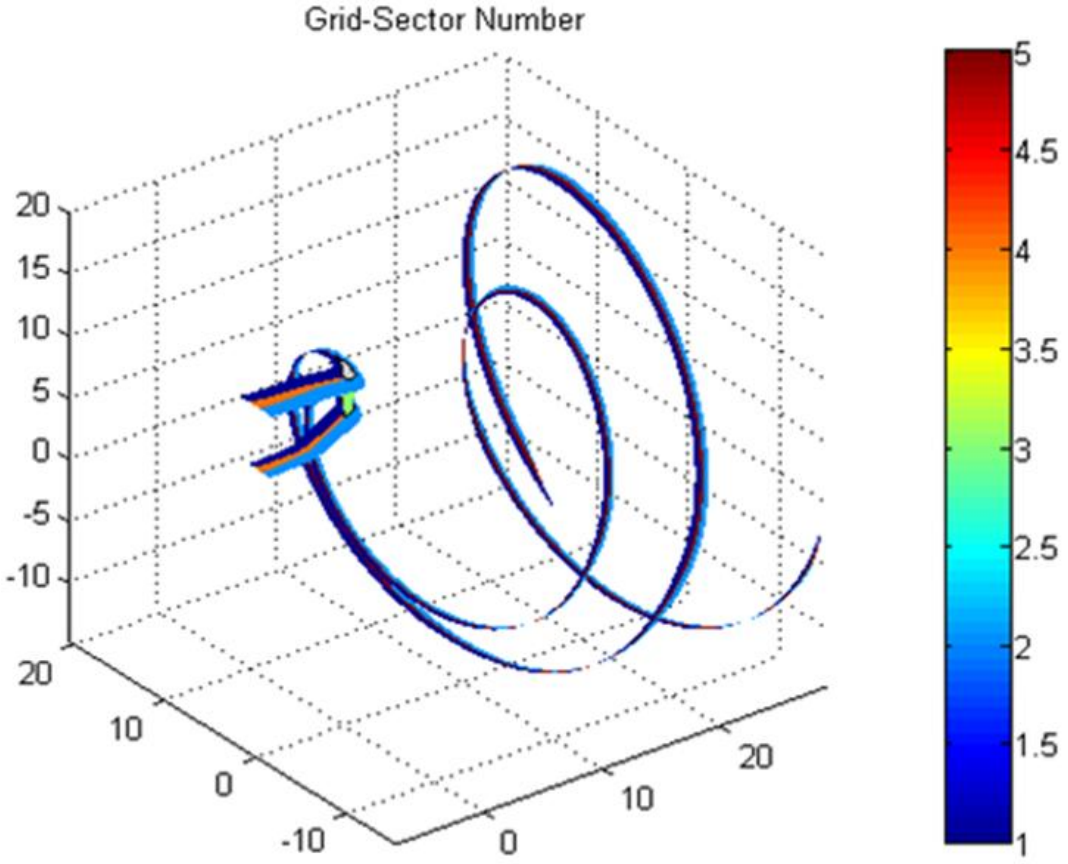

Figure A.6 – Ribbon-like 3-D computational domain for the TRF passage.

To study grid independence, the flow solver was run with the three grids with the isolation valve assumed to be fully open. Simulations were run on the airfoil at six different span locations to obtain surface distributions of static pressure and isentropic Mach number. The difference between the results for all three grids was very small. Additionally, upon closer inspection, the difference between the results of the 1st and 2nd grid is greater than the difference between the results of the 2nd and 3rd grid, showing a

desirable progression of results as the grid is refined. The recorded mass flow rates were 39.46, 38.51, and 38.06 kg/s (87.0, 84.9, and 83.9 lbm/s) for grids 1, 2, and 3, respectively, which also shows evidence of convergence to an unchanging flow rate in the passage. The design mass flow rate for the RTV is 37.69 kg/s (83.1 lbm/s). Thus, it is safe to say that Grid 3 with 1.5 million grid cells is sufficiently refined for analysis of the changing isolation valve position effects on flow parameters in the TRF passage and on the RTV. Figure A.6 is the final grid for the ribbon geometry of the TRF passage with the five grid sectors identified. The figure only shows the grid sectors on the ID and OD of the ribbon geometry and it can be seen where the geometry gets its name. It can be seen how the grid travels straight axially with the flow prior to the vane and then turns due to the vane and spirals around the flow passage until it reaches the end. The 3-D flow can be examined at any i, j, or k-plane in the radial direction and the sides of the flow domain are drawn as a continuous plane between the tangential edges of the ID and OD ribbons. When copied 23 times in the tangential direction, the complete vane annulus, ID wall and OD wall contours can be seen.

Flow Solver and Settings

The 3-D solver used for these simulations is called *Leo*, by author Dr. Bob Ni [166]. It is used by AFRL specifically for flows inside gas turbine engines. The discretization scheme is called the Ni scheme, a finite volume solver for structured or unstructured grids, based on the Lax-Wendroff scheme [167] and is second order in space and time. It is an explicit solver that uses implicit residual smoothing, implicit dual time-stepping, and the Wilcox 1998 k-ω turbulence model. The k-ω turbulence model is one

of many widely used Reynolds Averaged Navier Stokes (RANS) two-equation models. For example, k-ω differs from k-ε in that it uses an equation for specific dissipation rate based on a more detailed set of closure coefficients and auxiliary relations.

The flow in this work is assumed to be steady. All flow cases were run to 12,000 iterations which provided sufficient convergence of residuals of density, momentum and energy to 10e-4 or less. The boundary conditions were as follows: the inlet of the 3-D passage sector was set as a pressure inlet, the downstream outlet was set as a pressure outlet, the curved sides of the computational domain were set to periodic boundary conditions so flow could be simulated for the entire 360-degree annulus, and the ID wall, OD wall, and pressure and suctions sides of the vanes were set as no-slip walls. The initial conditions were set to the planned vane-only TRF test conditions – total temperature of 444 K, total pressure of 6.8 atm and a total pressure at the passage exit (back pressure) of 0.68 atm psia. The flow is assumed to be an ideal gas.

The post-processor used in this work is a Tecplot^{TM}-compatible MATLAB interface integrated into the AFRL Turbine Design and Analysis System (TDAAS) [6]. TDAAS allows the interrogation of data from the LEO runs through user-friendly graphical user interface in which contours, X-Y plots, and 3-D plots of many different flow parameters can be generated.

CFD Results

The average midspan dimensionless wall distance y^+ (equal to $u_\tau y/\nu$ where u_τ is the friction velocity) calculated by the *Leo* solver on the final grid (grid 3) was approximately 2.5, which is generally acceptable for the turbulence model being used.

Based on a calculated Reynolds number of 361,000, the turbulent boundary layer height was found to be 0.073 cm (0.029 in). The resulting leading edge first grid cell height at the airfoil surface was $2.54e10^{-5}$ cm ($1.0e10^{-4}$ in), which allows for 12 cells in the boundary layer.

Upon inspection of the LEO flow solver results for seven isolation valve positions, it was found that the first five flow cases showed essentially no difference in flow properties in the passage and on the vane. In addition, the flow in the passage stayed supersonic for much of the passage after the vane. It was originally thought that for a variation of five different valve positions, significant differences in flow parameters would be seen on the vane and throughout the passage. Also, with a vane designed to have an exit Mach number of 0.88, supersonic flow in the area of the passage between the vane annulus and the isolation valve was not expected either. This initial result may make sense since there is not a full stage installed in the passage and a high passage inlet-to-outlet pressure ratio of 10. Since little difference was seen for valve positions up to 76% closed, only the valve-closed positions of 76%, 84% and 91% were further analyzed. A 98% closed case was also explored, however only the coarsest grid was able to be generated for such a small space in the closed isolation valve and thus the results are likely to be inaccurate.

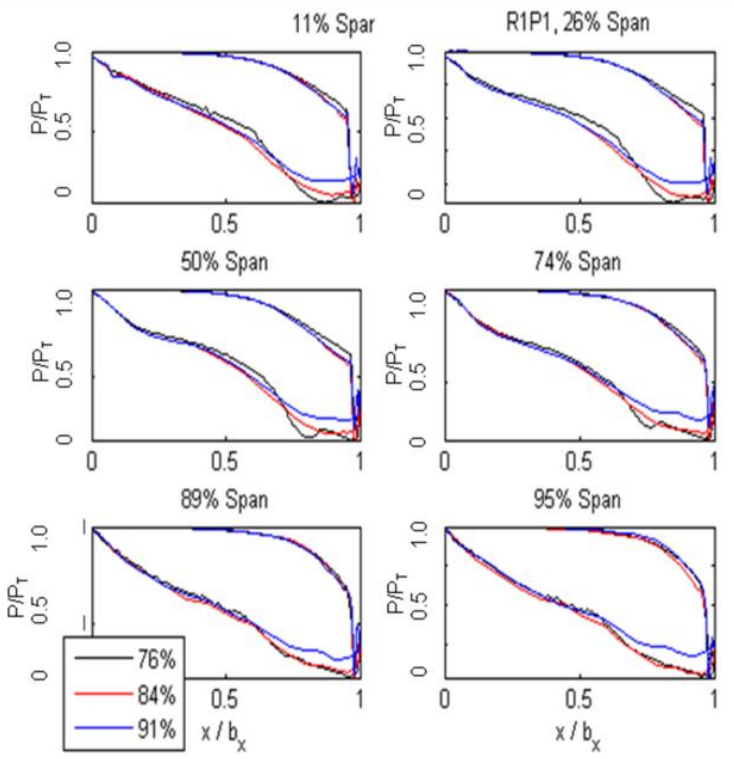

Figure A.7 – Static pressure distributions on the RTV at six spanwise locations.

Figure A.7 is the static pressure distributions over the vane surface for the isolation valve 76%, 84% and 91% closed cases at six different spanwise locations. The top lines are for the pressure side and the bottom lines are for the suction side of the vane. The x-axes signify normalized axial chord and its value zero at the LE and one at the TE. The effect of closing the isolation valve on the static pressure loadings is subtle however the values on the pressure side of the vane (the top set of plots in every box) remain high over a large portion of the vane indicating that there is little in the passage to reduce the pressure. Overall, the distributions do not change much with respect to valve position and additional investigation of the simulations is required.

Isentropic Mach number (M_{is}) contours for the three closing cases (from left to right) for a portion of the vane annulus and the ID surface over the length of the passage

is shown in Figure A.8. The magnitude of M_{is} for all three cases is high—as high as Mach 2.5 for the 76% closed case at the passage outlet. The Mach number at the passage, as expected, decreases as the valve closes, but it is still high. Instead of the flow being choked in the C-D nozzle at the location of the valve as in the case of the Euler simulation[6] of a more subsonic vane design, the flow is choked at the vane, accelerates downstream and chokes again in the nozzle and accelerates further above Mach 2.0. Also, it can be seen that the shocks formed just after the vane row decrease in strength as the isolation valve is closed and are subdued in the 91% closed case. Overall, though, the flow velocity is much higher than typically seen in a high pressure turbine rig.

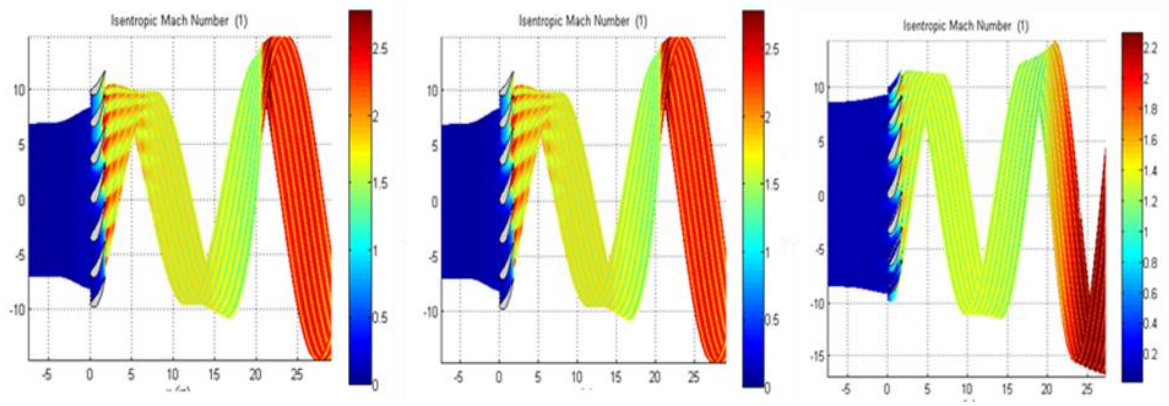

Figure A.8 – Isentropic Mach number contours over a portion of the annulus for the TRF isolation valve at 76% (left), 84% (middle), and 91% closed (right) positions.

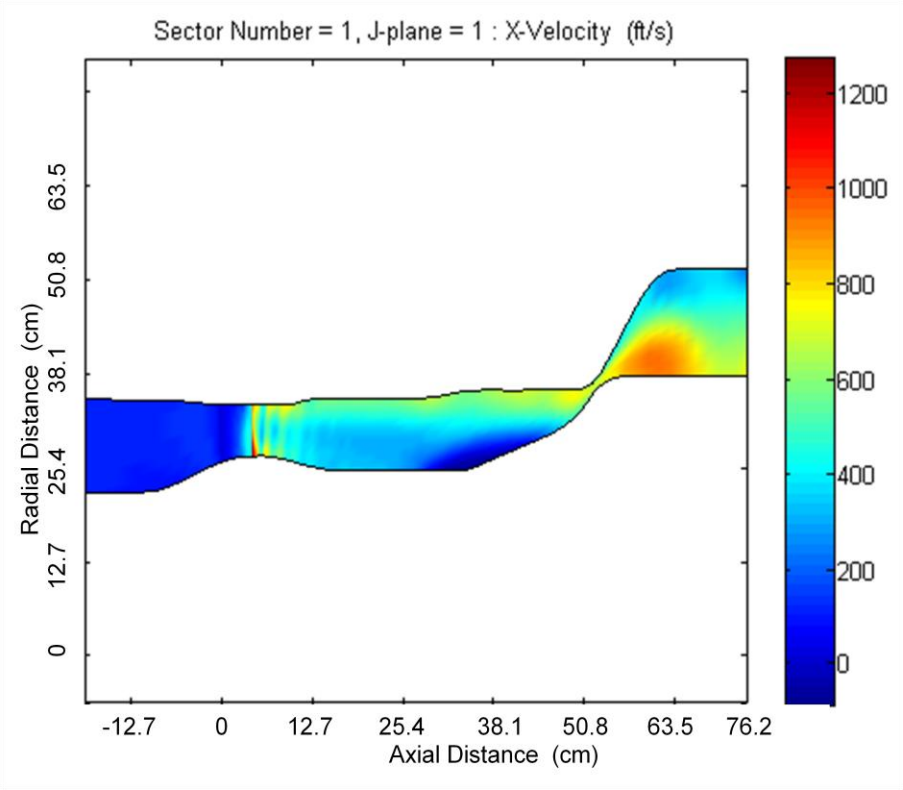

Figure A.9 – X-velocity contours for computational domain center j-plane for 76% closed case.

For the 76% closed isolation valve position, the domain centerline j-plane x-velocity contour for the length of the TRF passage is given in Figure A.9. The figure shows evidence of strong shocks downstream of the vane (as well as for the other two positions whose contours are not shown). Between the vane row and the isolation valve, there is clearly an area of relatively high velocity flow near the OD of the passage. This high-speed OD flow velocity increases as the valve closes. A large area of separation, perhaps shock-induced, is also apparent between the vane and the C-D nozzle. This area grows as the valve is closed. Lastly, there is a second shock lying in the end of the passage caused by the nozzle throat at the valve.

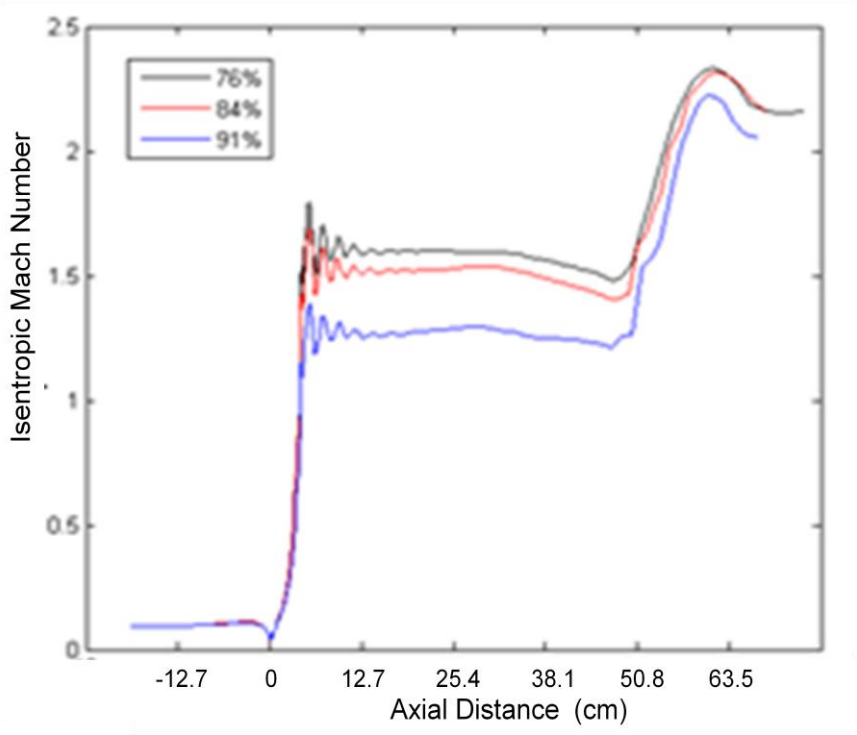

Figure A.10 – Axial distribution of Isentropic Mach number in the TRF passage.

Figure A.10 is a plot of M_{is} at midspan (the middle radial k-plane) over the length of the TRF passage for the three different percentage closed cases. It can be seen that not until more than 84% closed does the Mach number decrease to a level close to the vane design levels. Even at 91% closed the vane exit Mach number is well above 1.0. After x = 0 at the leading edge of the vane, the fluctuations for all three simulations again indicate shocks that are generated downstream of the vane and also that the flow velocity further increases through the isolation valve at approximately x = 20 in the figure. Closing the isolation valve lowers the Mach number in the passage, but more work may be necessary to set up the correct design flow properties on the vane.

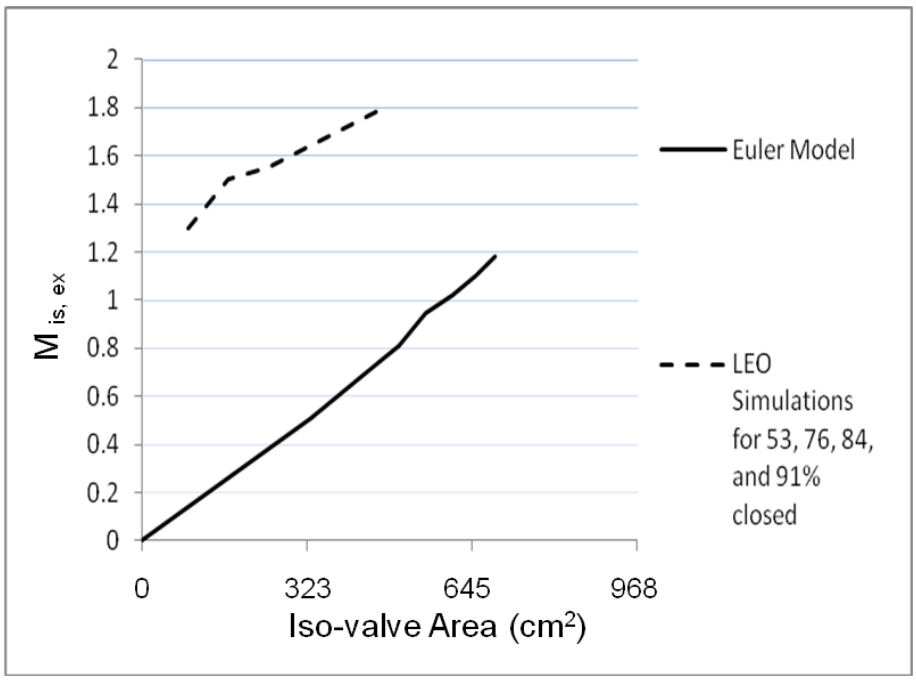

Figure A.11 – Mach number vs. Iso-valve area (initial CFD results).

The plot in Figure A.11 provides additional evidence that the flow with the current conditions is too fast to take accurate engine-representative temperature and pressure data. It compares four closing isolation valve cases from the current study to the Euler simulation [178] performed previously for the vane design with full vane and blade stage assumed. While the RTV design is much different than the previous design, to ensure reasonableness in the flow set up over the vane, the plots of vane exit Mach number with isolation valve area should match better than they do in Figure A.11. This shows that with a blade also simulated in the TRF passage that the flow behaves at velocities more like what is expected. It can be seen that the slopes of the two plots match which may indicate that the flow is trending properly with respect to the reduction in flow area. The problem may be solved by either changing the initial conditions or the boundary conditions of the flow. For example, to change the initial conditions, the flow

solver can be run to examine how changes in the dump tank back pressure affect the results. If the boundary conditions are modified, in order to set up the appropriate flow for the vane, a blade or de-swirler may be necessary downstream of the vane to keep the excessive velocities down. Or the extent of the flow domain in the TRF passage may be simplified and the new results examined. First, the effects of changing the exit pressure conditions are covered.

Effects of Varying Back Pressure

Under the assumption that other considerations are necessary with the vane-only configuration in the TRF such as varying the initial conditions, and specifically the outlet pressure conditions, supplemental cases were explored. Boundary conditions for the following cases were also modified as the flow in the passage was simulated with the isolation valve in the fully open position. With a stage installed (vane and blade annulus), traditionally, it is enough to control the stage pressure ratio and other flow parameters using just the isolation valve while keeping dump tank pressures near vacuum. In the initial runs in this work for varying valve position, the back pressure is only 0.68 atm. For a vane-only configuration, an design, that the dump tank pressure for the current hardware design, creating design-representative flow conditions on the vane should be easily obtained by altering the back pressure. Therefore, TRF flow was simulated with 3.40, 4.08, and 4.76 atm (50, 60 and 70 psia) back pressure. Figure A.12 is the spanwise M_{is} loading over normalized axial chord for the three different TRF dump tank back pressures in which it is apparent that as the pressure increases, the exit Mach number decreases to levels comparable to the design levels for the RTV. Here, the vane

suction side lines are on top and the pressure side lines are on the bottom in each plot. Upon closer inspection of the exit Mach at midspan, the back pressures give the following values: 3.40 atm gives 1.1, 4.08 atm gives 0.85, and 4.76 atm gives 0.85. This shows that back pressures greater than or equal to 4.0 atm are likely to be sufficient to give proper flow conditions at the vane exit for the current passage geometry and extent of the computational domain.

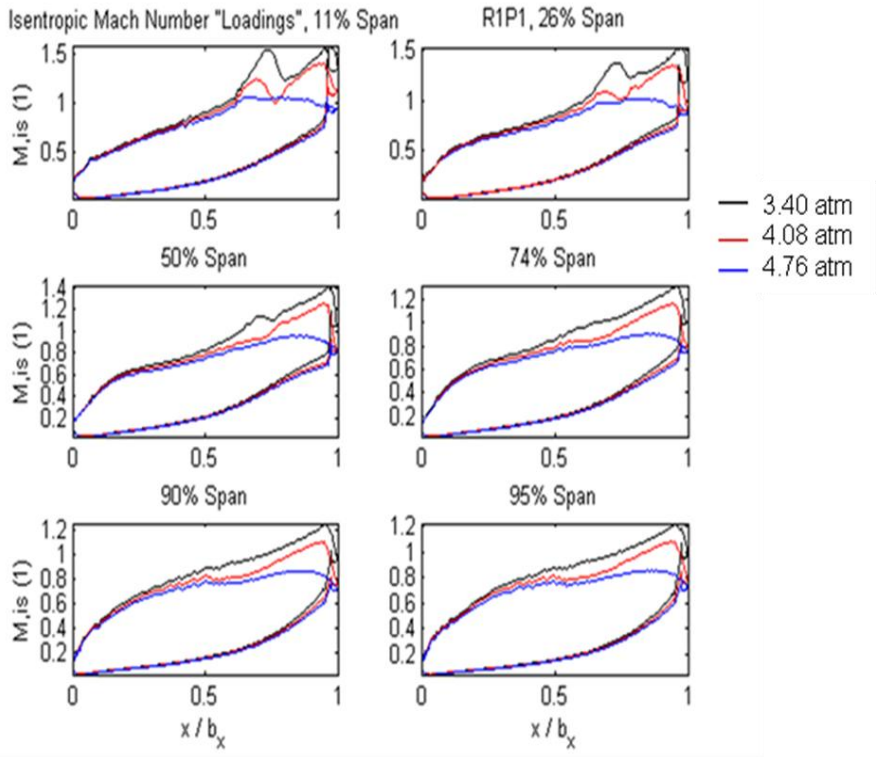

Figure A.12 – Mach number on the RTV surfaces at six span locations for three back pressure settings.

Figure A.13 is a static pressure contour plot at the centerline j-plane for the length of the TRF passage with 4.08 atm back pressure set at the outlet. This shows that shocks after the vane are still present; however there is not an area of further acceleration and high-velocity flow between the vane and isolation valve and no second shock due to the

C-D nozzle as seen previously. This appears to be a logical result, but vane only runs should not require high back pressure to blowdown into. Next, results from modifications to the flow geometry, specifically in the area of the isolation valve, will be examined.

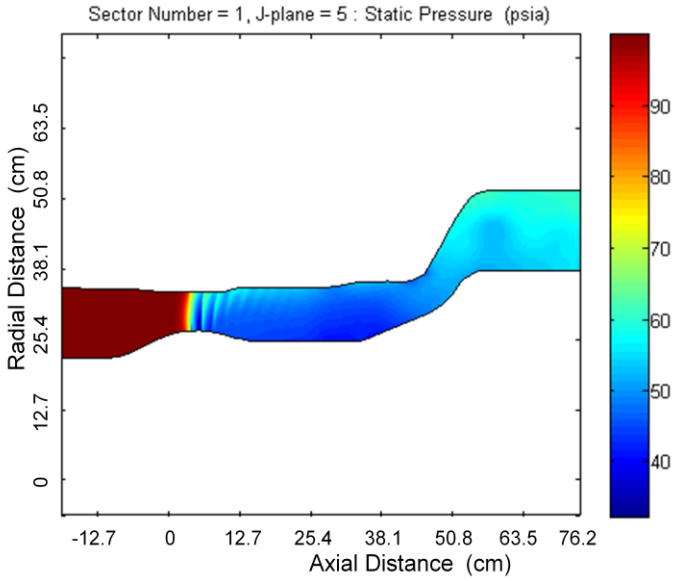

Figure A.13 – TRF passage static pressure contour with 4.08 atm back pressure setting.

Results with Modified Passage Exit Geometry

To further study the high velocity phenomena in the passage from the initial results, the flow geometry was terminated at the site of the minimum area in the C-D nozzle which becomes smaller as the isolation valve closes. It is suggested that the abnormally high velocity flow originally seen through the passage and through the C-D nozzle is due to difficulties of the flow solver resolving the details in the diverging part of the passage just before the dump tanks in the TRF. The use of a structured grid requires that all cells in the radial direction span the length of the flow path. The strong shock and

potential separation created by such a tight compression followed by the rapid expansion likely causes non-physical mass flow errors in the simulations. A brief comparison of the mass flow rate calculated just before the C-D nozzle and at the original passage outlet showed inconsistencies that require attention. With the new geometry, the flow path converges and does not diverge substantially downstream of the valve. The flow boundary was generated by connecting a straight line between the ID and OD at the location of minimum distance. The OD geometry was modified such that much finer valve-closing intervals could be studied while conserving the appropriate curvature, thus a wider array of cases were examined than in the initial results.

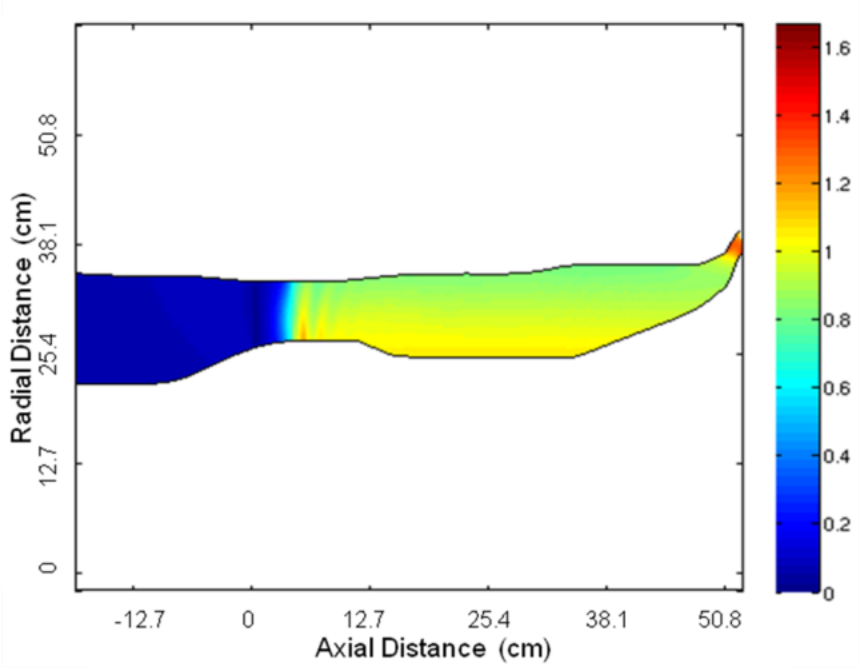

Figure A.14 – Mach number contour for modified TRF passage geometry with outlet plane at the throat of the isolation valve nozzle.

After running the solver with the same operating conditions as the original simulations, the results appeared to make much better physical sense than expected for

the design conditions. Figure A.14 is an M_{is} contour plot with the new flow exit geometry showing much lower velocities at the vane exit and in the C-D nozzle relative to the results from the original geometry. The figure also shows how the new flow outlet is defined. Figure A.15 is a set of M_{is} distributions on the vane at six spanwise locations for four different valve settings. It can be seen that as the valve closes, the vane exit isentropic Mach number ($M_{is,ex}$) is reduced and in the range of expectation for its design. Close inspection of $M_{is,ex}$ at the trailing edge showed that with the valve set to 7.42 cm closed the design conditions on the vane were met. Now the proper valve setting for the vane-only configuration in the TRF is known and can be implemented in the experiments.

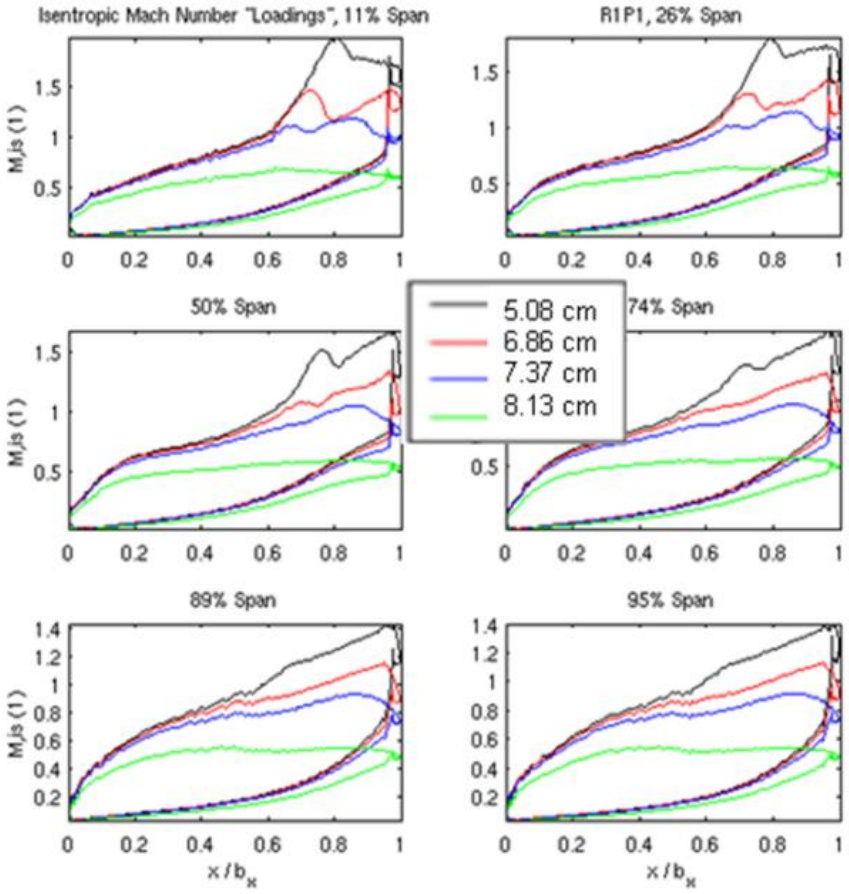

Figure A.15 – Effect of isolation valve position on vane isentropic Mach number distributions with new passage geometry.

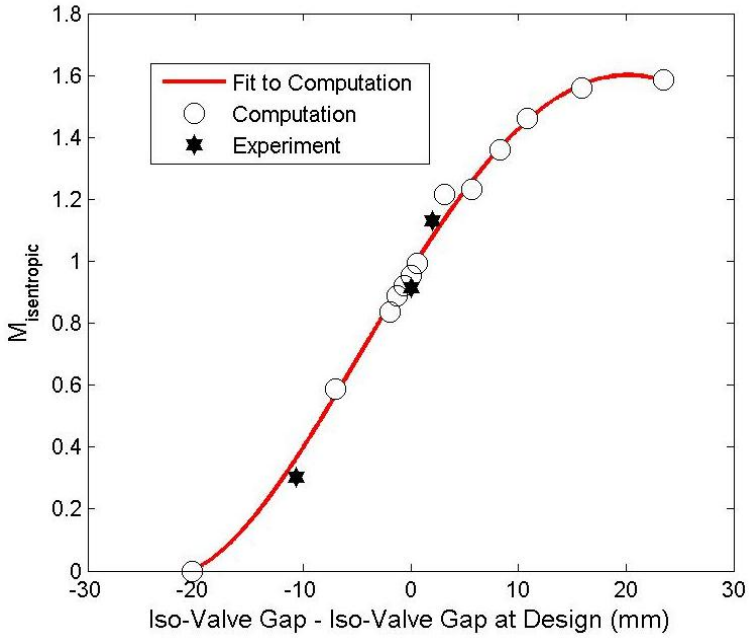

Figure A.16 – Relationship between isolation valve position and vane exit isentropic Mach number.

Comparison of CFD Predictions with TRF Pressure Data

The main objective of this work was to generate a relationship between the isolation valve settings in the TRF and the resulting flow properties on the vane, specifically $M_{is,ex}$. This relationship is plotted in Figure A.16. The x-axis is centered to zero at the valve setting that matches the design conditions for the RTV. In the plot, a total of 16 valve settings are fit with a curve. The three black filled isolation valve set points represent settings that were run experimentally. It was found that the flow properties on the vane were extremely sensitive to the valve settings. The new results are more comprehensive than the original study, but they are not significantly different.

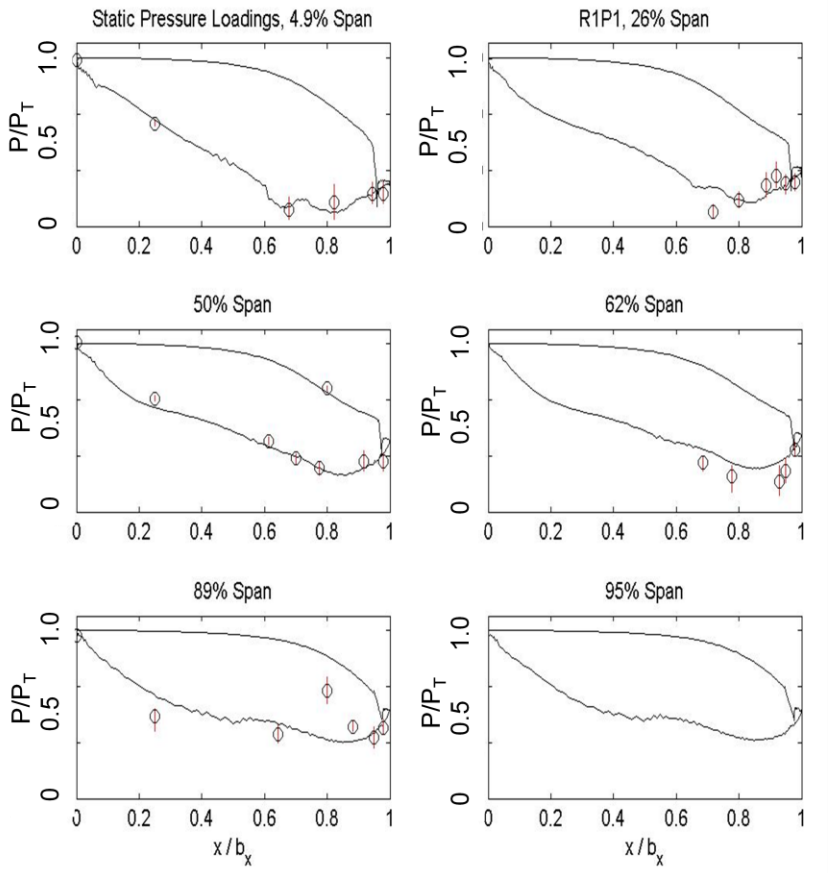

Figure A.17 – Prediction of RTV midspan pressure loading at six span locations with TRF data.

Plots in Figure A.17 give the predictions of the vane static pressure distributions at six spanwise locations plotted against TRF data for the design isolation valve setting. Five of the six span locations in the figure match locations on the vane that were instrumented with flush-mounted pressure transducers in the experiments. This shows how well the *Leo* flow solver along with the modified 3-D TRF passage geometry predicted the flow. Predictions at all span locations match the TRF data very well except in the plot at 89% span. Therefore, with the modified exit geometry, the LEO flow solver sufficiently predicted the flow in the TRF passage and adequately found the ideal valve setting for vane-only runs.

Conclusions

In the 3-D viscous steady CFD analysis of a vane-only configuration for the Turbine Research Facility, using a proper grid, the changes in flow properties on the vane and in the passage were not as expected with the original computational domain extending past the C-D nozzle of the valve. Initial predictions of the flow in the passage showed very high velocities across the vane and even higher velocities and shocks just after the isolation valve. This rapid convergence and divergence near the end of the passage resulted in errors in calculations of mass flow which affected the results upstream at the location of the vane. Performing simulations with the valve fully open and three high back pressure initial conditions gave flow properties without high-velocity anomalies and with vane properties much closer to design values. Next, the flow geometry was modified by cutting off the back end of the passage a small distance downstream of the isolation valve throat and the predictions were redone with a more detailed array of valve settings. This resulted in the identification of the ideal valve setting which gave flow properties on the Research Turbine Vane that matched its design conditions. Comparison of these predictions to TRF data at the same valve setting showed an accurate match in terms of pressure distributions on the vane.

Turbine Research Facility Data on RTV Baseline Cooling Design

The objective of testing currently ongoing at the AFRL Propulsion Directorate is to assess the aerodynamic and thermal performance of the High-Impact Technologies (HIT) Research Turbine stage and one half in order to advance the state-of-the-art for high temperature, greater efficiency turbine engines.

Figure A.18 - Image of the AFRL Turbine Research Facility (TRF).

The Turbine Research Facility is a full-scale experimental blowdown rig designed to obtain time-accurate unsteady pressure, surface temperature, and surface heat flux data from various installed single shaft turbine hardware designs [173]. An image of the facility is given in Figure A.18, in which flow goes from left to right starting in the upstream pressurized tank, through the test section and into dump tanks. Surface temperature is monitored using surface mounted thermocouples on the vanes, static pressure data is gathered using taps leading to Kulite transducers on the surface at varying span locations, and heat flux data is obtained using custom-designed non-intrusive thin-film double-sided heat flux gauges. Heat flux data is obtained from vanes with film cooling holes as well as without. Sections of the vane annulus are designed and instrumented in such a way as to obtain separate measurements of both uncooled and cooled heat flux, surface temperature, and surface pressure. The TRF is capable of

operating as a one-and-a-half stage (inlet vane, rotor and low-pressure vane) or in the case of the current work, a vane-only configuration. The TRF operates at flow conditions that are non-dimensionally consistent with the turbine environment. As stated before, the vane design of experimentation here is called the HIT RTV. An isolation valve located in the nozzle portion of the flow passage downstream of the test section can be set to varying flow area intervals which in turn sets the test duration, stage pressure ratio, and mass flow rate. The isolation valve displaces axially and is located in the middle of a converging-diverging (C-D) nozzle.

Under normal operation, nitrogen (N_2) in the upstream tank is pressurized and heated to the appropriate conditions for the installed hardware design for a given run, released by way of the main valve through the inlet vane test section through the flow passage and the isolation valve, and into two downstream dump tanks initially at near-vacuum pressures. The back pressure in the dump tanks can be set between 0.68 atm and 4.76 atm. Typical run times are on the order of 2.5 seconds for the main flow. Nominal experimental inlet conditions based on the vane operational design point are an initial total pressure of 6.8 atm (100 psia) and initial total temperature of 444 K (800 °R). However, in order to match the design value for the total coolant-to-mainstream pressure ratio ($P_{t,c}/P_{t,\infty}$) of 1.05, and since the coolant flow pressure could not be widely varied, the main flow pressure was scaled down below 6.8 atm. The resulting value of $P_{t,c}/P_{t,\infty}$ for all TRF data presented here is approximately 1.02.

The objective of this study is to make an initial examination of critical heat transfer data measured by double-sided thin film heat flux gauges from the TRF with only the vane annulus installed and glean any insights from the potential reduction in heat

flux due to the addition of film-cooling in the operational setting. Insights can also be gleaned from the performance of the instrumentation as intended, realistic levels of temperature and heat flux in a gas turbine engine, as well as if there is enough available data in the rig to accurately model all aerothermal aspects when assigning CFD boundary conditions.

The flow conditions for the RTV experiments involve inlet profiles as explained in the methodology of the dissertation. The inlet total pressure profile was mostly uniform at about 4.46 atm (65.5 psi). The inlet total temperature profile from the upstream rake had a peak temperature near midspan of 443 K (798 °R) and decreased to 440 K (793 °R) at both endwalls. The downstream static pressure was measured to be 2.68 atm (39.43 psi). Vanes in the wheel are numbered 1 to 23, starting at 12 o'clock (looking aft), going clockwise. The uncooled vane of interest is vane 5 at about 2 o'clock and the cooled vane of interest is vane 16 at about 8 o'clock on the wheel. The two upstream instrumentation rakes, while they each only traversed 120°, they swept a path that fully covers vanes 5 and 16 as well as a few vanes on either side of each. This gives accurate CFD inlet conditions knowing that there may be some variation throughout the wheel and the readings belong to the respective vanes simulated. The uncooled vane 5 surface temperature was 333.73 K (600.71 °R) and the cooled vane 16 surface temperature was 316.42 K (569.55 °R), which governed the isothermal wall settings for the CFD. As measured by the last sensor in the coolant chain before the vane internal plenums, the coolant temperature for the rear plenum and its four PS rows of holes was 243.24 K (437.84 °R) and the temperature for the front plenum was 278.27 K (500.88 °R).

The vane surfaces are instrumented with heat flux gauges at varying streamwise and spanwise locations. These gauges require both the top and bottom gauges to be working to acquire heat flux. The top gauge was capable of measuring surface temperature. Figure A.19, for example, is the uncooled and cooled vanes of interest with their respective midspan heat flux instrumentation. Clearly, the thin films are non-intrusive to the flow. More detailed information on the instrumentation in the TRF can be found in the paper by Anthony et al. [21]. Depending on the span location and the vane, there were between five and ten gauges distributed in the axial direction. Naturally, the SS tended to have more gauges because its surface distance is longer than the PS, and the uncooled vanes tend to have more gauges than the cooled since there is less surface space to work with between film-cooling hole rows.

Figure A.19 - Cooled vane 16 (left) and uncooled vane 5 (right) instrumented with midspan double sided heat flux gauges.

All reduced heat transfer data was realized using the methods of Oldfield [179], which is standard for this type of semi-infinite substrate thin film heat flux gauge. Heat conduction was modeled using the semi-infinite solid assumption. MATLAB codes created by Oldfield were used to perform an infinite impulse response technique to

deboost, filter, and convert raw voltage data to heat flux. Figure A.20 is a diagram of the nominal instrumentation plan for the RTV vane wheel in the TRF.

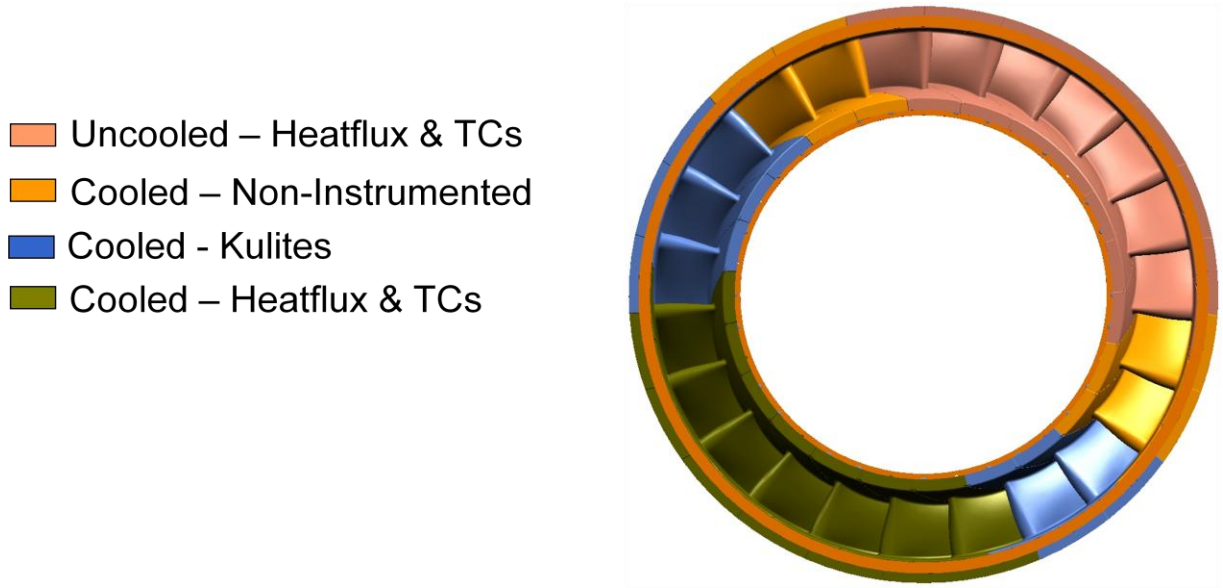

Figure A.20 - TRF HIT RTV instrumentation arrangement for the vane annulus.

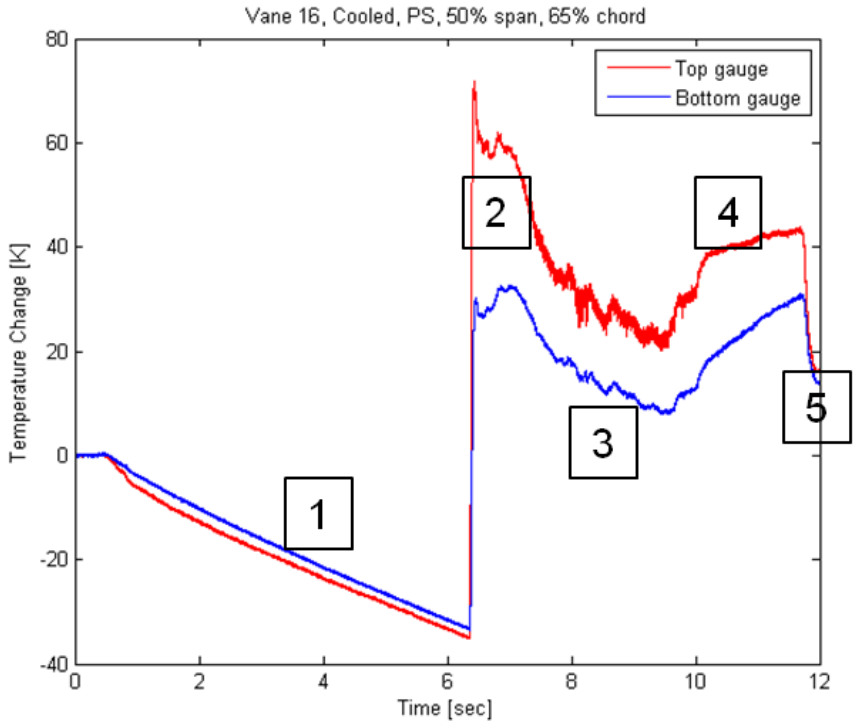

Figure A.21 - Sample time traces of bottom- and top-gauge temperature change [K].

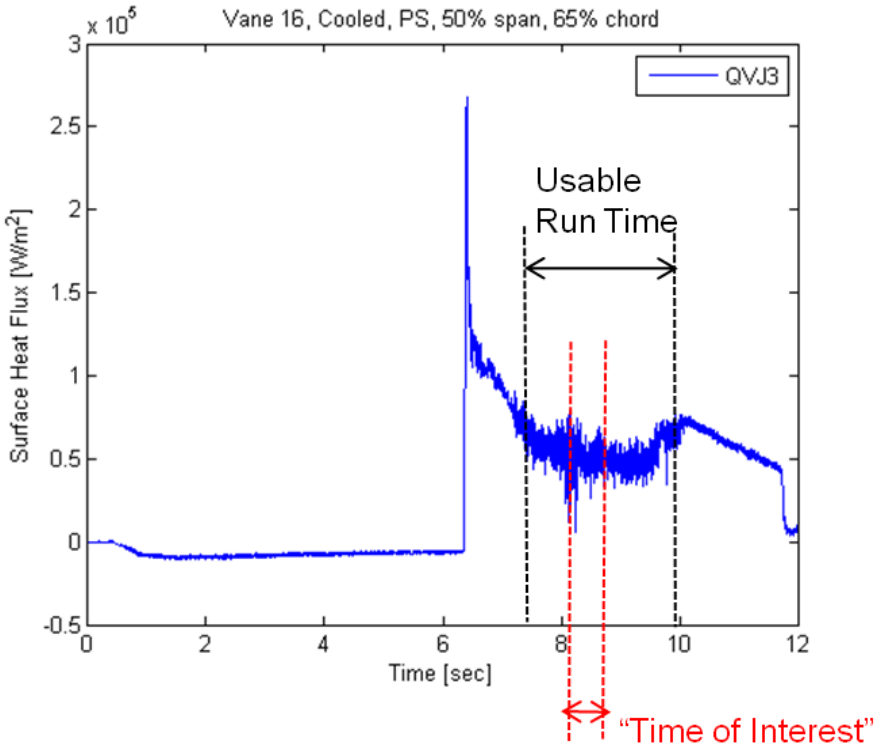

b)

Figure A.22 - Sample time traces of derived heat flux [W/m^2].

Heat flux gauges in the TRF on the vane use high-frequency thin film resistance. Traces of voltage from double-sided heat flux gauges are converted to traces of temperature for both the top and bottom gauges in the double-sided arrangement. The heat flux is derived by a digital filter solution for the time-varying heat conduction equation using the measured top and bottom thin film temperatures and known thermal properties of the Kapton layer. The uncertainty in top-gauge temperature measurements is ±0.6 K and using Monte Carlo analyses, the uncertainty in heat flux propagates to a worst-case value of ±18%. However, more work is going into investigating the gauge-to-gauge uncertainty changes, if any, over the surface of the vane at different span and axial locations. The plot in Figure A.21 is surface temperature traces for the cooled vane PS at

midspan at 65% chord position and Figure A.22 is the derived heat flux. N_2 coolant originally at cryogenic temperatures and the appropriate pressures is released into the line which leads to the vane plenums in the vanes picking up heat along the way. Intense preparation went into ensuring that the coolant was at the right conditions at the exit of the cooling holes before the mainstream hot flow was allowed through the test section. The traces (as seen in Figure A.21) clearly show: 1) a cool-down period before the main flow starts due to the coolant coming into the vane plenums and injecting out of the holes, 2) a transient period just after the main flow is allowed through the test section, 3) a fairly steady period, 4) a period showing the shut-off of cooling flow where the traces begin to rise again, and 5) the short final period showing the dissipation of main flow. The period of steadiness between the main flow startup transient and the coolant shutoff is where the 2.5 second typical run time of the TRF is derived from. In Figure 22, it can roughly be seen from approximately the 7.5 second mark to the 10.0 second mark. However, all inlet total temperature, inlet total pressure, vane surface temperature, and heat flux were taken from the time of interest being from 8.0 to 8.5 seconds. All reported heat flux results are calculated by averaging the fluctuating signal in this time of interest for a given thin film gauge measurement. This smaller period of time within the total run time ensures the least variation of a number of flow parameters. It also avoids the enthalpy increase from the startup transient and gives enough time for film-cooling to be established. In addition, it avoids the later changes in flow properties due to the termination of cooling. More details on the importance of avoiding the main flow transient startup in obtaining critical heat transfer data is reported on in the work of Johnson et al. [180]. The 2.5-second run time of the AFRL TRF is significantly longer

than the 100 ms run time of the Oxford Isentropic Light Piston Tunnel and 200 ms run time of the Ohio State University's Turbine Test Facility. The hump seen in temperature traces that is not seen for uncooled vane traces, just after the transient startup, shows film cooling flow establishment. Depending on the specific experimental logistics of cooling supply, this may mean previous work by the Oxford and OSU groups may not have been long enough to take accurate heat flux readings in the presence of film cooling.

The heat flux gauges are double-sided, meaning there is a "top" gauge exposed to the main flow and a "bottom" gauge that lies against the vane metal surface not exposed to any main flow. These two gauges are separated by a thin kapton layer. All heat flux and temperature data is time-averaged after extensive signal processing for a half-second time period centered within the typically 2.5 second quasi-steady run time of the TRF. Due to limited data channel capacities, obtaining data at six span locations required three TRF runs that will be reported here: run 110, run 204, and run 303. Figures A.23, A.24, and A.25 are vane surface temperature distributions for six spans for the cooled and uncooled vanes, as well as the embedded thermocouple measurements for vane metal temperature during the run. Pressure side data is plotted on the left half and suction side data is plotted on the right half of the figures with the leading at edge in the center. In general, with film cooling, the surface temperatures are significantly lower for all spans, especially on the SS. Cooling does not lower the surface temperature on the PS as much as it does on the SS due to the typical thickness of the boundary layer on each side. On the PS, with a positive pressure gradient thinning the boundary layer, the benefit is not as great as for a thicker, perhaps transitioned boundary layer that covers a majority of the SS. All of the plots tend to show relative increases in temperature near the LE (at x/b_x =

0) and at the TE, which is typical of heat transfer trends over a vane surface. With cooling, the surface temperature at its lowest points tends to decrease closer to its vane's metal temperature level compared to the uncooled vane. At some points, it even dips below the metal temperature level. Also with cooling, the differences in surface temperature between two spans is lower compared to the uncooled vane, which may indicate that the film spreads over the surface fairly evenly and may influence secondary flow effects present on a vane without cooling near the endwalls, whose span locations (5%, 95%) tend to have the highest temperature levels of all the spans.

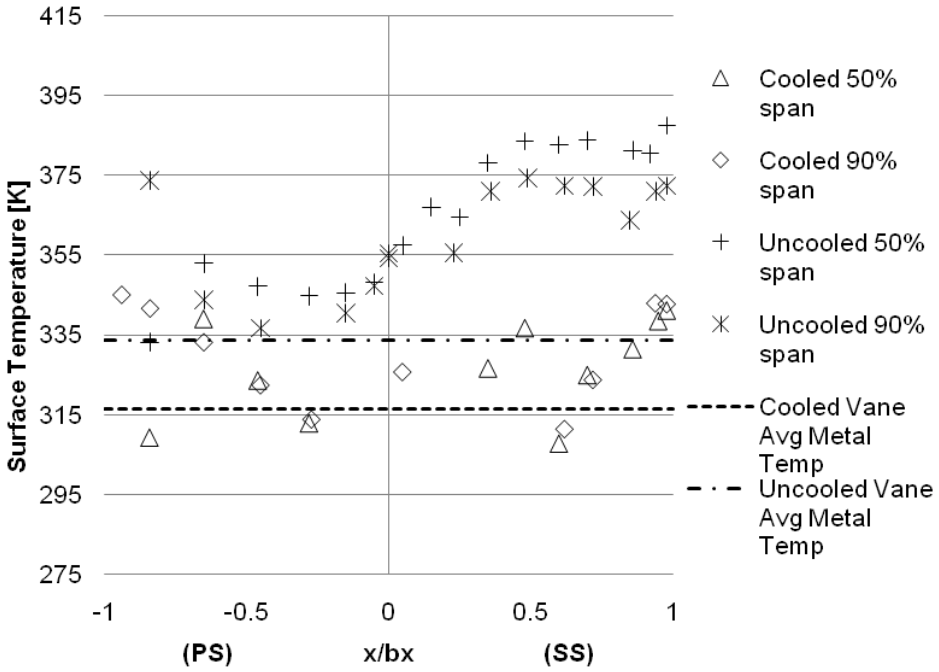

Figure A.23 – Top-gauge RTV cooled and uncooled surface temperature distributions for TRF run 110 covering data at 50 and 90% span locations.

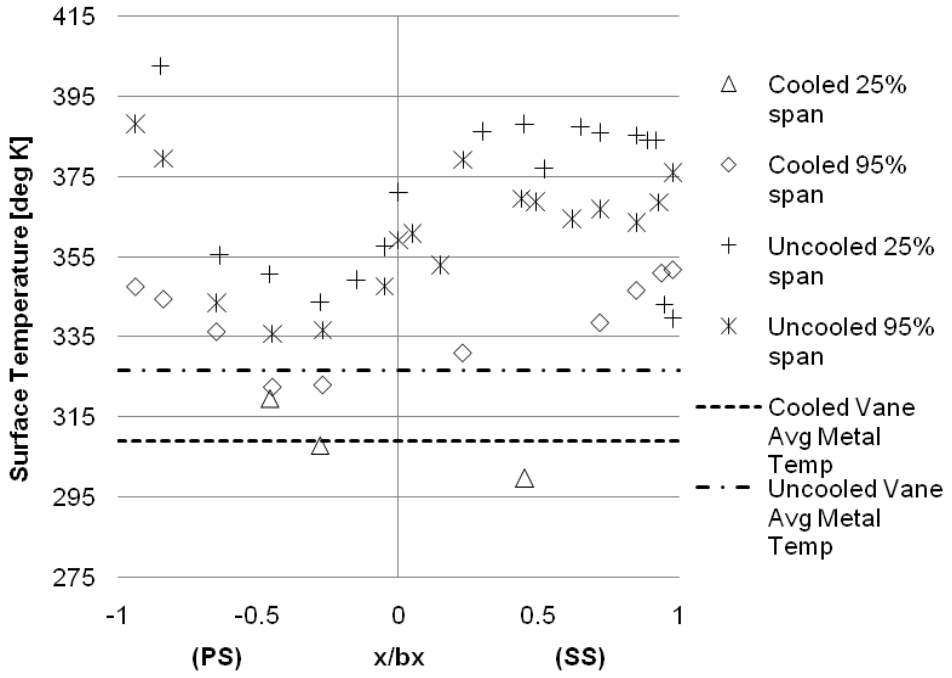

Figure A.24 – Top-gauge RTV cooled and uncooled surface temperature distributions for TRF run 204 covering data at 25 and 95% span locations.

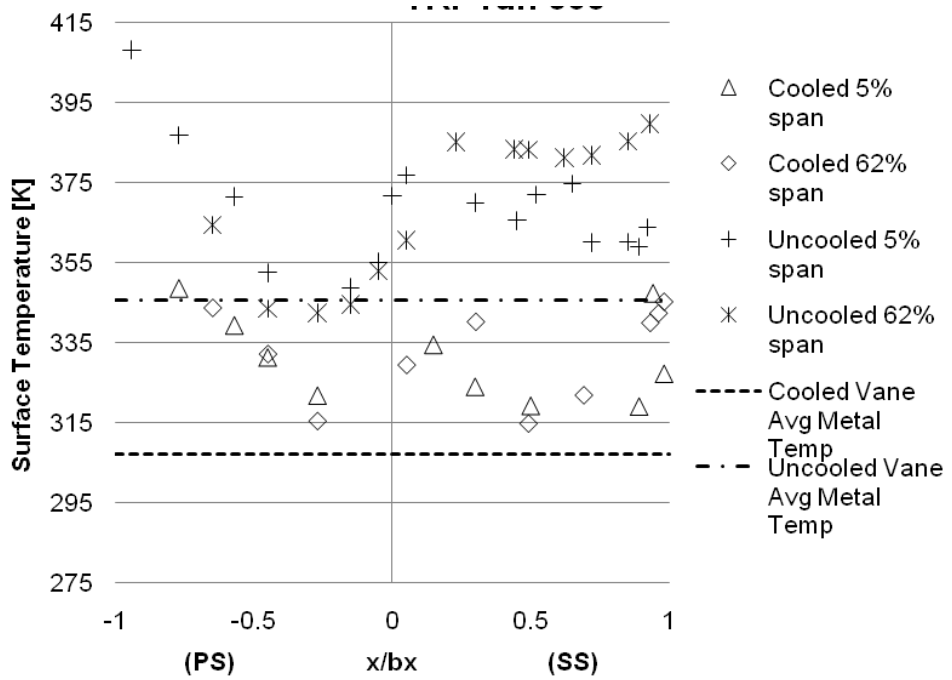

Figure A.25 – Top-gauge RTV cooled and uncooled surface temperature distributions for TRF run 303 covering data at 5 and 62% span locations.

Figure A.26 is vane surface heat flux distributions for two span locations for the RTV with and without film cooling with an emphasis on repeatability, which shows the difference in the heat transfer measurements between two subsequent runs (302 and 303). It can be seen that there are often less heat flux measurements relative to temperature measurements available over the vane chord as heat flux requires both a bottom and top gauge to be functioning properly. One obvious trend is that the run-to-run variation for the uncooled heat flux is on average much less than for the cooled heat flux. Assuming the rig is working perfectly, this may indicate that there may be some degree of inherent unsteadiness in the case of a vane with film cooling. In general for both plots, the run-to-run variation appears to be largest near the LE, especially on the SS. This area of high curvature and adverse pressure gradient in the developing boundary layer may be affecting by the degree of mixing that exists in the surface-normal direction. Overall, the heat flux trends over the surface closely follow the temperature distributions and this is true for most of the results at all span locations. This makes sense as the calculated heat flux highly depends on the temperature levels. Repeatability plots for surface temperature are given in Figure A.27. The difference between the test section total inlet temperatures between the two runs was less than 2 K, and it can be seen that the majority of the differences in the temperature measurements is very small and approximately at this value.

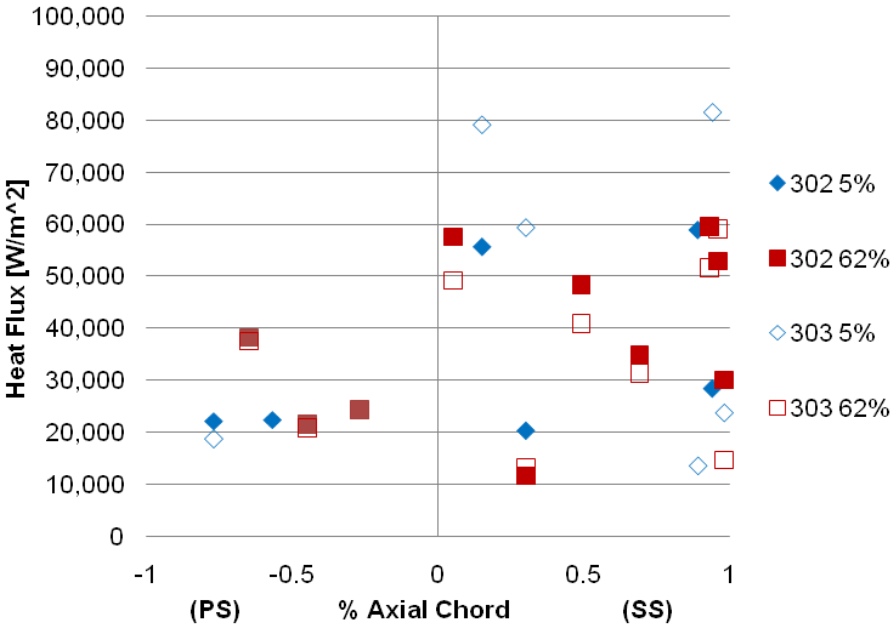

a)

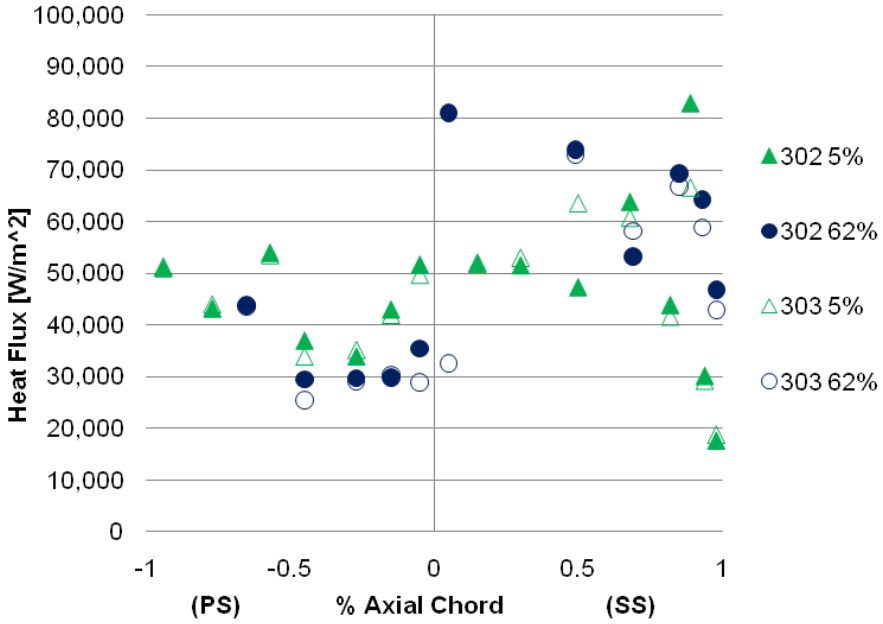

b)

Figure A.26 – Heat flux measurement repeatability between subsequent TRF runs 302 and 303 with measurements at 5% and 62% span for a) a cooled vane and b) an uncooled vane.

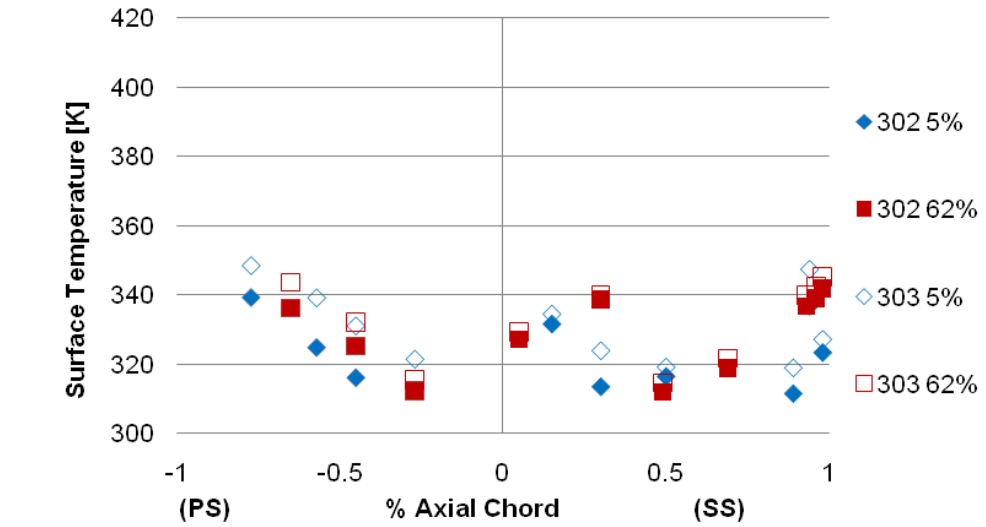

a)

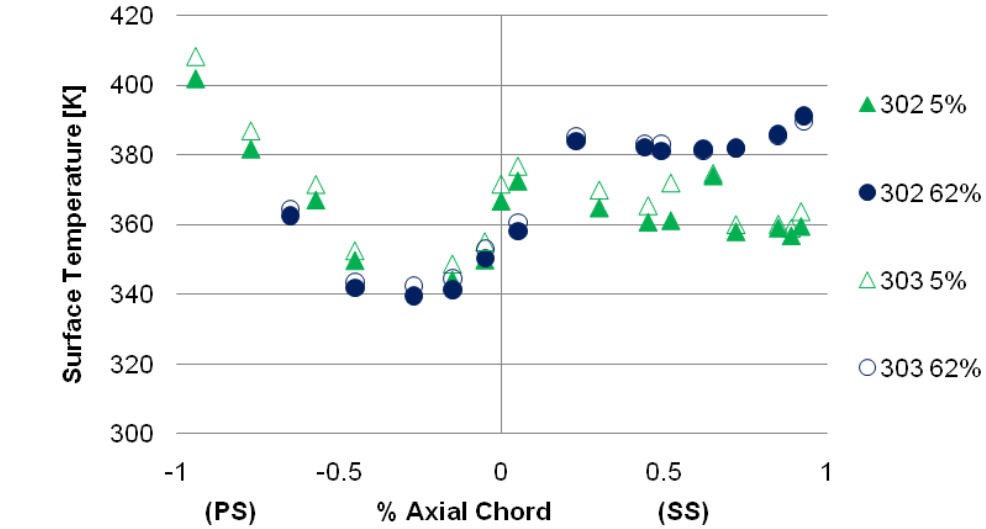

b)

Figure A.27 – Surface temperature measurement repeatability between subsequent TRF runs 302 and 303 with measurements at 5% and 62% span for a) a cooled vane and b) an uncooled vane.

Figure A.28 is vane distributions of the temperature difference between the top and bottom thin films for working heat flux gauges at three span locations. The temperature difference is present due to the top gauge being exposed to the hot main flow and the bottom gauge lying between the kapton layer that separates the two gauges and the metallic vane surface. While the greatest variation in the change in temperature

between spans on average belongs to the cooled vane readings, the difference in temperature magnitude between gauges is generally lower than for the vane without cooling. This is expected as the heat flux at the surface is generally reduced over most of the vane surface in the presence of film cooling.

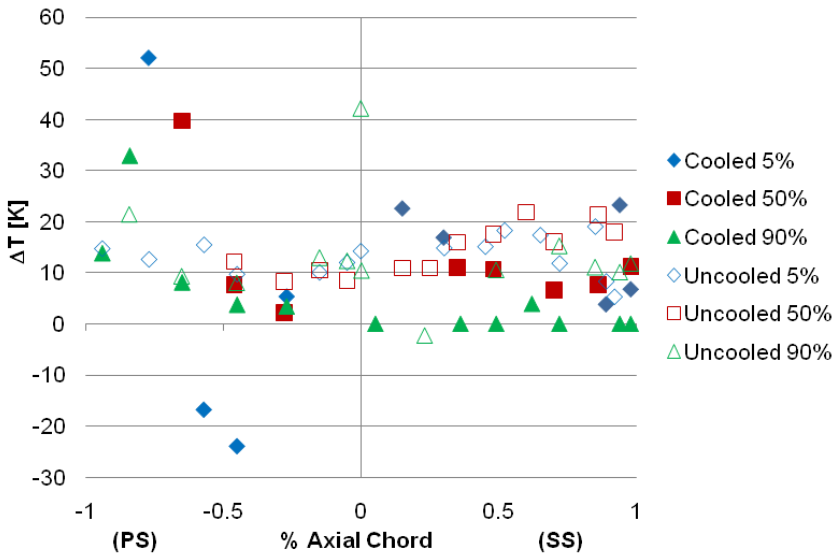

Figure A.28 – Double-sided heat flux gauge top-to-bottom temperature differences for the cooled and uncooled RTV at three different span locations.

Double-Sided Thin Film Heat Flux Gauges

The thin-film heat flux gauge has been used in countless past applications for performing experimental heat transfer measurements in short duration high-temperature turbine-representative flows. It is a device consisting of a thin metal element having a very small heat capacity bonded to the surface of an insulating substrate. The insulator may have a thin film gauge placed on one side or both sides. Double-sided gauges were used here for the Turbine Research Facility (TRF) blowdown facility experiments to obtain heat flux data on the Research Turbine Vane. The polyimide flexible substrate

used 50 microns thick and the gauges themselves are a platinum metal layer 500-Å thick. When subjected to a change in heat flux like the one that occurs in the full-wheel TRF tests, properly calibrated platinum films can be used to determine the temperature history of the substrate surface to obtain the transient heat transfer characteristics. When basic theory concerning transient heat conduction is employed and the properties of the substrate are known (ρ, c_p, k), the heat flux between the top and bottom gauges can be readily calculated. See Figure A.29 for a diagram of a metal surface cross-section with a double-sided heat flux gauge.

According to Dunn [4], in short duration transient test rigs, the available test time governs the substrate thickness onto which the gauge is painted (professionally sputtered in this case). However, in slowly varying or steady state facilities such as the TRF with 2.5 second run times, Equation A.1 can be used:

$$\dot{q}'' = k/a(T_1 - T_2) \tag{A.1}$$

T_1 and T_2 are the top and bottom thin film temperatures and a is the dielectric thickness. In the past, thin film temperature signals were converted to heat flux by an electrical analogue circuit. Here, heat flux is deduced from the measured voltage versus time history using a computationally efficient digital impulse response filtering method which approximates the solution of the differential equations governing one-dimensional heat conduction through the double-sided gauge [21]. A recent article by Oldfield also provides a thorough explanation the signal processing and digital filtering as applied here [179].

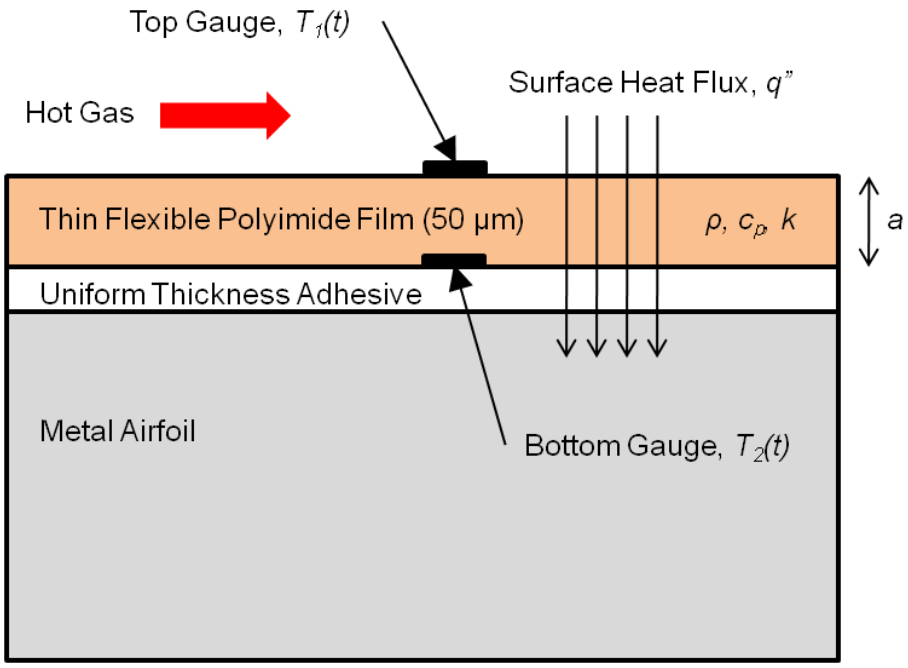

Figure A.29 - Double-sided thin film gauge diagram.

APPENDIX B: Validation of CEEF CFD against TRF Experimental Data

The following comparison of the CEEF CFD simulations to TRF experimental data for the Research Turbine Vane (RTV) is provided to give a general assessment of the current strengths and weaknesses of the *Leo* code which is used in the optimization in this work. While there are very few validation works available for review and comparison in open literature for engine-representative fully cooled turbomachinery components for multiple span locations, especially for heat transfer phenomena, the following results represent a best effort to assess the level of accuracy that the CFD provides. This level of CFD is not typically known to be able to resolve the detailed physics of film cooling flow, but does resolve general differences in temperature in order to redistribute cooling flow on a surface. It should be noted up front that, assuming the experimental data itself is accurate, the CFD is better at simulating the flow on certain areas of the vane surface than others and additional work is required to further mature the code so that all aspects of the TRF experiments are modeled.

Here, RANS cooling estimated external flow (CEEF) CFD simulations are conducted using the Wilcox k-ω turbulence model within a code called *Leo* on a three-dimensional fully film-cooled modern turbine inlet vane called the High Impact Technologies RTV. External flows at the same design-level coolant and main flow conditions as stated in the methodology are modeled along with their interaction with film cooling injected from the vane leading edge, pressure side (PS), suction side (SS), trailing edge, and hub and tip endwalls. As mentioned in the methodology, the film cooling is estimated using a local source term in the governing equations for the added

mass flux at the appropriate locations in the fluid domain along the vane surface. Cooled and uncooled isothermal vane simulations are conducted and compared to vane-only configuration heat flux data obtained in the AFRL TRF short-duration blowdown facility.

First, the cooled predictions of surface pressure at different span locations are compared with experimental data in Figure B.1. Vane surface pressure data was only available at 5%, 25%, and 50% spans at a few axial locations as seen in the figure. Where the data is available (denoted by red asterisks with black circles), it is seen that it is predicted well. Also, due to the effects of the cooling injection on both surfaces, large pressure fluctuations consistent with film-cooling hole rows is simulated by the CFD.

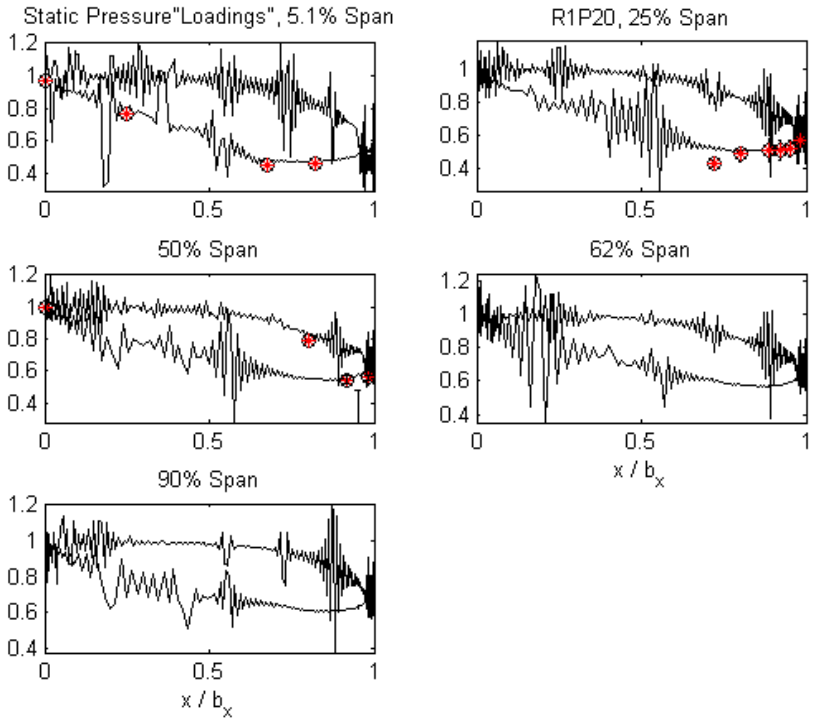

Figure B.1 - Vane surface pressure distributions at five span locations with film-cooling, CFD plotted against available TRF measurements.

The results presented next provide film cooled vane near-wall gas temperature ($T_{\infty,nw}$) as defined previously in the dissertation and near-wall heat flux predictions on a

3D full-scale operational turbine vane. Recalling from the methodology, $T_{\infty,nw}$ is meant to represent T_s within the CEEF CFD which uses an isothermal wall condition, and this parameter ultimately compares reasonably well with measured surface data from the TRF. Use of this parameter in the optimization also showed that it provided a good temperature characteristic to cause a redistribution of flow in order to cool the pressure surface. The TRF data obtained by AFRL gives some of the first heat flux data in a blowdown facility with greater than two full seconds of run time which can be compared to steady-state CEEF CFD predictions.

First, predictions of experimental uncooled RTV surface temperature using $T_{\infty,nw}$ from the CEEF CFD are given in Figures B.2 through B.7. Plots are provided at all six span locations where experimental data was measured: 5%, 25%, 50%, 62%, 90%, and 95% span locations. In each plot, a laminar, transitional, and fully turbulent CFD prediction is given. Also, for each plot, pressure side (PS) is on the left half and suction side (SS) is on the right with the leading edge (LE) at the center. At 5% span in Figure B.2, clearly there is under-prediction of surface temperature on the SS by about 4 or 5% of the magnitude of the experimental surface temperature over the entire length of the surface. The trend of decreasing measured surface temperature is still followed by the CFD, however. On the left half of the figure, on the PS, experimental surface temperature is predicted reasonably by CEEF CFD up to about 50% of the chord length. After this, the prediction gets gradually worse toward the trailing edge (TE) where the turbulent predictions are off by as much as 12%. In the experiment, flow on the PS appears to be transitional and then becomes fully turbulent with the combination of secondary flow further increase temperature levels downstream. In the experiments, near

the hub at this location, there is strong secondary flow due to the endwalls that is likely causing higher temperatures here. At the stagnation point where the near-wall gas temperature is predicted well, the secondary flow has not yet developed.

In Figure B.3 for 25% span, the PS is now much better predicted than the SS. This is a common theme seen for the uncooled vane at most span locations. Only near the TE on the PS is the TRF data under-predicted—by as much as 11%. On the SS, however, the predictions are farther from measurements than they were for 5% span as they are off by as much as 9% of the experimental levels. Something about the CFD is not capturing the effects of an adverse pressure gradient even with the assumption of fully turbulent flow. Unlike this work, an optimization of a cooling array on the SS may require more investigation as a result. Since this work deals with optimization on the PS of the vane, these discrepancies are not currently a concern.

At midspan in Figure B.4, the temperature is predicted very well again over most of the length of the pressure side using the fully turbulent assumption while the SS is still not captured well and is off by about 8% over most of the surface length. It appears that in the TRF experiments there is immediate transition to turbulence on the SS. It also appears that there may be a normal shock at the TE near the midspan locations as indicated by a sudden small rise in measured surface temperature. Predictions at midspan are cooler than at 5% and 25%, however the TRF temperatures are higher on the SS at midspan.

Surface temperatures on the PS at 62%, 90%, and 95% are also predicted well by $T_{\infty,nw}$ up until about two-thirds of the surface length towards the TE and the flow may be more laminar here, as the experimental data lines up with the laminar predictions better at

these span locations. Past two-thirds of the surface length on the PS, the predictions become gradually worse in the plots for locations closer to the shroud, as the predictions near the TE go from a difference of 3% to 12% of experimental magnitudes. On the other hand, the SS predictions get better for span locations closer to the shroud as predictions are off by about 7% at 62% span and 5% at 95% span. At all span locations on the SS, the general trend of higher temperatures near the LE followed by a gradual decrease towards the TE is followed by the predictions. Overall, for the purposes of the optimization, the uncooled RTV PS is predicted well at most span locations except near the hub and for most of the surface length except near the TE, especially closer to the shroud.

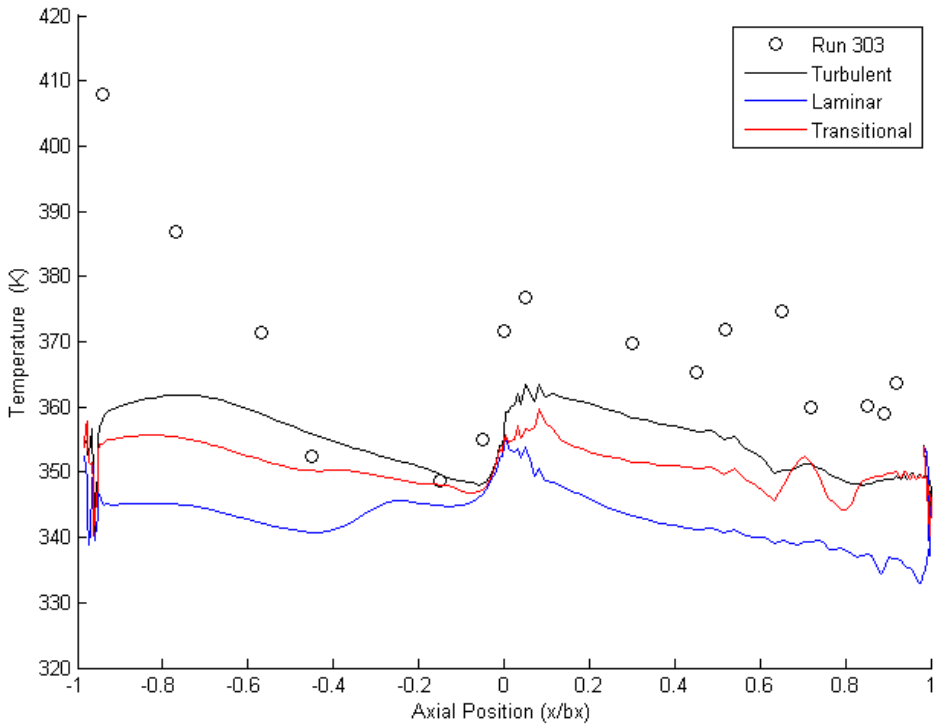

Figure B.2 - Comparison of CEEF CFD predictions using $T_{\infty,nw}$ and TRF experimental uncooled vane surface temperature at 5% span.

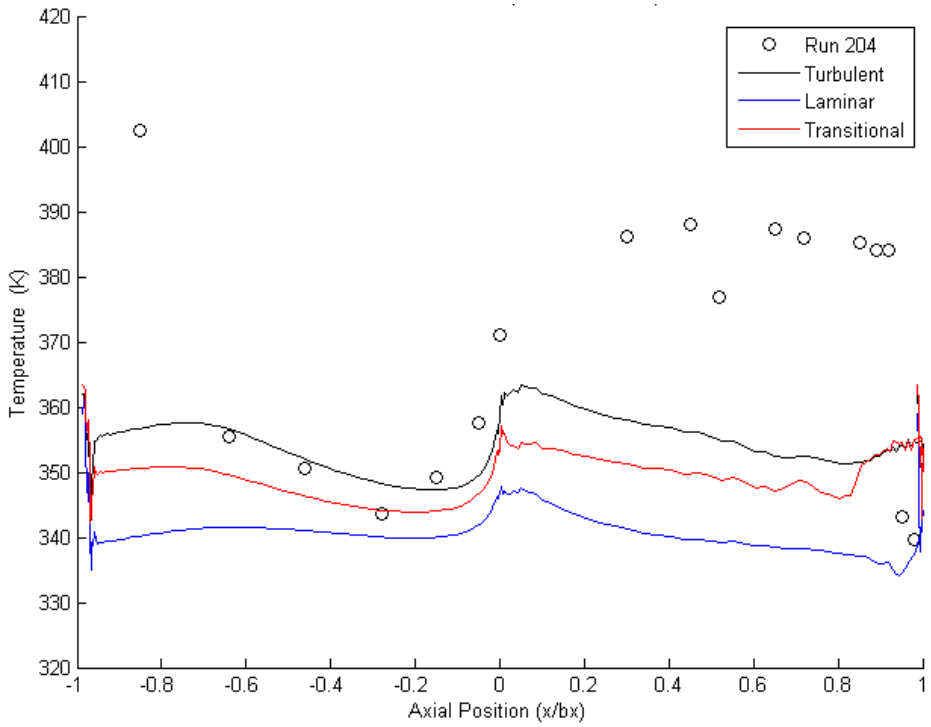

Figure B.3 - Comparison of CEEF CFD predictions using $T_{\infty,nw}$ and TRF experimental uncooled vane surface temperature at 25% span.

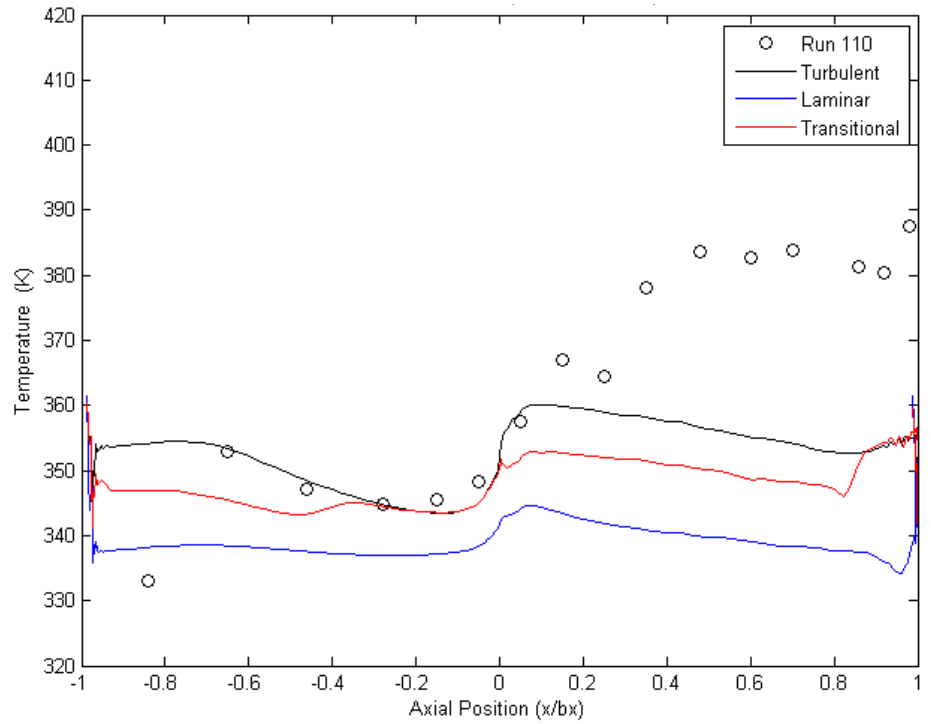

Figure B.4 - Comparison of CEEF CFD predictions using $T_{\infty,nw}$ and TRF experimental uncooled vane surface temperature at 50% span.

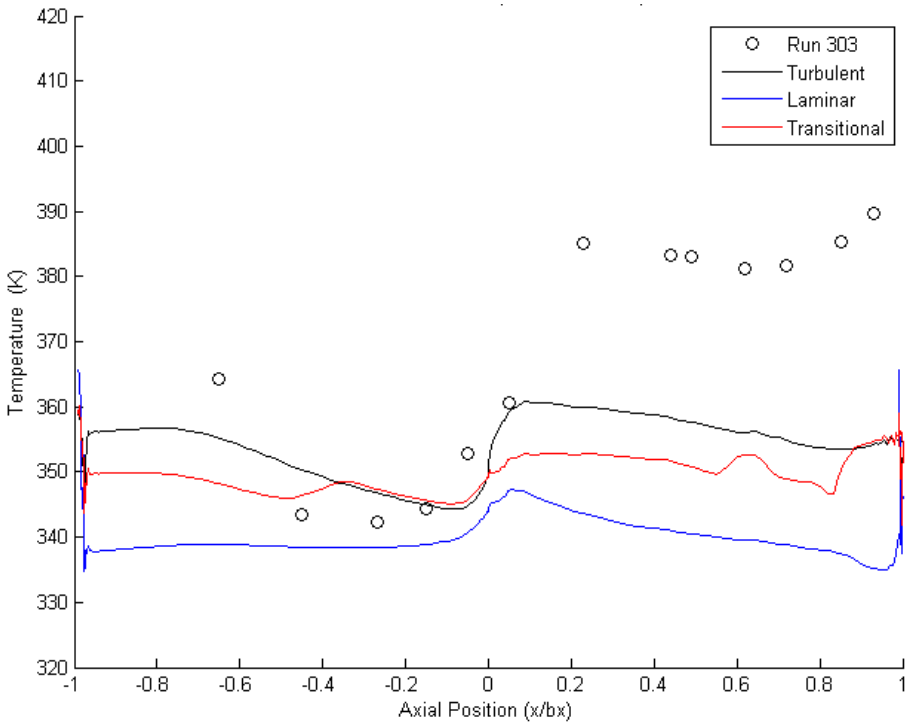

Figure B.5 - Comparison of CEEF CFD predictions using $T_{\infty,nw}$ and TRF experimental uncooled vane surface temperature at 62% span.

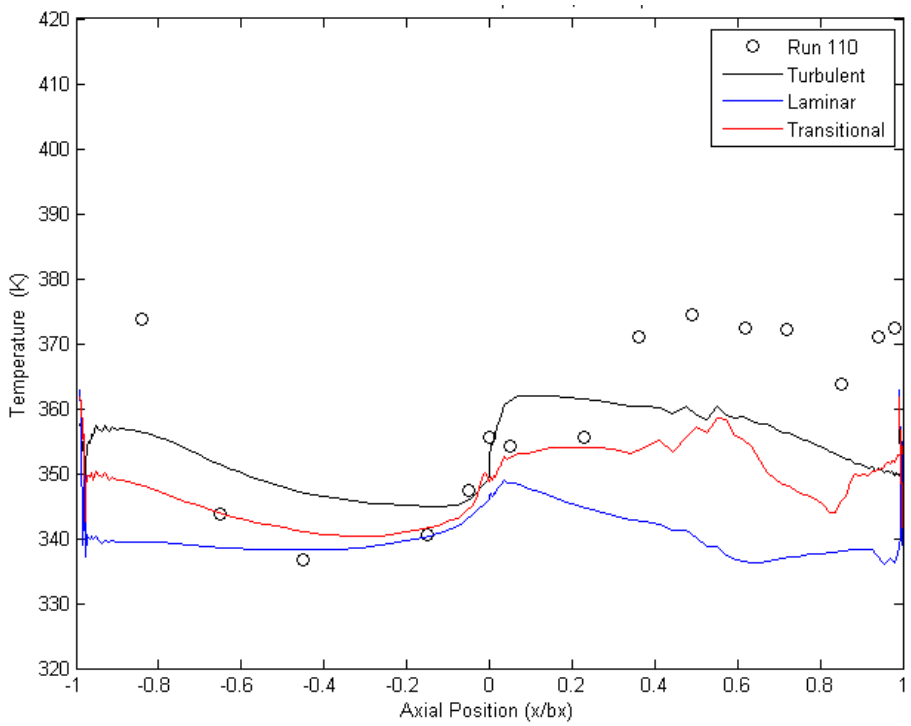

Figure B.6 - Comparison of CEEF CFD predictions using $T_{\infty,nw}$ and TRF experimental uncooled vane surface temperature at 90% span.

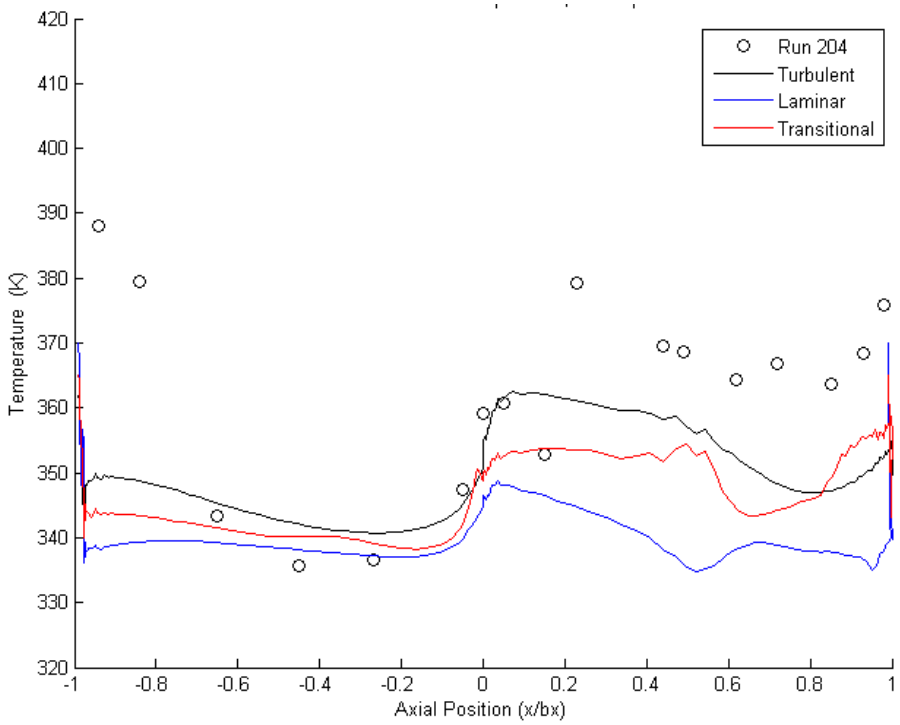

Figure B.7 - Comparison of CEEF CFD predictions using $T_{\infty,nw}$ and TRF experimental uncooled vane surface temperature at 95% span.

Predictions of surface temperature from TRF data using $T_{\infty,nw}$ are discussed next for the same six span locations on the vane with film cooling. With film cooling, a clear pattern arises due to the presence of discrete axial points of cooling air injection into the simulated flow. Heat flux gauges in TRF experiments could only be placed between cooling hole rows, so using data points as a reference, it can be seen how the surface temperature predictions drop abruptly at a cooling hole row then gradually increases until the rows of cooling holes is encountered. Thus, data can only be predicted where the temperatures are rising as the previous cooling hole rows lose their effectiveness with axial distance.

In Figure B.8, for 5% span, except for on the SS near the LE and TE, the CFD under-predicts levels of near-wall gas temperature. The presence of secondary flow

combined with cooling flow may be causing the large swings in temperature between cooling holes predicted here. Naturally, in more turbulent flow, the CFD predicts higher temperatures than for the laminar assumption when film cooling is present, and this turbulent prediction better matches experimental data on the PS up to about two-thirds of the surface distance. Up to this point, the trend of a steady increase in the experimental data between cooling hole rows is roughly followed by the predictions which are off by as much as 9% of experimental magnitudes.

In Figure B.9, with limited available data at 25% span, surface temperature is better predicted by $T_{\infty,nw}$ and the changes in temperature due to film cooling has recessed in magnitude relative to the hub and its secondary flow effects. However, it is hard to say with no data on the PS closer to the TE whether the CFD is predicting the experimental levels as well. In addition, as seen in multiple plots before, the prediction on the PS gets slightly worse towards the TE. Overall, at 25% span, the level of prediction accuracy is inconclusive.

At midspan in Figure B.10 and 62% span in Figure B.11, it appears that transition to turbulence is occurring on both sides of the vane. Boundary layer relaminarization, indicated by the drop in experimental temperatures downstream of the initial rise near the LE, can be seen on the SS. Unfortunately, PS temperatures are not predicted well by $T_{\infty,nw}$ in the CEEF CFD past about one-third of the surface distance. For the experimental data available, predictions are off by up to 6% of experimental magnitudes. Also, for midspan, there may be relaminarization as one experimental data point near the TE is predicted well by the CFD.

At 90% and 95% span in Figures B.12 and B.13, temperatures on the PS especially near the LE are predicted sufficiently but higher experimental temperature are observed downstream. SS experimental temperature is captured better at 90% span than 95% span. On the PS, the same under-prediction trends are seen that gradually worsen toward the TE. The 95% span case is better predicted on the PS than for 90% span, but this is because there is a lack of cooling holes here so it is more like an uncooled case. At 90% span the PS predictions are off by as much as 10% of experimental magnitudes.

With film cooling and without, the CEEF CFD does require maturation in terms of how it models the flow especially for adverse pressure gradients. Then again, in the experiments, it may be that the upper gauge, being displaced from the metal surface by a kapton layer, is registering higher temperatures than would be expected operationally at the surface. Since the CFD does not simulate the presence of a kapton layer due to the heat flux gauges, this is likely one reason that temperatures are under-predicted on many locations on the vane. Of course, in a real engine, thermal barrier coatings (TBCs) exist with thermal conductivities near the level of the kapton in the thin film gauges used in the TRF. So, the next logical step would be to model the kapton or a TBC in the CFD, which should be addressed in future work. Finally, concerning the vane PS, for which the cooling distribution was optimized in this work, predictions are off by as much as 10% with film cooling with better prediction occurring closer to the LE.

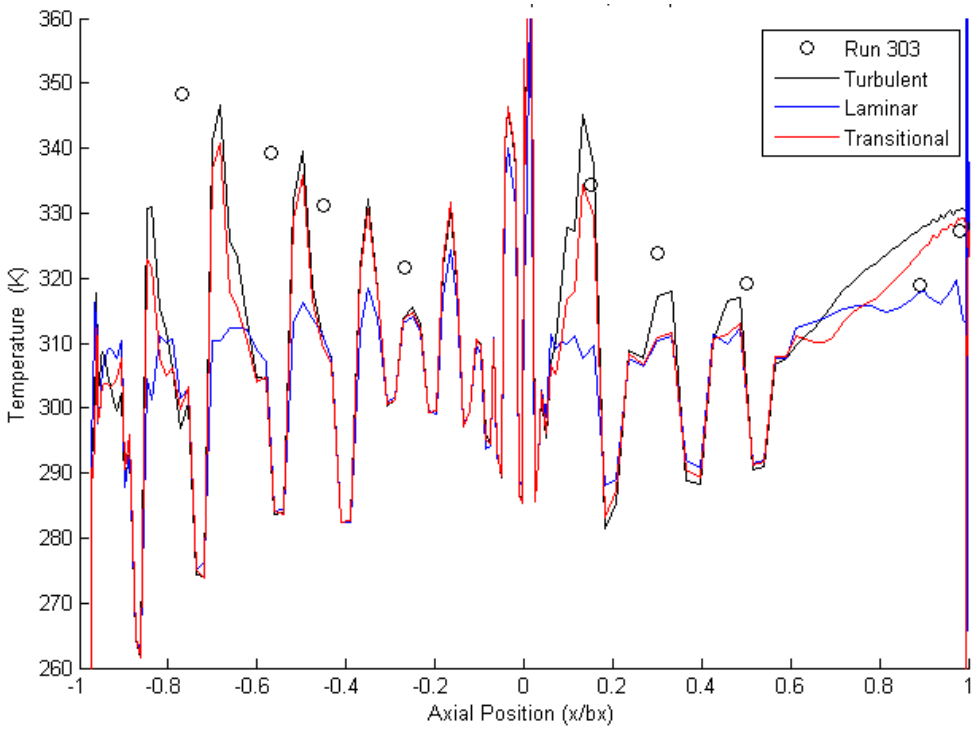

Figure B.8 - Comparison of CEEF CFD predictions using $T_{\infty,nw}$ and TRF experimental cooled vane surface temperature at 5% span.

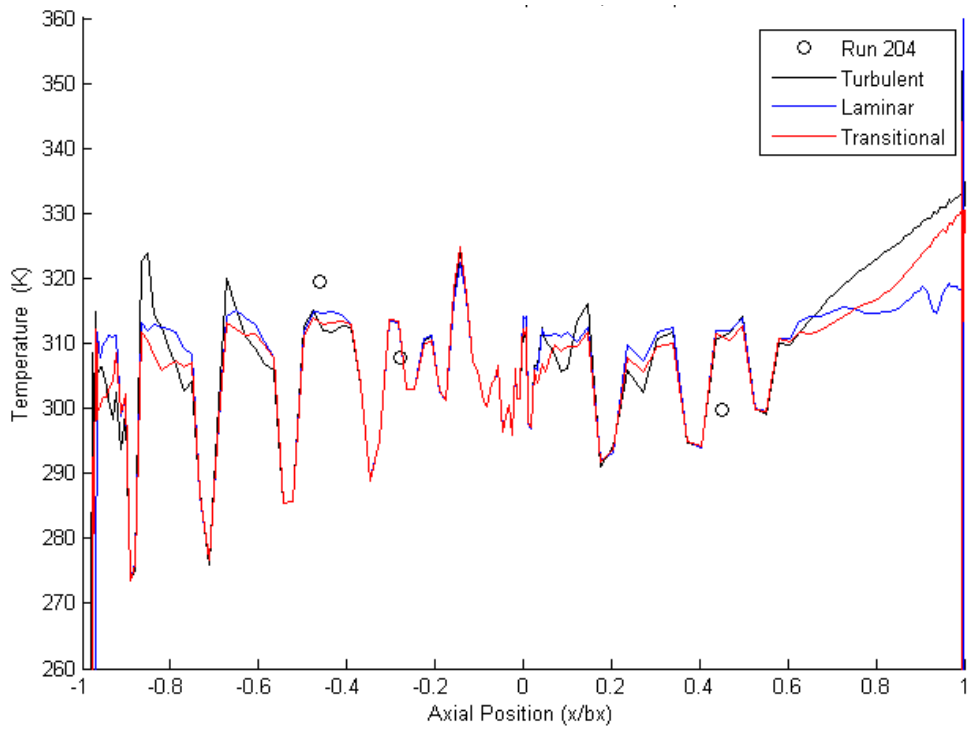

Figure B.9 - Comparison of CEEF CFD predictions using $T_{\infty,nw}$ and TRF experimental cooled vane surface temperature at 25% span.

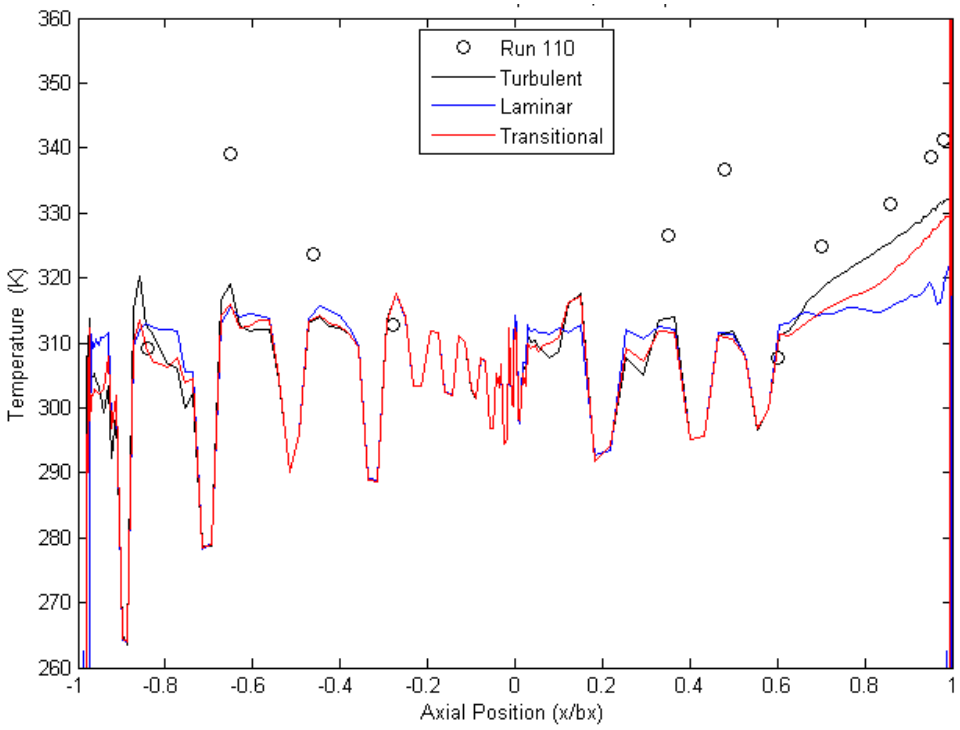

Figure B.10 - Comparison of CEEF CFD predictions using $T_{\infty,mw}$ and TRF experimental cooled vane surface temperature at 50% span.

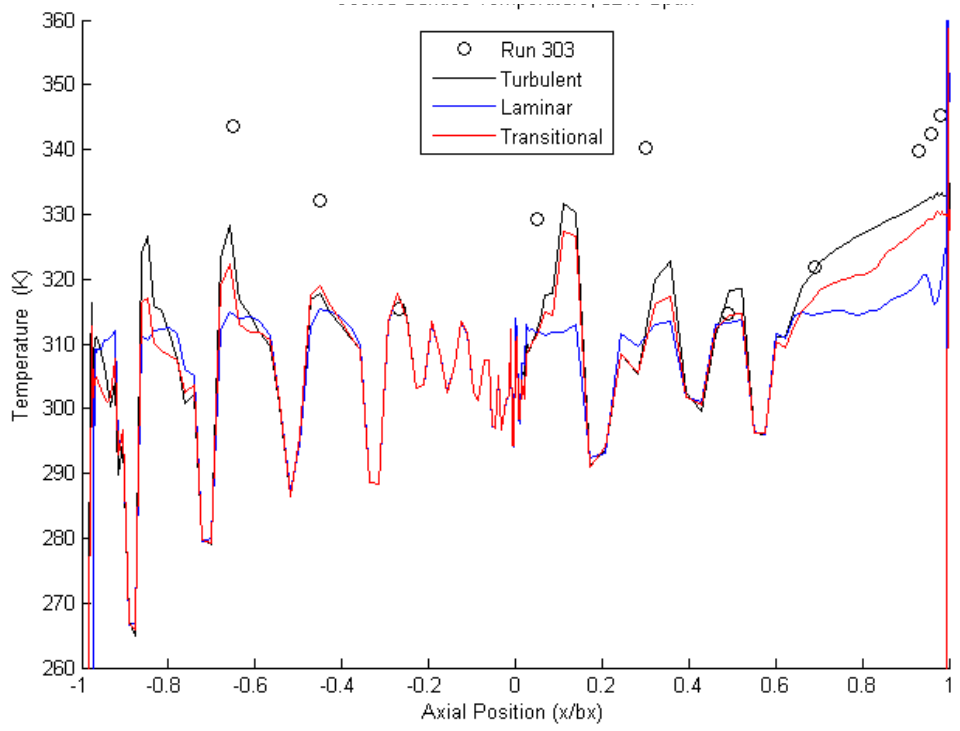

Figure B.11 - Comparison of CEEF CFD predictions using $T_{\infty,mw}$ and TRF experimental cooled vane surface temperature at 62% span.

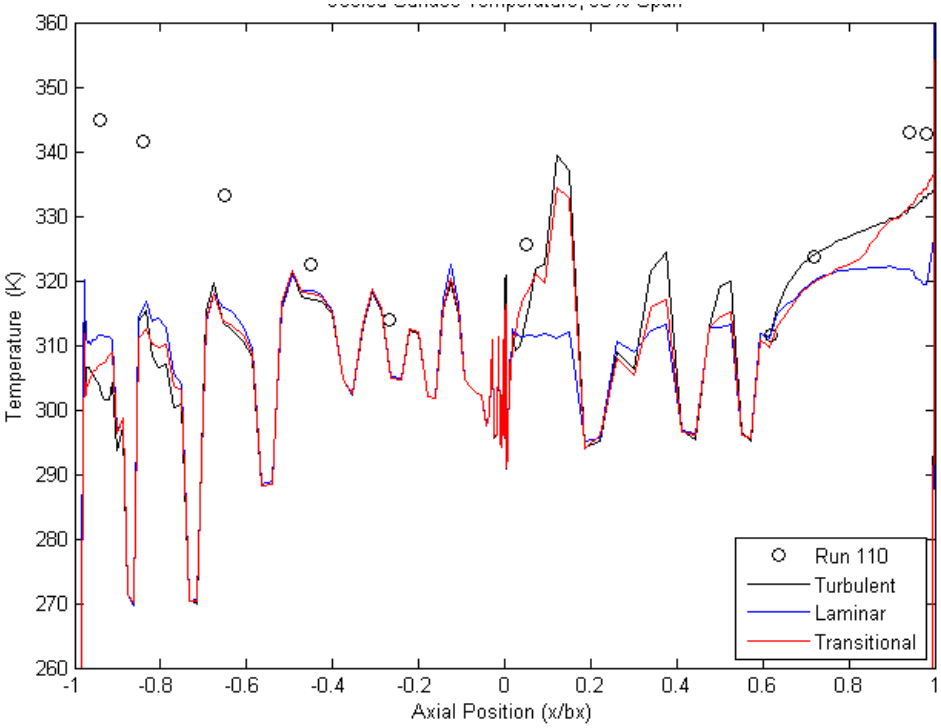

Figure B.12 - Comparison of CEEF CFD predictions using $T_{\infty,mw}$ and TRF experimental cooled vane surface temperature at 90% span.

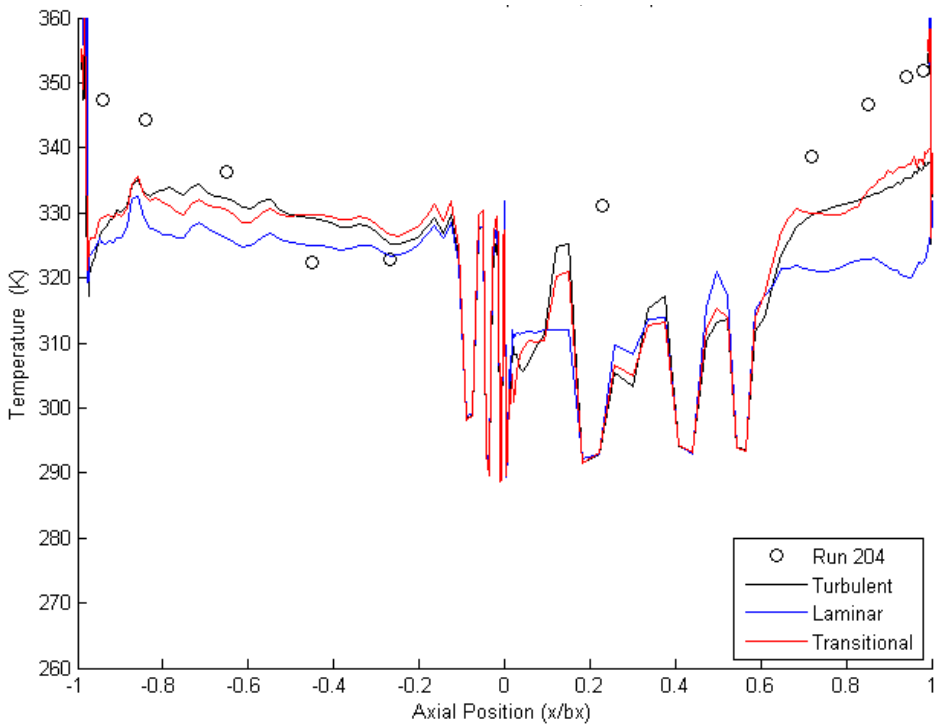

Figure B.13 - Comparison of CEEF CFD predictions using $T_{\infty,mw}$ and TRF experimental cooled vane surface temperature at 95% span.

Now, looking at uncooled vane near-wall heat flux predictions (as defined previously in the CEEF CFD results) against TRF data, it can be seen that experimental heat flux is generally better predicted on both sides of the vane than experimentally-measured surface temperature. Heat flux experimental data is shown with error bars based on uncertainties cited in previous work [21]. Again, laminar, transitional, and turbulent near-wall heat flux predictions are given with the data. These prediction plots have discrete jumps due to one value of heat flux being given per grid cell. So, step changes in heat flux predictions are just a function of the estimation using the grid, not the flow itself.

For most of the plots in Figures B.14 through B.19, areas of high heat flux are seen on the PS near the TE and near the LE on the SS. At 5% and 25% span for Figures B.14 and B.15, laminar heat flux is predicted well over most of the PS and the upstream half of the SS. After about mid-chord on the SS, transition to a turbulent boundary layer appears to drive up heat flux in the experimental data towards the TE. On the PS at 5% span the flow appears to be laminar over most of the surface. On the PS at 25% span, the experimental data show an increase followed by a decrease past about half the surface chord. This may be due to transition followed by relaminarization which is common on pressure surfaces.

At 50% and 62% span, in Figures B.16 and B.17, the experimental data is likely showing that there is more transition occurring on both the PS and SS at these span locations relative to closer to the hub, since the experimental data can be seen matching the laminar predictions close to the LE and matching the turbulent predictions closer to

the TE. This is more evident for the SS than the PS. Still, on the PS at these span locations, the experimental data falls well within the bounds of the predictions.

At 90% span in Figure B.18, there is an obvious rise in PS heat flux fin the experiments near the TE that is modeled by the turbulent prediction. A gradual change from a laminar to turbulent boundary layer can be seen on the PS for the experiments. The transitional predictions model the TRF data best on the SS at this location. Except for one point on the SS, the CFD models heat flux well at this span location, especially assuming turbulent flow. At 95% span, despite the endwall effects near the shroud, the boundary layer is likely laminar in the experiments based on how the laminar predictions match experiments on both the PS and SS. This may indicate that the endwall secondary flow effects are weaker at the shroud than at the hub.

Overall, for the uncooled vane, the experimental heat flux is represented reasonably well on both the PS and SS by the near-wall heat flux simulated by the CEEF CFD in the optimization results. The greatest disparities are observed between experiments and predictions on the SS near the LE.

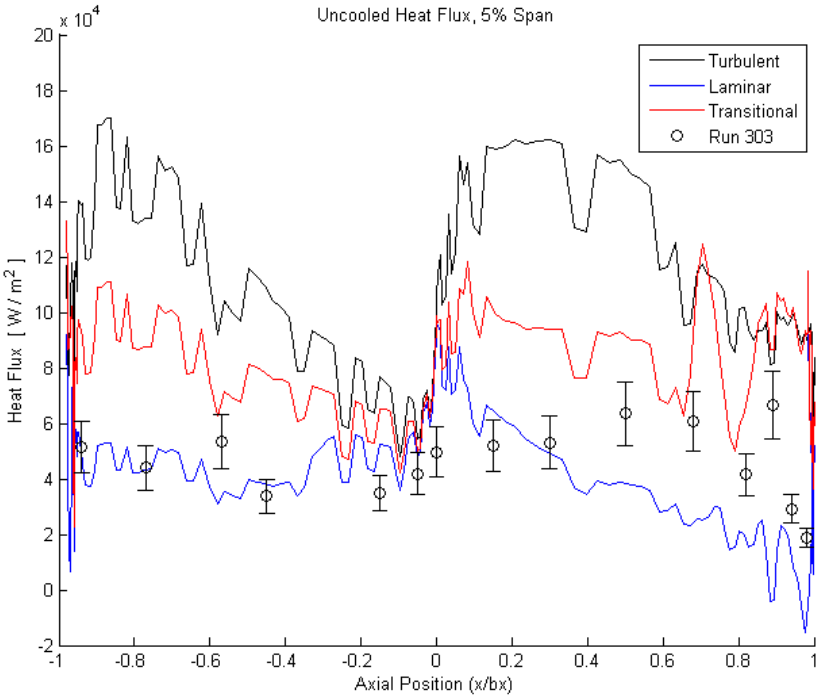

Figure B.14 - Comparison of CEEF CFD predictions using near-wall *q"* and TRF experimental surface heat flux at 5% span for the uncooled vane.

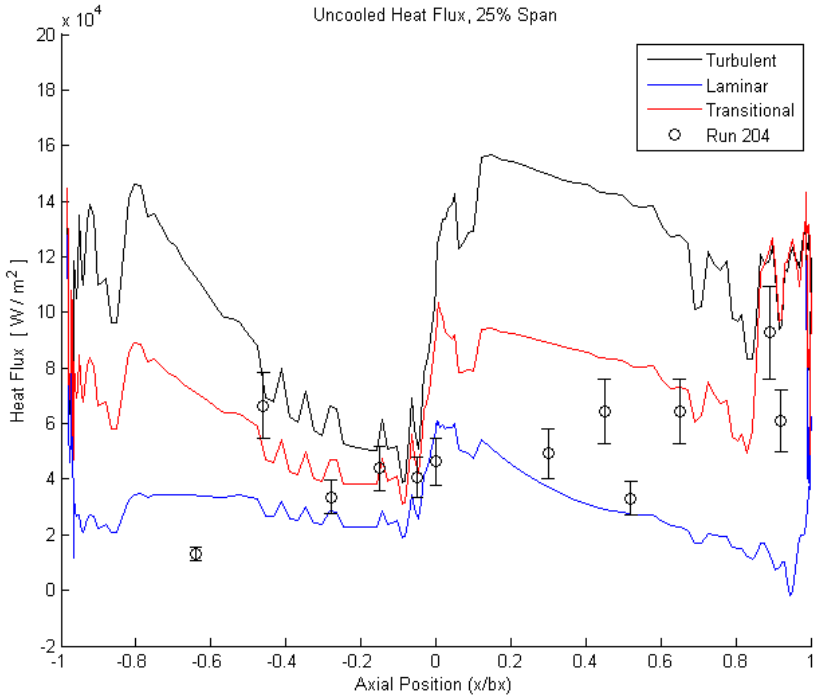

Figure B.15 - Comparison of CEEF CFD predictions using near-wall *q"* and TRF experimental surface heat flux at 25% span for the uncooled vane.

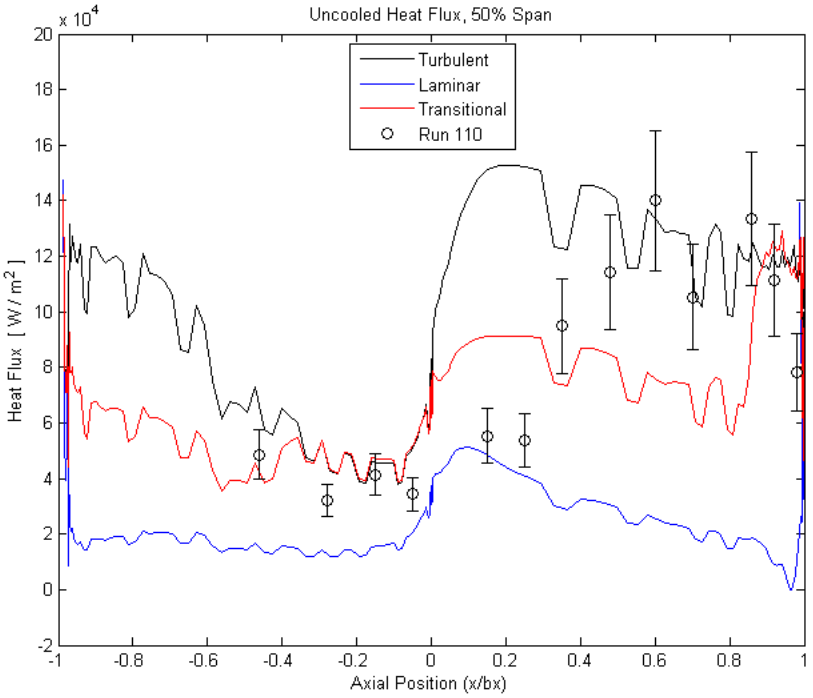

Figure B.16 - Comparison of CEEF CFD predictions using near-wall *q"* and TRF experimental surface heat flux at 50% span for the uncooled vane.

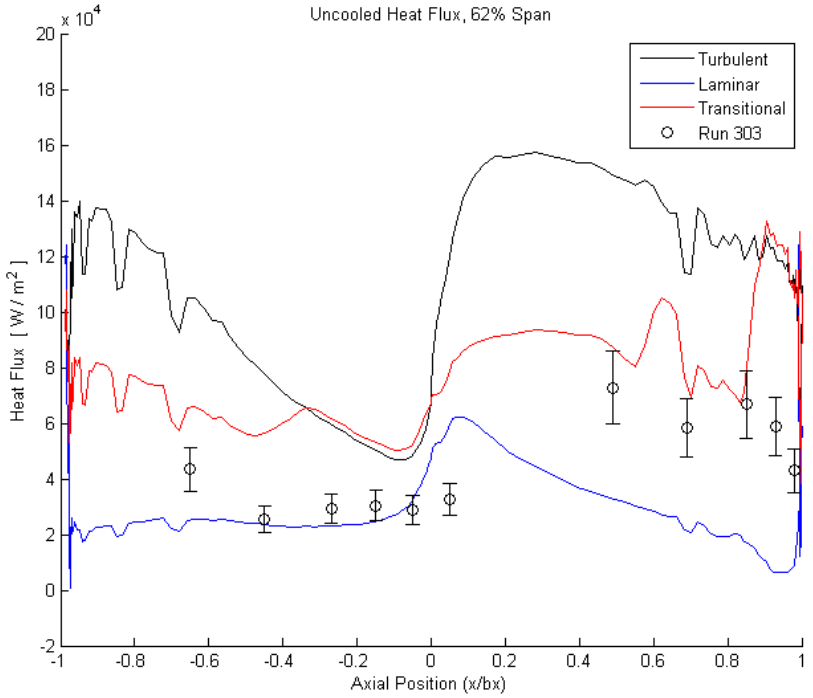

Figure B.17 - Comparison of CEEF CFD predictions using near-wall *q"* and TRF experimental surface heat flux at 62% span for the uncooled vane.

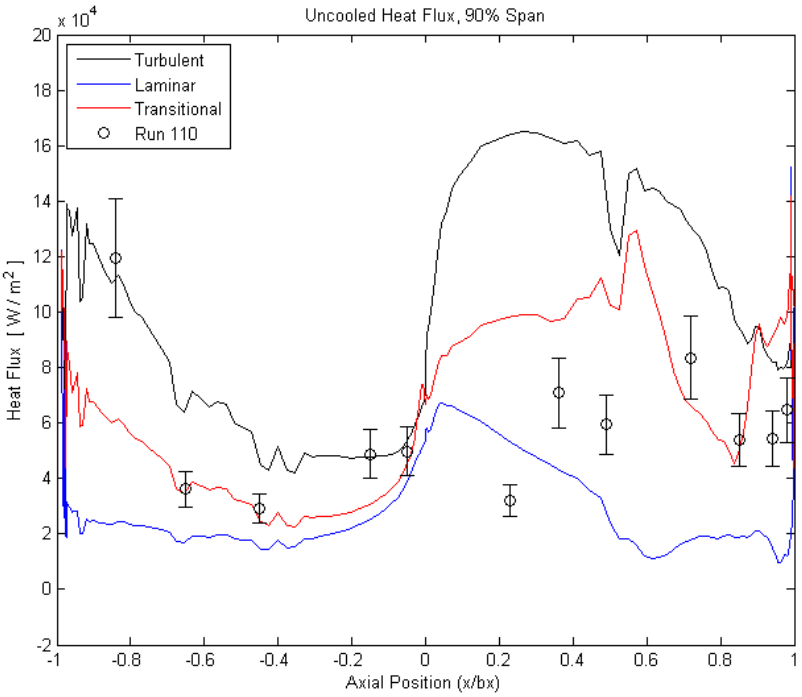

Figure B.18 - Comparison of CEEF CFD predictions using near-wall *q"* and TRF experimental surface heat flux at 90% span for the uncooled vane.

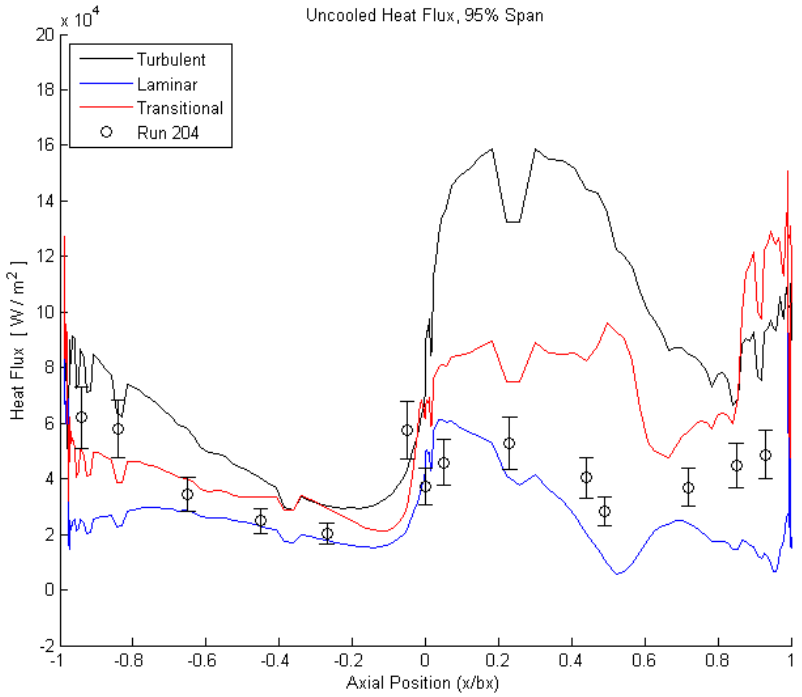

Figure B.19 - Comparison of CEEF CFD predictions using near-wall *q"* and TRF experimental surface heat flux at 95% span for the uncooled vane.

The last set of plots shows near-wall heat flux prediction with film cooling for the CEEF CFD against heat flux gauge surface measurements from the TRF. The spikes in simulated heat flux are of a much greater magnitude than for temperature. Also, the differences in the laminar, transitional and turbulent heat flux predictions with film cooling are far less than in the case of temperature, especially with film cooling simulated. In other words, near-wall heat flux predictions with film cooling appear to be more independent of the state of the boundary layer. Still, levels of experimental heat flux data between film cooling rows can be compared to CEEF CFD predictions.

There is little data to compare to at 5% span in Figure B.20, but the available measurements on the SS are predicted well. The one available PS experimental data point is under-predicted by about 5% while the experimental data on the SS is matched well by predictions. The 25% span in Figure B.21 is another location where little experimental heat flux data is available, but the two data points on the PS are predicted well by the CEEF CFD near-wall heat flux.

At midspan in Figure B.22, more experimental data points are available for comparison to predictions and the measured surface heat flux is predicted well with film cooling on both sides of the vane. This is true at 62% span in Figure B.23 as well, except on the suction side near the LE.

At 90% span, much like at midspan, the LE heat flux is predicted well along with the rest of the PS and SS, except very close to the TE on the PS. At 95% span in Figure B.25, PS heat flux is over-predicted by the laminar assumption by about 50% of experimental magnitudes, while the SS heat flux is highly under-predicted near the LE. This is mostly attributed to the fact that there are fewer cooling holes near the endwall on

the PS than on the SS. Still, heat flux trends are captured well by the CEEF CFD and levels of heat flux near the TE is predicted accurately, despite the apparent changes in the state of the boundary layer at that location on the vane. Overall, the near-wall heat flux estimation in the CEEF CFD predicts measured surface heat flux well for most of the PS and SS at multiple span locations. While the temperatures are not predicted as well as the heat flux measurements with film cooling, the fact that the CEEF CFD is accurately modeling wall-normal temperature gradients adds confidence to the relative near-wall heat flux performance provided between the baseline and optimized cooling array in the results section of this work. It should also be noted that while there are a few disparities in the predictions for heat flux with film cooling, the disparities are very small relative to the large magnitude of the heat flux spikes caused by film cooling.

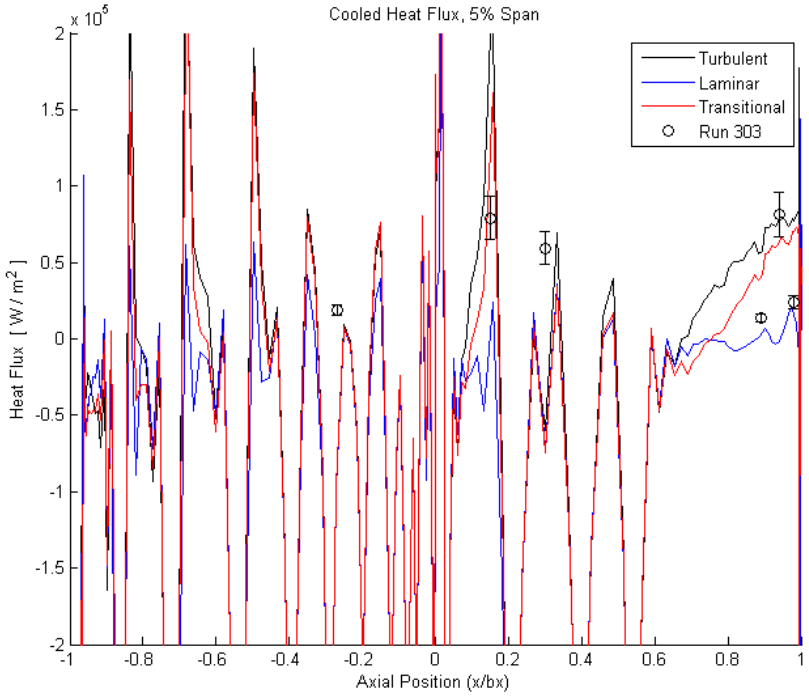

Figure B.20 - Comparison of CEEF CFD predictions using near-wall *q"* and TRF experimental surface heat flux at 5% span for the cooled vane.

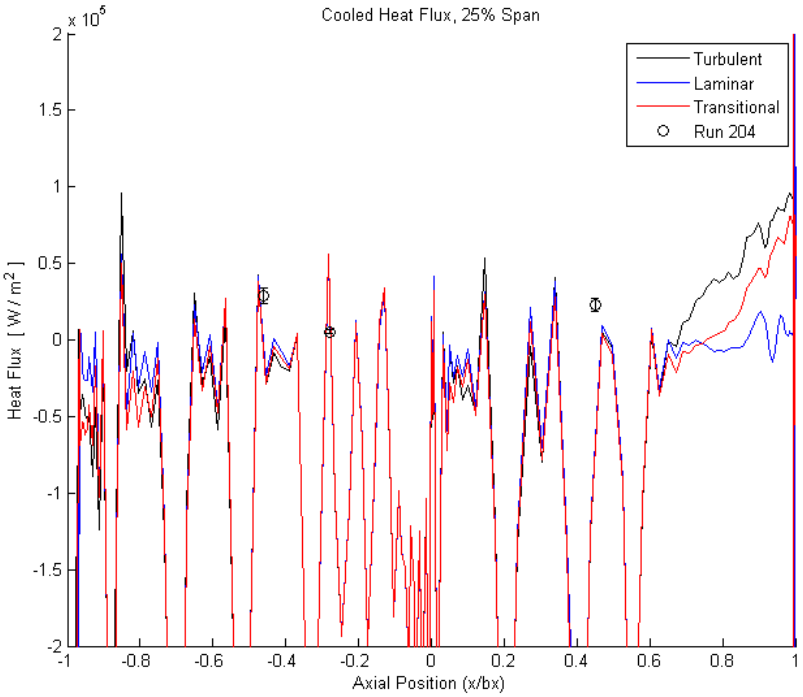

Figure B.21 - Comparison of CEEF CFD predictions using near-wall *q"* and TRF experimental surface heat flux at 25% span for the cooled vane.

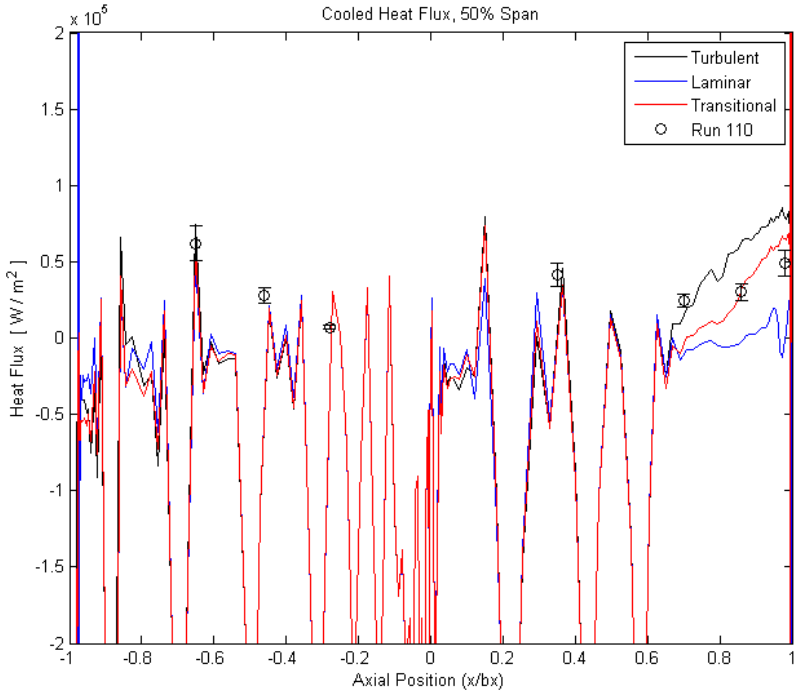

Figure B.22 - Comparison of CEEF CFD predictions using near-wall *q"* and TRF experimental surface heat flux at 50% span for the cooled vane.

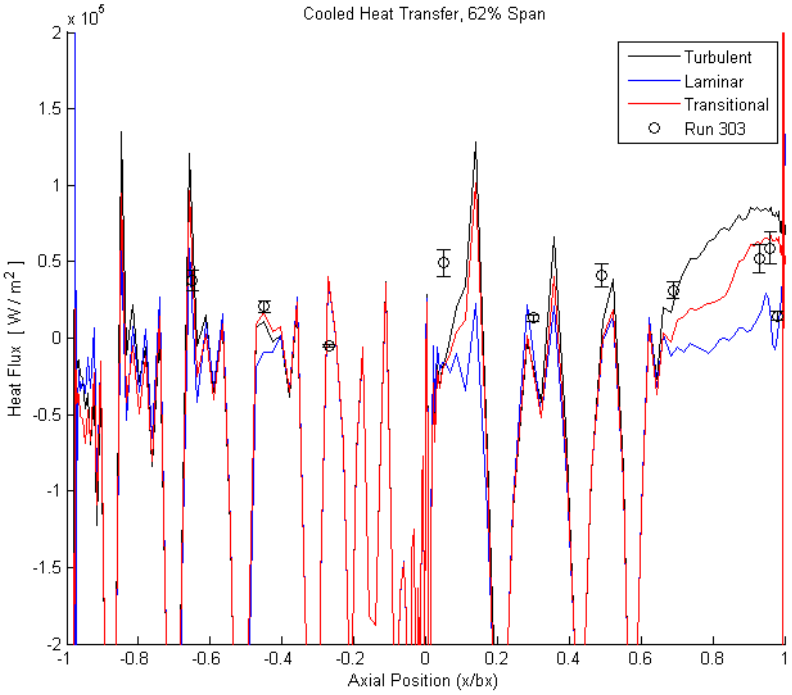

Figure B.23 - Comparison of CEEF CFD predictions using near-wall *q"* and TRF experimental surface heat flux at 62% span for the cooled vane.

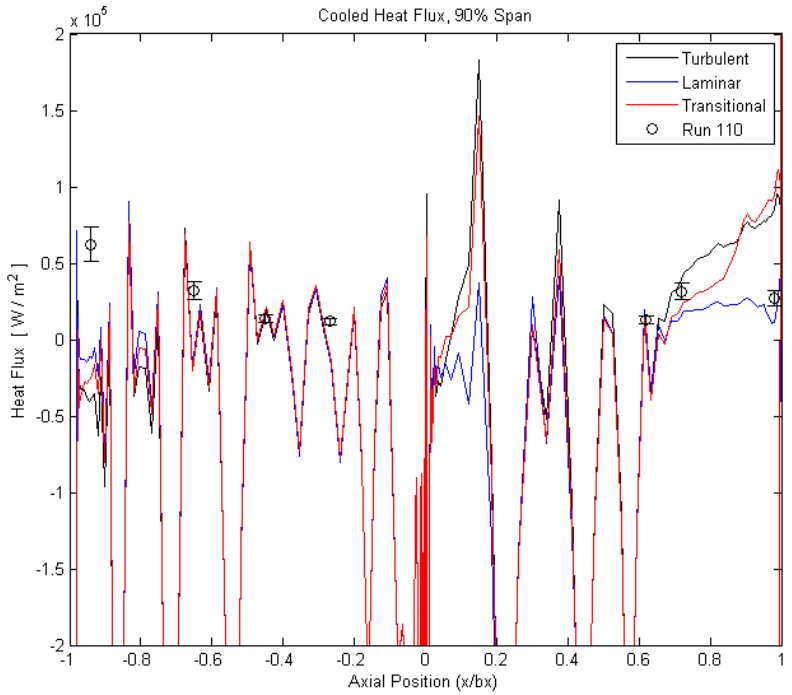

Figure B.24 - Comparison of CEEF CFD predictions using near-wall *q"* and TRF experimental surface heat flux at 90% span for the cooled vane.

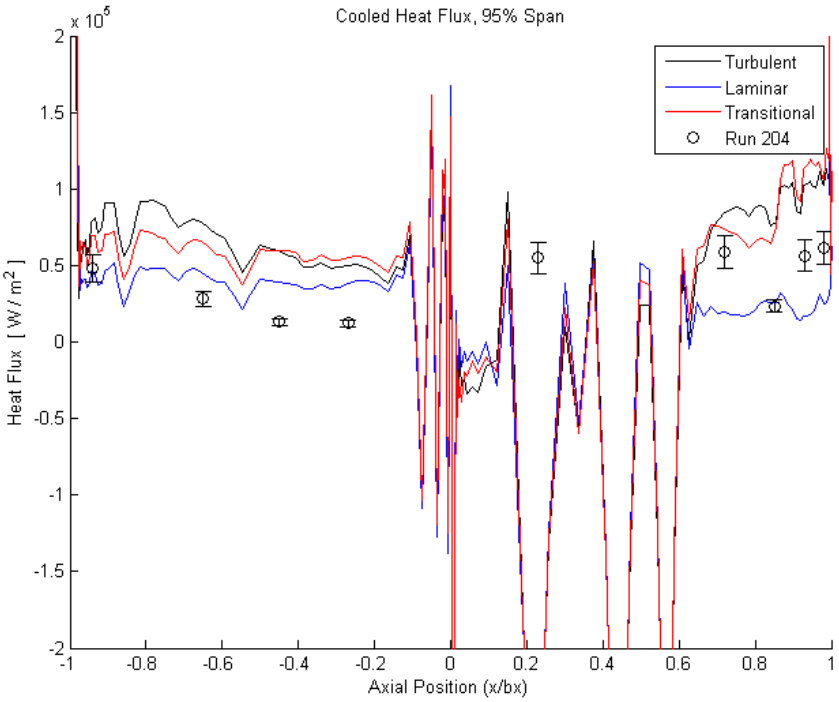

Figure B.25 - Comparison of CEEF CFD predictions using near-wall *q"* and TRF experimental surface heat flux at 95% span for the cooled vane.

Using the near-wall values of temperature and heat flux from the CEEF CFD with an isothermal boundary condition has shown that when compared with experimental surface heat transfer data, heat flux is better predicted than temperature. For the temperature alone, the PS levels are better predicted than on the SS. With respect to the optimization, one weakness of the CEEF CFD is under-prediction of PS temperatures with film cooling, which were off by at most 10% of the experimental magnitudes. Clearly, more work is necessary to capture SS heat transfer phenomena in adverse pressure gradients and PS heat transfer with film cooling. Any current weakness in the CFD may be attributed to the fact that it does not model a kapton layer for the heat flux gauges that are present in the experiments and the coarseness of the grid use relative to the small-scale flow features caused by film cooling. It should be reiterated that this form

of CFD is not meant to resolve the smallest physical features of the flow, but rather to provide aggregate estimates of cooling performance such that it can be utilized thousands of times rapidly as part of a design tool. As the optimization here concerns the pressure surface only, and since heat flux in the presence of film cooling is predicted well, and temperatures with film cooling are predicted well on the PS near the LE, the CEEF CFD solver, associated turbulence model, and proposed use of near wall gas temperature ($T_{\infty,nw}$) and near-wall heat flux in making comparisons between the baseline and optimized cooling designs is deemed adequate for discerning major changes between cooling designs within the optimization. With level of validation detail is not seen in open literature, this form of CFD is not perfectly accurate, and certainly not as accurate as conjugate heat transfer CFD which would add months of computational time to the current optimization. Thus, experimental flat plate infrared thermography is conducted in the current work to evaluate relative performance of the baseline and optimized cooling arrays. This in turn provides added confidence that the computational optimization has set out what it was intended to do and added confidence in the relative experimental results on the sections of the vane surface where the CEEF CFD best matched experimental data.

APPENDIX C: Validation of CHT CFD against TRF Experimental Data

The CHT CFD simulations were compared to the results of experiments by Anthony et al. [21] in the Air Force Research Laboratory Turbine Research Facility (TRF). The TRF is a full-scale full-wheel experimental blowdown rig designed to obtain time-accurate unsteady pressure, surface temperature, and surface heat flux data from various installed single shaft turbine hardware designs and is capable of stage-and-one-half configurations. Before stage-and-one-half runs with the rotating hardware, tests were conducted with only the inlet guide vane wheel installed. Vane surface heat transfer measurements on vanes with and without film cooling were obtained for the High Impact Technologies (HIT) Research Turbine Vane (RTV) at its design conditions.

The TRF operates at flow conditions that are non-dimensionally consistent with the turbine environment. The rig uses pressurized Nitrogen in an upstream tank and a downstream dump tank at near vacuum pressures. The back pressure in the dump tanks can be set between 0.68 atm and 1.00 atm. The usable run time is approximately 2.5 seconds and is started by a main valve which opens the test section to the pressurized main flow. Multiple stream-wise and span-wise locations on different cooled and uncooled vanes were assessed for heat transfer. Numerous stream-wise measurements at six span locations are reported here: 5%, 25%, 50%, 62%, 90% and 95%. Heat flux data is obtained using custom-designed non-intrusive thin-film double-sided heat flux gauges. Surface temperature is measured by the top gauge in a heat flux gauge pair. Top and bottom gauges are separated by a kapton layer. Depending on the span location and the vane, there were between five and ten gauges distributed in the axial direction on a side.

Naturally, the SS tended to have more gauges because its surface distance is longer than the PS, and the uncooled vanes tend to have more gauges than the cooled since without cooling hole rows, there is more surface length on which gauges can be placed. It should be noted that no thermal barrier coating was used in experiments or simulated in the CFD. In addition, the adhesive and kapton layers from the heat flux gauges were not simulated in the CFD, since while the conjugate code is maturing, it cannot currently model layers above the metal surface.

Different sections of the vane wheel measure different flow properties, as only so many measurements can be obtained from a single vane. In addition, with a limited but still vast amount of data acquisition channels, data is taken for comparison to CFD from three different TRF runs that all ran at the vane design conditions. There were small differences between run conditions and these can be considered negligible. Surface temperature is also monitored using surface mounted thermocouples on the vanes and static pressure data is gathered using taps leading to Kulite transducers on the surface at varying span locations. Nominal experimental inlet conditions based on the vane operational design point are an initial total pressure of 6.8 atm (100 psia) and initial total temperature of 444 K (800 °R). However, in order to match the design value for the total coolant-to-mainstream pressure ratio ($P_{t,c}/P_{t,\infty}$) of 1.05, and since coolant flow pressure could not be widely varied, the main flow pressure was scaled to levels below 6.8 atm. All other flow conditions modeled are the same as those mentioned in the methodology for both types of CFD in this work.

Comparing the conjugate heat transfer RTV CFD simulations to the TRF experiements at the same conditions, plots are given which show either heat flux or

surface temperature at six different span locations. In the plots, flow is going from left to right, with LE on the left and the TE on the right. Looking at the PS on the uncooled RTV, Figures C.1 and C.2 are comparisons of surface q'' and T_s, respectively. The heat flux, shown with error bars based on fully-propagated error of ±18%, is mostly under-predicted for much of the PS except near the LE. This may be due to the CFD modeling the flow with less turbulence than actually exists in the TRF. The TRF is estimated to have low turbulence intensity in the freestream at about 2%. The k-ω turbulence model used also may not be picking up increased turbulence in the boundary layer. It appears that from the measurements, the flow in the experiments transition to turbulent flow at mid-chord. The CFD appears to estimating that there is little or no boundary layer transition over the entire chord for all span locations. Running the CFD with a proper transition model instead may ultimately aid in capturing areas of higher heat flux. The CFD predicts higher heat flux near the hub and shroud while the experiments show more variation between span locations.

The surface temperature comparison in Figure C.2 shows an over-prediction for the uncooled PS over the surface length of about 50 K (12% of the experimental magnitudes) that decreases towards the TE. The error in these measurements is approximately ±2 K and is too small to show as error bars here. Both the CFD and experiments show a drop in T_s after the LE followed by a gradual increase towards the TE, with the experiment showing slightly more variation between spans. This trend of high heat flux at the LE and TE on the PS is also seen in the CEEF CFD. Through much iteration, it was ultimately found that this over prediction is due to the fact that the uncooled is more transient than steady, as explained in the body of the dissertation, and

the fact that these results used vane metal temperature rather than the top heat flux gauge as an initial wall temperature setting for the CFD. For the uncooled vane, the lack of a heat sink, unlike that in the case with film cooling, means that the surface temperature solution will rise with the number of iterations towards the hot gas temperature. Corrections to this convergence problem for the maturing CHT CFD code are in work.

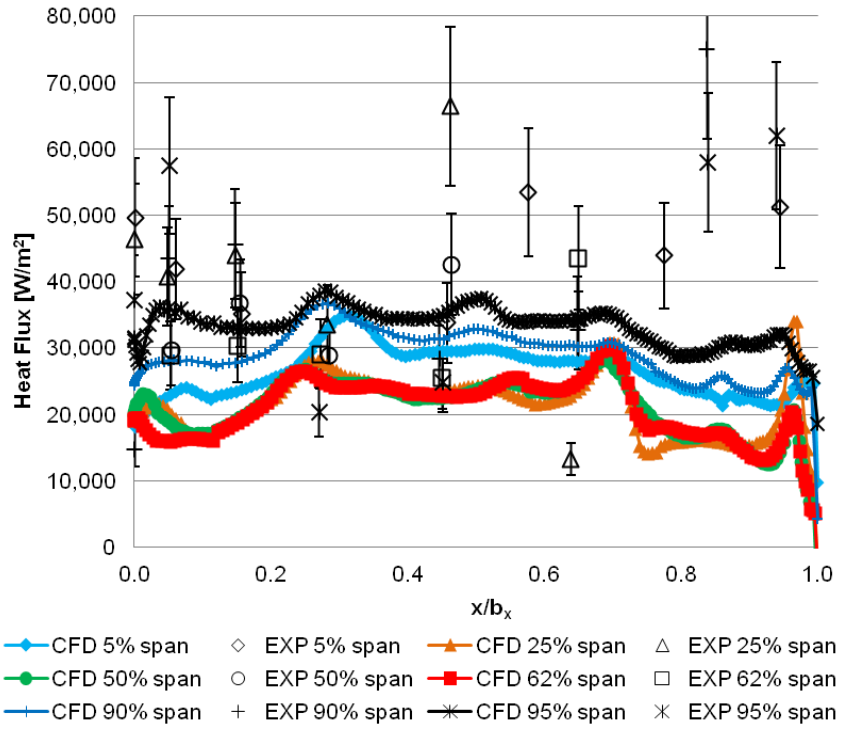

Figure C.1 – Uncooled RTV PS heat flux [W/m^2] at six span locations comparing CHT CFD to TRF experiments.

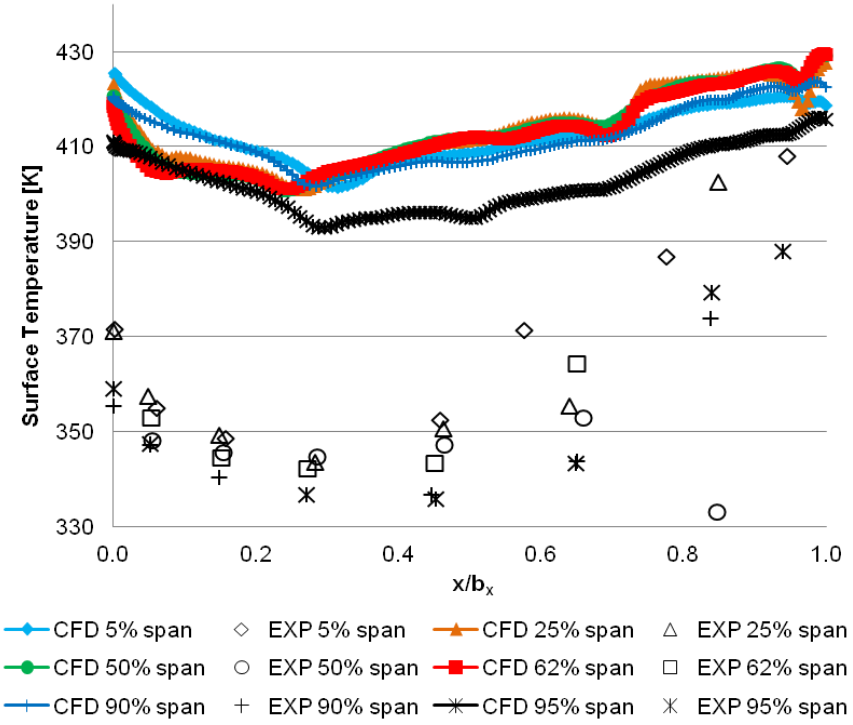

Figure C.2 – Uncooled RTV PS T_s [K] at six span locations comparing CHT CFD to TRF experiments.

Figures C.3 and C.4 are the results with film cooling for the PS of the vane. Due to the scale of the predicted heat flux, error bars are omitted for the experimental data in the case of the cooled RTV. In general, in the presence of film cooling, the heat flux is predicted by the CFD well. Since it is known that heat flux gauges can only be placed squarely between cooling hole rows, it is clear where cooling hole rows lie and their influence on the predicted surface heat flux. As seen in previous plots in the dissertation, the characteristic drop in *q"* at a cooling hole row followed by a steady increase up to the next cooling hole row can be seen here. Again, on film cooled surfaces there is less room for heat flux gauges, although of the available measurements, the CFD predicts the measurements well within their error bounds at most span locations near the shroud. At these locations, the CFD is predicting higher heat flux due to the lack of cooling holes

relative to other spans while the measurements clearly show a lower level at multiple axial surface locations. Meanwhile, the experimental *q"* is lower with film cooling, however comparisons can only be made at discrete axial chord locations between cooling hole rows where gauges exist. It is hard to say what the experimental data looks like between points of available instrumentation, which may actually be more cyclic like the predictions. This highlights the advantages of experiments that provide more continuous data to be compared to CFD, like the use of infrared thermography on a flat plate PS cooling array model. Both the experiment and CFD show slightly increasing levels of *q"* between cooling hole rows with chord length. The inter-row heat flux is likely increasing due to the boundary layer becoming more turbulent. The CFD shows interestingly shows that the smallest spikes in *q"* near the LE is at 62% span and the highest spikes in *q"* are also at 62% span near the TE. Meanwhile at 95% span it can be seen that there is little or no effect of film cooling. The CFD also shows a higher degree of variation between spans than the experiments show.

Cooled T_s, shown in Figure C.4, is under-predicted across the length of the PS by about 40 K (12% of the experimental magnitudes) except at the highly-cooled area of the PS where heat flux is predicted well. The CFD predicts a low temperature region at the site of the first few shaped hole rows on the PS while the experiments do not appear to see this, following more closely the trend of the 95% span CFD. The higher span locations appear to be predicted better than lower spans near the hub in the regions between the cooling hole rows where the CFD predicts peaks in temperature between rows. But without higher experimental instrumentation resolution, it is difficult to tell if

the experiments follow the peaks and valleys of the CFD. The under-prediction may also be due to the fact that a kapton layer is not simulated here that exists in the experiments.

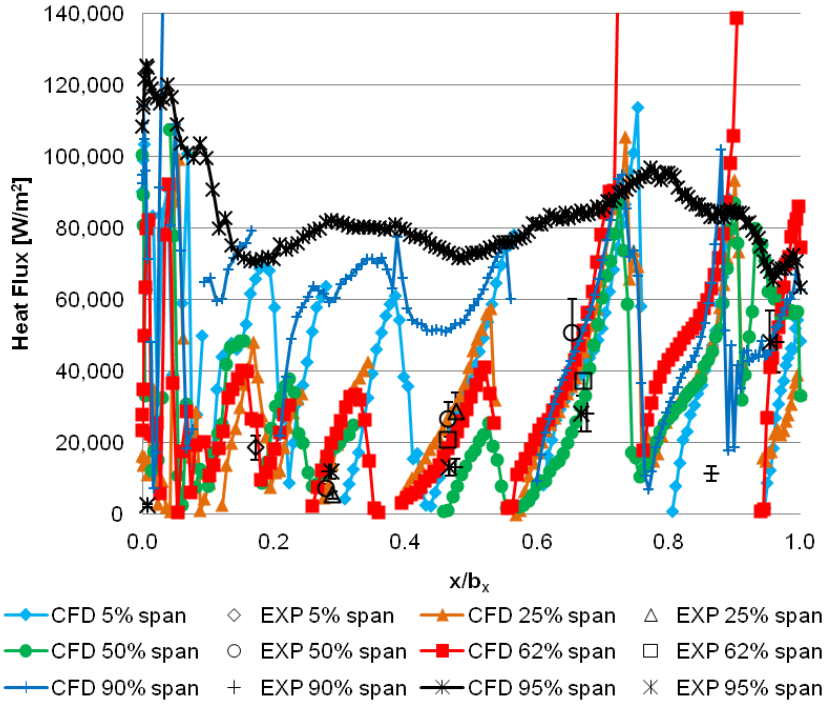

Figure C.3 – Cooled RTV PS heat flux [W/m^2] at six span locations comparing CHT CFD to experiments.

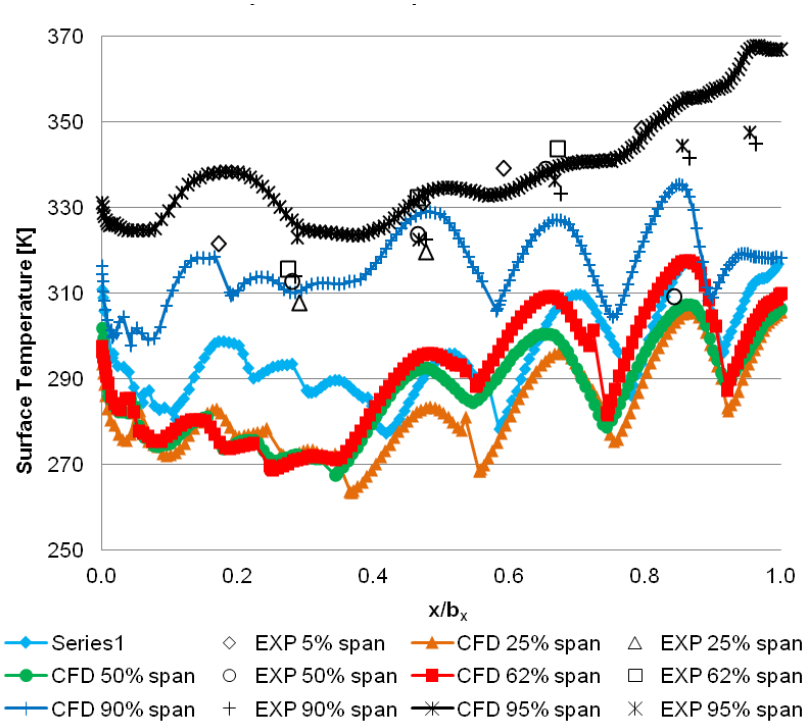

Figure C.4 – Cooled RTV PS T_s [K] at six span locations comparing CHT CFD to experiments.

The current work is intended to simulate the engine-representative environment and realistic 3-D geometry of the Turbine Research Facility for a modern turbine vane with and without film cooling using the most accurate CFD methods available. The conjugate assessment includes the effects of solid conduction in the simulations and factors in the internal plenum flows, cooling hole passages, and external main flows within the fluid domain. In looking at the experimental data alone, the TRF runs found both heat flux and surface temperature to be generally lower with film cooling.

Disparities in the predictions by the CHT CFD may be attributed to a number of factor which include, but are not limited to:

- Since thermal phenomena take much longer to setup relative to pressure field phenomena, the TRF may not reach steady-state conduction levels over the

relatively short (while quite long for rigs of its kind) test time of 2.5 seconds. Therefore, future work will entail running the CHT CFD with solid conduction turned off, effectively providing a full-grid fluid assessment of the internal plenums, each cooling passage and the external flow with an isothermal wall boundary, and ultimately comparing it to the experimental heat transfer measurements.

- In the case of film cooling, a steady assumption of the CHT CFD may not be accurate. Inherent fluctuations in the flow due to film cooling injection on the vane surface may make half-second time-averaged values of heat flux more inaccurate than they really are. Even for uncooled vanes, the internal plenum conditions may be less steady than originally thought.
- Without instrumentation on the inside surface of the vane wall in the coolant plenums, it is hard to say how the coolant temperature is changing between the site of the existing instrumentation, used to set boundary conditions in CFD, before entering the vane and the injection plane at the vane surface.
- Much of the TRF instrumentation lies in areas of steep heat flux or temperature gradients as seen in the contour plots, which increases the chances of not predicting experimental measurements as well.
- The CHT CFD may require a more robust transition model that can do a better job predicting temperature in the vane stagnation region.
- The stream-wise orientation of the heat flux gauges, and resulting axial averaging, may not be as accurate as measurements which orient the gauges in the span-wise direction.

- Due to the current maturity level of the CHT code, the kapton and adhesive layers were not simulated by the CHT CFD.
- As mentioned, the uncooled case is inherently transient and requires further work to determine appropriate cooling outlet conditions that simulates the uncooled vane cooling flows in the TRF.

This resulting validation of an emerging CHT CFD code provides conjugate heat transfer predictions for a fully cooled engine-ready part in realistic flow conditions. Overall, the CHT simulations fared better predicting heat flux than temperature. With code maturation ongoing, *Leo* can one day be a reliable heat transfer-validated CFD code with film-cooling. Few, if any, CFD codes used in previous works in open literature have been completely validated for heat transfer assessments, even without film cooling present. These plots constitute some of the first attempts to run CFD with such realistic conditions and geometry, as well as the first attempts to directly compare conjugate simulations of heat flux to the same geometry and conditions in a highly-instrumented blowdown turbine ground test facility.

For the purposes of this optimization work, while the CHT CFD code can be improved, simulations of both the vane and flat plate in their respective experimental environments in the current work provide information regarding the relative similarities and differences that are likely observed between the geometries. Assuming the CHT CFD is more accurate and rigorous than the CEEF CFD, and knowing the conjugate similarities can be seen at multiple span locations, this adds confidence that the relative experimental flat plate results between the baseline and optimized designs represent what would be expected if the two designs were to be tested on a vane in the TRF.

References

[1] Han, J. C., Dutta, S., and Ekkad, S. V., *Gas Turbine Heat Transfer and Cooling Technology*, Taylor & Francis, New York, 2000.

[2] Mattingly, J. D., *Aircraft Engine Design, 2nd Edition*. American Institute of Aeronautics and Astronautics (AIAA) Education Series, Reston, VA, 2002.

[3] Bogard, D. G. and Thole, K. A., "Gas Turbine Film Cooling," *Journal of Propulsion and Power*, Vol. 22, March-April 2006, pp. 249-269.

[4] Dunn, M. G., "Convective Heat Transfer and Aerodynamics in Axial Flow Turbines," *ASME Journal of Turbomachinery*, Vol. 123, No. 4, 2001, pp. 637-686.

[5] USAF Chief Scientist, "Technology Horizons: A Vision for Air Force Science & Technology During 2010-2030," AF/ST-TR-10-01-PR, Vol.1, 2010.

[6] Clark, J. P., Koch, P. J., Ooten, M. K., Johnson, J. J., Dagg, J., McQuilling, M. W., Huber, F., and Johnson, P. D., 2009. "Design of Turbine Components to Answer Research Questions in Unsteady Aerodynamics and Heat Transfer." Technical Report AFRL-RZ-WP-TR-2009-2180, AFRL.

[7] Dunn, M.G. and Stoddard, F. J., "Studies of Heat Transfer to Gas Turbine Components," Calspan Corporation, Buffalo, New York, 1977, pp. 1-48.

[8] Goldstein, R. J., "Film Cooling," *Advances in Heat and Mass Transfer*, Academic Press, San Diego, Vol. 7, 1971, pp. 321-379.

[9] Bunker, R. S., "Gas Turbine Heat Transfer: Ten Remaining Hot Gas Path Challenges," *ASME Journal of Turbomachinery*, Vol. 129, April 2007, pp. 193-201.

[10] Bunker, R.S., "A Review of Shaped Hole Turbine Film-Cooling Technology," *ASME Journal of Heat Transfer*, Vol. 127, April 2005, pp. 441-453.

[11] Thole, K. A., Gritsch, M., Schulz, A., and Wittig, S., "Flowfield Measurements for Film Cooling Holes with Expanded Exits," Proceedings of the ASME Turbo Expo 1996, paper 96-GT-174.

[12] Dittmar, J., Schulz, A., and Wittig, S., "Assessment of Various Film cooling Configurations Including Shaped and Compound Angle Holes Based on Large- Scale Experiments," *ASME Journal of Turbomachinery*, Vol. 125, January 2003, pp. 57-64.

[13] Burdet, A., Abhari, R. S., and Rose, M. G., "Modeling of Film Cooling—Part II: Model for Use in Three-Dimensional Computational Fluid Dynamics," *ASME Journal of Turbomachinery*, Vol. 129, 2007, pp. 221-231.

[14] Harrison, K. L. and Bogard, D. G., "Use of the Adiabatic Wall Temperature in Film Cooling to Predict Wall Heat Flux and Temperature," Proceedings of the ASME Turbo Expo 2008, June 9-13, paper GT2008-51424.

[15] Dyson, T.E., Bogard, D. G., and Bradshaw, S. D., "Evaluation of CFD Simulations of Film Cooling Performance on a Turbine Vane Including Conjugate Heat Transfer Effects," Proceedings of the ASME Turbo Expo 2012, paper GT2012-69107.

[16] Incropera, F. P. and DeWitt, D. P., *Fundamentals of Heat and Mass Transfer*, 5th Ed., John Wiley & Sons, 2002, pp. 395.

[17] Thole, K. A., Sinha, A., Bogard, D. G., and Crawford, M. E., "Mean Temperature Measurements of Jets with a Crossflow for Gas Turbine Film Cooling Application," Rotating machinery Transport Phenomena, edited by J. H. Kim and W. J. Yang, Hemisphere, New York, 1992, pp. 69-85.

[18] Welsh, W. E., "Review of Results of an Early Rocket Engine Film-Cooling Investigation at the Jet Propulsion Laboratory," Technical Report No. 32-58, March 1961.

[19] Wieghardt, K., "Hot Air Discharge for De-Icing," Translated by the American Astronautical Foundation, Translation F-TS-919-RE, December 1946.

[20] Terry, J. E. and Caras, G. J., "Transpiration and Film Cooling of Liquid Rocket Nozzles," RSIC-535, March 1966.

[21] Anthony, R. J., Clark, J. P., Kennedy, S. W., Finnegan, J., Rademacher, R., Johnson, P. D., Hendershot, J., and Downs, J., "Flexible Non-Intrusive Heat Flux Instrumentation for the AFRL Research Turbine," Proceedings of the ASME Turbo Expo 2011, paper GT2011-46853.

[22] Papell, S. S., "Effect of Gaseous Film Cooling of Coolant Injection Through Angled Slots and Normal Holes," NASA Technical Note D-299, September 1960.

[23] Teekaram, A., Forth, C., and Jones, T. V., "The Use of Foreign Gas to Simulate the Effects of Density Ratios in Film Cooling," *ASME Journal of Turbomachinery*, Vol. 111, 1989, pp. 57-62.

[24] Hartnett, J. P., Birkebak, R. C., Eckert, E. R. G., "Velocity Distributions, Temperature Distributions, Effectiveness and Heat Transfer for Air Injected Through a Tangential Slot Into a Turbulent Boundary Layer," *ASME Journal of Heat Transfer*, Vol. 83, 1961, pp. 293-306.

[25] McCall, J. F., "Discrete Film Cooling In A Rocket With Curved Walls," Ph.D. Thesis, Air Force Institute of Technology, Wright-Patterson AFB, OH, 2009.

[26] Brown, A. and Saluja, C. L., "Film Cooling from a Single Hole and a Row of Holes of Variable Pitch to Diameter Ratio," *International Journal of Heat and Mass Transfer*, Vol. 22, 1979, pp. 525-533.

[27] Hoffs, A., Drost, U., and Bolcs, A., "An Investigation of Effectiveness and Heat Transfer on a Showerhead-Cooled Cylinder," Proceedings of the ASME Turbo Expo 1997, paper 97-GT-69.

[28] Schneider, M., Parneix, S., and von Wolfersdorf, J., "Effect of Showerhead Injection on Superposition of Multi-Row Pressure Side Film Cooling with Fan Shaped Holes," Proceedings of the ASME Turbo Expo 2003, paper GT2003-38693.

[29] Sellers, J. P., "Gaseous Film Cooling with Multiple Injection Stations," *AIAA Journal*, Vol. 1, No. 9, pp. 2154-2156.

[30] Muska, J. F., Fish, R. W., and Suo, M., "The Additive Nature of Film Cooling From Rows of Holes," *ASME Journal of Engineering for Power*, 1976, pp. 457-464.

[31] Blair, M. F., "Influence of Free-Stream Turbulence on Boundary Layer Transition in Favorable Pressure Gradients," *ASME Journal of Engineering for Power*, Vol. 104, 1984, pp. 743-750.

[32] Montomoli, F., D'Ammaro, A., and Uchida, S., "Uncertainty Quantification and Conjugate Heat Transfer: A Stochastic Analysis," Proceedings of the ASME Turbo Expo 2012, paper GT2012-68203.

[33] Bunker, R. S., "The Effects of Manufacturing Tolerances on Gas Turbine Cooling," *ASME Journal of Turbomachinery*, Vol. 131, 2009, pp. 041018-1 to -11.

[34] Leylek, J. H. and Zerkle, R. D., "Discrete-Jet Film Cooling: A Comparison of Computational Results with Experiments," *ASME Journal of Turbomachinery*, Vol. 116, 1994, pp. 358-368.

[35] Hoda, A. and Acharya, S., "Predictions of a Film Coolant Jet in Crossflow With Different Turbulence Models," *ASME Journal of Turbomachinery*, Vol. 122, 2000, pp. 558-569.

[36] Harrison, K. L. and Bogard, D. G., "Comparison of RANS Turbulence Models for Prediction of Film Cooling Performance," Proceedings of the ASME Turbo Expo 2008, paper GT2008-51423.

[37] Bianchini, C., Facchini, B., Mangani, L., and Maritano, M., "Heat Transfer Performances of Fan-Shaped Film Cooling Holes, Part II – Numerical Analysis," Proceedings of the ASME Turbo Expo 2010, paper GT2010-22809.

[38] Garg, V. K. and Gaugler, R. E., "Effect of Coolant Temperature and Mass Flow on Film Cooling of Turbine Blades," *International Journal of Heat and Mass Transfer*, Vol. 40, No. 2, 1997, pp. 435-445.

[39] Buck, F. A., Walters, D. K., Ferguson, J. D., McGrath, E. L., and Leylek, J. H., "Film Cooling on a Modern HP Turbine Blade Part I: Experimental & Computational Methodology and Validation," Proceedings of the ASME Turbo Expo 2002, paper GT2002-30470.

[40] Hiedmann, J. D., Rigby, D. L., and Ameri, A. A., "A Three-Dimensional Coupled Internal/External Simulation of a Film-Cooled Turbine Vane," *ASME Journal of Turbomachinery*, Vol. 122, April 2000, pp. 348-359.

[41] Walters, D. K. and Leylek, J. H., "A Detailed Analysis of Film-Cooling Physics: Part I—Streamwise Injection With Cylindrical Holes," *ASME Journal of Turbomachinery*, Vol. 122, January 2000, pp. 102-112.

[42] Kohli, A. and Thole, K. A., "A CFD Investigation on the Effects of Entrance Crossflow Directions to Film-Cooling Holes," 32nd National Heat Transfer Conference, Vol. 12, ASME, New York, 1997, pp. 223-232.

[43] Choi, D., "A Navier-Stokes Analysis of Film Cooling in a Turbine Blade," Proceedings of the 31st Aerospace Sciences Meeting, paper No. AIAA 93-0158.

[44] Sargison, J. E., Guo, S. M., Oldfield, M. L. G., Jones, T. V., and Rawlinson, A. J., "A Heat Transfer Study of a Film Cooled Nozzle Guide Vane," Proceedings of the RTO AVT Symposium, 2001.

[45] Laskowski, G. M., Tolpadi, A. K., and Ostrowski, M. C., "Heat Transfer Predictions of Film Cooled Stationary Turbine Airfoils," Proceedings of the ASME Turbo Expo 2007, May 14-17, paper GT2007-27497.

[46] Haldemann, C. W., Mathison, R. M., Dunn, M. G., Southworth, S. A., Harral, J. W., and Heltland, G., "Aerodynamic and Heat Flux Measurements in a Single-Stage Fully Cooled Turbine--Part II: Experimental Results," *ASME Journal of Turbomachinery*, Vol. 130, April 2008, pp. 021016-1 to 11.

[47] Mathison, R. M., Haldemann, C. W., and Dunn, M. G., "Heat Transfer for the Blade of a Cooled Stage and One-Half High-Pressure Turbine, Part I: Influence of Cooling Variation," Proceedings of the ASME Turbo Expo 2010, paper GT2010-22713.

[48] Mathison, R. M., Wishart, M. B., Haldemann, C. W., and Dunn, M. G., "Temperature Predictions and Comparison with Measurements for the Blade Leading Edge and Platform of a 1-1/2 Stage Transonic HP Turbine," Proceedings of the ASME Turbo Expo 2010, paper GT2010-22987.

[49] Haldemann, C. W., Mathison, R. M., and Dunn, M. G., "Fully-Cooled Single-Stage HP Transonic Turbine, Part II – Influence of Cooling Mass Flow Changes and Inlet Temperature Profiles on Blade and Shroud Heat-Transfer," Proceedings of the ASME Turbo Expo 2010, paper GT2010-23445.

[50] Tartanville, B. and Hirsch, C., "Modeling Film Cooling for Turbine Blade Design," Proceedings of the ASME Turbo Expo 2008, paper GT2008-50316.

[51] Burd, S. W. and Simon, T. W., "The Influence of Coolant Supply Geometry on Film Coolant Exit Flow and Surface Adiabatic Effectiveness," Proceedings of the ASME Turbo Expo 1997, paper 97-GT-25.

[52] Bohn, D., Ren, J., and Kusterer, K., "Conjugate Heat Transfer Analysis for Film Cooling Configurations with Different Hole Geometries," Proceedings of the ASME Turbo Expo 2003, June 16-19, paper GT2003-38369.

[53] Montomoli, F., Adami, P., Della Gatta, S., and Martelli, F., "Conjugate Heat Transfer Modelling in Film Cooled Blades," Proceedings of the ASME Turbo 2004, June 14-17, paper GT2004-53177.

[54] Na, S., Williams, B., Dennis, R. A., Bryden, K. M., and Shih, T. I-P., "Internal and Film Cooling of a Flat Plate with Conjugate Heat Transfer," Proceedings of the ASME Turbo Expo 2007, May 14-17, paper GT2007-27599.

[55] Dhiman, S. and Yavuzkurt, S., "Film Cooling Calculations with an Iterative Conjugate Heat Transfer Approach Using Empirical Heat Transfer Coefficient Corrections," Proceedings of the ASME Turbo Expo 2010, June 14-18, paper GT2010-22958.

[56] Zhao, L. and Wang, T., "An Investigation of Treating Adiabatic Wall Temperature as the Driving Temperature in Film Cooling Studies," Proceedings of the ASME Turbo Expo 2011, paper GT2011-46012.

[57] Chandran, P. M. D., Halder, P., Panda, R. K., and Prasad, B. V. S. S. S., "A Comparative Study of Film Cooling Effectiveness on a Flat Plate with Adiabatic and Conjugate Conditions for Different Hole Shapes," Proceedings of the ASME Turbo Expo 2012, paper GT2012-69142.

[58] Panda, R. K. and Prasad, B. V. S. S. S., "Conjugate Heat Transfer from a Flat Plate with Combined Impingement and Film Cooling," Proceedings of the ASME Turbo Expo 2012, paper GT2012-68830.

[59] Heidmann, J. D., Kassab, A. J., Divo, E. A., Rodriguez, F., and Steinthorsson, E., "Conjugate Heat Transfer Effects on a Realistic Film-Cooled Turbine Vane," Proceedings of the ASME Turbo Expo 2003, June 16-19, paper GT2003-38553.

[60] Facchini, B., Magi, A., and Scotti Del Greco, A., "Conjugate Heat Transfer Simulation of a Radially Cooled Gas Turbine Vane," Proceedings of the ASME Turbo Expo 2004, June 14-17, paper GT2004-54213.

[61] Yamane, T., Yoshida, T., Enomoto, S., Takaki, R., and Yamamoto, K., "Conjugate Simulation of Flow and Heat Conduction with a New Method for Faster Calculation," Proceedings of the ASME Turbo Expo 2004, June 14-17, paper GT2004-53680.

[62] Kusterer, K., Bohn, D., Sugimoto, T., and Tanaka, R., "Conjugate Calculations for a Film-Cooled Blade Under Different Operating Conditions," Proceedings of the ASME Turbo Expo 2004, June 14-17, paper GT2004-53719.

[63] Luo, J. and Razinsky, E. H., "Conjugate Heat Transfer Analysis of a Cooled Turbine Vane Using the V2F Turbulence Model," Proceedings of the ASME Turbo Expo 2006, May 8-11, paper GT2006-91109.

[64] Bamba, T. Yamane, T., and Yoshitaka, F., "Turbulence Model Dependencies on Conjugate Simulation of Flow and Heat Conduction," Proceedings of the ASME Turbo Expo 2007, May 14-17, paper GT2007-27824.

[65] Zhenfeng, W., Peigang, Y., Zhaoyuan, G., and Wanjin, H., "BEM/FDM Conjugate Heat Transfer Analysis of a Two-Dimensional Air-Cooled Turbine Blade Boundary Layer," *Journal of Thermal Science*, Vol. 17, No. 3, 2008, pp. 199-206.

[66] Ledezma, G. A., Laskowski, G. M., Dees, J. E., and Bogard, D. G., "Overall and Adiabatic Effectiveness Values on a Scaled Up Simulated Gas Turbine Vane: Part II—Numerical Solutions," Proceedings of the ASME Turbo Expo 2011, paper GT2011-46616

[67] Dees, J. E., Bogard, D. G., Ledezma, G. A., and Laskowski, G. M., "The Effects of Conjugate Heat Transfer on the Thermal Field Above a Film Cooled Wall," Proceedings of the ASME Turbo Expo 2011, paper GT2011-46617.

[68] Dyson, T. E., Bogard, D. G., and Bradshaw, S. D., "Evaluation of CFD Simulations of Film Cooling Performance on a Turbine Vane Including Conjugate Heat Transfer Effects," Proceedings of the ASME Turbo Expo 2012, paper GT2012-69107.

[69] Ho, K. S., Urwiller, C., Konan, S. M., Liu, J. S., and Aguilar, B., "Conjugate Heat Transfer Analysis for Gas Turbine Cooled Stator," Proceedings of the ASME Turbo Expo 2012, paper GT2012-68196.

[70] Mangani, L., Cerutti, M., Maritano, M, and Spel, M., "Conjugate Heat Transfer Analysis of NASA C3X Film Cooled Vane with an Object-Oriented CFD Code," Proceedings of the ASME Turbo Expo 2012, paper GT2012-23458.

[71] Hylton, L. D., Nirmalan, V., Sultanian, B. K., and Kaufman, R. M., "The Effects of Leading Edge and Downstream Film Cooling on Turbine Vane Heat Transfer," NASA Tech report 168015, 1988.

[72] Ni, R. H., Humber, W., Fan, G., Johnson, P. D., Downs, J., Clark, J. P., and Koch, P. J., "Conjugate Heat Transfer Analysis of a Film-Cooled Turbine Vane," Proceedings of the ASME Turbo Expo 2011, paper GT2011-45920.

[73] Dulikravich, G. S., Martin, T. J., Dennis, B. H., and Foster, N. F., "Multidisciplinary Hybrid Constrained GA Optimization," Evolutionary Algorithms in Engineering and Computer Science: Recent Advances and Industrial Applications, 1999.

[74] Dulikravich, G. S., "Aerodynamic Shape Design and Optimization," Proceedings of the 29th Aerospace Sciences Meeting, AIAA paper 91-0476.

[75] Quagliarella, D. and Della Cioppa, A., "Genetic Algorithms Applies to the Aerodynamic Design of Transonic Airfoils," AIAA paper 94-1896-CP.

[76] Obayashi, S. and Tsukhara, T., "Comparison of Optimization Algorithms for Aerodynamic Shape Design," *AIAA Journal*, Vol. 35, No. 8, August 1997, pp. 1413-1415.

[77] DeFalco, I., "An Introduction to Evolutionary Algorithms and their application to the Aerofoil Design Problem – Part II: the Results," Institute for Research on Parallel Information Systems (IRSIP), National Research Council of Italy.

[78] Durbin, P., Eaton, J., Laskowski, G., and Vicharelli, A., "Transonic Cascade Measurements to Support Turbulence Modeling," Air Force Office of Scientific Research, Contractors Meeting in Turbulence and Rotating Flows, 2004, pp. 57-62.

[79] Dennis, B. H., Dulikravich, G. S., Han, Z. X., "Constrained Shape Optimization of Airfoil Cascades Using a Navier-Stokes Solver and a Genetic/SQP Algorithm," Proceedings of the ASME Turbo Expo 1999, paper 99-GT-441.

[80] Dennis, B. H., Dulikravich, G. S., Han, Z. X., "Optimization of Turbomachinery Airfoils with a Genetic/Sequential-Quadratic-Programming Algorithm," *AIAA Journal of Propulsion and Power*, Vol. 17, No. 5, 2001, pp. 1123-1128.

[81] Anguita, D., Cravero, C., Filz, C., and Rivieccio, F., "An Innovative Technique for the Aerodynamic Design of Turbine Blade Profiles Using Artificial Intelligence," Proceedings of the 33rd AIAA Fluid Dynamics Conference, Orlando, FL, 2003.

[82] Demeulenaere, A., Ligout, A., and Hirsch, C., "Application of Multipoint Optimization to the Design of Turbomachinery Blades," Proceedings of the ASME Turbo Expo 2004, paper GT2004-53110.

[83] Arnone, A., Bonaiuti, D., Focacci, A., Pacciani, R., and Del Greco, A. S., "Parametric Optimization of a High-Lift Turbine Vane," Proceedings of the ASME Turbo Expo 2004, paper GT2004-54308.

[84] Oyama, A., Liou, M., and Obayashi, S., "Transonic Axial-Flow Blade Optimization: Evolutionary Algorithms/Three-Dimensional Navier-Stokes Solver," AIAA Journal of Propulsion and Power, Vol. 20, No. 4, 2004, pp. 612-619.

[85] Johnson, J. J., "Optimization of a Low Heat Load Turbine Nozzle Guide Vane," M.S. Thesis, Air Force Institute of Technology, 2006.

[86] Oksuz, O. and Akmandor, I. S., "Axial Turbine Blade Aerodynamic Optimization Using a Novel Multi-Level Genetic Algorithm," Proceedings of the ASME Turbo Expo 2008, paper No. GT2008-50519.

[87] Oksuz, O. and Akmandor, I. S., "Multi-Objective Aerodynamic Optimization of Axial Turbine Blades Using a Novel Multi-Level Genetic Algorithm," Proceedings of the ASME Turbo Expo 2008, paper GT2008-50521.

[88] Larocca, F., "Multiple Objective Optimization and Inverse Design of Axial Turbomachinery Blades," *AIAA Journal of Propulsion and Power*, Vol. 24, No. 5, 2006, pp. 1093-1099.

[89] Arabnia, M and Ghaly, W., "A Strategy for Multi-Point Shape Optimization of Turbine Stages in Three-Dimensional Flow," Proceedings of the ASME Turbo Expo 2009, paper GT2009-59708.

[90] Sivashanmugam, V. K., Arabnia, M., and Ghaly, W., "Aero-Structural Optimization of an Axial Turbine Stage in Three-Dimensional Flow," Proceedings of the ASME Turbo Expo 2010, paper GT2010-23406.

[91] Boselli, P. and Zangeneh, M., "An Inverse Design Based Methodology for Rapid 3D Multi-Objective/Multidisciplinary Optimization of Axial Turbines," Proceedings of the ASME Turbo Expo 2011, paper GT2011-46729.

[92] Cuciumita, C. F., Vilag, V. A., Silvestru, V., and Porumbel, I., "Genetic Algorithm for Gas Turbine Blading Design," Proceedings of the ASME Turbo Expo 2011, paper GT2011-46171.

[93] Kawatsu, K., Tani, N., Shimagaki, M., Uchiumi, M., Yamanishi, N., Mitsuhashi, K., and Mizuno, T., "Multi Objective Optimization of a Supersonic Axial Turbine Blade Row Shape for a Rocket Engine Turbopump," Proceedings of the 47th AIAA/ASME/SAE/ASEE Joint Propulsion Conference, AIAA paper 2011-5784.

[94] Kammerer, S., Mayer, J. F., Stetter, H., Paffrath, M., Wever, U., amd Jung, A. R., "Development of a Three-Dimensional Geometry Optimization Method for Turbomachinery Applications," *International Journal of Rotating Machinery*, Vol. 10, No. 5, 2004, pp. 373-385.

[95] Li, H., Song, L., Li, Y., and Feng, Z., "2D Viscous Aerodynamic Shape Optimization for Turbine Blades Based on Adjoint Method," Proceedings of the ASME Turbo Expo 2009, paper GT2009-59999.

[96] Luo, J., Xiong, J., Liu, F., and McBean, I., "Three-Dimensional Aerodynamic Design Optimization of a Turbine Blade by Using an Adjoint Method," Proceedings of the ASME Turbo Expo 2009, paper GT2009-60115.

[97] Wang, D. X. and Li, Y. S., "3D Direct and Inverse Design Using NS Equations and the Adjoint Method for Turbine Blades," Proceedings of the ASME Turbo Expo 2010, paper GT2010-22049.

[98] Dulikravich, G. S., Martin, T. J., and Han, Z. X., "Aero-Thermal Optimization of Internally Cooled Turbine Blades," Proceedings of the 4th ECCOMAS CFD Conference, 1998.

[99] Muller, S. D., Walther, J. H., and Koumoutsakos, P. D., "Evolution Strategies for Film Cooling Optimization," Technical Note, *AIAA Journal*, Vol. 39, No. 3, 2000, pp. 537-539.

[100] Rajadas, J. and Chattopadhyay, A., "Application of Design Optimization to Turbomachinery Design," Proceedings of the 9th AIAA/ISSMO Symposium on Multidisciplinary Analysis and Optimization, AIAA paper 2002-5662.

[101] Talya, S. S., Chattopadhyay, A., and Rajadas, J. N., "Multidisciplinary Design Optimization Procedure for Improved Design of a Cooled Gas Turbine Blade," *Engineering Optimization*, Vol. 34, No. 2, 2002, pp. 175-194.

[102] Favaretto, C. F. F. and Funazaki, K., "Application of Genetic Algorithms to Design of an Internal Turbine Cooling System," Proceedings of the ASME Turbo Expo 2003, paper GT2003-38408.

[103] Dennis, B. H., Egorov, I. N., Dulikravich, G. S., and Yoshimura, S., "Optimization of a Large Number of Coolant Passages Located Close to the Surface of a Turbine Blade," Proceedings of the ASME Turbo Expo 2003, paper GT2003-38051.

[104] Lee, K. D. and Kim, K. Y., "Shape Optimization of a Laidback Fan-Shaped Film-Cooling Hole to Enhance Cooling Performance," Proceedings of the ASME Turbo Expo 2010, paper GT2010-22398.

[105] Mousavi, A. and Nadarajah, S. K., "Adjoint-Based Multidisciplinary Design Optimization of Cooled Gas Turbine Blades," Proceedings of the 49th Aerospace Sciences Meeting, AIAA paper 2011-1131.

[106] Lad, B., He, L., and Romero, E., "Validation of the Immersed Mesh Block (IMB) Approach Against a Cooled Transonic Turbine Stage," Proceedings of the ASME Turbo Expo 2012, paper GT2012-68779.

[107] El-Ayoubi, C., Ghaly, W., and Hassan, I., "Optimization of Film Cooling Holes on the Suction Side of a High Pressure Turbine Blade," Proceedings of the ASME Turbo Expo 2012, paper GT2012-69773.

[108] Lee, K. D., Kim, S. M., and Kim, K. Y., "Numerical Analysis of Film-Cooling Performance and Optimization for a Novel Shaped Film-Cooling Hole," Proceedings of the ASME Turbo Expo 2012, paper GT2012-68529.

[109] Goldstein, R. J., Rask, R. B., and Eckert, E. R. G., "Film Cooling with Helium Injection into an Incompressible Air Flow," *International Journal of Heat and Mass Transfer*, Vol. 9, 1966, pp. 1341-1350.

[110] Mayle, R.E. and Camarata, F. J., "Multihole Cooling Film Effectiveness and Heat Transfer," *ASME Journal of Heat Transfer*, November 1975, pp. 534-538.

[111] Sasaki, M., Takahara, K., Kumagai, T., and Hamano, M., "Film Cooling Effectiveness for Injection from Multirow Holes," *ASME Journal of Engineering for Power*, Vol. 101, 1979, pp. 101-108.

[112] Wittig, S., Schulz, A., Gritsch, M., and Thole, K. A., "Transonic Film-Cooling Investigations: Effects of Hole Shapes and Orientations," Proceedings of the ASME Turbo Expo 1996, paper 96-GT-222.

[113] Sweeney, P. C. and Rhodes, J. F., "An Infrared Technique for Evaluating Turbine Airfoil Cooling Designs," *ASME Journal of Turbomachinery*, Vol. 122, January 2000, pp. 170-177.

[114] Schulz, A., "Infrared Thermography as applied to Film Cooling of Gas Turbine Components," *Measurement Science and Technology*, Vol. 11, 2000, pp. 948- 956.

[115] Baldauf, S., Schulz, A., and Wittig, S., "High-Resolution Measurements of Local Effectiveness from Discrete Hole Film Cooling," *ASME Journal of Turbomachinery*, Vol. 123, October 2001, pp. 758-765.

[116] Baldauf, S., Schulz, A., and Wittig, S., "High-Resolution Measurements of Local Heat Transfer Coefficients from Discrete Hole Film Cooling," *ASME Journal of Turbomachinery*, Vol. 123, October 2001, pp. 749-757.

[117] Brauckmann, D. and von Wolfersdorf, J., "Application of Steady State and Transient IR-Thermography Measurements to Film Cooling Experiments for a Row of Shaped Holes," Proceedings of the ASME Turbo Expo 2005, paper GT2005-68035.

[118] Saumweber, C. and Schulz, A., "Interaction of Film Cooling Rows: Effects of Hole Geometry and Row Spacing on the Cooling Performance Downstream of the Second Row of Holes," Proceedings of the ASME Turbo Expo 2003, paper GT2003-38195.

[119] Lu, Y., Dhungel, A., Ekkad, S. V., and Bunker, R. S., "Film Cooling Measurements for Cratered Cylindrical Inclined Holes," *ASME Journal of Turbomachinery*, Vol. 131, January 2009, pp. 011005-1 to -12.

[120] Dhungel, A., Lu, Y., Phillips, W., Ekkad, S. V., and Heidmann, J., "Film Cooling From a Row of Holes Supplemented With Antivortex Holes," *ASME Journal of Turbomachinery*, Vol. 131, April 2009, pp. 021007-1 to -10.

[121] Kim, Y. J. and Kim, S. M., Influence of Shaped Injection Holes on Turbine Blade Leading Edge Film Cooling," *International Journal of Heat and Mass Transfer*, Vol. 47, 2004, pp. 245-256.

[122] Dittmar, J., Jung, I. S., Schulz, A., Wittig, S., and Lee, J. S., "Film Cooling from Rows of Holes – Effect of Cooling Hole Shape and Row Arrangement on Adiabatic Effectiveness," *Annals NY Academy of Sciences*, pp. 321-328.

[123] Waye, S. K. and Bogard, D. G., "High Resolution Film Cooling Effectiveness Comparison of Axial and Compound Angle Holes on the Suction Side of a Turbine Vane," Proceedings of the ASME Turbo Expo 2006, paper No. GT2006- 90225.

[124] Martini, P. and Schulz, A., "Experimental and Numerical Investigation of Trailing Edge Film Cooling by Circular Coolant Wall Jets Ejected From a Slot With Internal Rib Arrays," *ASME Journal of Turbomachinery*, Vol. 126, April 2004, pp. 229-236.

[125] Waye, S. K. and Bogard, D. G., "High Resolution Film Cooling Effectiveness Measurements of Axial Holes Embedded in a Transverse Trench with Various Trench Configurations," Proceedings of the ASME Turbo Expo 2006, paper GT2006-90226.

[126] Ekkad, S. V., Ou, S., and Rivir, R. B., "A Transient Infrared Thermography Method for Simultaneous Film Cooling Effectiveness and Heat Transfer Coefficient Measurements from a Single Test," *ASME Journal of Turbomachinery*, Vol. 126, October 2004, pp. 597-603.

[127] Ekkad, S. V., Ou, S., and Rivir, R. B., "Effect of Jet Pulsation and Duty Cycle on Film Cooling From a Single Jet on a Leading Edge Model," *ASME Journal of Turbomachinery*, Vol. 128, July 2006, pp. 564-571.

[128] Novak, L., Mori, M., and Sekavcnik, M., "Heat Transfer Study in Rotating Cascade Using IR Thermography and CFD Analyses," *Heat and Mass Transfer*, Vol. 44, 2008, pp. 559-567.

[129] Davidson, F. T., Kistenmacher, D. A., and Bogard, D. G., "Film Cooling with a Thermal Barrier Coating: Round Holes, Craters and Trenches," Proceedings of the ASME Turbo Expo 2012, paper GT2012-70029.

[130] Davidson, F. T., Kistenmacher, D. A., and Bogard, D. G., "A Study of Deposition on a Turbine Vane with a Thermal Barrier Coating and Various Film Cooling Geometries," Proceedings of the ASME Turbo Expo 2012, paper GT2012-70033.

[131] Kinell, M., Utriainen, E., Najafabadi, H. N., Karlsson, M., and Barabas, B., "Comparison of Gas Turbine Vane Pressure Side and Suction Side Film Cooling Performance and the Applicability of Superposition," Proceedings of the ASME Turbo Expo 2012, paper GT2012-68994.

[132] Johnson, J. J., King, P. I., Clark, J. P., Lethander, A. T., Ni, R. H., and Humber, W., "Validation of Flat Plate Infrared Assessment for Vane Pressure Side Film Cooling Designs," Proceedings of the 47th AIAA/ASME/SAE/ASEE Joint Propulsion Conference & Exhibit, paper 2011-5606.

[133] Nicholson, J.H, Forest, A. E., Oldfield, M. L. G., and Schultz, D. L. "Heat Transfer Optimized Turbine Rotor Blades—An Experimental Study Using Transient Techniques", *ASME Journal of Engineering for Gas Turbines and Power*, Vol. 106, January 1984, pp. 173-182.

[134] Schuler, B. J., Kerrebrock, J. L., and Merchant, A., "Experimental Investigation of an Aspirated Fan Stage," Proceedings of the ASME Turbo Expo 2002, paper GT2002-30370.

[135] Goldstein, R. J., Eckert, E. R. G., and Burggraf, F., "Effects of Hole Geometry and Density on Three-Dimensional Film Cooling," *International Journal of Heat and Mass Transfer*, Vol. 17, 1974, pp. 595-607.

[136] Schmidt, D. L., Sen, B., and Bogard, D. G., "Film Cooling With Compound Angle Holes: Adiabatic Effectiveness," *ASME Journal of Turbomachinery*, Vol. 118, 1996, pp. 807-813.

[137] Zhang, L., Yin, J., and Moon, H. K., "The Effect of Compound Angle on Nozzle Suction Side Film Cooling," Proceedings of the ASME Turbo Expo 2012, paper GT2012-68357.

[138] Chen, P. H., Hung, M. S., and Ding, P. P., "Film Cooling Performance on Curved Walls With Compound Angle Hole Configuration," Annual NY Academy of Sciences, Vol. 934, 2001, pp. 353-360.

[139] Ito, S., Goldstein, R. J., and Eckert, E. R. G., "Film Cooling of a Gas Turbine Blade," *ASME Journal of Engineering for Power*, Vol. 100, 1978, pp. 476-481.

[140] Teekaram, A. J. H., Forth, C. J. P., and Jones, T. V., "Film Cooling in the Presence of Mainstream Pressure Gradients," *ASME Journal of Turbomachinery*, Vol. 113, 1991, pp. 484-492.

[141] Mayhew, J. E., Baughn, J. W., and Byerley, A. R., "The Effect of Freestream Turbulence on Film Cooling Adiabatic Effectiveness," Proceedings of the ASME Turbo Expo 2002, paper GT2002-30172.

[142] Schmidt, D. L. and Bogard, D. G., "Effects of Free-stream Turbulence and Surface Roughness on Film Cooling," Proceedings of the ASME Turbo Expo, paper 96-GT-462.

[143] Cutbirth, J. M., and Bogard, D. G., "Evaluation of Pressure Side Film Cooling With Flow and Thermal Field Measurements—Part II: Turbulence Effects," *ASME Journal of Turbomachinery*, Vol. 124, 2002, pp. 678-685.

[144] Schmidt, D. L., Sen, B., and Bogard, D. G., "Film Cooling With Compound Angle Holes: Heat Transfer," *ASME Journal of Turbomachinery*, Vol. 118, 1996, pp. 800-806.

[145] Cutbirth, J. M., and Bogard, D. G., "Evaluation of Pressure Side Film Cooling With Flow and Thermal Field Measurements—Part I: Showerhead Effects," *ASME Journal of Turbomachinery*, Vol. 124, 2002, pp. 670-677.

[146] Han, J. C. and Mendenhale, A. B., "Flat-Plate Film Cooling with Steam Injection Through One Row and Two Rows of Inclined Holes," *ASME Journal of Turbomachinery*, Vol. 108, 1986, pp. 137-144.

[147] Sinha, A. K., Bogard, D. G., and Crawford, M. E., "Gas Turbine Film Cooling: Flowfield Due to a Second Row of Holes," *ASME Journal of Turbomachinery*, Vol. 113, 1991, pp. 450-456.

[148] Fric, T. F. and Campbell, R. P., "Method for Improving the Cooling Effectiveness of a Gaseous Coolant Stream Which Flows Through a Substrate, and Related Articles of Manufacture," U.S. Patent No. 6,383,602, 2002.

[149] Rhee, D. H., Lee, Y. S., and Cho, H. H., "Film Cooling Effectiveness and Heat Transfer of Rectangular-Shaped Film Cooling Holes," Proceedings of the ASME Turbo Expo 2002, paper GT2002-30168.

[150] Rhee, D. H., Lee, Y. S., and Cho, H. H., "Film Cooling and Thermal Field Measurements for Staggered Rows of Rectangular Film Cooling Holes," Proceedings of the ASME Turbo Expo 2002, paper GT2003-38608.

[151] Sargison, J. E., Guo, S. M., Oldfield, M. L. G., Lock, G. D., and Rawlinson, A. J., "A Converging Slot-Hole Film-Cooling Geometry—Part 1: Low-Speed Flat-Plate Heat Transfer and Loss," *ASME Journal of Turbomachinery*, Vol. 124, 2002, pp. 453-460.

[152] Sargison, J. E., Guo, S. M., Oldfield, M. L. G., Lock, G. D., and Rawlinson, A. J., "A Converging Slot-Hole Film-Cooling Geometry—Part 2: Transonic Nozzle Guide Vane Heat Transfer and Loss," *ASME Journal of Turbomachinery*, Vol. 124, 2002, pp. 461-471.

[153] Zuniga, H. A. and Kapat, J. S., "Effect of Increasing Pitch-to-Diameter Ratio on the Film Cooling Effectiveness of Shaped and Cylindrical Holes Embedded in Trenches," Proceedings of the ASME Turbo Expo 2009, paper GT2009-60080.

[154] Dorrington, J. R., Bogard, D. G., and Bunker, R. S., "Film Effectiveness Performance for Coolant Holes Embedded in Various Shallow Trench and Crater Depressions," Proceedings of the ASME Turbo Expo 2007, paper GT2007-27992.

[155] Kross, B. and Pfitzner, M., "Numerical and Experimental Investigation of the Film Cooling Effectiveness and Temperature Fields Behind a Novel Trench Configuration at High Blowing Ratio," Proceedings of the ASME Turbo Expo 2012, paper GT2012-68357.

[156] Kusterer, K., Elyas, A., Bohn, D., Sugimoto, T., Tanaka, R., and Kazari, M., "Film Cooling Effectiveness Comparison Between Shaped- and Double Jet Film Cooling Holes in a Row Arrangement," Proceedings of the ASME Turbo Expo 2010, paper GT20010-22604.

[157] Kusterer, K., Tekin, N., Bohn, D., Sugimoto, T., Tanaka, R., and Kazari, M., "Experimental and Numerical Investigations of the Nekomimi Film Cooling Technology,".

[158] Vehr, J. W., "Cross-flow Film Cooling Passages," U.S. Patent number 4,653,983, 31 March 1987.

[159] Johnson, J. J., King, P. I., Clark, J. P., Lethander, A. T., and Posada, N. A., "Infrared Assessment of an Optimized Vane Pressure Side Film Cooling Array," Proceedings of the International Mechanical Engineering Conference and Exposition 2012, paper IMECE2012-87829.

[160] Bunker, R. S., "Film Cooling Effectiveness Due to Discrete Holes Within a Transverse Surface Slot," Proceedings of the ASME Turbo Expo 2002, paper GT2002-30178.

[161] Bai, J. T., Zhu, H. R., and Liu, C. L., "Film Cooling Characteristic of Double-Fan-Shaped Film Cooling Holes," Proceedings of the ASME Turbo Expo 2009, paper GT2009-59318.

[162] Nasir, H., Acharya, S., and Ekkad, S., "Improved Film Cooling from Cylindrical Angled Holes with Triangular Tabs: Effect of Tab Orientations," *International Journal of Heat and Fluid Flow*, Vol. 24, 2003, pp. 657-668.

[163] Liu, J. S., Malak, M. F., Tapia, L. A., Crites, D. C., Ramachandran, D., Srinivasan, B., Muthiah, G., and Venkataramanan, J., "Enhanced Film Cooling Effectiveness with New Shaped Holes," Proceedings of the ASME Turbo Expo 2010, paper GT2010-22774.

[164] Sakai, E., Takahashi, T., and Agata, Y., "Experimental Study on Effects of Internal Ribs and Rear Bump on Film Effectiveness," Proceedings of the ASME Turbo Expo 2012, paper GT2012-68268.

[165] Luque, S., Batstone, J., Gillespie, D. R. H., Povey, T., and Romero, E., "Full Thermal Experimental Assessment of a Dendritic Turbine Vane Cooling Scheme," Proceedings of the ASME Turbo Expo 2012, paper GT2012-69910.

[166] Ni, R.H., "Advanced Modeling Techniques for New Commercial Engines," 1999, XIV ISOABE Conference, Florence, Italy, 5-10 September.

[167] Lax, P. D., and Wendroff, B., "Difference Schemes for Hyperbolic Equations with High Order Accuracy," Communications on Pure and Applied Mechanics, Vol. 17, 1964, pp. 381-398.

[168] Wilcox, D. C., Turbulence Modeling for CFD (2nd Ed.), DCW Industries, Inc., 1998, pp. 119-125.

[169] Manzi, J., "The Origin of Species and Everything Else: Coping With Evolution and Religion," *National Review*, October 2007, pp. 42-46.

[170] Johnson, J. J., King, P. I., Clark, J. P., Anthony, R. J., Koch, P. J., Ooten, M. K., Kasik, E. A., and Ni, R. H., "Three-Dimensional Film-Cooled Vane CFD Simulations and Preliminary Comparison to Experiments," Proceedings of the 49th AIAA Aerospace Sciences Meeting, paper AIAA-2011-0499.

[171] Johnson, J. J., King, P. I., Clark, J. P., Lethander, A., and Ooten, M. K., "Infrared Assessment Of Overall Effectiveness Of A Modern Turbine Vane Cooling Scheme," Proceedings of the 2010 AIAA Joint Propulsion Conference, paper AIAA 2010-7026.

[172] Johnson, J. J., King, P. I., Clark, J. P., Anthony, R. J., Koch, P. J., Ooten, M. K., Finnegan, J., Kobelak, M., Johnson, P. D., and Huber, F., " Three-Dimensional Viscous CFD Predictions of Vane-Only Configuration of a Full-Scale Experimental Turbine Rig," Proceedings of the 46th AIAA/ASME/SAE/AASE Joint Propulsion Conference, paper AIAA 2010-7027.

[173] Polanka, M. D., Hoying, D. A., Meininger, M., and McArthur, C. D., "Turbine Tip and Shroud Heat Transfer and Loading Part A: Parameter Effects Including Reynolds Number, Pressure Ratio and Gas to Metal Temperature Ratio", *ASME Journal of Turbomachinery*, Vol. 125, 2000, pp. 97-106.

[174] Rai, M. M., 1987, "Navier-Stokes Simulations of Rotor-Vane Interaction Using Patched and Overlaid Grids," *AIAA Journal of Propulsion and Power*, Vol. 3, pp. 387-396.

[175] Adamczyk, J. J., 2000, "Aerodynamic Analysis of Multi-Stage Turbomachinery Flows in Support of Aerodynamic Design," *ASME Journal of Turbomachinery*, Vol. 122, pp. 189-217.

[176] Clark, J. P., Stetson, G.M., Magge, S.S., Dunn, M.G., and Haldemann, C.W., 2000, "The Effect of Airfoil Scaling on the Unsteady Aerodynamics of a 1 and 1/2 Stage Transonic Turbine and a Comparison with Experimental Results", ASME paper 2000-GT-446.

[177] Clark, J. P., Aggarwala, A. S., Velonis, M. A., Magge, S. S., and Price, F. R., 2002, "Using CFD to Reduce Resonant Stresses on a Single-Stage, High-Pressure Turbine Blade," ASME paper GT2002-30320.

[178] Johnson, P. D., "Euler Model Simulation of the TRF Isolation Valve", Pratt & Whitney, 1996.

[179] Oldfield, M. L. G, "Impulse Response Processing of Transient Heat Transfer Gauge Signals," Proceedings of the ASME Turbo Expo 2006, paper GT2006-90949.

[180] Johnson, J. J., Clark, J. P., Flanagan, M. J., "RANS Simulations of Turbine Vane Heat Transfer in Short Duration, Shock-Tunnel Experiments," Proceedings of the 43rd AIAA/ASME/SAE/AASE Joint Propulsion Conference, paper AIAA 2007-5000.

Vita

Major Jamie J. Johnson was born 26 December 1980 in Doylestown, Pennsylvania, the son of Jack J. and Kaylene S. Johnson. He attended Central Bucks High School West in Doylestown and graduated in 1998. Upon graduating high school he entered undergraduate studies at The Pennsylvania State University in University Park, Pennsylvania. In May of 2002, he graduated with a Bachelor of Science degree in Aerospace Engineering and after completing the Air Force R.O.T.C. program, he was commissioned a Second Lieutenant in the USAF.

His first assignment was for the Air Force Research Laboratory in the Turbine Division of the Propulsion Directorate as a turbine research engineer. In 2004, he became a full time student at the Graduate School of Engineering and Management at the Air Force Institute of Technology (AFIT) where he received Master's Degrees in both Aeronautical and Astronautical Engineering. Following that, he was assigned to the Launch and Range Systems Wing within the Space and Missile Systems Center (SMC) at Los Angeles AFB, California where he contributed to technical risk reduction and sat on-console for 11 DoD satellite launches. In Aug 2009, he returned to full-time study at AFIT as a PhD student in Aeronautical Engineering and in March 2011, he was granted candidacy. After graduation with a PhD, he will return to SMC and work for the Space Superiority Systems Directorate.

REPORT DOCUMENTATION PAGE		Form Approved OMB No. 0704–0188

1. REPORT DATE (DD–MM–YYYY)	2. REPORT TYPE	3. DATES COVERED (From — To)
30-08-2012	PhD Dissertation	Aug 2009 – Aug 2012

4. TITLE AND SUBTITLE	5a. CONTRACT NUMBER
GENETIC ALGORITHM OPTIMIZATION OF A FILM COOLING ARRAY ON A MODERN TURBINE INLET VANE	5b. GRANT NUMBER 5c. PROGRAM ELEMENT NUMBER
6. AUTHOR(S) Johnson, Jamie J., Major, USAF	5d. PROJECT NUMBER 5e. TASK NUMBER 5f. WORK UNIT NUMBER
7. PERFORMING ORGANIZATION NAME(S) AND ADDRESS(ES) Air Force Institute of Technology Graduate School of Engineering and Management (AFIT/ENY) 2950 Hobson Way , WPAFB OH 45433-7765	8. PERFORMING ORGANIZATION REPORT NUMBER AFIT/DS/ENY/12-02
9. SPONSORING / MONITORING AGENCY NAME(S) AND ADDRESS(ES) Air Force Research Laboratory Aerospace Systems Directorate Turbine Division, Turbine Branch 1950 5th, WPAFB, OH 45433	10. SPONSOR/MONITOR'S ACRONYM(S) AFRL/RQTT 11. SPONSOR/MONITOR'S REPORT NUMBER(S)

12. DISTRIBUTION / AVAILABILITY STATEMENT
APPROVED FOR PUBLIC RELEASE; DISTRIBUTION UNLIMITED

13. SUPPLEMENTARY NOTES
This material is declared a work of the U.S. Government and is not subject to copyright protection in the United States.

14. ABSTRACT

In response to the need for more advanced gas turbine cooling design methods that factor in the 3-D flowfield and heat transfer characteristics, this study involves the computational optimization of a pressure side film cooling array on a modern turbine inlet vane. Latin hypersquare sampling, genetic algorithm reproduction, and Reynolds-Averaged Navier Stokes (RANS) computational fluid dynamics (CFD) as an evaluation step are used to assess a total of 1,800 film cooling designs over 13 generations. The process was efficient due to the *Leo* CFD code's ability to estimate cooling mass flux at surface grid cells using a transpiration boundary condition, eliminating the need for remeshing between designs. The optimization resulted in a unique cooling design relative to the baseline with new injection angles, compound angles, cooling row patterns, hole sizes, a redistribution of cooling holes away from the over-cooled midspan to hot areas near the shroud, and a lower maximum surface temperature. To experimentally confirm relative design trends between the optimized and baseline designs, flat plate infrared thermography assessments were carried out at design flow conditions. Use of flat plate experiments to model vane pressure side cooling was justified through a conjugate heat transfer CFD comparison of the 3-D vane and flat plate which showed similar cooling performance trends at multiple span locations. The optimized flat plate model exhibited lower minimum surface temperatures at multiple span locations compared to the baseline. Overall, this work shows promise of optimizing film cooling to reduce design cycle time and save cooling mass flow in a gas turbine.

15. SUBJECT TERMS
Film Cooling, High Pressure Turbines, Heat Transfer, Optimization, Genetic Algorithms, Infrared Thermography, Conjugate Heat Transfer, RANS CFD

16. SECURITY CLASSIFICATION OF:			17. LIMITATION OF ABSTRACT	18. NUMBER OF PAGES	19a. NAME OF RESPONSIBLE PERSON Dr. Paul I. King
a. REPORT U	b. ABSTRACT U	c. THIS PAGE U	UU		19b. TELEPHONE NUMBER (Include Area Code) (937)255-3636, ext 4628

Standard Form 298 (Rev. 8-98)
Prescribed by ANSI Std. Z39.18